Study of the optical properties of nanostructured thermochromic coatings containing vanadium dioxide nanoparticles

Cindy Peralle

N°d'ordre NNT : 2020LYSEM025

THESE de DOCTORAT DE L'UNIVERSITE DE LYON
opérée au sein de
l'Ecole des Mines de Saint-Etienne

Ecole Doctorale N° 488
Sciences, Ingénierie, Santé

Spécialité de doctorat : Sciences et Génie des Matériaux
Discipline : (Eventuellement)

Soutenue publiquement le 03/12/2020, par :
Cindy Péralle

Etude des propriétés optiques de revêtements thermochromes nanostructurés à base de VO_2

Study of the optical properties of nanostructured thermochromic coatings containing VO_2 nanoparticles

---

Devant le jury composé de :

Chenal, Jean-Marc, Professeur, INSA Lyon	Président
Schwob, Catherine, Professeure, Institut des NanoSciences de Paris	Rapporteure
Flury, Manuel, Maître de conférences HDR, INSA Strasbourg	Rapporteur
Faucheu, Jenny, Professeure, Mines Saint-Etienne	Directrice de thèse
Charrière, Renée, Maitre-assistant, Mines Saint-Etienne	Encadrante de thèse

Spécialités doctorales :	Responsables :	Spécialités doctorales :	Responsables :
SCIENCES ET GENIE DES MATERIAUX	K. Wolski, Directeur de recherche	MATHEMATIQUES APPLIQUEES	O. Roustant, Maître-assistant
MECANIQUE ET INGENIERIE	S. Drapier, Professeur	INFORMATIQUE	O. Boissier, Professeur
GENIE DES PROCEDES	F. Gruy, Maître de recherche	SCIENCES DES IMAGES ET DES FORMES	JC. Pinoli, Professeur
SCIENCES DE LA TERRE	B. Guy, Directeur de recherche	GENIE INDUSTRIEL	N. Absi, Maître de recherche
SCIENCES ET GENIE DE L'ENVIRONNEMENT	D. Graillot, Directeur de recherche	MICROELECTRONIQUE	Ph. Lalevée, Professeur

EMSE : Enseignants-chercheurs et chercheurs autorisés à diriger des thèses de doctorat (titulaires d'un doctorat d'État ou d'une HDR)

ABSI	Nabil	MR	Génie industriel	CMP
AUGUSTO	Vincent	MR	Génie industriel	CIS
AVRIL	Stéphane	PR	Mécanique et ingénierie	CIS
BADEL	Pierre	MA(MDC)	Mécanique et ingénierie	CIS
BALBO	Flavien	PR	Informatique	FAYOL
BASSEREAU	Jean-François	PR	Sciences et génie des matériaux	SMS
BATTON-HUBERT	Mireille	PR	Sciences et génie de l'environnement	FAYOL
BEIGBEDER	Michel	MA(MDC)	Informatique	FAYOL
BLAYAC	Sylvain	MA(MDC)	Microélectronique	CMP
BOISSIER	Olivier	PR	Informatique	FAYOL
BONNEFOY	Olivier	PR	Génie des Procédés	SPIN
BORBELY	Andras	MR(DR2)	Sciences et génie des matériaux	SMS
BOUCHER	Xavier	PR	Génie Industriel	FAYOL
BRODHAG	Christian	DR	Sciences et génie de l'environnement	FAYOL
BRUCHON	Julien	MA(MDC)	Mécanique et ingénierie	SMS
CAMEIRAO	Ana	MA(MDC)	Génie des Procédés	SPIN
CHRISTIEN	Frédéric	PR	Science et génie des matériaux	SMS
DAUZERE-PERES	Stéphane	PR	Génie Industriel	CMP
DEBAYLE	Johan	MR	Sciences des Images et des Formes	SPIN
DEGEORGE	Jean-Michel	MA(MDC)	Génie industriel	Fayol
DELAFOSSE	David	PR0	Sciences et génie des matériaux	SMS
DELORME	Xavier	MA(MDC)	Génie industriel	FAYOL
DESRAYAUD	Christophe	PR	Mécanique et ingénierie	SMS
DJENIZIAN	Thierry	PR	Science et génie des matériaux	CMP
BERGER-DOUCE	Sandrine	PR	Sciences de gestion	FAYOL
DRAPIER	Sylvain	PR	Mécanique et ingénierie	SMS
DUTERTRE	Jean-Max	MA(MDC)		CMP
EL MRABET	Nadia	MA(MDC)		CMP
FAUCHEU	Jenny	MA(MDC)	Sciences et génie des matériaux	SMS
FAVERGEON	Loïc	CR	Génie des Procédés	SPIN
FEILLET	Dominique	PR	Génie Industriel	CMP
FOREST	Valérie	MA(MDC)	Génie des Procédés	CIS
FRACZKIEWICZ	Anna	DR	Sciences et génie des matériaux	SMS
GARCIA	Daniel	MR(DR2)	Sciences de la Terre	SPIN
GAVET	Yann	MA(MDC)	Sciences des Images et des Formes	SPIN
GERINGER	Jean	MA(MDC)	Sciences et génie des matériaux	CIS
GOEURIOT	Dominique	DR	Sciences et génie des matériaux	SMS
GONDRAN	Natacha	MA(MDC)	Sciences et génie de l'environnement	FAYOL
GONZALEZ FELIU	Jesus	MA(MDC)	Sciences économiques	FAYOL
GRAILLOT	Didier	DR	Sciences et génie de l'environnement	SPIN
GROSSEAU	Philippe	DR	Génie des Procédés	SPIN
GRUY	Frédéric	PR	Génie des Procédés	SPIN
HAN	Woo-Suck	MR	Mécanique et ingénierie	SMS
HERRI	Jean Michel	PR	Génie des Procédés	SPIN
KERMOUCHE	Guillaume	PR	Mécanique et Ingénierie	SMS
KLOCKER	Helmut	DR	Sciences et génie des matériaux	SMS
LAFOREST	Valérie	MR(DR2)	Sciences et génie de l'environnement	FAYOL
LERICHE	Rodolphe	CR	Mécanique et ingénierie	FAYOL
MALLIARAS	Georges	PR	Microélectronique	CMP
MOLIMARD	Jérôme	PR	Mécanique et ingénierie	CIS
MOUTTE	Jacques	CR	Génie des Procédés	SPIN
NAVARRO	Laurent	CR		CIS
NEUBERT	Gilles			FAYOL
NIKOLOVSKI	Jean-Pierre	Ingénieur de recherche	Mécanique et ingénierie	CMP
NORTIER	Patrice	PR	Génie des Procédés	SPIN
O CONNOR	Rodney Philip	MA(MDC)	Microélectronique	CMP
PICARD	Gauthier	MA(MDC)	Informatique	FAYOL
PINOLI	Jean Charles	PR	Sciences des Images et des Formes	SPIN
POURCHEZ	Jérémy	MR	Génie des Procédés	CIS
ROUSSY	Agnès	MA(MDC)	Microélectronique	CMP
ROUSTANT	Olivier	MA(MDC)	Mathématiques appliquées	FAYOL
SANAUR	Sébastien	MA(MDC)	Microélectronique	CMP
SERRIS	Eric	IRD		FAYOL
STOLARZ	Jacques	CR	Sciences et génie des matériaux	SMS
TRIA	Assia	Ingénieur de recherche	Microélectronique	CMP
VALDIVIESO	François	PR	Sciences et génie des matériaux	SMS
VIRICELLE	Jean Paul	DR	Génie des Procédés	SPIN
WOLSKI	Krzystof	DR	Sciences et génie des matériaux	SMS
XIE	Xiaolan	PR	Génie industriel	CIS
YUGMA	Gallian	CR	Génie industriel	CMP

Mise à jour : 24/08/2020

Acknowledgements

First of all, I would like to thank La Région Auvergne Rhône-Alpes and Labex Manutech SISE for the financial support in this work.

Warm thanks to Jenny Faucheu for her implication throughout these three years. She always gave me good comments and advices to improve my work. Thanks to her sharing her vision and experience, I not only learnt about the scientific aspect of this work, but also a lot about myself. I am glad to have worked with her.

Special thanks to Renée Charrière for always being available when I needed advices on pretty much everything. She is full of ideas and hugely contributed to the quality of this work. It was such a pleasure to work with her and I am so grateful for all the time and energy she invested.

Of course, thank you to the members of this jury for accepting the invitation to my defense and grading my work. Their very pertinent questions lead to a fruitful discussion. Also, thank you for your interest while being so kind to me.

Thank you to the technicians, especially Max Boudes, for teaching me how to prepare and observe the samples shown in this thesis. Thank you to Laetitia Vieille for the infrared analysis and Nathalie Peillon for the X-Ray analysis of the VO_2 powder. Results of these analysis are however not presented in this thesis. I am still thankful for their contribution in my investigation.

Thank you to Julie Fortin for organizing scientific events and allowing me to share about this project with the public.

Then, I would like to warmly thank all my colleagues from K4 and J3 for the good atmosphere in our office, the afterwork parties and activities over the weekend. Also thank you to all the PhD students I met during the PhD parties, as well as their organizers. Thank you, Joseph, for the scalpel I used to prepare one sample.

Thank you to my family for the constant support and for coming to my defense. I would not have been able to go this far without them all. Same goes to my friends, especially Sophie, Mihail, Gautier and Robin who joined my defense.

Finally, I would like to thank a few special people who made my stay in Saint-Etienne much more pleasant. First, my Japanese teacher for the lessons I had in parallel to this PhD, the tons of homework and the Japanese parties, as well as the delicious bento boxes. And then, the former owners of the local Asian store Pai Lenh for providing me with cooking ingredients, especially my mom's rice, and for driving me to the hospital when I was sick.

Table of Contents

Introduction

Vanadium dioxide (VO_2) is an inorganic compound having a thermochromic phase transition from semiconducting to metallic at a characteristic transition temperature. This phase transition, discovered by Morin in 1959 [1], is followed by multiple changes of the material physical properties. Among them, large variations of its optical and thermal properties (refractive index, reflectance, transmittance, emissivity) are observed at the phase transition. For example, a pure VO_2 film layer passively encounters a significant transmittance decrease in the near infrared region at a temperature of 68°C. As about half of the total solar energy reaching the ground is located in this spectral region, this property made VO_2 interesting for use as an energy-efficient window coating [2,3]. For this kind of application, parameters such as luminous and solar transmittances, respectively describing the material visual transparency and the ratio of solar energy transmitted through the material, are used to quantify the material performances for this target application. While the first parameter should remain high to ensure a transparent window in all weather conditions, the second one should significantly decrease at higher temperatures in order to limit the light transmitted through the coated window in warm conditions.

Other applications are interested in another property change at the VO_2 phase transition: the material emissivity, defined as the ratio between the energy radiated by a material surface to the energy radiated by a perfect emitter (blackbody) at the same temperature. A pure VO_2 film encounters an emissivity decrease from about 0.6 to 0.1 when the temperature increases and goes through the VO_2 transition temperature [4]. While camouflage applications require an emissivity decrease as the temperature increases, which is what is naturally obtained for VO_2 film [4] or nanoparticles [5], the opposite effect is required for energy-efficient coatings for buildings and satellites. Metallic substrates such as aluminum have, for example, been used to successfully revert this emissivity switch [6]. As for the energy-efficient window coatings, the current state of the art presents various VO_2-based materials having promising optical properties towards such applications, like a $TiO_2/VO_2/TiO_2/VO_2/TiO_2$ multilayer film [7] or a nanocomposite consisting of VO_2 nanoparticles dispersed in a polymer [8].

Inspired by the promising performances of polymer nanocomposites containing VO_2 nanoparticles, this thesis explores the effects of a material nanostructuration in the case of a nanostructured polymer composite containing VO_2 nanoparticles. Periodically structured materials with a spatial period in the same order as the light wavelength are called photonic crystals (PhC). Depending on the structural parameters (like the particles size or structure period) and materials refractive index, a range of forbidden frequencies called photonic bandgap (PBG) can be generated, resulting in a controllable (in size and position) reflectance peak. In particular, opal photonic crystals consist in stacked polymer spheres arranged in a face-centered cubic (fcc) lattice and can be manufactured using techniques like self-assembly techniques, relatively simpler than other techniques used to manufacture photonic crystals, like lithography techniques, but has a few drawbacks like an undesired structural disorder introduced during the manufacturing process [9]. Such inexpensive 3D structures are attractive as they allow the fabrication of large-scale low-cost 3D photonic crystals.

Combining the thermochromic property of VO_2 with the reflectance peak brought by the material nanostructuration is made by introducing VO_2 nanoparticles in the interstices of a polymer opal photonic crystal, analogous to carbon nanoparticles introduced in a polymer opal photonic crystal interstices by Baumberg et al. [10]. The optical properties of such material are numerically studied in this thesis. An optical model based on the Fourier modal method (FMM) is used in order to predict the material optical performances for each selected application.

After a quick introduction of the optical vocabulary used along this thesis, the first chapter introduces the two main aspects of this work. On one hand, the VO_2 optical properties will be presented, along with a description of the state-of-the-art associated with each selected application. On the other hand, the photonic crystals and their photonic bandgaps will be introduced, with a particular focus on the opal photonic crystals, their manufacturing process and optical properties. Finally, a description of a few commonly used numerical models used to model the optical properties of periodic structures is given.

The second chapter presents a few validation tests of the developed model, on aspects like material and structure. The VO_2 is described by two distinct complex refractive indexes, one for each cold and warm state. A progressive approach is made towards modelling a complex 3D structure using a numerical method typically used for only 1D and 2D periodic structures. An approximation is also made and presented in this second chapter: the simplified model does not consider each single VO_2 nanoparticle individually but an averaged material consisting of VO_2 nanoparticles dispersed in a polymer. The opal interstices containing these VO_2 nanoparticles are thus described by an effective refractive index, and the accuracy of such approximation is evaluated.

The third chapter is focused on the material optical properties in the visible and near infrared region. In these spectral regions, the luminous and solar transmittances are calculated through the model as this chapter is oriented towards an application as energy-efficient coating for windows. A particular attention is made on the impact of the structure on the material optical properties.

The fourth chapter is, in a similar approach as the previous chapter, focused on the mid infrared region. This time, the material emissivity is the main interest and targeted applications are energy-efficient coating for buildings and satellites, as well as camouflage applications. The structural parameters are adjusted in order to optimize the impact of ordering on the material emissivity. A few ideas are then explored for possible enhanced performances towards these target applications.

The fifth chapter aims at introducing structural disorder in the model in order to better describe real materials. A description of how it is technically introduced in the program is given. In order to allow a comparison between numerical and experimental optical behaviors, tests are performed on a 2D structure, a porous alumina 2D photonic crystal, as one sample was locally manufactured in our laboratory. Manufacturing a polymer opal containing VO_2 nanoparticles was unfortunately not possible during this thesis. Structural parameters extracted from scanning electron microscopy (SEM) micrographs are injected into the model to allow the calculation of the material spectral reflectance, which are then compared to the reflectance experimentally measured by a spectrophotometer.

Chapter 1 State of the art

In this chapter the fundamentals and current state of the art about vanadium dioxide properties and photonic crystals with a focus on polymer opals will be presented. This chapter will be divided into four main sections. First of all, the fundamentals of materials optical properties will be presented, with an introduction to light energetic quantities and their implication in describing the optical properties of materials. These definitions will be further used in order to describe the optical behavior of the materials studied in this thesis. Then, in a second section, these quantities will be used to describe the optical properties of vanadium dioxide. Vanadium dioxide is a promising material for the applications considered in this thesis because of its thermochromic property. Since combining an ordered nanostructure with a thermochromic material such as vanadium dioxide may improve these interesting optical properties, the third section will be focused on the optical properties of nanostructured gratings called photonic crystals. Finally, these properties will be studied in this thesis using numerical methods. A list of the most commonly used optical models will be presented in the last section.

1.1. Generalities on materials optical properties

In this first section, quantities used to describe material optical properties will be introduced.

1.1.1. Energetic definitions

This section aims at introducing a few definitions used to quantify light energy flow emitted at a source and received at a sensor.

First of all, the radiant power (or radiant flux) ϕ counts the energy traveling through a surface in a certain amount of time. It is a flow of energy per unit time (J/s = W). The radiant power per unit surface arriving at a surface S_{in} is called irradiance and denoted by E. The radiant power per unit surface leaving a surface S_{out} is called exitance (or emittance) and denoted by M. These last quantities are expressed as differential flux per differential area:

$$M = \frac{d\phi}{dS_{out}} \tag{1. 1}$$

$$E = \frac{d\phi}{dS_{in}} \tag{1. 2}$$

Light propagation can be described as a function of a spatial direction in 3D. In order to introduce the 3D directional aspect, the notion of solid angles is now introduced. This solid angle is the 3D extension of 2D angles and is expressed in steradians (sr). Considering a sphere of radius 1 centered on the viewpoint P, we define the solid angle of an object as the area of the projection of this object on this sphere. Thus, similarly to 2D angle definition, considering a sphere with a radius r, the solid angle $d\Omega$ is defined as the ratio of the intercepted area on the sphere dS over the square of the sphere radius:

$$\mathrm{d}\Omega = \frac{dS}{r^2} \tag{1. 3}$$

With this directional aspect in mind, we introduce the radiant intensity I which describes the radiant power traveling in a certain direction per unit solid angle:

$$I = \frac{d\phi}{d\Omega} \tag{1. 4}$$

and the radiance L which describes the power leaving an area S_{out} in a certain direction per unit solid angle and apparent surface:

$$L = \frac{d^2\phi}{dS_{out}\cos(\theta)\,d\Omega}. \quad (1.\,5)$$

θ is defined as the angle between the normal to dS_{out} and the direction of light propagation $\vec{\Omega}$, as shown in **Figure 1**.

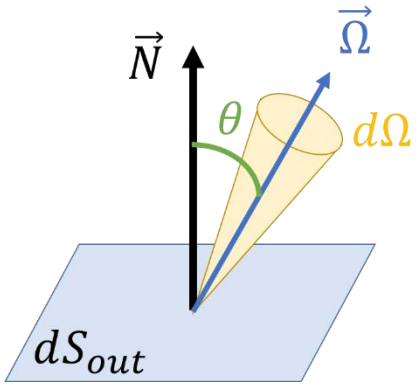

Figure 1: Schematic representation of the light emitted from the surface dS_{out} in the cone defined by the solid angle $d\Omega$ in a direction θ relatively to the surface normal.

All the definitions presented in this section, along with their units, are summed up in **Table 1**.

Name	Mathematical definition	Unit
Radiant power	ϕ	W
Exitance or emittance	$M = \frac{d\phi}{dS_{out}}$	W.m^{-2}
Irradiance	$E = \frac{d\phi}{dS_{in}}$	W.m^{-2}
Radiant intensity	$I = \frac{d\phi}{d\Omega}$	W.sr^{-1}
Radiance	$L = \frac{d^2\phi}{dS_{out}\cos(\theta)\,d\Omega}$	W.m^{-2}.sr^{-1}

Table 1: Summary of light energetic quantities.

To take into account possible variations of the previous quantities with the wavelength λ, we introduce the spectral radiant power ϕ_λ, the spectral exitance M_λ, the spectral irradiance E_λ, the spectral radiant intensity I_λ and the spectral radiance L_λ. These quantities are defined as:

$$\phi_\lambda = \frac{d\phi}{d\lambda} \quad (1.\,6)$$

$$M_\lambda = \frac{dM}{d\lambda} \quad (1.\,7)$$

$$E_\lambda = \frac{dE}{d\lambda} \quad (1.\,8)$$

$$I_\lambda = \frac{dI}{d\lambda} \quad (1.\ 9)$$

$$L_\lambda = \frac{dL}{d\lambda} \quad (1.\ 10)$$

1.1.2. Refractive index, reflectance, transmittance, absorbance

From an optical point of view, materials are generally described by their optical refractive index. This value, denoted n, is a dimensionless value which describes how light interacts with this material. For example, the higher the index, the slower the light travels inside the medium. This is described by:

$$v = \frac{c}{n} \quad (1.\ 11)$$

with v the light velocity inside the medium of refractive index n and c the celerity in vacuum ($c = 2.997925.10^8$ m.s^{-1}). This index can depend on the light wavelength and in this case the material is called dispersive. It is also common to use the dielectric function ε instead of the refractive index. Both are linked by:

$$\varepsilon = n^2 \quad (1.\ 12)$$

The refractive index can be real or complex. The imaginary component is called the extinction coefficient. This name is related to the fact that a higher extinction coefficient means that the light irradiance is more reduced during its propagation inside this material, resulting in a lower irradiance at the end.

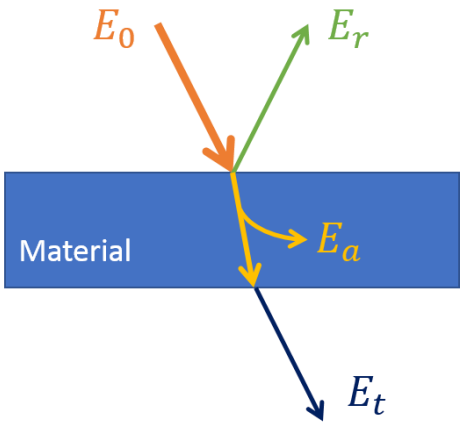

Figure 2: Light interactions at a material interface, showing the incident (E_0), reflected (E_r), transmitted (E_t) and absorbed (E_t) irradiances.

In a 1D propagation along the x-axis, the Beer-Lambert law states that the irradiance after a propagation of a distance d in the absorbing material is [11]:

$$E(x) = E_0\, e^{-\alpha\, d} \quad (1.\ 13)$$

with E_0 the incident irradiance and α the absorption coefficient defined as:

$$\alpha = \frac{4\pi\ Im(n(\lambda))}{\lambda} \quad (1.\ 14)$$

with $Im(n(\lambda))$ the imaginary component of the material refractive index (extinction coefficient) at a wavelength λ. A high extinction coefficient thus leads to a more absorbing material.

The material absorptance A is a coefficient ($0 \leq A \leq 1$) describing the ratio of absorbed light in a material. It is defined as the ratio of the absorbed to the incident irradiances:

$$A(\lambda) = \frac{E_a(\lambda)}{E_0(\lambda)} \tag{1. 15}$$

with $E_a(\lambda)$ and $E_0(\lambda)$ respectively the absorbed and incident irradiances at a wavelength λ as shown in **Figure 2**. In a similar way, the reflectance and transmittance are defined as:

$$R(\lambda) = \frac{E_r(\lambda)}{E_0(\lambda)} \qquad \text{and} \qquad T(\lambda) = \frac{E_t(\lambda)}{E_0(\lambda)} \tag{1. 16}$$

with $I_r(\lambda)$ and $I_t(\lambda)$ respectively the irradiances of the reflected and transmitted light at a wavelength λ. Because of the energy conservation principle in a closed system, these ratios are linked together by:

$$1 = R(\lambda) + T(\lambda) + A(\lambda) \tag{1. 17}$$

This equation means that the incoming light is either reflected, transmitted or absorbed by the material.

1.1.3. Luminous and solar transmittance

Materials optical properties can also be translated into parameters related to a specific source or sensor. For applications related to the sun radiation, which is the case for applications considered in this thesis (energy-efficient coating materials for windows for example), it is interesting to define a performance criterion estimating how much solar radiation is transmitted through a material. This parameter is called the solar transmittance T_{sol} and is defined as the spectral transmittance weighted over the solar irradiance spectrum:

$$T_{sol}(\tau) = \frac{\int E_\lambda^{AM1.5}(\lambda)\, T(\lambda)\, d\lambda}{\int E_\lambda^{AM1.5}(\lambda)\, d\lambda}, \tag{1. 18}$$

with $E_\lambda^{AM1.5}$ the global AM1.5 solar irradiance spectrum for air mass 1.5. This corresponds to the sum of the direct normal irradiance from the Sun, the light scattered by the atmosphere and the diffuse light reflected by the ground, considering a 48.2° angle of the Sun with reference to the zenith (solar zenithal angle) facing a 37° tilted surface with reference to the horizon (see **Figure 3**) [12]. This spectrum is shown in **Figure 4**.

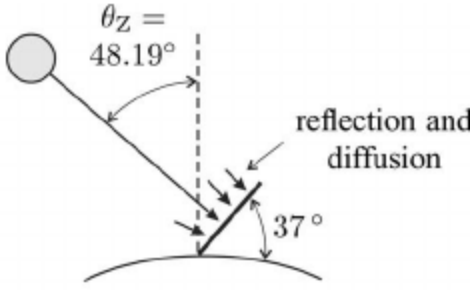

Figure 3: Illustration of the global AM1.5 solar radiation. Extracted from [12].

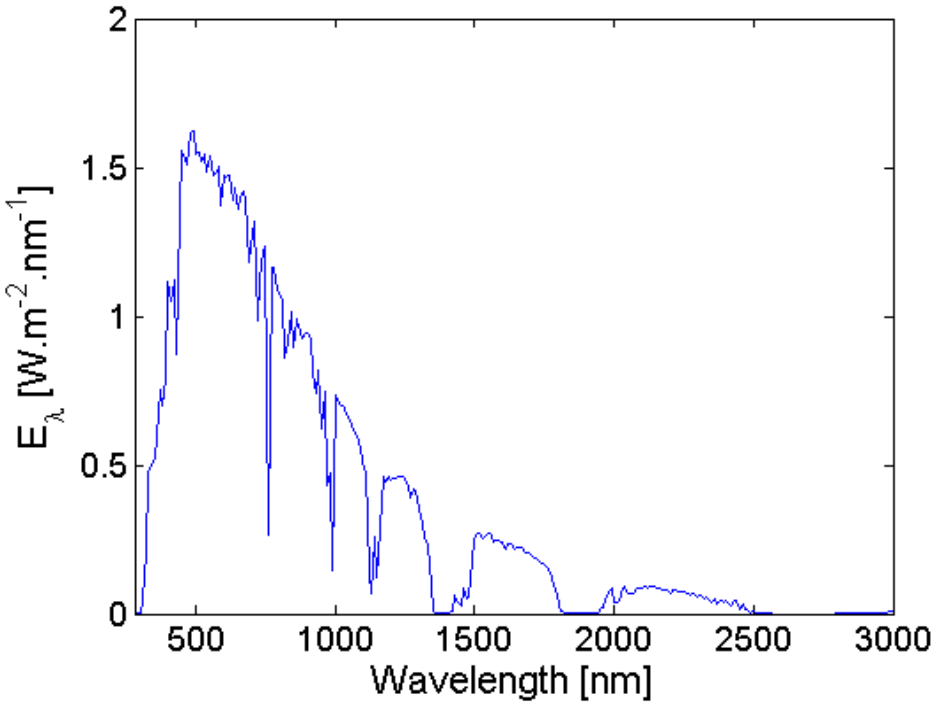

Figure 4: Solar irradiance spectrum of global AM1.5 (extracted from [13]*).*

According to **Figure 4**, the incoming solar energy has significant values in the visible and near infrared regions. Indeed, about 99% of the total energy is located in these two regions ($\lambda \in [350\ \text{nm}; 2500\ \text{nm}]$), with over 52% of the total irradiance in the near infrared region ($\lambda \in [700\ \text{nm}; 2500\ \text{nm}]$). This means that in the calculation of T_{sol}, the spectral transmittance $T(\lambda)$ has an influence in the result only in spectral regions with higher $E_\lambda^{AM1.5}$. We can thus limit the integration range from 350 to 2500 nm.

Replacing spectral transmittance by spectral reflectance, we also define the solar reflectance as:

$$R_{sol}(\tau) = \frac{\int E_\lambda^{AM1.5}(\lambda)\, R(\lambda)\, d\lambda}{\int E_\lambda^{AM1.5}(\lambda)\, d\lambda} \qquad (1.\ 19)$$

Similarly to the solar transmittance, another interesting performance criterion useful for applications considered in this thesis (smart windows) is used to describe how transparent a material is to our human eye. This parameter is called the luminous transmittance and is defined as the spectral transmittance weighted over the eye sensitivity:

$$T_{lum}(\tau) = \frac{\int V(\lambda)\, T(\lambda)\, d\lambda}{\int V(\lambda)\, d\lambda}, \qquad (1.\ 20)$$

with $V(\lambda)$ the spectral sensitivity of the light-adapted eye [14] shown in **Figure 5**. This curve shows how much the human eye is sensitive to each visible wavelength, with a maximum value in the green color around 555 nm. Based on the values of $V(\lambda)$, we consider that for the calculation of T_{lum}, the integration range can be set from 380 to 780 nm.

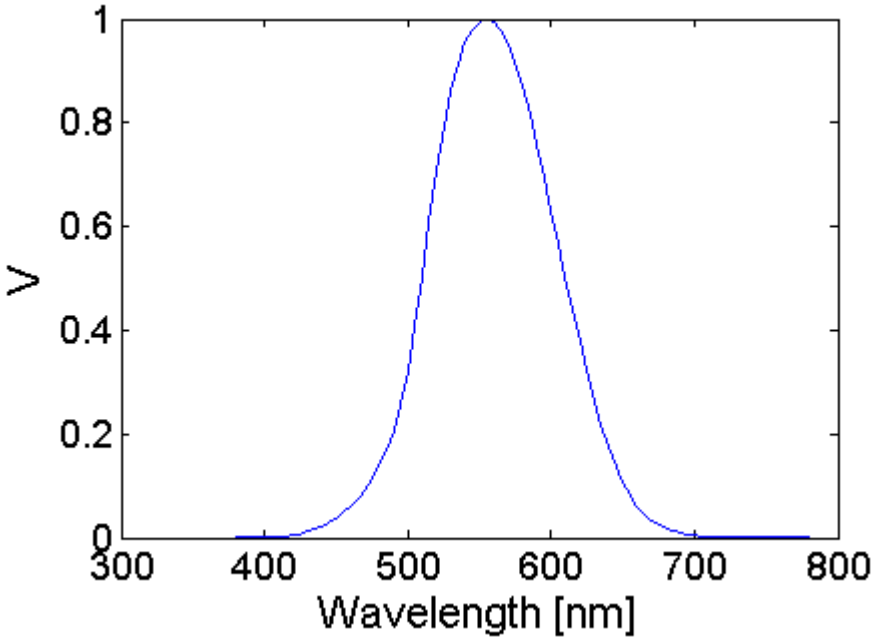

Figure 5: Spectral sensitivity of the light-adapted eye, extracted from [14].

Similarly, we define the luminous reflectance as:

$$R_{lum}(\tau) = \frac{\int V(\lambda)\, R(\lambda)\, d\lambda}{\int V(\lambda)\, d\lambda}. \tag{1. 21}$$

1.1.4. Blackbody and emissivity

The absorbed light is also later emitted by the material in the form of a thermal radiation which depends on the material temperature. A common description of the light emitted by a material is the blackbody radiation. A blackbody is a theoretical material that absorbs all incoming light (thus the "black") and emits all of it, it is thus a perfect absorber and emitter. The blackbody spectral radiance B_λ is given by Planck's law as a function of light wavelength λ and material temperature τ:

$$B_\lambda(\lambda, \tau) = \frac{2hc^2}{\lambda^5} \frac{1}{\exp\left(\frac{hc}{k_B\, \tau\, \lambda}\right) - 1} \tag{1. 22}$$

with h the Plank constant ($h = 6.62618.10^{-34}\,\mathrm{J.s}$), k_B the Boltzmann constant ($k_B = 1.38066.10^{-23}\,\mathrm{J.K^{-1}}$) and c the light celerity ($c = 2.997925.10^{8}\,\mathrm{m.s^{-1}}$) [15].

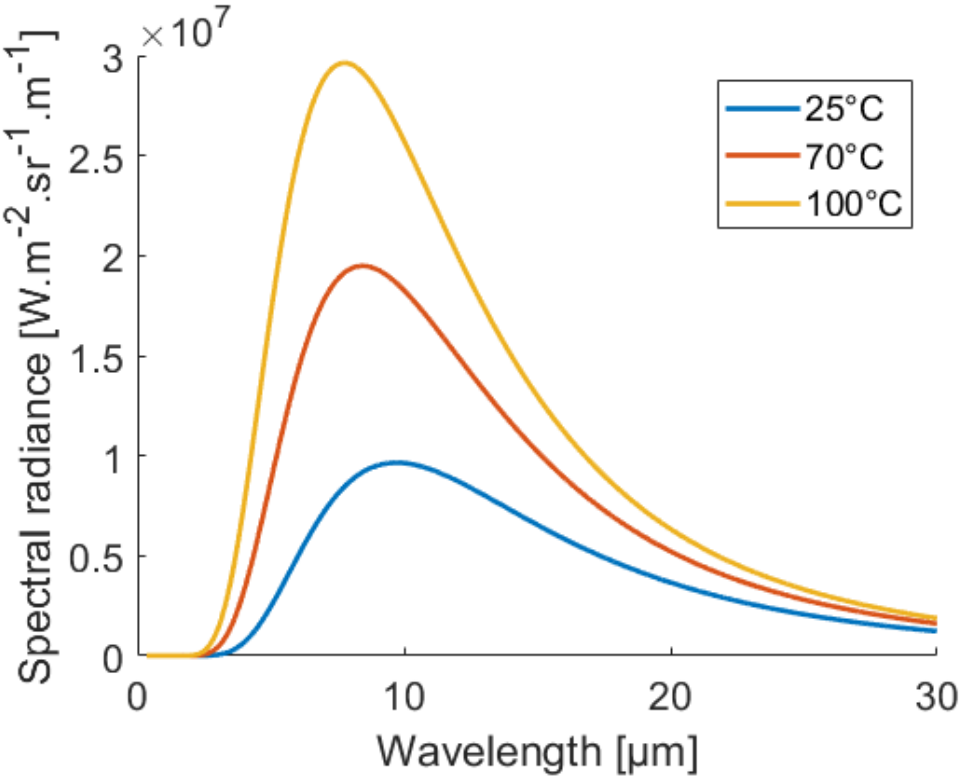

Figure 6: Blackbody spectral radiance in the mid infrared region, for different temperatures of the body.

A representation of this spectral radiance for different temperatures (25°C, 70°C and 100°C) is shown in **Figure 6**. As the temperature increases, the maximum radiance increases and blueshifts. This blueshift is well described by Wien's law:

$$\lambda_{max} = \frac{b}{\tau} \tag{1. 23}$$

with λ_{max} the wavelength position of the radiance peak, b a constant ($b \approx 2.897771955.10^{-3}$ m·K) and τ the material temperature. Also, it is worth noting that at the considered temperatures the blackbody radiation occurs in the mid infrared range. For example, at a temperature of 25 °C the peak is located at a wavelength of almost 10 µm.

Integrating the spectral radiance over a whole hemisphere gives the spectral exitance of the material. This integration results in:

$$M_\lambda(\lambda) = \pi\, B_\lambda(\lambda) \tag{1. 24}$$

However, a real material does not behave like a blackbody. A real material actually emits less power than a blackbody at the same temperature and its emissive power is quantified by the material emissivity ϵ. The emissivity ϵ ($0 \leq \epsilon \leq 1$) is defined as the spectral emittance ratio between the real material $M_{\lambda,real}$ and the blackbody M_λ at the same temperature τ:

$$\epsilon = \frac{\int M_{\lambda,real}(\lambda,\tau)\, d\lambda}{\int M_\lambda(\lambda,\tau)\, d\lambda} \tag{1. 25}$$

The integration ranges over the whole emittance spectrum, which depends on the body temperature.

The real material emittance can be expressed as:

$$M_{\lambda,real}(\lambda,\tau) = \epsilon_\lambda(\lambda,\tau)\, M_\lambda(\lambda,\tau) \quad (1.\ 26)$$

with ϵ_λ the spectral emissivity of the body. This results in a general definition of ϵ as the integrated spectral emissivity weighted by the theoretical blackbody spectral emittance at a given temperature τ:

$$\epsilon = \frac{\int \epsilon_\lambda(\lambda)\, M_\lambda(\lambda,\tau) d\lambda}{\int M_\lambda(\lambda,\tau)\, d\lambda} \quad (1.\ 27)$$

In addition, Kirchhoff law states that at thermal equilibrium for a Lambertian material (a body which emits the same radiance in all directions) [16]:

$$\epsilon_\lambda(\lambda) = A(\lambda) \quad (1.\ 28)$$

According to equation (1. 17), this spectral absorptance is also equal to $1 - R(\lambda) - T(\lambda)$. As a result, the material emissivity ϵ can be obtained through [6]:

$$\epsilon = \frac{\int \big(1 - R(\lambda) - T(\lambda)\big)\, M_\lambda(\lambda,\tau)\, d\lambda}{\int M_\lambda(\lambda,\tau)\, d\lambda}, \quad (1.\ 29)$$

where the integration should range over the wavelength range where the integrand has significant values.

1.1.5. Surface temperature

A material surface temperature T_s can be obtained from parameters like the solar reflectance R_{sol} and the emissivity ϵ using the thermal balance of a horizontal surface under the sun [17,18]:

$$(1 - R_{sol})\, E_{sun} = \epsilon\sigma \left(T_s^4 - T_{sky}^4\right) + h_c\, (T_s - T_{air}) \quad (1.\ 30)$$

where E_{sun} is the total solar irradiance (integrating $E_\lambda^{AM1.5}$ from 280 nm to 3000 nm gives $E_{sun} \approx 1000\ \mathrm{W.m^2}$) and σ is the Stefan-Boltzmann constant ($\sigma = 56.685.10^{-8}\ W.m^{-2}.K^4$). T_{sky} is the sky temperature, it depends on the air temperature T_{air} and the weather conditions. Various formula can be found in the literature [19], but in this thesis, we chose to calculate T_{sky} by [20]:

$$T_{sky} = 0.0552 \times T_{air}^{1.5} \quad (1.\ 31)$$

h_c is the convection coefficient which describes the heat transfer between the material and the fluid surrounding it. At the surface, this coefficient depends on various factors including the type of fluid, its velocity and the temperature difference between the material and the fluid. In the absence of wind, a wall has a convection coefficient of about 5 $W.m^{-2}.K^{-1}$ for a 30°C temperature difference.

In all future calculations, unless stated otherwise, these parameters are set to $T_{air} = 25°C$ (leading to $T_{sky} \approx 11°\mathrm{C}$ (*Equation (1. 31)*) and $h_c = 5\ \mathrm{W.m^{-2}.K^{-1}}$.

1.2. Vanadium dioxide properties and applications

1.2.1. Vanadium dioxide intrinsic physical properties

Vanadium dioxide (VO_2) is an inorganic compound among the vanadium oxides group [21]. In different environmental conditions, VO_2 shows variety of crystalline phases. A phase diagram on a wide range of temperature (from 0 to 120°C) and pressure (from 0 to 40 GPa) is shown in **Figure 7**. In those temperature and pressure ranges, five different VO_2 phases are identified: the insulating monoclinic phases M1 and M1' and three metallic phases which are the tetragonal rutile R, the orthorhombic O and monoclinic X.

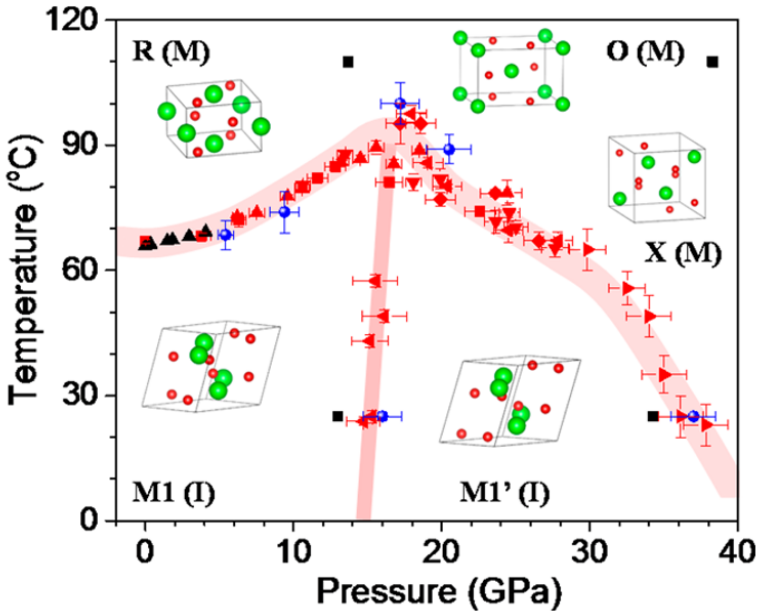

Figure 7: Vanadium dioxide phase diagram containing the insulating (I) M1 and M1' phases and the metallic (M) R, O and X phases. The crystal structure of each phase is represented with vanadium (green) and oxygen atoms (red). The red, blue and black dots are obtained from Raman, electrons and X-Ray Diffraction measurements respectively. [22]

The VO_2 most famous phases are the M1 (monoclinic, space group P21/c) and R (tetragonal, P42/mnm) phases, both obtained at relatively limited pressure (< 14 GPa) compared to the other three phases referred above. The VO_2 insulating metallic transition (IMT) occurs at a transition temperature of about τ_c = 68°C in the case of a pure VO_2 film. This phase transition is characterized by a change of the VO_2 physical properties such as an increase of its electric conductivity and a drop of its near infrared optical transmittance (see Figure 11). These variations of optical properties due to a change of temperature are called thermochromic properties and such material is said to be a thermochromic material. Morin has discovered the thermochromic properties of vanadium dioxide in 1959 [1].

1.2.2. Vanadium dioxide optical properties

1.2.2.1. VO_2 refractive index

The refractive index of VO_2 films has been measured, most of them are made through ellipsometry techniques [23–27] and results in terms of dielectric functions are summed up in **Figure 8**. The real and imaginary parts of the dielectric function in the case of semiconducting and metallic VO_2 are represented as a function of wavelength in the visible and near infrared spectral regions (since VO_2 is a dispersive material). Results from different teams are shown and there is a relatively good consensus on the VO_2 dielectric function in these spectral regions. The VO_2 dielectric function used in this thesis is the curve labelled Mlyuka et al. 2009.

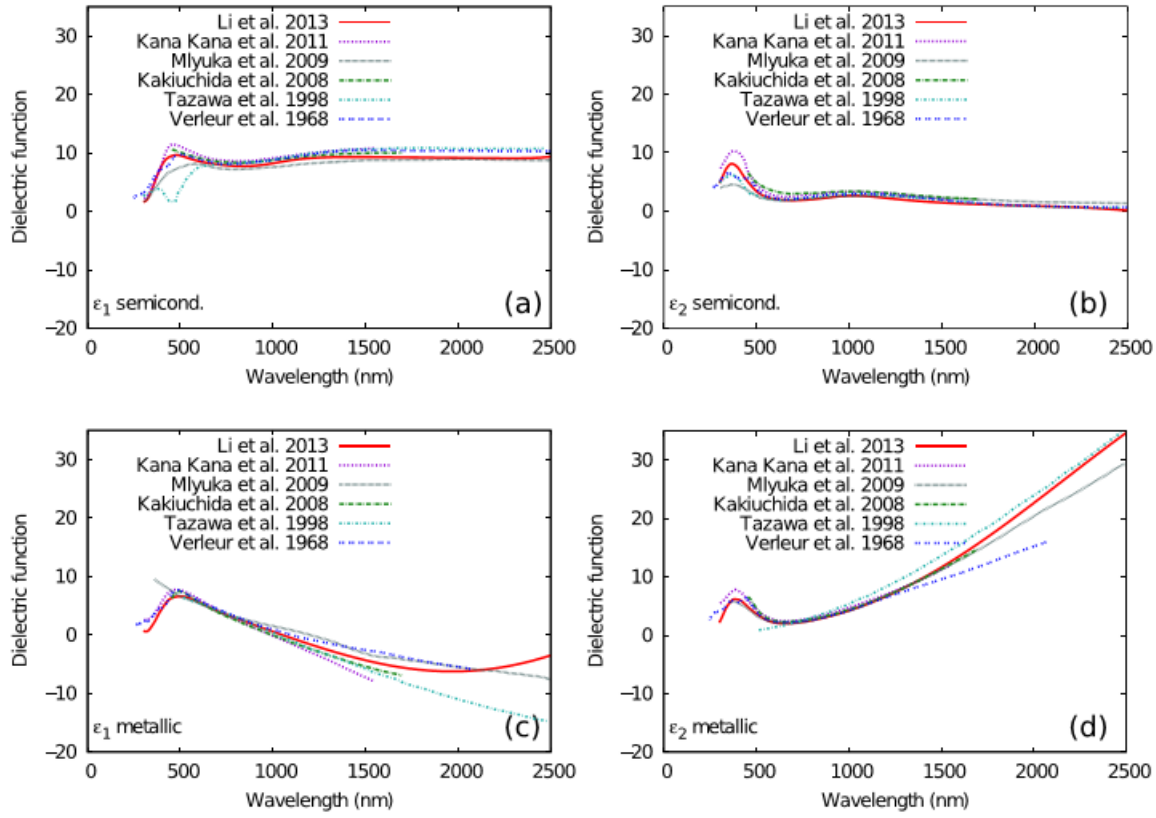

Figure 8: Real ε_1 (a,c) and imaginary ε_2 (b,d) parts of the dielectric functions of the VO_2 semiconducting (a,b) and metallic (c,d) phases [28].

It is worth noting that the imaginary part of the VO_2 dielectric function in warm conditions (metallic) (**Figure 8d**) is higher than in cold conditions (semiconducting) (**Figure 8c**), especially in the near infrared region (800-2500 nm), going from about -3 to over 30 at a wavelength of 2500 nm. This means that as the temperature increases and VO_2 undergoes the phase transition from semiconducting to metallic, it absorbs more near infrared light.

Moreover, the change in the VO_2 refractive index is not abrupt at the phase transition. It is actually a progressive process as the temperature gets around the transition temperature. **Figure 9** shows these changes for a 80 nm thick VO_2 film deposited on a silicon substrate coated with a 9 nm thick TiO_2 seed layer (used to promote VO_2 crystalline form [29,30]) as the temperature increases from 20°C to 90°C.

The progressive changes for increasing temperatures can clearly be seen, as pointed out by the figure arrows.

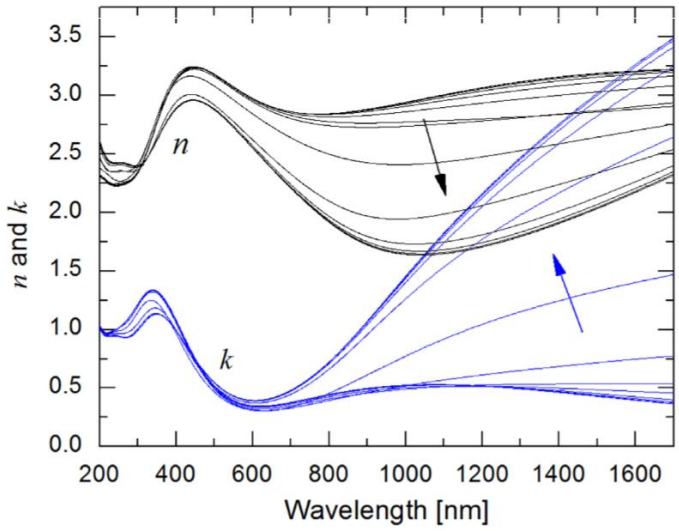

Figure 9: Real (n) and imaginary (k) parts of the refractive index of a 80 nm thick VO_2 film deposited on a silicon substrate with a 9 nm thick TiO_2 seed layer. The arrows indicate an increasing temperature from 20°C to 90°C (5°C step) [31].

While there seems to be a consensus about the VO_2 refractive index for thin films up to a wavelength of 2500 nm, for higher wavelengths diverging results have been proposed [6,32,33]. The VO_2 refractive index in the infrared region (from 2.5 to 30 µm) used in this thesis are extracted from [6] and shown in **Figure 10** for both semiconducting and metallic VO_2 phases.

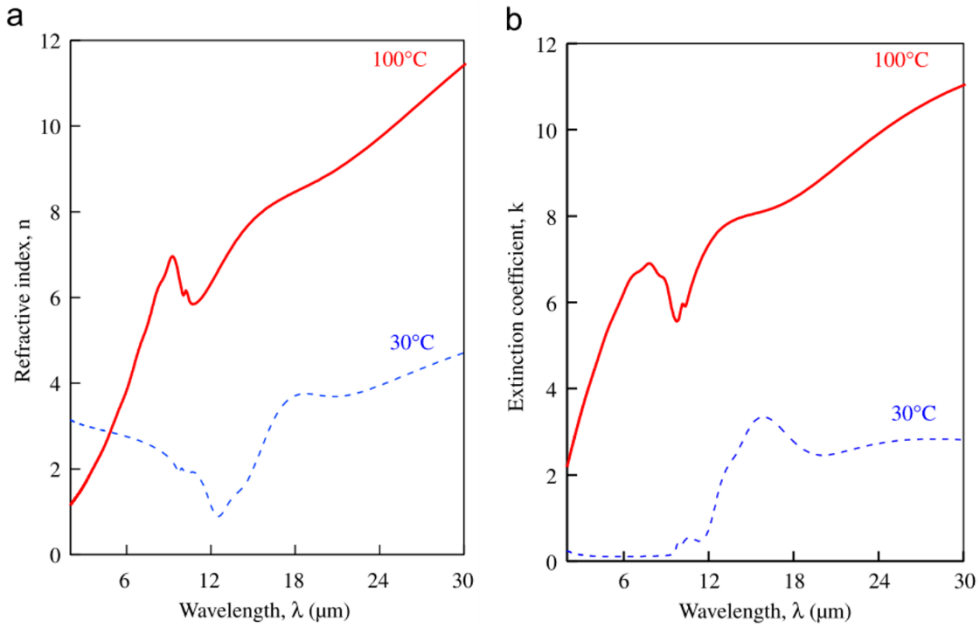

Figure 10: VO_2 refractive index (a) and extinction coefficient (b) as a function of wavelengths in the near- and mid infrared region, in cold and warm conditions [6].

The progressive change of VO_2 refractive index as a function of the temperature (**Figure 9**) will not be considered in this thesis. VO_2 will be considered as a material having two possible phases, semiconducting (cold) and metallic (warm) phases, each of them described by their respective refractive indexes from the visible to mid infrared spectral regions.

1.2.2.2. VO_2 spectral, luminous and solar transmittances

In order to quantify the coating performances for applications like coatings for smart windows (see **Section 1.2.3.1**), parameters such as luminous and solar transmittances are used. These parameters are commonly used in this field, so it will be later possible to compare our coating performances to existing materials using these commonly used integrated transmittance values. Based on *Equations (1. 18)* and *(1. 20)*, the luminous and solar transmittances are obtained by the weighted integration of the material spectral transmittance. In this section we are interested in the case of a pure VO_2 film. The VO_2 spectral transmittance and integrated luminous and solar transmittances will be presented.

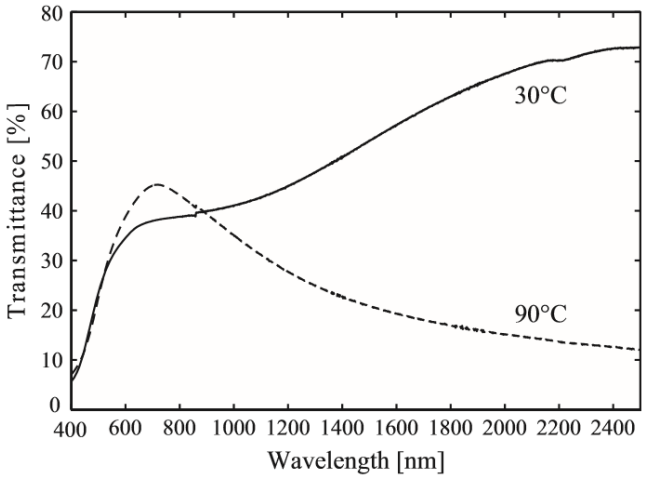

Figure 11: Measured transmittance spectra of a 75 nm thick VO_2 film deposited by magnetron sputtering on a glass substrate at 30°C and 90°C [34].

The VO_2 phase transition causes a significant change in the material refractive index, which translates in a change of its transmittance properties. This change in the VO_2 spectral transmittance is illustrated in **Figure 11** for a 75 nm thick pure VO_2 film deposited by magnetron sputtering on a glass substrate at 30°C and 90°C in the visible and near infrared regions. Across the VO_2 phase transition, while the visible transmittance only slightly changes, there is a significant drop of near infrared transmittance (61% at 2500 nm).

Spectral transmittances can be integrated in order to calculate luminous and solar transmittances. We present here the computed data obtained for another system: a model material consisting of a pure VO_2 film on a dielectric substrate having a refractive index of 1.5. **Figure 12** shows the luminous and solar transmittances of this system, computed as a function of the film thickness in both VO_2 phases using Fresnel equations [35] and the definition of the integrated luminous and solar transmittances (*Equations (1. 18)* and *(1. 20)*). The VO_2 refractive indexes used for this calculation are also presented in [36].

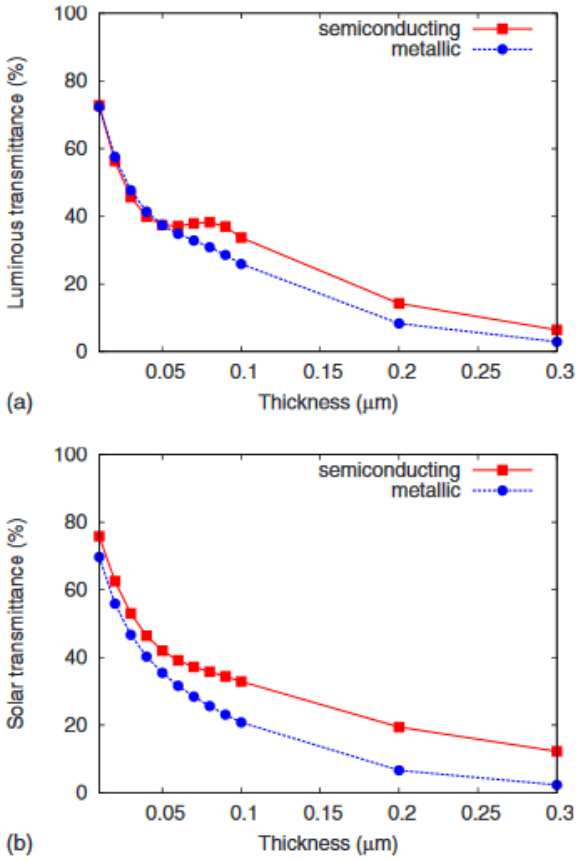

Figure 12: Computed luminous (a) and solar (b) transmittances as a function of thickness of pure VO_2 films on a substrate having a refractive index of 1.5 in semiconducting and metallic states [36].

Thicker films are more opaque, especially in the case of the more absorbing metallic VO_2 film, so both luminous and solar transmittances decrease with increasing film thickness. In addition, a thinner film means lower amount of thermochromic material, which tends to make the two curves related to semiconducting and metallic VO_2 phases close to each other. This figure shows that the luminous and solar transmittances are influenced by parameters like the VO_2 film thickness, which will be a parameter of interest in our study.

1.2.2.3. VO_2 emissivity

While transparent energy-efficient coatings require optimized T_{lum} and ΔT_{sol} values, in the case of opaque materials it is more relevant to optimize the coating emissivity ϵ. In practice the VO_2 emissivity can be measured combining a thermal camera and a thermometer, while the sample is being heated. Indeed, as the sample actual temperature τ_{real} increases, which is measured by the thermometer, the intensity of the emitted light increases too according to Planck's law (see **Figure 6**). The emitted light radiated from the material surface is captured by the thermal camera in a spectral window corresponding to the camera sensitivity (for example a typical spectral window is from 8 to 14 µm). An apparent temperature τ_{app} is measured with the camera, based on this emitted light and a reference emissivity ϵ_{ref}. Plotting τ_{app} as a function of τ_{real} can lead to an approximate value of ϵ [6]. In reference [37], the VO_2 emissivity will be estimated using this method.

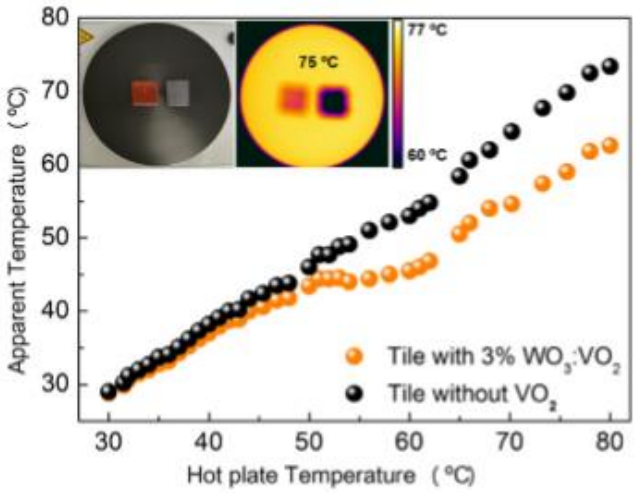

Figure 13: Apparent temperature as a function of the hot plate temperature for two tiles, one regular ceramic and one surface coated with VO_2 (doped with WO_3). Insets are optical and infrared camera photographs of the tiles. [37]

Figure 13 represents τ_{app} as a function of the hot plate temperature (linked to τ_{real}) used to heat two ceramic glassy tiles: a reference uncoated tile and a tile coated with VO_2 nanoparticles doped with WO_3. For this second sample, the VO_2 nanoparticles were produced by hydrothermal synthesis assisted by microwave irradiation and the coating was deposited on this ceramic tile surface by spray coating with posterior annealing [37]. The curve associated with the reference sample has a linear increase of τ_{app} as a function of τ_{real}, while the thermochromic VO_2 material exhibits two regions linked to the two cold and warm VO_2 phases. The VO_2 phase transition occurs before 50°C (this lower transition temperature is due to the WO_3 doping), leading to a lower τ_{app} at warmer temperatures compared to the reference sample. This means that even though both samples have the same τ_{real}, the VO_2 sample has a lower τ_{app} after the VO_2 phase transition. This can be explained by the fact that less light is emitted from the heated sample, when the VO_2 is in its warm state. Its emissivity has thus decreased.

Based on this kind of curves it is possible to obtain the material emissivity in cold and warm conditions. Indeed, knowing the reference emissivity ϵ_{ref} and the slope of the curve in both regions, the material emissivity for each VO_2 phase is given by [6]:

$$\epsilon = \epsilon_{ref} \frac{\delta\tau_{app}}{\delta\tau_{real}} \tag{1. 32}$$

where $\frac{\delta\tau_{app}}{\delta\tau_{real}}$ represents the slope of the curve. A material emissivity can thus be experimentally obtained using this equation.

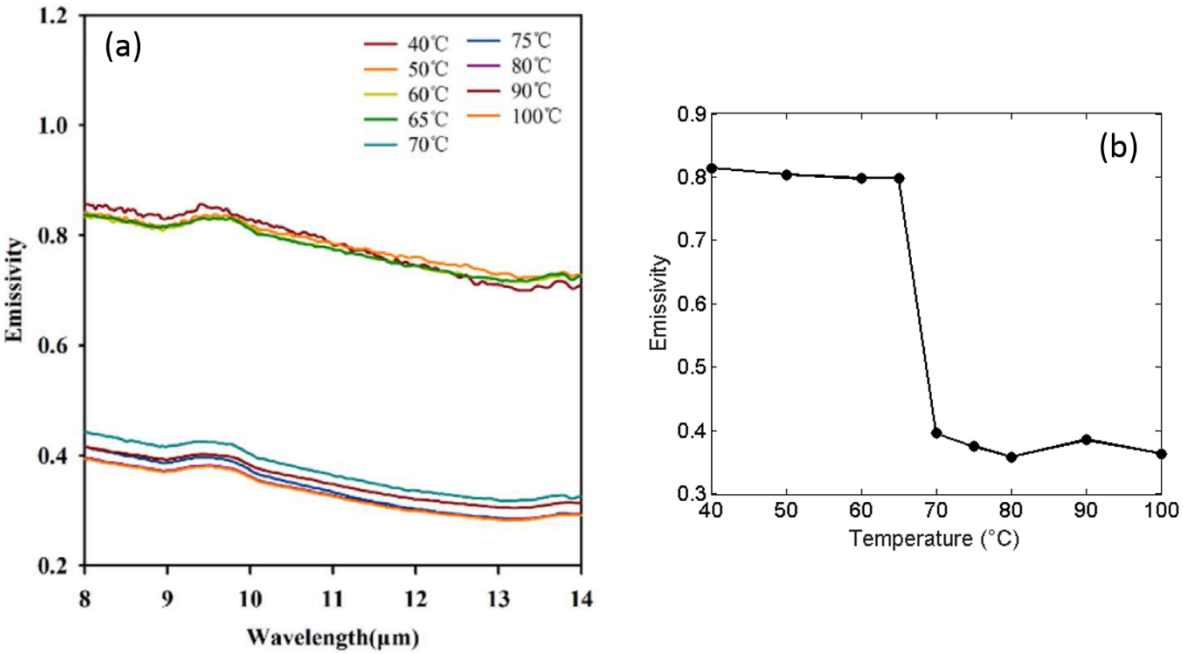

Figure 14: VO_2 nanopowder spectral emissivity at different temperatures from 40°C to 100°C in the far-infrared spectral region (8-14 µm) (a) and its integrated emissivity vs temperature (b), extracted from [5].

The emissivity of VO_2 pellets produced from VO_2 nanopowders synthetized by a single-step hydrothermal method is presented in **Figure 14** [5]. **Figure 14a** shows the spectral emissivity of these VO_2 pellets in the far-infrared region from 8 to 14 µm, for different sample temperatures from 40 to 100°C. The material spectral emissivity shows two distinct behaviors: lower temperatures (up to 65°C) present a higher emissivity (around 0.8) while higher temperatures (from 70°C) present a lower emissivity (around 0.4). This is due to the VO_2 phase transition, which causes the material emissivity to significantly drop from a high value (about 0.8) to a lower value (about 0.4). The integrated emissivity over the spectral range 8 to 14 µm leads to **Figure 14b**. This figure represents the VO_2 emissivity as a function of the material temperature. This representation clearly shows the emissivity drop at the VO_2 phase transition occurring at 68°C.

Based on these measurements, it is possible to obtain the material emissivity modulation $\Delta\epsilon$ defined as the difference between the material emissivity in cold and warm conditions:

$$\Delta\epsilon = \epsilon_{cold} - \epsilon_{warm} \quad (1.\ 33)$$

Using the method presented in this section, it is thus possible to measure the material emissivity based on the material apparent and real temperatures, and then deduce an emissivity modulation which can then be used to quantify the performances of opaque VO_2-based materials for various applications as coatings for buildings, satellites or camouflage.

1.2.3. VO_2 applications and challenges

Vanadium dioxide thermochromic properties has attracted scientific interest for a wide field of applications. A first scientific community was interested in using VO_2 as a glazing coating material [2,3,38–42]. This requires the coating to be transparent, thus limiting the VO_2 concentration and coating thickness to very low values (few vol% in a 50 to few hundreds nm thick coating). The goal here is to enhance the thermal performances while keeping the material transparent. The spectral region of interest is the visible and near infrared regions. A second community is interested in using thick opaque thermochromic coatings for satellites [4,43–46] or camouflage applications [5,47–52]. In this case the interest is focused on the material emissivity at temperatures close to the transition temperature, so the spectral region of interest is shifted to the mid-infrared range.

1.2.3.1. Enhanced luminous transmittance T_{lum} and solar transmittance modulation ΔT_{sol}

For applications as an energy efficient window coating, two main parameters are used to quantify the coating performances: the luminous transmittance (defined in *Equation (1. 20)*) and the solar transmittance modulation defined as the solar transmittance difference between cold and warm conditions:

$$\Delta T_{sol} = T_{sol,cold} - T_{sol,warm} \quad (1.\ 34)$$

Similarly, we define the luminous transmittance modulation as:

$$\Delta T_{lum} = T_{lum,cold} - T_{lum,warm} \quad (1.\ 35)$$

One of the main challenges for using VO_2 as a glazing coating material is to increase both T_{lum} and ΔT_{sol} simultaneously. Indeed, the coating should be transparent in order to be coated on windows, so the luminous transmittance should be as high as possible in both cold and warm conditions. For the solar transmittance, the highest thermal impact is obtained when the coating prevents thermal energy from transmitting through the coating only during warm weather conditions. This leads to a maximum $T_{sol,cold}$ and minimum $T_{sol,warm}$, resulting in an ideally maximized ΔT_{sol}.

In this section some of the recent advances in maximizing these two values, T_{lum} and ΔT_{sol}, are presented. **Table 2** sums up a few VO_2-based promising systems for smart windows coatings reported in the literature. The performances of each material are compared through their luminous transmittance in the cold VO_2 phase $T_{lum,cold}$, and the solar transmittance modulation ΔT_{sol}. Most papers use $T_{lum,cold}$ and ΔT_{sol} as their performance parameters.

System	$T_{lum,cold}$	ΔT_{sol}	Ref.
Pure VO_2 film			
50 nm	33.9%	3.6%	[53]
170 nm	11.3%	11.4%	[53]
Multilayers			
$TiO_2/VO_2/TiO_2$	30.1%	10.2%	[54]
$TiO_2/VO_2/TiO_2/VO_2/TiO_2$	45%	12%	[7]
$TiO_2/SiO_2/VO_2$	17.8%	15.3%	[55]
Nanoporous VO_2 film	43.3%	14.1%	[3]
	50%	14.7%	[56]
VO_2 nanoparticles in polymer composite	45.6%	22.3%	[8]

Table 2: Optical and thermal performances of different materials containing thermochromic VO_2.

The performances of pure VO_2 films are quite limited. Indeed, a 50 nm thick VO_2 film has a solar transmittance modulation of 3.6% [53]. This value can be slightly increased by increasing the film thickness, but at a loss of material transparency. For example, increasing the thickness from 50 nm to 170 nm leads to an increase of ΔT_{sol} from 3.6% to 11.4%, but the luminous transmittance in cold conditions drops from 33.9% to 11.3% [53].

Other VO_2-based systems have been proposed with better performances, for example multilayer films. Three [54] and five-layer [7] films have been proposed using TiO_2/VO_2 alternating layers, allowing an increase of ΔT_{sol} to 12% in the case of a $TiO_2/VO_2/TiO_2/VO_2/TiO_2$ sandwich multilayer. This five-layer material has thicknesses of 40 and 130 nm for the VO_2 and TiO_2 layers respectively. The layers are produced by direct current reactive magnetron sputtering. Including a SiO_2 layer between a TiO_2 and a VO_2 layer allowed a further increase of ΔT_{sol} to 15.3%, at the expense of $T_{lum,cold}$ which suffers a drop of almost 30% compared to the five-layers film with TiO_2 and VO_2 only [55].

Increasing the material transparency was possible by introducing nanopores in a VO_2 film. Kang et al. [3] reported that nanoporous VO_2 films produced by polymer-assisted deposition with a mean pore size of 28 nm perform higher levels of transparency ($T_{lum,cold} = 43.3\%$) while maintaining comparable ΔT_{sol} (14.1%). These values were then further increased by Cao et al. [56] who used dip coating and lyophilization to produce nanoporous VO_2 films with higher performances ($T_{lum,cold} = 50\%$ and $\Delta T_{sol} = 14.7\%$).

In a way to further increase the ΔT_{sol} parameter, VO_2 nanoparticles have been used instead of VO_2 films. Due to the metallic nature of VO_2 in warm conditions, the use of nanoparticles introduces an absorption peak related to a plasmon effect [57], which depends on parameters like size and shape of the metallic nanoparticles, as well as the refractive index of the surrounding material. Placed in the near infrared spectral region, this absorption peak allows an increase of the solar transmittance modulation. A polymer-VO_2 composite reported in [8] performed high values of ΔT_{sol} (22.3%) while keeping a comparable level of transparency ($T_{lum,cold} = 45.6\%$). Such polymer-VO_2 composites not only perform great in terms of T_{lum} and ΔT_{sol} for applications as smart window coatings, but they are also flexible, which allows their use on curved surfaces as well.

1.2.3.2. Reverting the emissivity switch

Another interesting application for VO_2-based materials consists in energy efficient coatings for buildings and satellites. In this case, the parameter of interest is the material emissivity. A high emissivity means that the thermal energy is lost from the system as light is emitted to the surrounding environment. This means that for these applications, the material emissivity should be the lowest possible in cold weather conditions and the highest possible in warm weather conditions.

However, the emissivity of most VO_2-based systems is higher in cold than warm conditions. For example, for pure dense films, the emissivity is in cold state ϵ_{cold} = 0.63-0.67 and in warm state ϵ_{warm} = 0.11-0.26 [4]). VO_2 nanopowder encounters an emissivity decrease from $\epsilon_{cold} = 0.82$ to $\epsilon_{warm} = 0.36$ ($\Delta\epsilon = 0.46$) at the phase transition [5]. In order to reduce the gap between ϵ_{cold} and ϵ_{warm}, or even obtain a higher ϵ_{warm} than ϵ_{cold}, multilayered materials have been proposed.

Materials with high reflectivity such as metals can significantly reduce the material emissivity (according to **Equation (1. 29)**). Kang et al. showed that a noble metal coating on a VO_2 film can reduce the material emissivity [58]. Different films consisting of a Platinium (Pt) top layer deposited by

sputtering on a pure VO_2 film on fused silica substrates were prepared with different sputtering times, leading to different Pt quantities. **Figure 15** shows the measured emissivity of those films in cold and warm conditions. Higher quantities of Pt lead to a higher material reflectivity and thus a reduced emissivity.

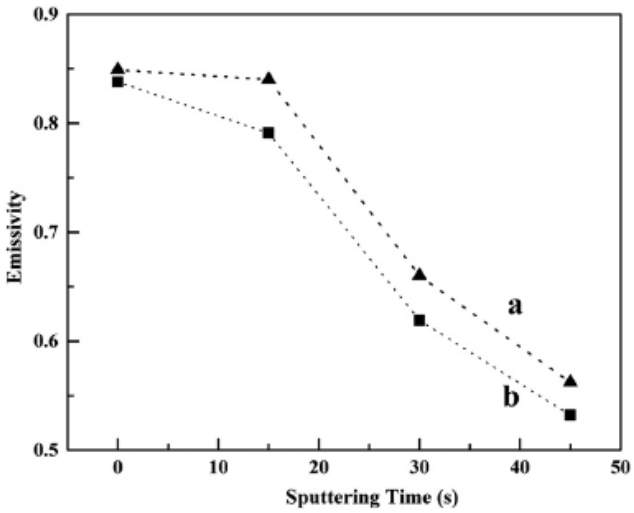

Figure 15: Pt/VO_2 two-layer films emissivity for increased quantities of Pt at 20°C (a) and 90°C (b). Emissivities are presented as a function of sputtering time used for deposition of the Pt top layer [58].

In this two-layer film, the values for both ϵ_{cold} and ϵ_{warm} decrease as expected, but their modulation $\Delta\epsilon$ does not seem to be so affected by the introduction of a Pt top layer. Other systems can nevertheless revert the emissivity modulation. Benkahoul et al. [6] proposed another metal containing material. An aluminum substrate under a 300 nm thick VO_2 film successfully reverted this $\Delta\epsilon$ to a negative value of $\Delta\epsilon$ = -0.22 (ϵ_{cold} = 0.20 and ϵ_{warm} = 0.42). It appears that the use of metallic materials can lead to better performances for applications as coatings for buildings or satellites.

1.2.3.3. Infrared camouflage applications

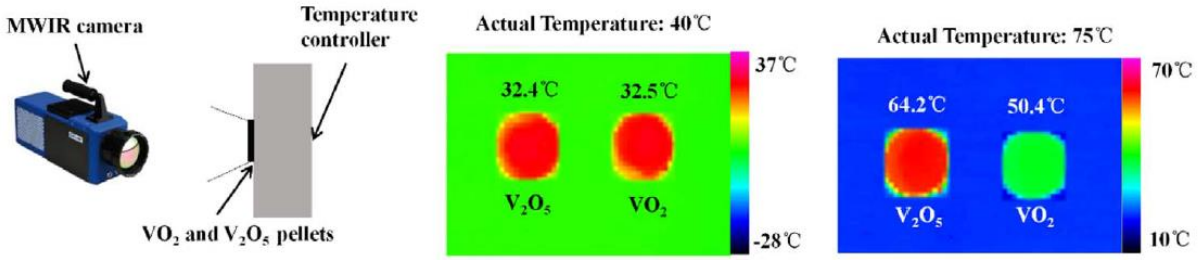

Figure 16: Infrared thermal images of VO_2 nanopowder pellets in the mid-IR spectral range. Pellets are 1 mm thick and have a 13 mm diameter. Extracted from [5].

Finally, the VO_2 emissivity switch at the phase transition is interesting for camouflage applications. Indeed, an infrared camera measures an apparent temperature τ_{app}. This temperature depends on the emitter real temperature τ_{real} and emissivity ϵ. As illustrated in **Figure 16** in the case of V_2O_5 pellets used as a reference sample and VO_2 pellets produced by a single-step hydrothermal method. Controlling the actual temperatures of both pellets, the images viewed by the infrared camera are shown for τ_{real} below and above the VO_2 transition temperature. At lower τ_{real}, the same τ_{app} is

observed for both samples. As the temperature increases, τ_{app} of the VO_2 pellet becomes significantly lower than the one of the V_2O_5 pellet. This is due to the VO_2 emissivity getting reduced across the phase transition, as discussed above. This lower τ_{app} may then be interpreted as a colder material by the camera. It is thus possible to "cheat" on a material temperature using a VO_2-based material. An example is about reducing emittance difference between a human body and its surroundings by covering this human with such material.

1.2.4. Vanadium dioxide synthesis

Taking advantage of VO_2 interesting thermochromic properties leads to a wide range of challenges related to its elaboration. The research related to finding convenient, cheap and reproducible elaboration techniques of both VO_2 films and nanoparticles are still in progress today. Synthesis of films and nanoparticles lead to two different approaches, each having their own preferred elaboration techniques and their related challenges. A quick presentation of these techniques and challenges will be made in this section, but their details are out of the scope of this thesis. The interested reader can refer to [59–61].

The first approach is about the elaboration of VO_2 films, either continuous or nanostructured films. Techniques typically used for thin film deposition have been performed in order to synthetize VO_2 films. These techniques include both physical and chemical processes, like direct current or radio frequency magnetron sputtering, chemical vapor deposition (CVD), pulsed laser deposition (PLD) or sol-gel techniques [61–65]. While CVD seems to be the most used technique for VO_2 film deposition, PLD, as a typical oxide film deposition technique, has been adapted to the deposition of VO_2 films relatively recently compared to the other methods [61,66].

The second approach consists in the synthesis of VO_2 nanoparticles, either directly deposited on a substrate or included into another material to form a composite. It appears that the mostly used elaboration route for VO_2 nanoparticle is a hydrothermal synthesis [59,67–70], consisting in reducing a precursor solution, typically V_2O_5 or NH_4VO_3, at both high pressure and temperature. Parameters such as the precursor and reducing agent choice, heating temperature and duration, as well as possible additives, are of high importance on the resulting material structural and optical properties. For example, higher temperatures or longer heating processes increase the resulting particle size (synthetized VO_2 nanoparticle sizes typically range from a few tens to a few hundreds nanometers), which have an influence on the material optical behavior [71,72]. Smaller particles are often preferred as their small size allows them to be incorporated into a composite system. Also, incorporation of dopants such as tungsten or magnesium leads to reduced phase transition temperatures, which can be interesting for applications like smart windows.

Table 3 sums up a few of the most used techniques for the synthesis of VO_2 films and particles, highlighting some of their advantages and drawbacks.

Approach	Elaboration technique	Advantages	Ref.
Films	Sputtering	Film uniformity Controllable speed Good adhesion Wide variety of possible substrates	[73–75]
	CVD	Film uniformity Reproducible	[76–78]
	PLD	Versatile Fast Cost-effective	[66,79]
	Sol-gel	Cheap Large-scale	[80,81]
Particles	Hydrothermal synthesis	Simple mode of operation	[82]

Table 3: VO_2 film and nanoparticle elaboration techniques.

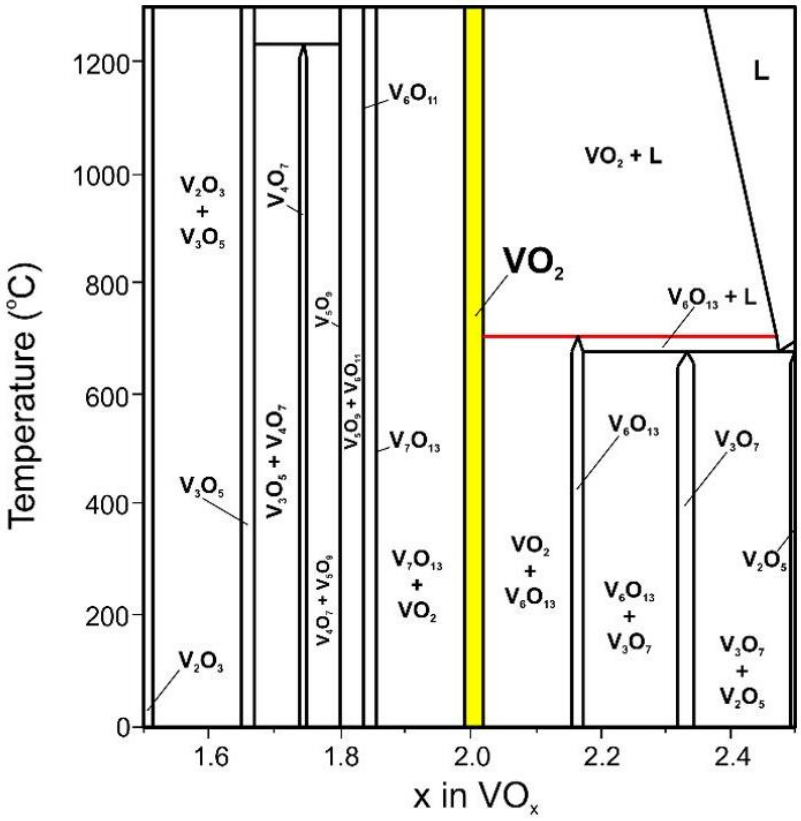

Figure 17: V_2O_3-V_2O_5 phase diagram [21]

A shared difficulty for the elaboration of both VO_2 films and nanoparticles is related to the wide variety of valence states that vanadium has. A phase diagram is shown in **Figure 17**, showing many possible variations of vanadium oxides from the less oxidized V_2O_3 to the most oxidized V_2O_5. VO_2 is highlighted in yellow, with an oxidation state of +2. It appears that considering the wide variety of vanadium oxides, it may be challenging to specifically target the vanadium dioxide VO_2. Even VO_2 itself has various polymorphs including those shown in **Figure 7**, as well as A, B, D, P, M and R obtained in other various conditions [82,83]. Among them, only the M and R phases have thermochromic properties. The VO_2(R)

can be obtained from VO_2(M) by a heating process. So the challenge is to synthetize only those thermochromic phases, while avoiding the formation of other VO_2 phases, or find a way to further transform those phases into the phases of interest. For hydrothermal synthesis of VO_2 nanoparticles, it has been shown that high temperature annealing causes an irreversible transition from VO_2(B) to VO_2(M) [69], but such further annealing causes the nanoparticles to grow and/or to agglomerate. In order to avoid that, coating these VO_2 nanoparticles with SiO_2 have been proposed [84]. The use of coating materials around VO_2 particles also have an anti-oxidation effect. Indeed, the thermochromic VO_2 is chemically unstable and at high temperatures (above 300°C) or in very humid environments, VO_2 films and particles tend to form a more stable and toxic V_2O_5. The VO_2 oxidation effect leads to a significant decrease of the material thermochromic property as the further oxidized species do not have this thermochromic property. As a result, it is important to shield the material against oxidation, especially in the case of nanoparticles, as the surface to volume ratio is more important than in the case of VO_2 films. Shielding VO_2 films and nanoparticles against oxidation is possible, by coating the film with a protective layer like an aluminum film [2] or using a VO_2/SiO_2 core-shell structure [85] for example.

1.2.5. Conclusion

The thermochromic vanadium dioxide undergoes a phase transition from semiconducting to metallic phase at a transition temperature of τ_c = 68°C in the case of a bulk VO_2 material. This transition leads to a drastic change of the material optical properties, like its refractive index, reflectance, transmittance and absorptance coefficients. Such property changes have motivated the study of VO_2-based materials as, for example, smart coatings for energy efficient windows, buildings and satellites, as well as camouflage applications. Each application requires ideal parameters: a smart glazing material requires high levels of luminous transmittance and solar transmittance modulation, while energy efficient coatings for buildings and satellites require a negative emissivity modulation. On the contrary, a positive emissivity modulation is required for camouflage applications. Among the reported VO_2-based materials used for smart windows applications, polymer-VO_2 composites showed particularly promising thermal performances in terms of luminous and solar transmittances. Concerning the emissivity of opaque materials, it seems interesting to increase the reflectivity in order to reduce the emissivity, especially in cold conditions. This is possible by a material structuration. The next section will be dedicated to the relationship between material structuration and optical properties.

1.3. Photonic crystals

1.3.1. Definition

Photonic crystals (PhC) are nanostructured materials, with a spatially periodic refractive index in one, two or three directions. The crystal is then respectively called a 1D, 2D and 3D photonic crystal [86]. Examples of photonic crystals are illustrated in **Figure 18** and **Figure 21**. **Figure 18a** is a stack of periodic layers forming a 1D PhC, while **Figure 18b** represents a 2D PhC of patterned nanowires. **Figure 21a**

shows closed-packed spheres forming a 3D PhC, while **Figure 21b** is the opposite situation with spherical holes and filled interstices forming another 3D PhC.

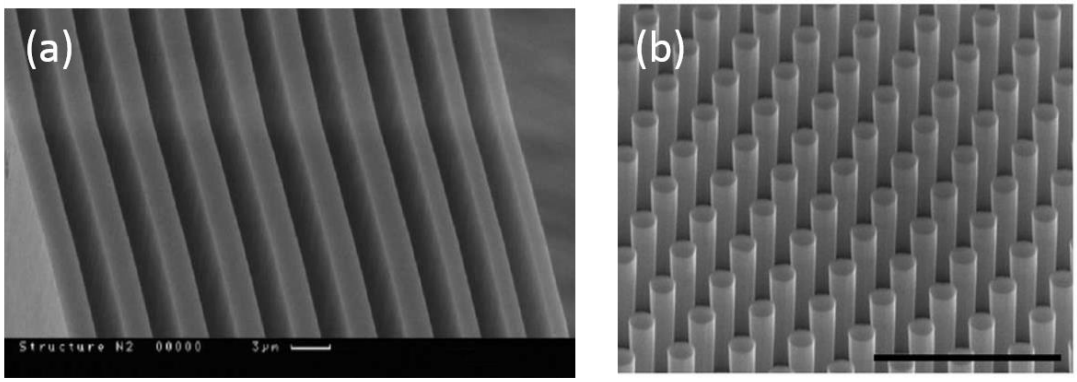

Figure 18: SEM micrograph of a 1D (a) and a 2D (b) photonic crystal. The scale bar in (a) represents 3 µm, and in (b), 1 µm. Images extracted from [87,88].

The term "photonic crystal" was introduced by Yablonovitch in 1987 [89], by analogy with the atomic crystals in which the atoms positions are periodically organized. In crystalline materials only electrons having certain energies are allowed to travel inside the material. This gives rise to allowed and forbidden energies. A range of forbidden energies form what is called an electronic bandgap. Electrons having an energy inside this bandgap cannot propagate inside the crystal. Photonic crystals have a similar behavior with photons instead of electrons: photons can propagate only when their frequency is allowed by the crystal, and there are forbidden frequencies forming a Photonic BandGap (PBG) inside the photonic crystal. This bandgap is a complete bandgap if light of any direction and polarization with a frequency inside this PBG cannot propagate inside the material. Otherwise it is called a pseudogap if the propagation is forbidden for only certain directions and/or polarization. Which frequencies are allowed or forbidden mostly depends on the crystal structural parameters, such as for example the refractive index of the material, its structure (pattern, period…), as well as the incident light properties (direction and polarization).

1.3.2. Band diagram

A band diagram is a representation of the dispersion relation inside the crystal, which means light frequencies ω as a function of the light direction of propagation (represented by the wave vector **k**). Note that directions of propagation are not defined in the real domain, but in the reciprocal space. Unit is thus m^{-1}. The vectors in the reciprocal space ($\mathbf{a}^*$,$\mathbf{b}^*$,$\mathbf{c}^*$) are defined based on the vectors in the real space (**a**,**b**,**c**) by the following relationships:

$$\boldsymbol{a}^* = \frac{2\pi(\boldsymbol{b}\times\boldsymbol{c})}{\boldsymbol{a}.(\boldsymbol{b}\times\boldsymbol{c})} \quad ; \quad \boldsymbol{b}^* = \frac{2\pi(\boldsymbol{c}\times\boldsymbol{a})}{\boldsymbol{b}.(\boldsymbol{c}\times\boldsymbol{a})} \quad ; \quad \boldsymbol{c}^* = \frac{2\pi(\boldsymbol{a}\times\boldsymbol{b})}{\boldsymbol{c}.(\boldsymbol{a}\times\boldsymbol{b})} \tag{1. 36}$$

where . denotes the dot product and × the cross product.

Band diagrams allow a graphical representation of allowed and forbidden frequencies inside a crystal, as a function of the direction of propagation in the reciprocal space. This kind of representation is

commonly used in order to easily locate the different bandgaps inside a crystal. A frequency associated with no direction of propagation can be understood as a forbidden frequency inside the crystal, meaning that this frequency is inside a PBG.

Band structures depend on dimensionless sizes: a crystal consisting of spherical particles of radius r placed on an array of periodicity a has the same band structure as the same crystal having spherical particles of radius $2r$ on an array of periodicity $2a$. The characteristic length is the ratio $\frac{r}{a}$, namely the ratio between the particle size and the lattice period. We introduce the normalized frequency ω^{norm} defined as:

$$\omega^{norm} = \frac{\omega a}{2\pi c} = \frac{a}{\lambda_0} \tag{1. 37}$$

with a the cell parameter, λ_0 the light wavelength in vacuum and c the light celerity. Since the crystal is perfectly periodic, it is only necessary to consider one period. In the reciprocal space, this primitive cell is represented by the first Brillouin zone. Band diagrams are thus a representation of the allowed frequencies as a function of directions of propagation (wave vectors $\boldsymbol{k}$) in the first Brillouin zone.

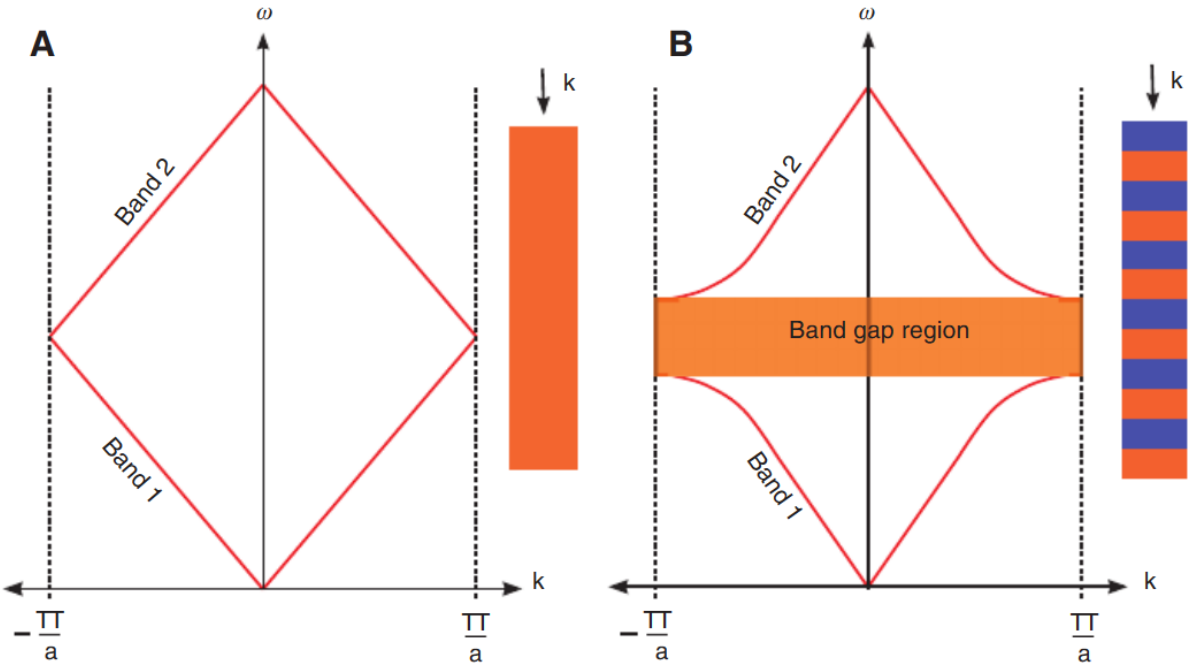

Figure 19: Band diagram of a homogeneous material (a) and a 1D photonic crystal (b) [90].

Figure 19 shows an example of a band diagram for a homogeneous material and for a simple 1D photonic crystal of spatial period a. A complete description in the frequency domain in this case is obtained for wave vectors from $-\pi/a$ to π/a. A schematic representation of the structure is shown next to the corresponding band diagram. Different colors mean different refractive indexes. The difference between both structures is the introduction of a 1D periodicity, represented by stacked layers of two different materials in orange and blue. This periodicity is responsible for the creation of a bandgap, along the propagation direction $\boldsymbol{k}$ normal to the material surface.

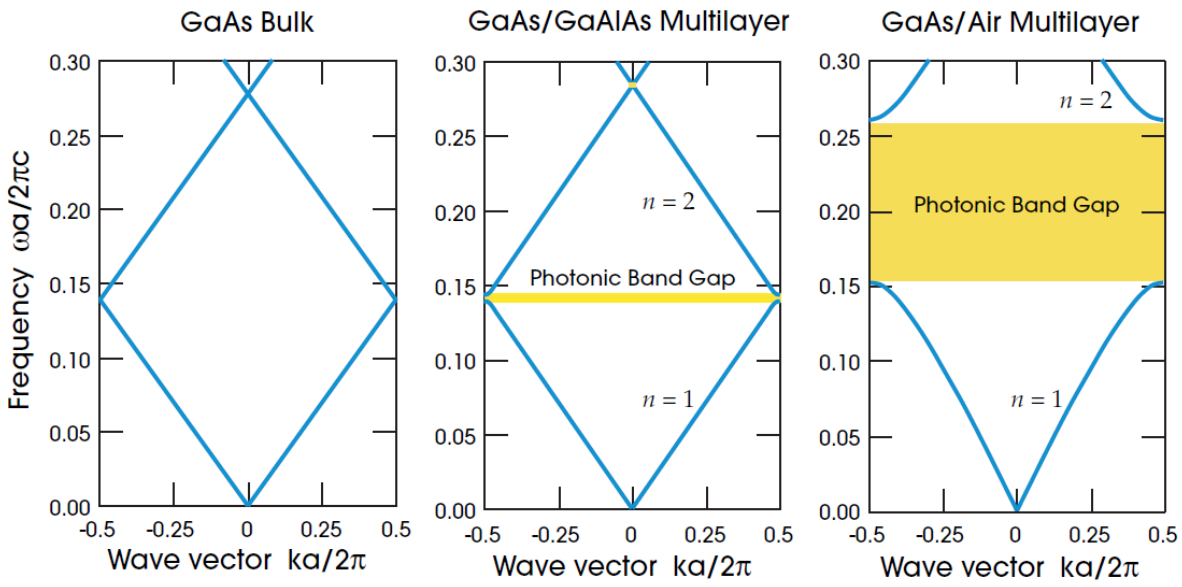

Figure 20: Band diagrams of a GaAs bulk (left), GaAs/GaAlAs multilayer (center) and GaAs/Air multilayer (right)

The size and position of this band gap mainly depends on the ratio between both materials thicknesses, and their refractive index contrast. Larger PBG appear for higher index contrasts [86]. **Figure 20** illustrates the increase of the PBG width with an increase of the refractive index contrast in a multilayer structure. Three band diagrams are represented. The left diagram is obtained in a GaAs bulk material with a refractive index of $n = \sqrt{13} \approx 3.6$. No bandgap is observed in this homogeneous material. The center diagram shows the band structure of a GaAs/GaAlAs multilayer structure. Compared to the previous diagram, a multilayer structure is introduced with a material having a refractive index $n = \sqrt{12} \approx 3.5$ close to the one of the other layer material, which leads to a quite low refractive index contrast $\Delta n \approx 0.1$. A thin PBG appears, highlighted in yellow on the diagram, due to the 1D periodicity in the structure. The diagram on the right is obtained when GaAlAs is now replaced by air, which has a lower refractive index of $n = 1$, leading to a higher refractive index contrast $\Delta n \approx 2.6$. This causes the PBG to become larger due to an increased refractive index contrast.

1.3.3. Opal photonic crystals

Among a wide variety of possible structures for photonic crystals, opal photonic crystals appear as a very attractive pattern due to their interesting optical properties and relative low fabrication costs. An opal photonic crystal is a 3D photonic crystal made of periodically packed spheres arranged in a face-centered (fcc) lattice [91], typically silica or polymer spheres. An opal photonic crystal is illustrated in **Figure 21a** with polystyrene spheres with a 220 nm diameter [92]. A similar photonic crystal structure is the inverse opal (**Figure 21b**) which is typically air holes surrounded by a matrix of higher refractive index. These expressions have been extended in terms of refractive indexes: direct opal photonic crystals spheres have a higher refractive index than the surrounding matrix. It is the opposite for inverse opal photonic crystals.

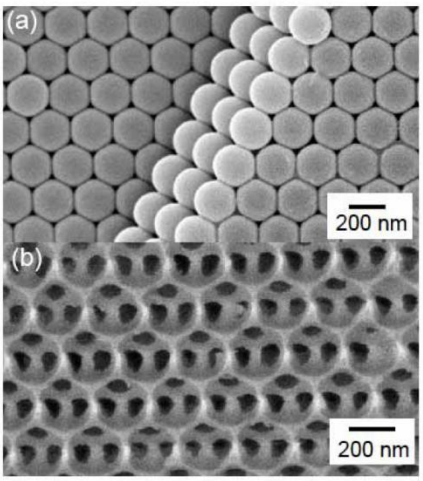

Figure 21: SEM micrograph of the (111) surface of a direct opal photonic crystal (a) and an inverse opal photonic crystal (b) [92].

1.3.3.1. Opal manufacturing processes

3D photonic crystals manufacturing processes usually imply complex challenges [93,94]. The lithography technique mostly used for 2D photonic crystals have difficulties to be extended to 3D [94]. Early studies were mostly theoretical or in the microwave range (which imply larger size scales, easier to manufacture).

These fabrication challenges made self-assembly techniques more attractive for the elaboration of 3D photonic crystals. Indeed, self-assembly is a bottom-up process in which the sedimentation of colloidal spheres allows the formation of large-scale well-organized structures at lower costs compared to the conventional lithography techniques. Such process is commonly used for the elaboration of self-organized artificial opal photonic crystals in which silica or polymer spheres are produced by emulsion polymerization [95,96]. A direct opal photonic crystal is obtained.

Inverse opal photonic crystals are obtained by using the initial spheres as templates and then filling the interstitial void spaces with a high index material. These interstices can be filled with different kinds of material, including liquid, solution or nanoparticles in a suspension [97]. It is also possible to calcinate the template spheres, which leaves air holes instead of the template spheres and consequently increases the refractive index contrast between the spheres and their surroundings as the refractive index of air ($n = 1$) is indeed lower than the average refractive index of silica or polymers ($n \approx 1.5$).

While self-assembly techniques appear to be a convenient way for manufacturing opal photonic crystals, this process also introduces unavoidable disorder into the structure. Using this technique, the spheres positioning may not be as well controlled as with other manufacturing techniques like lithography. The resulting photonic crystal may thus not be perfectly periodic.

1.3.3.2. Opal band structure and Bragg resonance

Unlike 1D or 2D photonic crystals, 3D photonic crystals can exhibit photonic bandgaps in all directions. Complete PBG are only possible in the case of a 3D periodicity, making 3D photonic crystals especially interesting materials.

Figure 22a shows the photonic band diagram of a direct opal photonic crystal consisting of closed packed spheres with a dielectric function of 13 ($n = \sqrt{13} \approx 3.6$), surrounded by air. According to this

diagram, opal photonic crystals do not have any complete photonic bandgap, but rather a low-frequency pseudogap along the [ΓL] direction, which corresponds to the crystallographic direction [111]. This direction is of interest in the study of opal photonic crystals [98]. This pseudogap gives rise to a strong angle-dependent reflection peak, due to Bragg interferences between the lattice planes [99]. The position of this peak can be predicted by the Bragg's law:

$$4\, d_{111}^2\, (\bar{n}^2 - sin^2\theta) = \lambda_{111}^2 \qquad (1.\ 38)$$

with d_{111} the spacing between two (111) crystallographic planes, $\bar{n}$ the material effective (average) refractive index, θ the incidence angle with respect to the normal to the surface (the normal to the surface is the [111] direction) and λ_{111} the wavelength position of the Bragg peak. So, according to this law, the position of this reflectance peak depends on both structural and illumination parameters. For example, a longer distance between the (111) planes, which means larger spheres in the case of a compact structure, leads to a red-shift of the Bragg resonance peak position. A higher incidence angle leads to a blue-shift of the resonance.

Unlike the direct opal photonic crystals, inverse opal photonic crystals have a complete PBG at higher frequencies (between the 8th and 9th bands) than the pseudogap in the corresponding direct opal photonic crystals. This PBG is shown in **Figure 22b**, which represents the band diagram of an inverse opal photonic crystal consisting of air holes surrounded by a material having a dielectric function of 13.

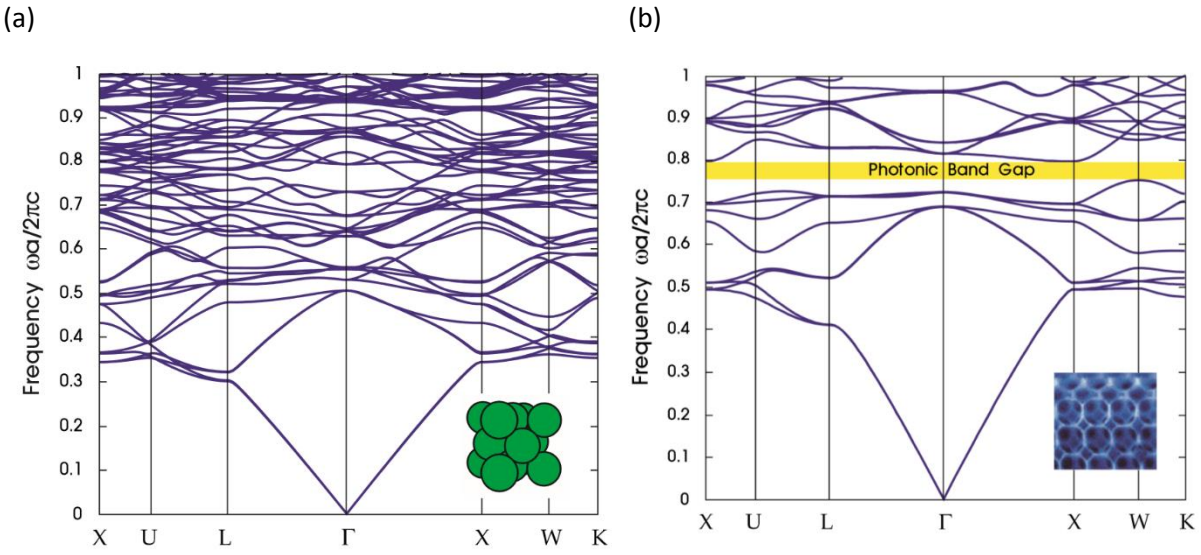

Figure 22: Photonic band diagram of an opal (a): face-centered cubic (fcc) lattice of close-packed dielectric spheres ($n = \sqrt{13}$) in air and of an inverse opal (b): fcc lattice of close-packed air spheres in dielectric medium ($n = \sqrt{13}$) [86].

1.3.3.3. Factors limiting bandgap effect in opal photonic crystals

Low refractive index contrast

Silica and polymers typically used in direct opal photonic crystals have an average refractive index of about 1.5, which is close to the refractive index of air. This leads to a relatively low refractive index contrast of $\Delta n \approx 0.5$ and thus a relatively thin bandgap. However, the bandgap still appears, even at low refractive index contrast.

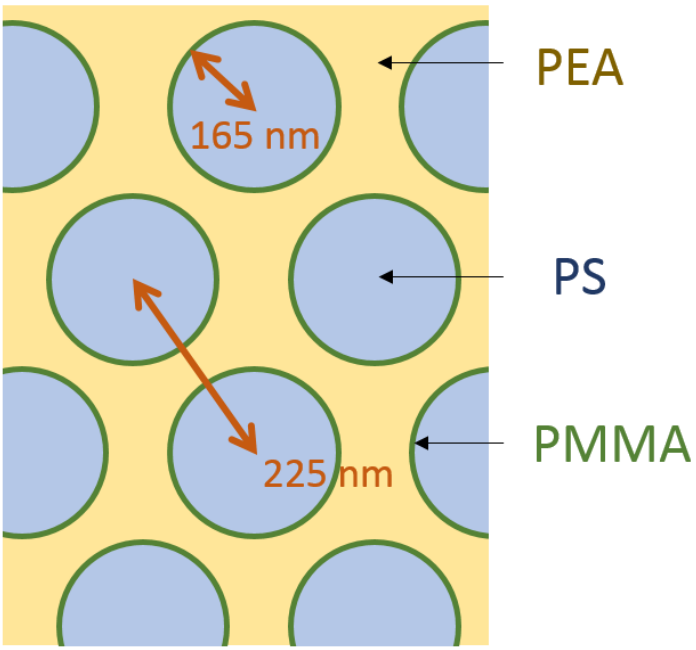

Figure 23: Schematic representation of the Ogreen material surface: PMMA coated PS spheres surrounded by PEA [100]*. In the axis perpendicular to the material surface ([111] direction), the distance between each sphere layer is* $d_{111} = 183$ *nm.*

Ruhl et al. [100,101] showed that the Bragg resonance can still be observed in opal photonic crystals containing only polymer materials: polystyrene (PS) spheres surrounded by poly(ethyl acrylate) (PEA), with a poly(methyl methacrylate) (PMMA) interlayer. This thin PMMA interlayer is used for manufacturing reasons and has no effect on the material optical properties. A schematic representation of the material surface is given in **Figure 23**. In this structure, the low index contrast of $\Delta n = 0.11$ ($n_{PS} = 1.58$; $n_{PEA} = 1.47$) still allows the apparition of a reflectance peak linked to a bandgap effect, as shown in its reflectance spectrum (**Figure 24**).

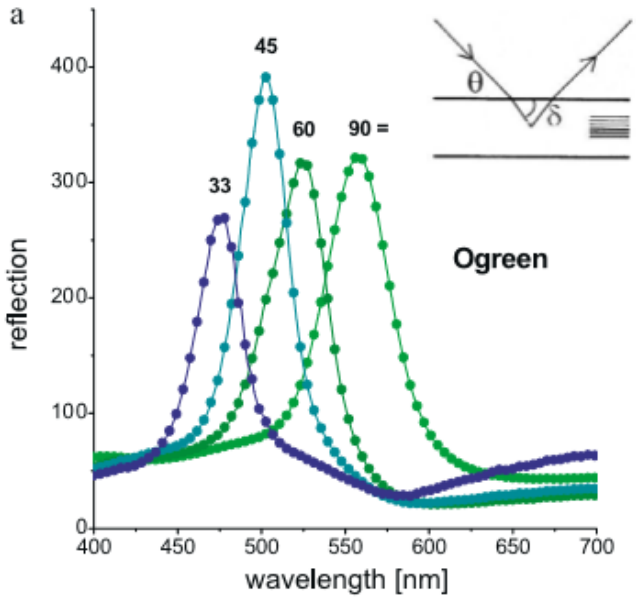

Figure 24: Reflection spectrum of the Ogreen film at different incidence angles (33, 45, 60 and 90°) with respect to the material surface (represented as θ in the inset). The reflection is given in arbitrary units [100].

Despite the low refractive index contrast, the reflectance spectra exhibit clear peaks. The position of these peaks is blue-shifted when the incidence angle becomes more oblique on the material surface

(lower incidence angles according to the **Figure 24**), as predicted by Bragg's law (*Equation (1. 38)*). Note that unlike in *Equation (1. 38)* where the incidence angle is defined with respect to the normal to the material surface, in **Figure 24**, the incidence angle is defined with respect to the material surface. In the following sections, unless differently said, the incidence angle θ will be defined relatively to the normal to the sample surface.

Introduction of an absorbing material

In this thesis an absorbing material (vanadium dioxide) is introduced into the system. The presence of such absorbing material has an effect on the crystal optical properties. It is possible to incorporate absorbing nanoparticles inside the interstices of an opal photonic crystal and observe resonant scattering events [102]. This means that while the reflectance peak remains, the light is no longer reflected in the specular direction (reflected angle equal to the incidence angle), but in a diffuse way (in a cone around the specular direction).

This phenomenon is illustrated in **Figure 25**. **Figure 25a** shows the experimental setup of reference [102]. An opal photonic crystal consisting of PS spheres (250 nm), surrounded by a mixture of carbon nanoparticles (0.20 wt%) and PEA is illuminated with an angle $\theta_{in} = 40°$ (with respect to the normal to the sample surface) and the reflected light is captured on a screen represented in **Figure 25b**. The light reflected in the specular direction ($\theta_{out} = 40°$) is represented by R, while the diffuse light scattered by the sample is denoted S. The intensity of these two components are represented as a function of wavelength in **Figure 25c**, along with the sum of them both. At a wavelength of about 580 nm there is a total $(S + R)$ reflectance peak represented by the red curve. This local maximum value is not due to a specular reflection (in black) like in opal photonic crystals containing no absorbing material, but it is due to a scattering peak (in blue). This shows that when introducing absorbing particles inside an opal photonic crystal a total reflectance peak is observed, due to resonant scattering.

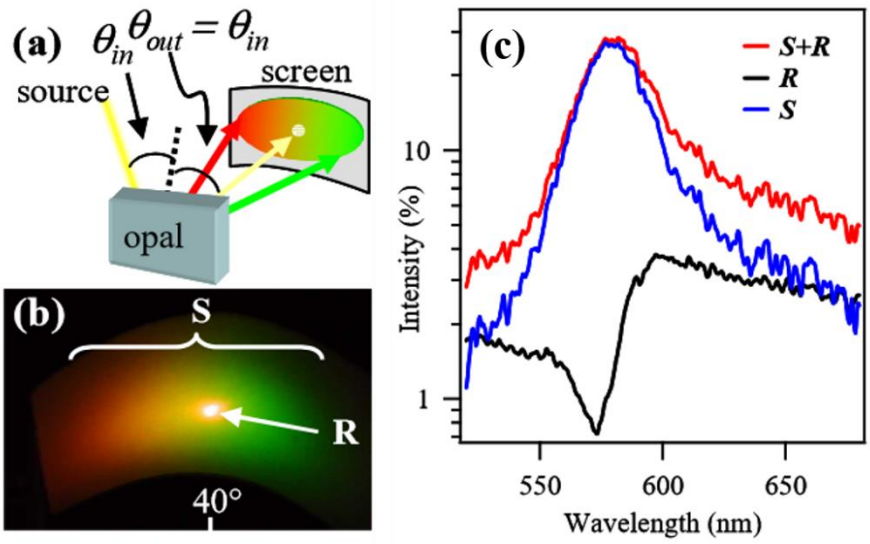

Figure 25: (a) Schematic representation of the setup used to measure the reflectance of an opal photonic crystal consisting of PS spheres surrounded by a mixture of carbon nanoparticles and PEA. (b) Optical image observed on the screen, with a light incident at a $\theta_{in} = 40°$ angle, showing the specular reflectance (R) and scattering (S). (c) Reflectance components of this opal sample at a 40° incidence angle [102].

1.3.4. Conclusion

The introduction of a periodic nanostructuration into the material leads to a reflectance peak called photonic bandgap. This PBG is closely related to the refractive index contrast between the structure and the surrounding material: the higher the refractive index contrast, the stronger and larger the bandgap. Opal photonic crystals represent a very attractive kind of nanostructured material due to their pseudogap along the [111] direction and their relative low fabrication costs compared to more conventional manufacturing processes. The pseudogap effect also remains at relatively low refractive index contrast, and in the presence of absorbing particles. Combining the resonance due to the pseudogap in opal photonic crystals with the intrinsic thermochromic property of VO_2 could lead to very interesting optical properties. For example, since highly reflective materials have lower emissivity, introducing a periodic nanostructuration could allow to decrease the far infrared emissivity of a VO_2-based material in its cold state. As seen in *Equation (1. 30)*, decreasing the far infrared emissivity increases the surface temperature. As explained in **section 1.2.3.1**, VO_2-based materials are interesting for energy-efficient windows as their near-infrared transmittance is lower in the VO_2 hot state than in its cold state. Nevertheless, the VO_2 emissivity is higher in its cold state, which has a negative impact on the surface temperature. Decreasing the far-infrared emissivity of a VO_2-based material by a periodical structuration could thus improve its energy saving performances.

The purpose of this thesis will be to investigate the effect of a periodic structuration of a VO_2-polymer composite on its optical properties through optical modelling. The next paragraph will thus be dedicated to the description of the optical models used in this thesis. As shown in reference [102], a polymer opal containing absorbing nanoparticles exhibits a resonant scattering effect at a wavelength corresponding to the opal pseudogap. The material structure chosen in this thesis will thus have a similar structure, in order to benefit from this effect to decrease the VO_2-composite cold state emissivity.

1.4. Modelling the optical behavior of periodically structured composites containing absorbing particles

In this thesis, the achievable optical properties (mainly reflectance and transmittance) of an opal photonic crystal containing VO_2 nanoparticles will be investigated through an optical model. To do so, different numerical methods can be used: temporal or frequency-based methods, in the real or Fourier space. Some of the most commonly used methods for modelling periodically structured composites are presented in this section. The first method is based on a homogenization of the material refractive index in order to have an "average optical behavior" (**Section 1.4.1**). The second method consists in solving the physical equations at each nod of a space and time mesh grid (**Section 1.4.2**). A third method consists in using the spatial periodicity in order to simplify the solving of physical equations (**Section 1.4.3**).

Instead of calculating the reflectance and transmittance properties of a periodically structured composite, it may be interesting to calculate its band diagram, especially in order to predict a photonic bandgap. For this purpose, a quick presentation of one typically used method will be presented in **Section 1.4.4**.

1.4.1. Effective medium theory (EMT)

Figure 26: Homogenization of the refractive indexes.

The first approach is to average the modeled material through an effective medium by computing an effective refractive index. A schematic representation of this process is given in **Figure 26** where a material composed of particles of refractive index n_i and a surrounding matrix of refractive index n_m is modelled by a material with an homogeneous effective refractive index n_{eff}.

The most commonly used models to calculate this effective index are Maxwell-Garnett [103] and Bruggeman [104] approximations. For example, Maxwell-Garnett approximation gives the effective refractive index as:

$$n_{eff}^2 = n_m^2 \frac{1+\frac{2}{3}f\alpha}{1-\frac{1}{3}f\alpha} \qquad \text{with} \qquad \alpha = \frac{n_i^2 - n_m^2}{n_m^2 + \frac{1}{3}\left(n_i^2 - n_m^2\right)} \tag{1. 39}$$

and f the filling factor (volume ratio of the inclusions in the material). However, these approximations are valid under certain conditions, for example the inclusions must be small compared to the wavelength of the incident light (see **Section 2.6.1**).

Then, using this calculated effective refractive index, to determine the material reflectance and transmittance properties, Fresnel coefficients can be used in the case of a unique layer [35], or Abeles matrices in the case of a more complex multilayer structure [105].

1.4.2. Finite-difference time domain (FDTD)

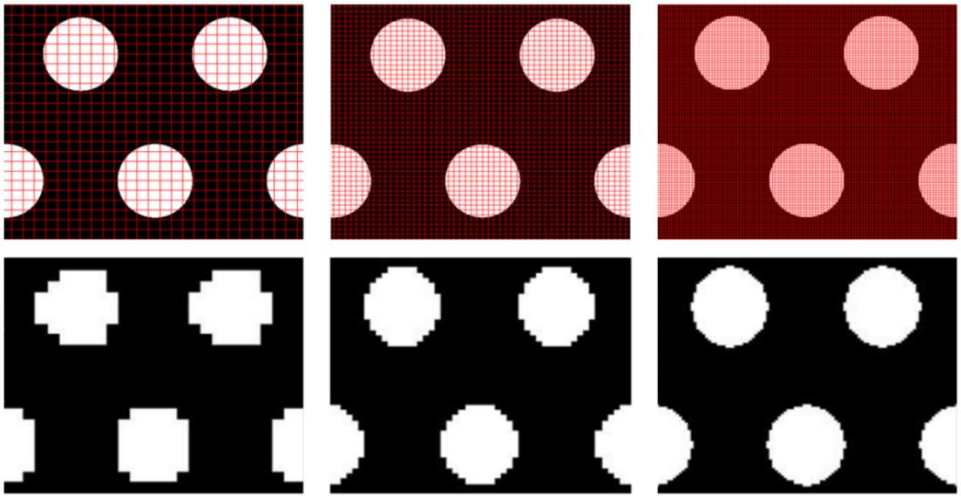

Figure 27: Spatial discretization of periodic circular shapes with different spatial mesh grid resolutions and their corresponding material representation [106].

The finite-difference time domain (FDTD) method [107] is a temporal method in the real space. It is commonly used in a wide range of numerical calculations, for numerous scientific fields. It can be used to calculate the interaction of an electromagnetic radiation for applications including waveguides [108–110], military (scattering from metallic surfaces) [111,112] and biology (absorption and cancer therapy) [113–115].

This method uses a spatial and temporal discretization of the system. An example with circular shapes is given in **Figure 27** with various mesh sizes, finer in the rightest panel. The grid is represented on the upper row, while the corresponding modelled material is shown below. A finer mesh results in a more accurate result, however this also leads to an increased amount of computational resources.

In our case, for electromagnetic computations, the derivatives of the Maxwell equations are replaced with finite differences. In 1D, the central finite difference of a function f at x_0 is:

$$\frac{df(x)}{dx}\Big|_{x=x_0} = \frac{f\left(x_0 + \frac{\Delta x}{2}\right) - f\left(x_0 - \frac{\Delta x}{2}\right)}{\Delta x} \quad (1.\ 40)$$

with Δx the mesh size in the x direction. A similar process is made for the temporal derivatives. Once all spatial and temporal derivatives in the Maxwell equations are replaced, solving the Faraday equation gives an "update equation" in the form of the magnetic field at a certain space and time node as a function of this field at a previous time and the electric field in the surrounding space nodes. The process is repeated for the Ampere equation, and so on until the whole considered time duration is covered.

This method, like other methods based on a meshing like finite element methods (which is instead a frequency-based method consisting in solving the equations inside finite elements), is quite efficient and allow the study of a wide variety of phenomena, as well as coupled physical phenomena. However, depending on the mesh size, it may also require a high amount of time and computational resources. Specific boundary conditions, like periodic boundary conditions, allow to reduce these resources in the case of perfectly periodic gratings.

1.4.3. Rigorous coupled-wave analysis (RCWA)

Unlike time-based methods, frequency-based methods are well adapted to periodic structures because this periodicity allows to consider only a primitive cell of the system (thus reducing the computational time and resources) and also to develop the general equations into Fourier series. Modal methods were developed in the mid-1960s in order to analyze the diffraction of periodic gratings. Among these modal methods, one of the most popular methods is the rigorous coupled-wave analysis (RCWA) method, developed by Moharam and Gaylord in 1981 [116]. This method, also known as Fourier modal method (FMM), gained a keen interest due to its simplicity and high efficiency. This method is well adapted for 2D gratings (2D transverse periodicity and translation invariance over the third direction) like the system represented in **Figure 29a**. However, poor convergence is observed for metallic gratings and transverse magnetic (TM) polarizations [117], due to high refractive index contrast and plasmon effects for the first one, and discontinuous functions for the latter. Note that other convergence issues could also arise, due to the truncated Fourier basis (limited number of Fourier components). Many algorithms were proposed in 1990s to solve the issues related to TM polarizations and metallic gratings. A new formalism proposed by Lalanne and Morris [118] and Granet and Guizal [119] in 1996 solved the convergence issue for one-dimensional metallic gratings and TM polarized electromagnetic field. Li [120] explained that this improvement is due to a better continuity of electromagnetic fields at the permittivity discontinuities and introduced new Fourier factorization rules in 1996.

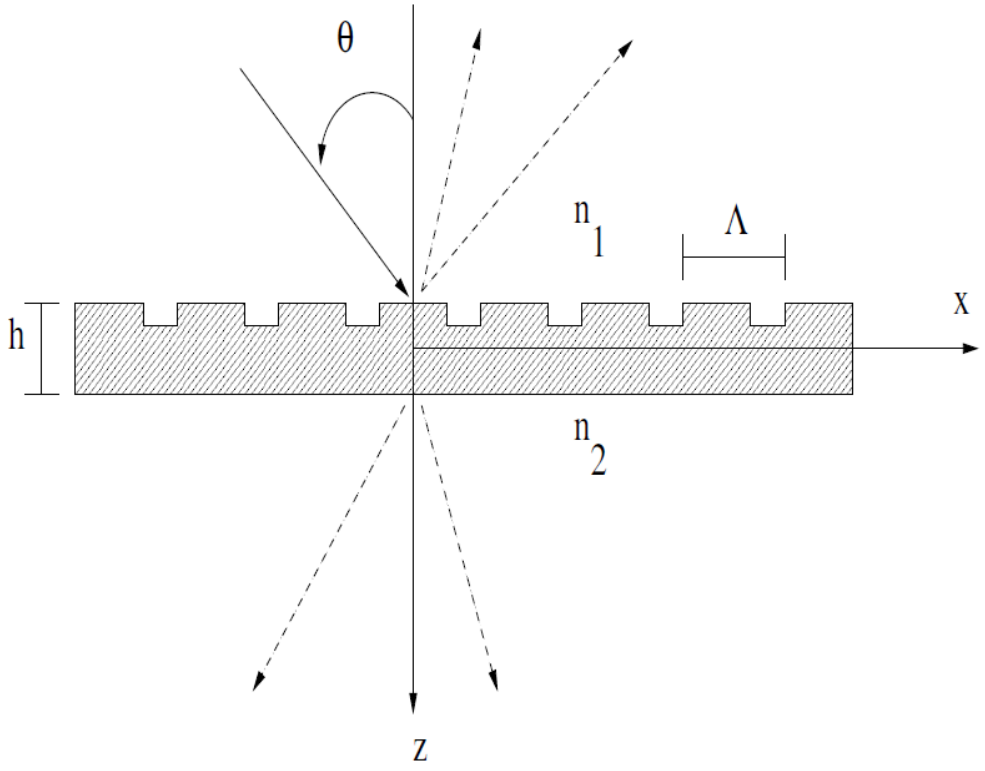

Figure 28: Schematic representation of a 2D grating (period Λ and thickness h). An incident light (incidence angle θ with respect to the normal to the material surface) generates diffracted lights of various orders. Extracted from [121].

The mathematical aspect is presented in [121,122] but the idea is to develop both fields and permittivities into Fourier series. For example, for a bi-dimensional periodic material (see **Figure 28**), the dielectric permittivity is written as:

$$\varepsilon_r(x) = \sum_n \varepsilon_n \, e^{j\frac{2\pi}{\Lambda}nx} \tag{1. 41}$$

with Λ the spatial period of the grating.

According to Bloch theorem, the electric field can then be written as a generalized Fourier series. The transverse electric (TE) polarized electric field can then be written as:

$$E_y = \sum_n S_n(z) \, e^{jk_x^n x} \tag{1. 42}$$

where k_x^n is the wavevector of the n^{th} order diffracted wave:

$$k_x^n = k_x + n\frac{2\pi}{\Lambda} \tag{1. 43}$$

$S_n(z)$ can be decomposed into forward and backward propagation modes:

$$S_n(z) = \sum_{m=1}^{n} w_{n,m} \left(a_m \, e^{-jk_0\lambda_m z} + b_m \, e^{jk_0\lambda_m (z-h)} \right) \tag{1. 44}$$

where h is the material thickness, and $w_{n,m}$ and λ_m are coefficients obtained from the Maxwell equations [121]. $k_0 = \omega/c$ is the wavevector norm which depends on the angular frequency ω and the light speed in vacuum c. For a temporal variation of the field given by $e^{j\omega t}$, the mode propagating with $e^{-jk_0\lambda_m z}$ propagates along the increasing z axis, while the mode with $e^{jk_0\lambda_m(z-h)}$ propagates along the decreasing z axis. a_m and b_m are thus the m-th order coefficients of the modes propagating respectively downward ($-k_0$) and upward ($+k_0$) (see **Figure 29**).

In the case of a multilayer structure (see **Figure 29b**), for each layer i in the structure, we define the column vectors:

$$a^{(i)} = \begin{pmatrix} a_1^{(i)} \\ \dots \\ a_n^{(i)} \end{pmatrix} \qquad \text{and} \qquad b^{(i)} = \begin{pmatrix} b_1^{(i)} \\ \dots \\ b_n^{(i)} \end{pmatrix} \tag{1. 45}$$

From there it is possible to link the arrays expressed in Equation (1. 45) using either a transfer matrix formalism (T-matrix) or a scattering matrix formalism (S-matrix), defined as:

$$\begin{pmatrix} a^{(N)} \\ b^{(N)} \end{pmatrix} = T(0,N) \begin{pmatrix} a^{(0)} \\ b^{(0)} \end{pmatrix} \qquad \text{and} \qquad \begin{pmatrix} a^{(N)} \\ b^{(0)} \end{pmatrix} = S(0,N) \begin{pmatrix} a^{(0)} \\ b^{(N)} \end{pmatrix}, \tag{1. 46}$$

for N stacked layers.

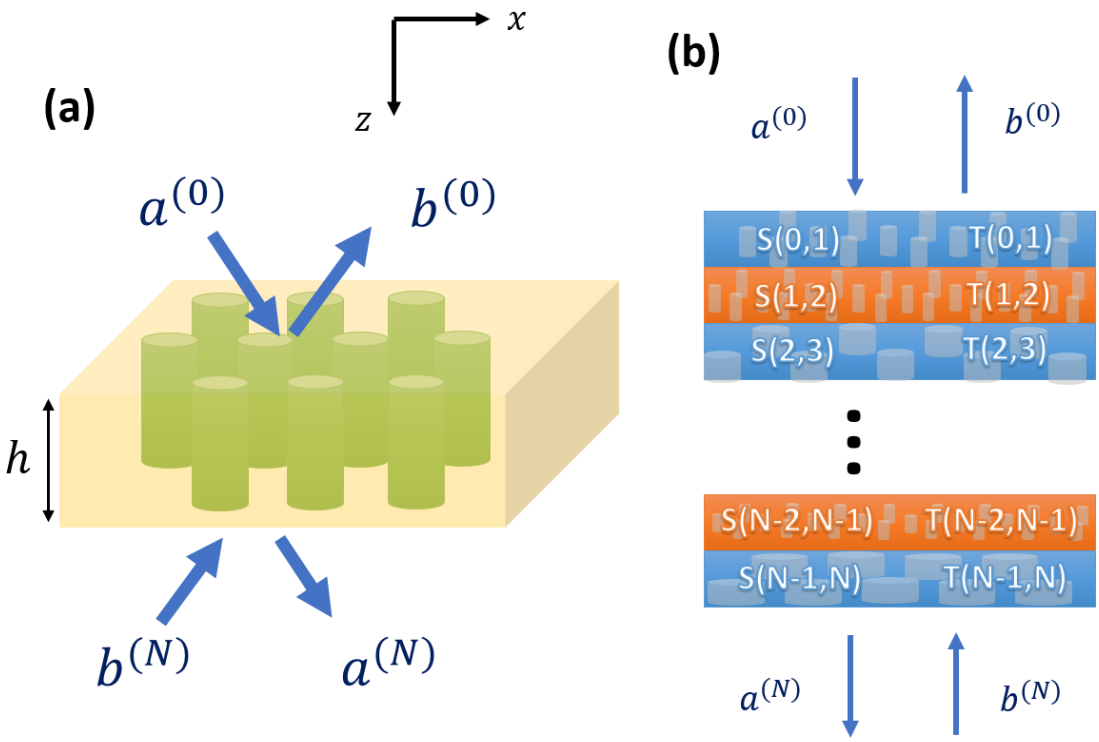

Figure 29: Schematic representation of a single (a) and a stack of (b) 2D periodic gratings, with incoming and outgoing electromagnetic waves denoted by their forward and backward modes. The scattering and transfer matrices are also written in each layer.

In the case of stacked periodic layers, as represented in **Figure 29b**, the problem consists in obtaining the global matrix linking the field amplitudes on both sides of the whole system of N stacked layers. To do so, successive matrices are computed. We can define the T-matrix and S-matrix for any layer i as:

$$\begin{pmatrix} a^{(i)} \\ b^{(i)} \end{pmatrix} = T(i-1,i) \begin{pmatrix} a^{(i-1)} \\ b^{(i-1)} \end{pmatrix} \quad \text{and} \quad \begin{pmatrix} a^{(i)} \\ b^{(i-1)} \end{pmatrix} = S(i-1,i) \begin{pmatrix} a^{(i-1)} \\ b^{(i)} \end{pmatrix}. \tag{1. 47}$$

In the case of the T-matrix, the global T-matrix of a system consisting of N stacked periodic layers, $T(0,N)$, is the product of each individual T-matrix:

$$T(0,N) = \prod_{i=1}^{N} T(i-1,i) = T(N-1,N)\, T(N-2,N-1) \ldots T(0,1) \tag{1. 48}$$

However, in the case of the scattering matrix, obtaining the global matrix for N stacked layers is more complex. Knowing each S-matrix for each individual layer i, it is possible to assemble the global S-matrix $S(0,N)$ for N stacked periodic layers by an iteration process [123]:

$$S(0,i+1) = \begin{pmatrix} S_{11}(0,i+1) & S_{12}(0,i+1) \\ S_{21}(0,i+1) & S_{22}(0,i+1) \end{pmatrix} \tag{1. 49}$$

with

$$S_{11}(0,i+1) = (I_{11}(i+1) - S_{12}(0,i)\, I_{21}(i+1))^{-1}\, S_{11}(0,i) \tag{1. 50}$$

$$S_{12}(0,i+1) = (I_{11}(i+1) - S_{12}(0,i)\, I_{21}(i+1))^{-1}\, (S_{12}(0,i)\, I_{22}(i+1) - I_{12}(i+1)) \tag{1. 51}$$

$$S_{21}(0,i+1) = S_{22}(0,i)\, I_{21}(i+1) S_{11}(0,i+1) + S_{21}(0,i) \quad (1.\ 52)$$

$$S_{22}(0,i+1) = S_{22}(0,i) I_{21}(i+1) S_{12}(0,i+1) + S_{22}(0,i) I_{22}(i+1) \quad (1.\ 53)$$

with $I_{jk}(i+1)$ the component of the j^{th} row and k^{th} column of the inverse transfer matrix at the $(i+1)^{\text{th}}$ interface defined as:

$$\begin{pmatrix} a^{(i)} \\ b^{(i)} \end{pmatrix} = I(i+1) \begin{pmatrix} a^{(i+1)} \\ b^{(i+1)} \end{pmatrix} \quad (1.\ 54)$$

We thus have

$$I(i+1) = T^{-1}(i,i+1)$$

Knowing $S(0,1)$ and $S(1,2)$ for the two first layers of a stacking, it is possible to calculate the scattering matrix $S(0,2)$ using Equation (1. 49), and similarly this recursive formula gives $S(0,3), S(0,4)$, up to $S(0,N)$.

While obtaining the global matrix seems easier using the T-matrix formalism, this formulation is relatively unstable compared to the S-matrix formalism. One main drawback is that it is rather limited to thin samples as integrating on higher thicknesses (deep gratings) may cause numerical overflows (growing exponential terms). The S-matrix avoids those overflows, which makes it more stable and versatile than the traditional transfer matrix approach [124–127].

The global scattering matrix can then be expressed as a function of the transmission and reflection amplitudes:

$$S(0,N) = \begin{pmatrix} r & t' \\ t & r' \end{pmatrix} \quad (1.\ 55)$$

where r, r', t and t' are the forward and backward reflection and transmission amplitudes respectively. When considering only one propagating mode above and below the stacked layers, $a^{(0)}$, $b^{(0)}$, $a^{(N)}$ and $b^{(N)}$ are composed of one single component. r, r', t and t are then linked to the forward and backward modes by:

$$r = \frac{b^{(0)}}{a^{(0)}} \quad (1.\ 56)$$

$$r' = \frac{a^{(N)}}{b^{(N)}} \quad (1.\ 57)$$

$$t = \frac{a^{(N)}}{a^{(0)}} \quad (1.\ 58)$$

$$t' = \frac{b^{(N)}}{b^{(0)}} \quad (1.\ 59)$$

Similarly, the transfer matrix can also be expressed in the same way:

$$T(0,N) = \begin{pmatrix} t - \frac{rr'}{t'} & \frac{r'}{t'} \\ -\frac{r}{t'} & \frac{1}{t'} \end{pmatrix} \quad (1.\ 60)$$

In our work the FMM method is used with a S-matrix formalism, through the MC Grating commercial software [128]. This software also includes codes based on a true modal method (TMM) which is not used in this work. This method, instead of using a Fourier expansion, considers a true modal basis and calculates the fields considering the boundary conditions at the grating walls [129,130].

1.4.4. Plane wave expansion (PWE)

A typical method used to calculate band diagrams of 1D, 2D or 3D photonic crystals is the plane wave expansion (PWE) method. This method is a frequency-domain method in the Fourier-space. It combines the Bloch theorem with a Fourier decomposition of the fields and permittivities. Injecting the resulting expressions into the Maxwell equations lead to an eigenvalue problem with the eigenvectors containing the elements of the fields decompositions and the eigenvalues depending on the frequencies ω. Solving this eigenvalue problem is possible numerically considering a finite number of elements in the decomposition. From there, a finite number of propagating modes are obtained and can be represented as allowed frequencies vs wavevector, which is the material band diagram.

1.5. Conclusion of this chapter

Thermochromic vanadium dioxide undergoes a phase transition from semiconducting to metallic phase at a transition temperature of 68°C for a pure VO_2 film. This transition is characterized by a significant change of the material optical properties. At higher temperatures, VO_2 near infrared transmittance and mid-infrared emissivity drops. These optical properties variations are interesting for applications including energy-efficient coatings for windows, buildings, satellites and camouflage applications. Depending on the application, different criteria are used to quantify the coating performances. For example, applications like energy-efficient coatings for buildings and satellites require a low emissivity in cold conditions and a high emissivity in warm conditions, which is the opposite behavior of a bulk VO_2 film. It may however be possible to address this problem by introducing a material nanostructuration. A polymer opal photonic crystal containing absorbing nanoparticles has a scattering resonance leading to a reduced emissivity. Introduced in a polymer opal photonic crystal, the absorbing VO_2 metallic phase may thus be an interesting coating material for buildings and satellites. In this thesis, the optical properties of a polymer opal photonic crystal containing VO_2 nanoparticles are studied through optical simulations using the Fourier modal method. An evaluation of the material performances regarding the different applications will be presented in the following chapters.

Chapter 2 – Model description and validation

In the previous chapter, the benefits of combining thermochromic VO_2 nanoparticles with the photonic bandgap effect due to material nanostructuration were highlighted. It was shown that an opal photonic crystal containing absorbing nanoparticles in the interstices generates resonances in the material total reflectance. In this thesis, an opal photonic crystal containing VO_2 nanoparticles in the opal interstices is modelled and optical simulations are performed in order to predict the material optical behavior. In this chapter the model will be described, with a focus on the tools and the implemented user interface, and then tested through comparisons with the optical behavior of well-known materials. In order to validate our model, the agreement between our simulation results and either simulation results obtained through other means or experimental results is tested. A progressive increase in the system complexity will be made along this chapter: from a single interface between two different materials to a thin layer and then a multilayer structure, and finally a 3D periodic structure such as the desired opal photonic crystal.

2.1. Model description

2.1.1. System description

In this thesis an opal photonic crystal containing VO_2 nanoparticles is modelled. This system is described in this section. The section is split into two parts: one focuses on the opal structure and its geometric parameters, and the other focuses on the modelling of the VO_2 particles inside the material.

2.1.1.1. Opal structure viewed along the [111] crystallographic direction

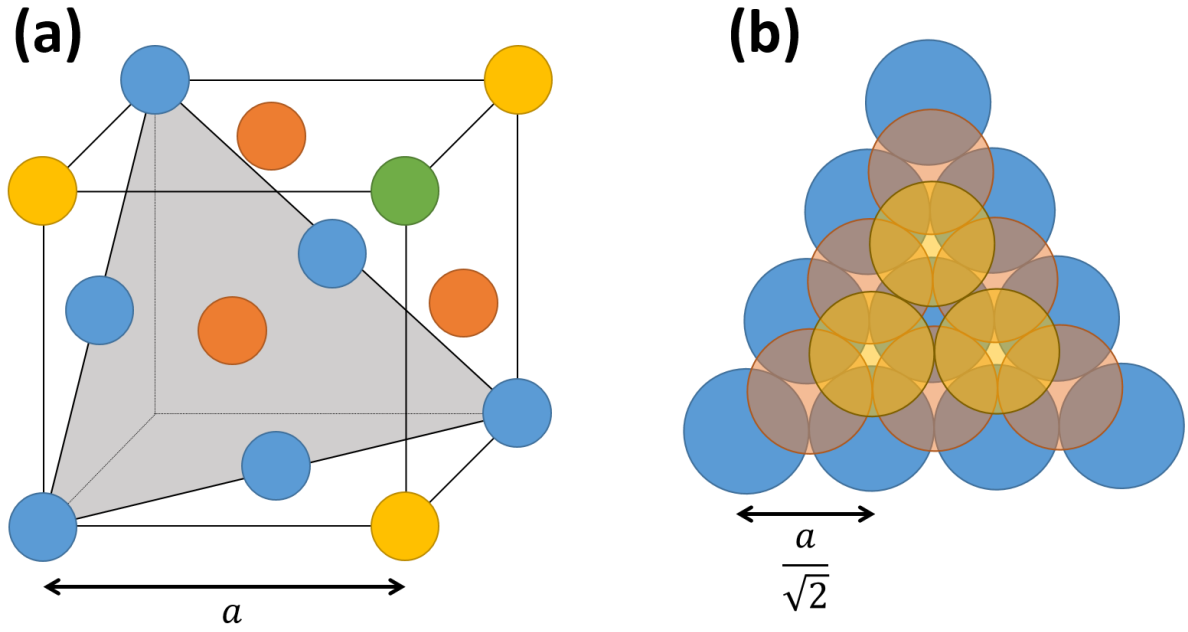

Figure 30 : Schematic representation of an opal structure viewed along the [001] (a) and [111] (b) crystallographic directions. The grey triangle links both figures as it represents one (111) plane. Different colors are used for different (111) planes. The lattice period is shown as a function of the cell parameter a. Reproduced from [131].

The system is a polymer opal photonic crystal containing vanadium dioxide nanoparticles. A schematic representation of an opal structure is presented in **Figure 30**. Such structure has an face centered cubic (fcc) lattice of cell parameter a as shown in **Figure 30a**. Polymer spheres are placed at each vertex and at the center of each face. Different colors are used for spheres placed on different planes with Miller indices (111) [132]. The grey triangle is one of these planes. Viewed along the [111] (see [133]) crystallographic direction, the structure is a superposition of triangular lattices of period $a/\sqrt{2}$, as shown in **Figure 30b**, and three of these planes represent a period in the [111] direction. These three (111) planes are represented with their respective colors corresponding to **Figure 30a**. The distance between each plane is:

$$d_{111} = \frac{a\sqrt{3}}{3} \tag{2. 1}$$

Each period along the [111] direction consisting in three (111) planes, the period in this direction is:

$$d_z = 3\, d_{111} = a\sqrt{3} \tag{2. 2}$$

Each plane can be modelled by a primitive cell which contains two spheres. Keeping in mind that each period contains three planes, this results in a total of 6 spheres in each period. Unlike **Figure 30a**, the representation in **Figure 30b** is a compact structure in order to better visualize the opal interstices. It is worth noting that the center of one sphere in a (111) plane corresponds to the center of an interstice on an adjacent plane. In this thesis, light will be injected with incidence planes containing the [111] direction.

2.1.1.2. Introduction of the VO_2 nanoparticles in the opal interstitial spaces

Inspired by the opal photonic crystal containing carbon nanoparticles in the interstitial spaces, produced by Baumberg et al. [10], we decide to model a polymer opal photonic crystal containing VO_2 nanoparticles in the opal interstices. One main limitation is related to these nanoparticles size. Indeed, in order to fit inside these interstitial spaces, their size is limited. The largest possible particle size depends on the number of particles, the cell parameter and the structure compacity. This limitation will be kept in mind when modelling our VO_2 nanoparticles in the future (see **Section 2.6**).

In this study the thermochromic VO_2 is represented by its two semiconducting and metallic phases. This implies that only these two phases are considered, while the phase transition is out of the scope of this work. In the optical model, VO_2 is then modelled with two different refractive indexes, respectively related to its semiconducting (cold) and metallic (warm) phases (see **Figure 8**).

Figure 31 is a schematic representation of the desired material, with polymer spheres (of material P_s) arranged in an opal structure, surrounded by a matrix made of a mixture of VO_2 nanoparticles and a polymer P_i.

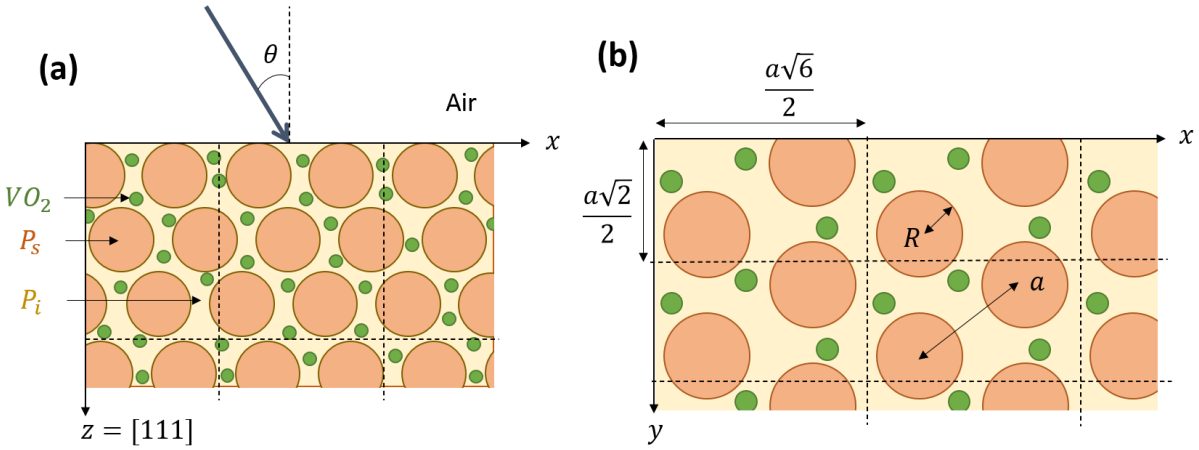

Figure 31: Schematic representation of a polymer opal consisting of polymer spheres P_s (radius R) surrounded by a mixture of VO_2 nanoparticles and a polymer P_i, view in the incidence plane (a) and top view (b). Dashed black lines refer to the edges of primitive cells.

2.1.2. Tool presentation and material definition

In this thesis spectral reflectance and transmittance calculations are performed using the MC Grating software. A quick description of this software is made in this section, with a focus on the material and structure description, the possible inputs and how a user can change these input parameters.

2.1.2.1. Generating spherical structures: the staircase approximation along the z-axis

The MC Grating software uses the FMM method combined with an S-matrix algorithm which solves the Maxwell equations through a Fourier decomposition in each stacked layer (see Chapter I). This method requires a material description as stacked layers. Each layer has a 2D periodicity in its plane and is invariant in the third direction. Defining z as the axis normal to the layers plane, periodic boundary conditions are applied in the x and y directions, which result in the material being infinite in both x and y directions. This means that in the case of a 2D photonic crystal, only one layer is required to model the whole crystal. However, in the case of a 3D photonic crystal, the third periodicity has to be introduced through the use of many stacked layers.

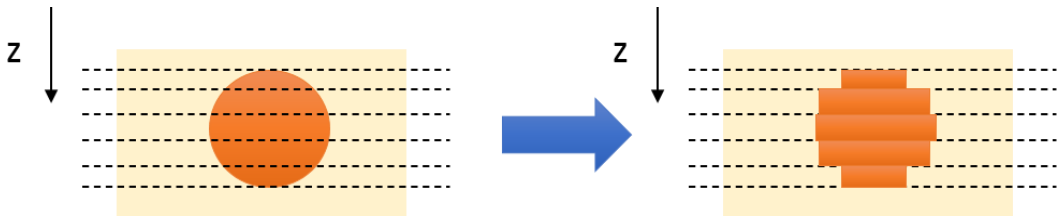

Figure 32: Principle of the staircase approximation illustrated in the case of a single sphere.

The opal structure we are modelling here introduces two main issues: a 3D periodicity and spherical elements. While the third periodicity can be introduced by repeating the same layers on top of each other, the spheres curved edges require a finer material description. Indeed, since each layer is invariant in the z direction, spheres curved edges cannot be accurately modelled. A staircase approximation is thus used in order to approximate the spheres. A schematic representation of this approximation is shown in **Figure 32** in the case of a single sphere. The perfect sphere shown on the

left is approximated by stacked cylinders sharing the same axis but with various radii. The structure shown on the right is then an approximation of the left figure, with the dashed lines representing the stacked layers defined in the model. A particular attention is required on the spatial resolution: thinner layers result in a more spherical structure and thus more accurate results, while also significantly increasing the number of layers used in the model, which leads to increased computation resources.

2.1.2.2. Generating spherical structures: computation of the cylinders radii

Along the direction normal to the surface, the staircase approximation allows the generation of curved structures through the approximation of spheres by stacked cylinders of various sizes.

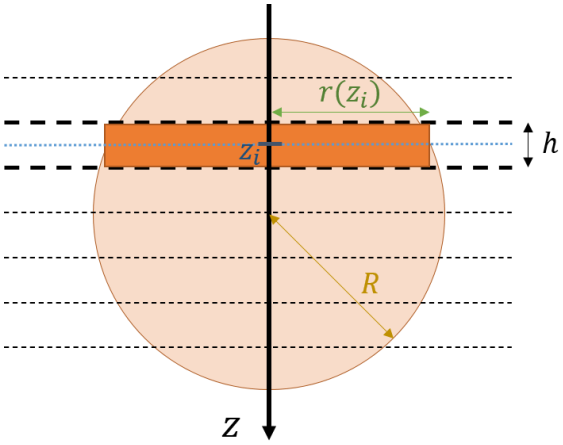

Figure 33: Illustration of the parameters implied in the generation of a sphere in the staircase approximation. The sphere of radius R is approximated by stacked cylinders of radii $r(z_i)$.

To illustrate how it works, we will consider one sphere from the opal structure. Its position is one of the six available spots in the primitive cell of the opal structure. Let this sphere center coordinates be (x_c, y_c, z_c). The model consists in stacked layers with a thickness defined by the spatial resolution (or layer thickness) h. For each layer i located from $z = z_i - h/2$ to $z = z_i + h/2$ with z_i the layer center position along the z axis (**Figure 33**), a cylinder is defined based on the 2D coordinates of its center position (x_c, y_c, z_i), and its radius $r(z_i)$ defined as:

$$r(z_i) = \sqrt{R^2 - (z_i - z_c)^2} \qquad (2.\ 3)$$

In the MC Grating software, a cylinder is defined by the 2D spatial coordinates of two points, represented by A and B in **Figure 34**. These points are the ones at a diagonal of the smallest rectangle containing the disk forming the top of the cylinder. Extending this to 3D, this disk becomes a cylinder with its height being the layer thickness. Keeping the same center position and varying the positions of both A and B points, the generated cylinder can have various radii. Doing the same process for all layers generates the desired sphere in 3D in the staircase approximation.

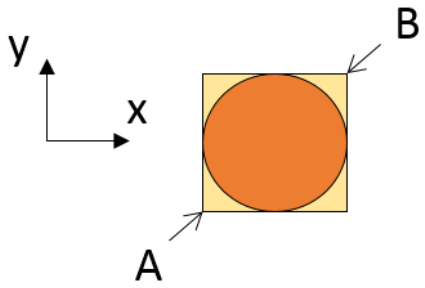

Figure 34: Cylinder definition by two points A and B at a diagonal of the smallest rectangle containing the disk forming the top of the cylinder.

2.1.2.3. User interface and input parameters

Generating spheres through multiple layers can be tedious for a whole opal structure consisting of numerous spherical particles. It was thus decided to generate the structures automatically using a Matlab user interface. Everything presented above is implemented in this interface. Structural parameters of the opal photonic crystal given by the user are translated into input data for the MC Grating software used to simulate the optical behavior of the generated material.

Input parameters include:

- Name of the output file which will then be opened in the MC Grating software
- Crystal cell parameter a
- Spheres and interstices refractive indexes, which can be complex and/or dispersive
- Opal sphere radius R
- Spatial resolution h (i.e. the layer thickness)
- Number of periods in x, y and z directions defined as a vector N containing three elements N_x, N_y and N_z
    - For example, $N_x = N_y = N_z = 1$ results in one parallelepiped delimited by the dashed lines in **Figure 31**
- Conditions of illumination:
    - Polarization
    - Angle of incidence defined by θ and ϕ (see **Figure 35**)
- Parameters related to disorder in the structure, if any (cf Chapter 5):
    - Sphere position variation (parameter σ_a)
    - Sphere radius variation (parameter σ_r)
    - Number of randomly removed spheres in the structure
- Scanning parameters
    - Choice of scanning parameter(s): wavelength, incidence angle θ, ϕ, etc.
    - For example, scanning along wavelengths allow to calculate spectral reflectance and/or transmittance values. The range and step are then required.

In MC Grating, the refractive indexes can be given either with constant values for non-dispersive materials, or with the name of any material from a list defined in another file. For practical reasons, a Matlab program has been developed to automatically generate new materials ready for this file, for example when calculating effective refractive indexes using Maxwell-Garnett approximation.

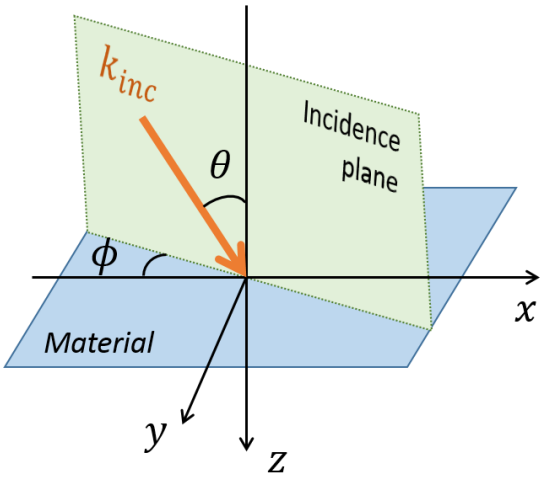

Figure 35: Schematic representation of the incident light on the material surface.

Useful information on how to input these data are also given in the program itself. With the various parameters listed above, this interface allows to generate a lot of different opal photonic crystal structures. These data are then translated for the MC Grating software, which will then calculate the desired optical properties. This is how we will generate the opal photonic crystals all along this thesis.

The desired material (**Figure 31**) and how it will be modelled were described above. We will now check the results given by the program. Since a 3D photonic crystal is a complex structure, this study will be made step-by-step with increasing complexity. The first step consists in computing the reflection and transmission coefficients of a single perfectly flat interface between two homogeneous materials. Then, a homogeneous VO_2 layer over a glass substrate with perfectly flat interfaces will be modeled. The next step will be to model multilayer thin films. Finally, an opal photonic crystal will be modeled.

2.2. Modeling of the reflection/transmission coefficients of single interfaces

Three different kinds of materials appear in this work: dielectric polymer, semiconducting VO_2 and metallic VO_2. The simple cases studied here to check the program will be an air/polymer interface and a polymer/VO_2 interface. In the case of the air/polymer interface, non-dispersive materials will be considered, and the variation of the reflection and transmission coefficients of this interface will be studied as a function of the incidence angle. In the case of the polymer/VO_2 interface, the dispersion of the VO_2 refractive index will be taken into account, as well as the two phases of VO_2. The reflection coefficient will thus be computed versus the light wavelength for the two phases of VO_2, for normally incident light.

Fresnel equations compute the reflection and transmission coefficients at an interface between two materials having refractive indexes n_1 and n_2 when illuminated with an incident angle θ_i (θ_t being the angle of the refracted light, see **Figure 36**) [35]:

$$R = \left| \frac{n_1 \cos\theta_i - n_2 \cos\theta_t}{n_1 \cos\theta_i + n_2 \cos\theta_t} \right|^2 \quad \text{and} \quad T = \frac{n_2 \cos\theta_t}{n_1 \cos\theta_i} \cdot \left| \frac{2\, n_1 \cos\theta_i}{n_1 \cos\theta_i + n_2 \cos\theta_t} \right|^2 \qquad (2.4)$$

These equations can be used when the layers are homogeneous and described by real refractive indexes, that is in the case of non-absorbing materials. A more general description of the Fresnel equations in the case where n_1 is real and n_2 is complex can be found for example in [134]. Note that for normally incident light, which is the case considered for the polymer/VO_2 interface, the equation (2. 4) remains valid for the reflection coefficient even when n_2 is complex. The reflection coefficient can thus be written as:

$$R = \left| \frac{n_1 - n_2}{n_1 + n_2} \right|^2 \qquad (2.5)$$

These equations will be used in comparison with our simulation results in order to validate the program in the case of a single interface.

2.2.1. Modeling of an interface between air and polymer

The first interface is an interface between air of refractive index n_1 = 1 and a dielectric material such as a polymer. Polymers have refractive indexes typically ranging from 1.3 to 1.7, so in this section the polymer refractive index is set to n_2 = 1.5. The light incident on the polymer surface has a transverse electric (TE) polarization and an incidence angle θ_i. A schematic representation is given in **Figure 36**.

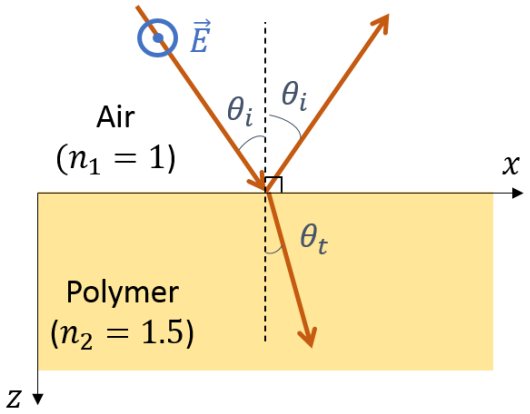

Figure 36: Air-polymer interface, with a TE-polarized incident light, and a θ_i incidence angle on the polymer surface.θ_t is the refracted angle inside the polymer.

Figure 37 shows the air/polymer interface total reflectance and transmittance values (also called reflection and transmission coefficients) for different incidence angles, obtained through our FMM program and the Fresnel equations.

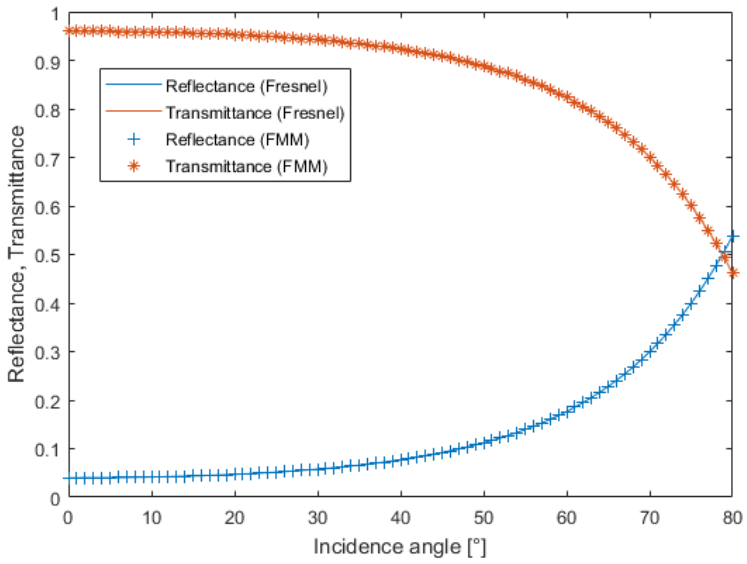

Figure 37: Total reflectance and transmittance of an air-polymer (n=1.5) interface for incidence angles from 0° to 80°, comparison between the FMM program and the Fresnel equations.

The results obtained with the Fresnel equations are presented in plain lines, while the ones simulated through the FMM program are shown with cross markers. Total reflectance and transmittance values are represented in blue and orange respectively. Reflectance and transmittance values obtained through FMM and through the Fresnel equations are perfectly in agreement in the case of an air-polymer interface, for incidence angles from 0° to 80°. These results show that the results obtained through the FMM simulation used in this work are in agreement with the theory predicted by the Fresnel equations in the case of an interface between air and a dielectric polymer modelled by its average refractive index 1.5.

This study about an air-polymer interface is comparable to a study for any interface between two non-absorbing materials. We are thus confident that the program works properly to compute the reflection and transmission coefficients of any interface between two non-absorbing materials.

2.2.2. Modeling of an interface between VO_2 and a dielectric material

The next interface studied in this section is an interface between VO_2 and a dielectric material such as air or a polymer. The difference compared to the previous interface is the introduction of a dispersive absorbent and thermochromic material. The dispersive aspect of VO_2 leads to a wavelength-dependent optical behavior. Its absorption property leads to a refractive index with complex values (see **Figures Figure** 8**, Figure** 9 and **Figure** 10). The thermochromic aspect of VO_2 introduces two different cases in this study for the cold (semi-conducting) and warm (metallic) phases of VO_2. For this study a polymer of refractive index n_1 = 1.5 is used, and a schematic representation of the interface is shown in **Figure 38**.

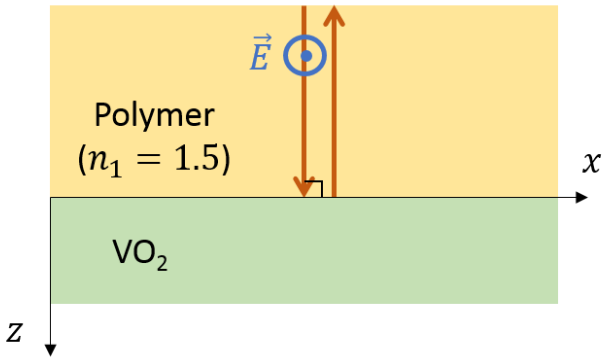

Figure 38: Illustration of a polymer-VO2 interface with normally incident light.

Figure 39 shows the total reflectance spectra of this polymer-VO_2 interface, with a normally incident light ($\theta_i = 0°$), for both VO_2 semiconducting and metallic phases. Plain blue lines are simulation results obtained through the FMM simulation program. These simulated spectral reflectances are compared to the values obtained through the Fresnel equations, shown in green markers.

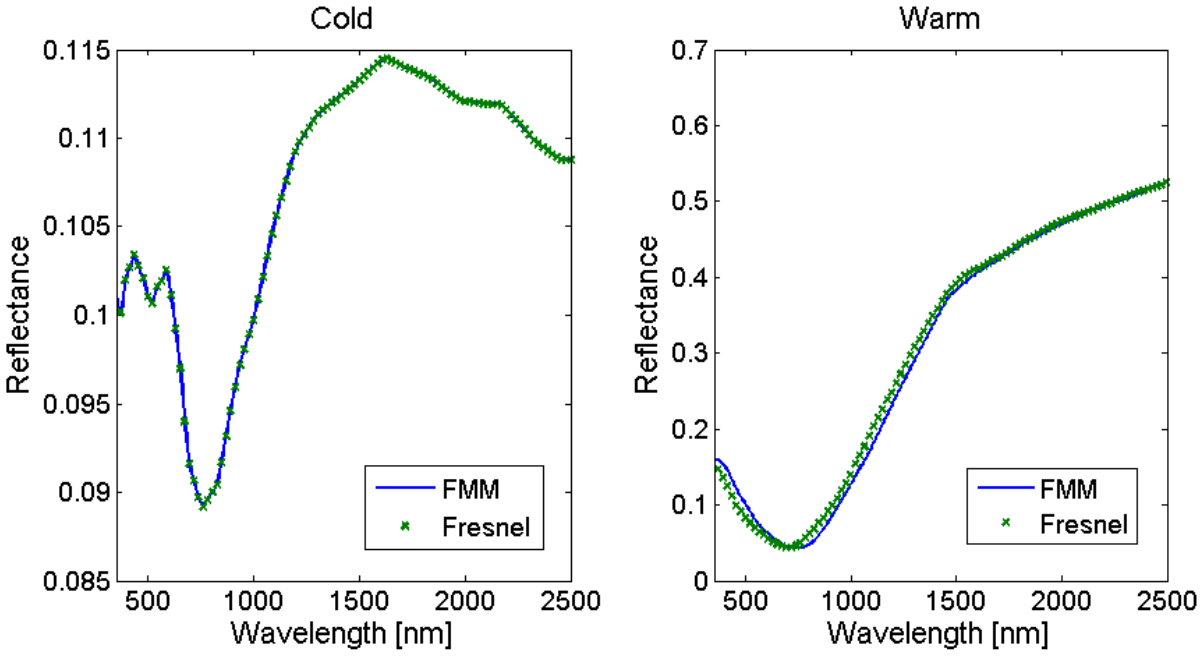

*Figure 39: Total reflectance spectra of an interface between a polymer (n_1=1.5) and VO_2 in cold (left) and warm (right) conditions, at normal incidence ($\theta_i = 0°$), calculated through the FMM program and Fresnel equations.The VO_2 refractive indexes are the ones obtained by Mlyuka et al. (see **Figure 8**)* [7].

For both cold and warm conditions, the spectral total reflectances at normal incidence obtained through these two different methods are in agreement. This study shows that the program developed in this thesis can correctly model the optical behavior of flat interfaces between two dielectric materials, and also between a dielectric material and a dispersive absorbent material such as VO_2.

2.3. Modeling of one layer of pure VO_2 material

Once a single interface properly modelled, the next step considered here is to model a material composed of two interfaces: a homogeneous film over a homogeneous substrate. For this study, a pure VO_2 layer of thickness e is modeled on a substrate having a refractive index $n_3 = 1.5$ (**Figure 40**). The VO_2 refractive indexes are extracted from [7].

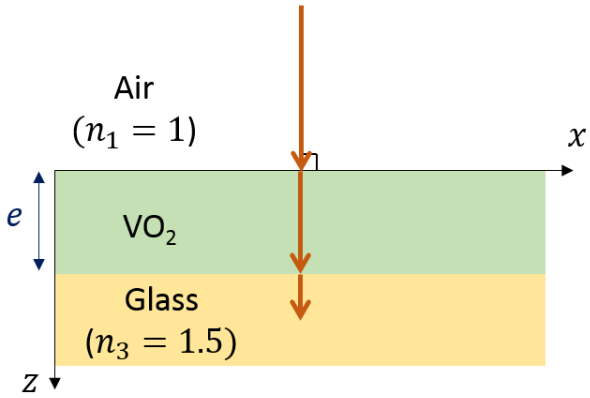

Figure 40: VO_2 layer with a thickness e on a glass substrate ($n_3 = 1.5$) and a normally incident light.

The material transmittance spectra in the visible and near infrared spectral regions are calculated using our program and compared with the results of Li et al. [36] obtained using a Fresnel equations based model. The comparison between these results are presented in **Figure 41** for different material thicknesses (e = 10, 20, 30, 50 and 100 nm). As VO_2 undergoes a phase transition at a certain transition temperature, the simulations are performed in both cold (**Figure 41a**) and warm (**Figure 41b**) conditions using the two different refractive indexes for both phases. Solid lines are obtained through our simulations using the FMM method, while dashed lines are results extracted from [36]. The same VO_2 refractive index is used for both calculations.

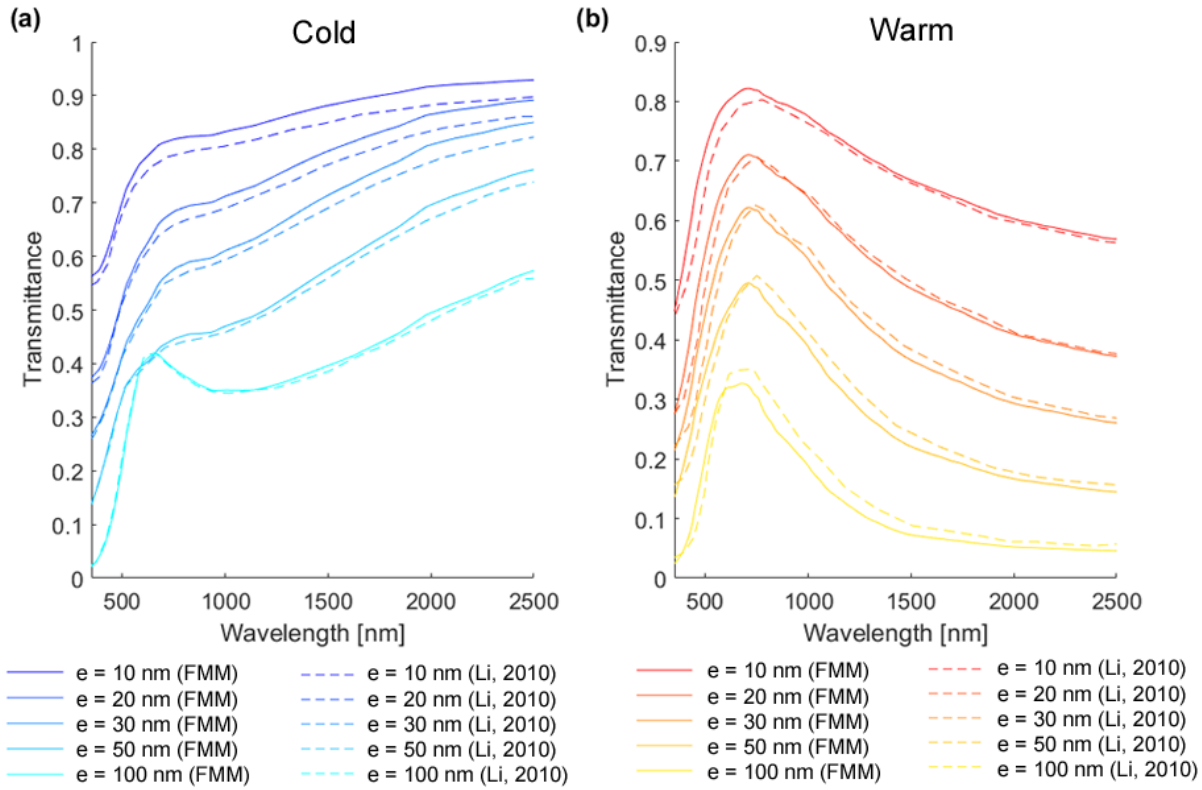

Figure 41: Computed spectral transmittances of a pure dense VO_2 film on a glass substrate (n=1.5), for different thicknesses (10, 20, 30, 50 and 100 nm), in cold (a) and warm (b) conditions (solid lines). Results are compared with [36] *(dashed lines).*

As the material thickness increases, the transmittance decreases for both cold and warm states as light is more absorbed in a thicker absorbing material. The VO_2 near-infrared transmittance is lower in the warm phase than in the cold one.

For each considered case, the results obtained through the FMM program and these of [36] are in good agreement, which comforts the proper working of our program in the case of a thin layer of pure VO_2 material over a glass substrate, and more generally in the case of thin homogeneous absorbing monolayers over a homogeneous substrate.

2.4. Modeling of multilayer periodic thin films containing non dispersive materials

We have shown that the program used in this thesis can successfully model the optical properties of one single interface and of thin homogeneous monolayers on top of a homogeneous substrate. The next step is to prove that it can also model a multilayer structure. More specifically, a 1D photonic crystal will be modelled in this section. A periodicity along the direction normal to the material surface (z-axis) will thus be introduced. This kind of structure is interesting as it introduces a first periodicity in the material, which is a first step before reaching the desired 3D periodicity of the opal structure.

The optical behavior of periodically structured materials can be modelled through two different aspects: either by their extrinsic properties such as reflectance and transmittance spectra, or by their band diagram (see **Section 1.3.2**). These representations are closely linked but different methods are used in order to obtain them. While our method calculates the extrinsic properties directly, other numerical methods are used to calculate band structures of photonic crystals. We will use a commonly used method (the Plane Wave Expansion (PWE) method) to obtain the band structure of a 1D photonic crystal, and check if the band diagram is coherent with our simulation results. Then experimental measurements will be performed on a real material consisting of a 1D photonic crystal. These measurements will also be compared to our simulation results.

2.4.1. Modeling of periodic multilayer thin films containing non-dispersive materials: comparison between the PWE method and our FMM program

First of all, in this section, a first comparison between two numerical models (FMM and PWE) will be performed. PWE is a method based on solving the Maxwell equations as an eigenvalue problem in a plane-wave basis. This method is typically used to calculate the band structure of photonic crystals having non-dispersive materials. This method can thus be used here, in the case of a multilayer consisting of stacked layers of periodically alternating non-dispersive materials of refractive index $n_1 = 1.64$ and $n_2 = 1.491$, corresponding respectively to the refractive indexes of polyethylene terephthalate (PET) and poly(methyl methacrylate) (PMMA) (see **Section 2.4.2**). The layers are stacked along the z-axis, each being 100 nm thick. Note that the PWE method models infinitely periodic materials, whereas in the FMM program, a total of 100 layers is considered. A schematic representation of the system is given in **Figure 42**.

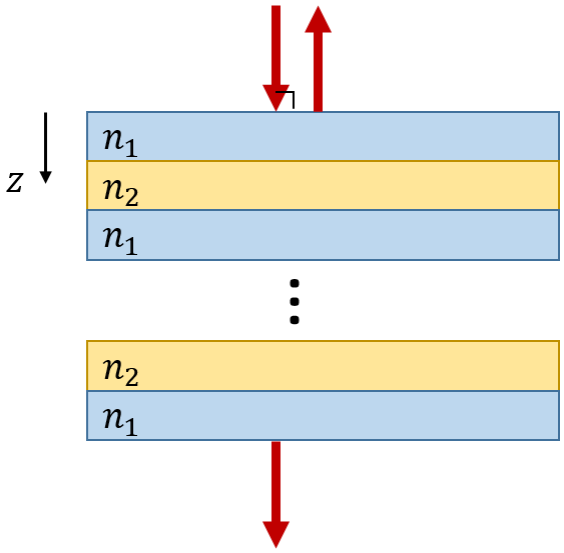

Figure 42: Schematic representation of a 1D photonic crystal illuminated with normally incident light.

The MIT Photonic Bands (MPB) software was used to calculate the band structure of such material at normal incidence, represented in **Figure 43**. The allowed frequencies are represented in black lines while two horizontal red lines indicate the edges of the complete photonic bandgap, located at normalized frequencies 0.31 and 0.33. These frequencies can be translated in terms of wavelengths using this relation:

$$\lambda = \frac{a}{\omega^{norm}} \tag{2. 6}$$

with λ the wavelength, ω^{norm} the normalized frequency and a the cell parameter. In this case, the cell parameter is also the period along z direction, so a = 200 nm as the period corresponds to two layers of 100 nm each. The obtained PBG at normal incidence for this material thus corresponds to wavelengths from 606 to 645 nm.

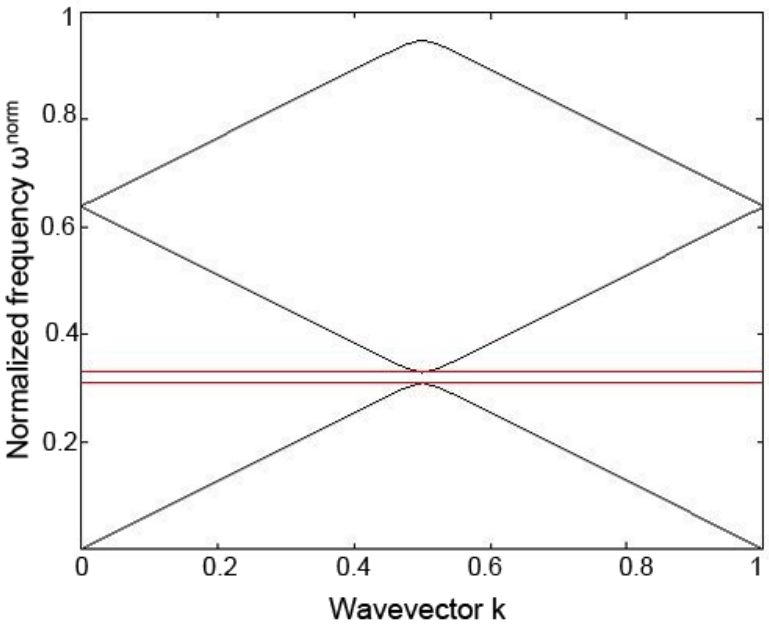

Figure 43: Band diagram of infinite periodic alternating PEA and PMMA layers with equal thicknesses and complete bandgap highlighted in red.

Keeping this PBG position in mind, we now calculate the spectral reflectance using the FMM program for the same material. Results are shown in **Figure 44** for a normally incident light on the material surface. The reflectance peak observed on this spectrum is due to the PBG effect occurring in this 1D photonic crystal. Measuring this peak full width at half maximum (FWHM) gives the PBG range from 606 to 654 nm. These values are comparable to the values obtained earlier through the PWE method (606 to 645 nm). Slightly different values can be explained by small inaccuracies while reading the reflectance spectrum and the band diagram.

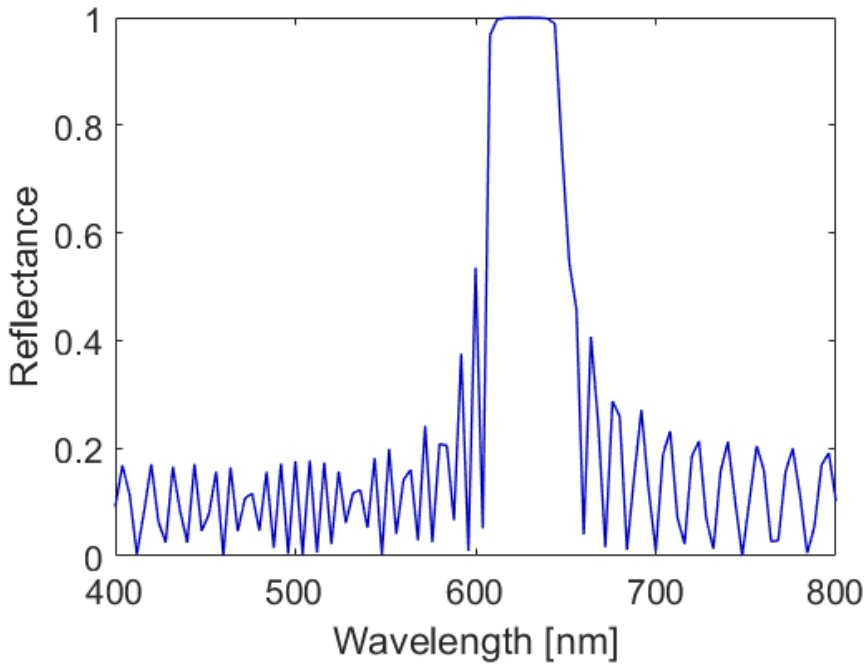

Figure 44: Calculated reflectance spectrum of 100 stacked periodically alternating 100 nm-thick layers of PET and PMMA at normal incidence, using the FMM program. The step in wavelength is 4 nm.

This agreement in terms of PBG position between two independent numerical methods make us confident in the proper working of the FMM program. To further increase this confidence, we will now compare these simulation results to experimental measurements.

2.4.2. Modeling of multilayer thin films containing non-dispersive materials: comparison between our FMM program and a real material

As a commercially available and cheap 1D grating material, the 3M Radiant Light film is an interesting material for our simulation of a 1D photonic crystal. It will allow the comparison between the simulation results and experimental measurements. A 3M (76918) CM592 Radiant Light film was used in this section.

The 3M Radiant Light film is an industrial material described as a polymer multilayer film, consisting of alternating PET and PMMA layers surrounded on both sides by a thicker PET shield layer. A schematic representation of such material is given in **Figure 42** by considering $n_1 = n_{PET} = 1.64$ and $n_2 = n_{PMMA} = 1.491$. A SEM micrograph (obtained by a MEB-FEG Supra 55VP from ZEISS) given in **Figure 45** is used to estimate the total number of layers and their thickness.

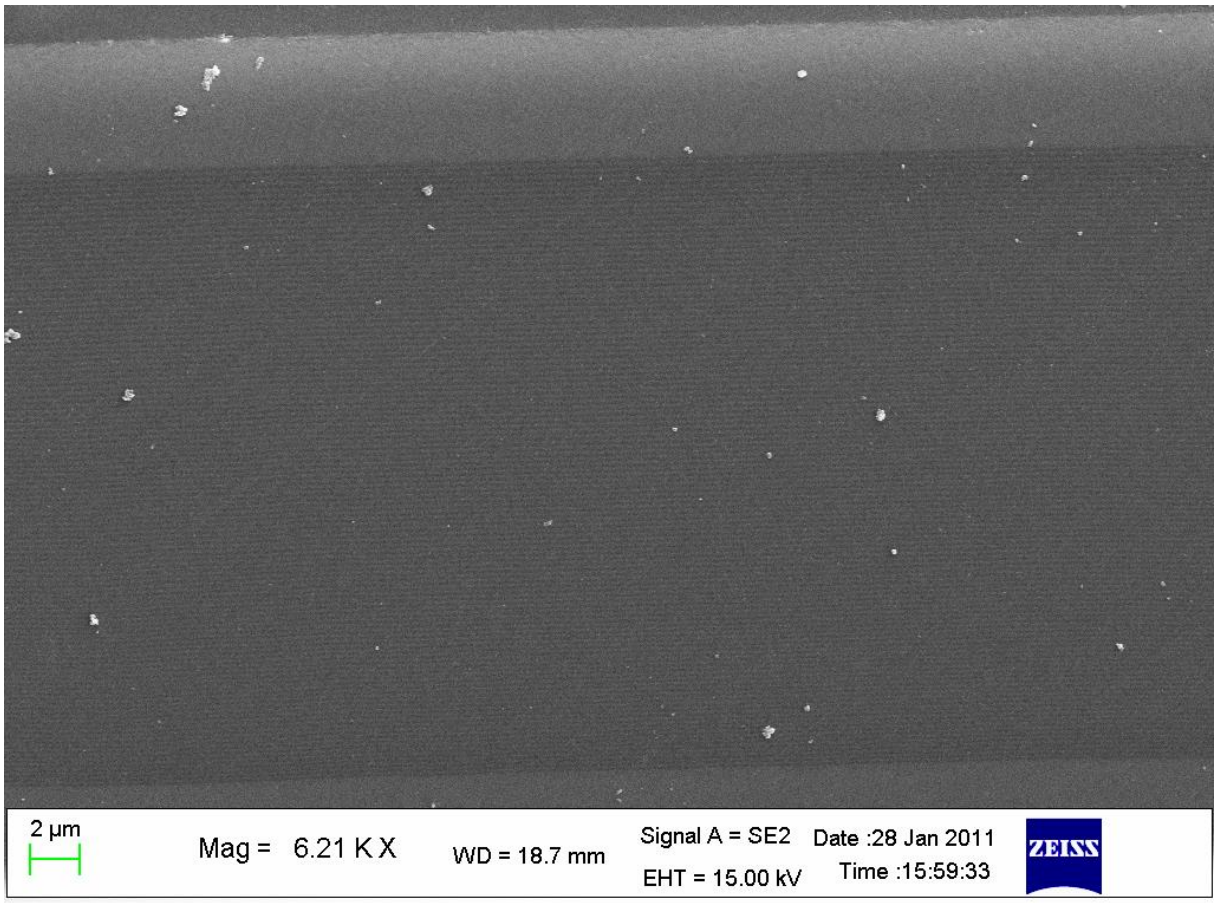

Figure 45: SEM micrograph of the 3M Radiant film (side view).

Approximately 100 layers of about 100 nm each are visible. However, the limited quality of this micrograph does not allow to obtain more accurate values. These approximated thickness values are used in our simulation.

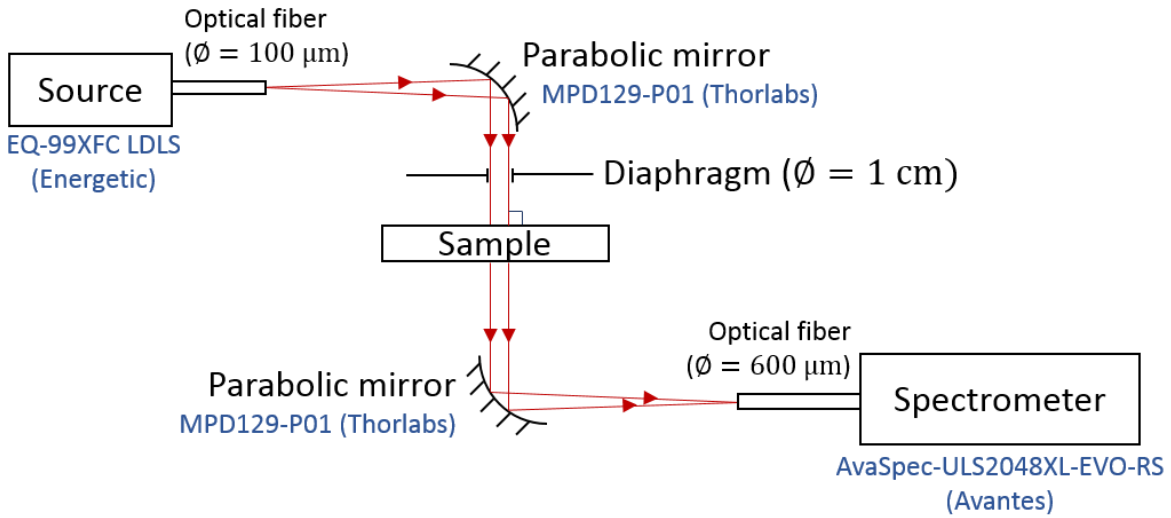

Figure 46: Schematic representation of the optical system used to measure the spectral transmittance at normal incidence of the 3M Radiant film.

For comparison with experimental measurements, the spectral transmittance of a 3M Radiant Light film has been measured using the optical system represented in **Figure 46**. The light emitted from an

EQ-99XFC LDLS light source from Energetic, connected to a 100 µm core diameter optical fiber, hits a MPD129-P01 parabolic mirror from THORLABS. The reflected light size is limited to 1 cm by a diaphragm before reaching the film surface at normal incidence. The transmitted light is then focused by a similar parabolic mirror into a 600 µm core diameter fiber connected to an AvaSpec-ULS2048XL-EVO-RS spectrometer from Avantes with a CCD sensor with a spectral resolution of about 2 nm.

The measurement results at normal incidence are presented as the blue curve of **Figure 47**. A large valley associated with a PBG effect is visible from about 580 nm to 750 nm. More precisely, inside this spectral region, it seems that the spectral transmittance describes three small valleys.

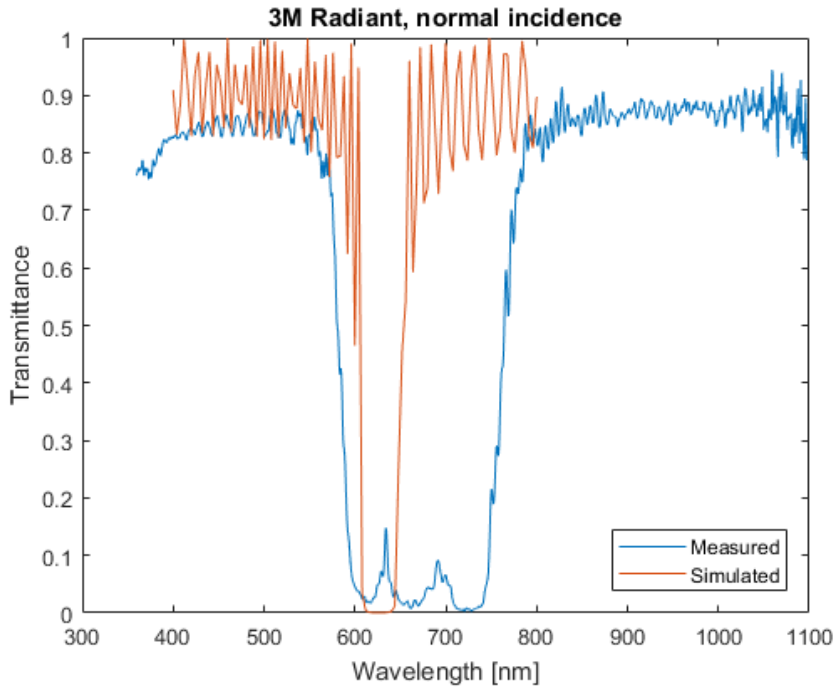

Figure 47: Comparison between the measured transmittance spectra of the 3M Radiant film and simulated transmittance spectra of 100 periodically alternating 100 nm-thick PET and PMMA layers.

In order to model the PBG effect in a similar structure, the spectral transmittance of a 1D photonic crystal consisting of 100 stacked alternating layers of PET ($n_{PET} = 1.64$) and PMMA ($n_{PMMA} = 1.491$), each layer being 100 nm thick, was calculated and shown as the orange line in **Figure 47**. This simulation result shows a much thinner bandgap. Also, the bandgap position is not centered on the same position as the experimental bandgap. One possible reason may be a cumulative effect of multiple bandgaps, due to a non-unique period in the 3M sample.

In order to investigate this possibility, a structure consisting of two stacked 1D photonic crystals, each having their own PBG effect, is modelled. A schematic representation is given in **Figure 48a**. The same materials are used in both of these 1D photonic crystals. However, the thickness is slightly different in order to shift the PBG. For this study the thicknesses are set to 100 nm for the top crystal and 112 nm for the bottom one. For each crystal, all of the 100 layers share the same thickness. The transmittance spectrum of such structure is presented in **Figure 48b**. Two valleys are observed, related to the two PBG effects coming from these two stacked crystals. This study shows that the larger valley observed in the 3M Radiant film may come from three stacked 1D photonic crystals with slightly different thicknesses. These layers thickness variations (on a nanometers scale), whether made on purpose or not, result in an enlarged PBG peak. Yet, a further investigation is out of the scope of our work. More accurate thickness measurements inside the material would be required in order to more correctly

simulate the optical behavior of the real material. The main goal here is not to find these parameters, but rather to prove that our model can successfully model the optical behavior of a 1D photonic crystal. This was reached by comparing the PBG position obtained with our FMM program with an independent numerical model as well as with experimental measurements.

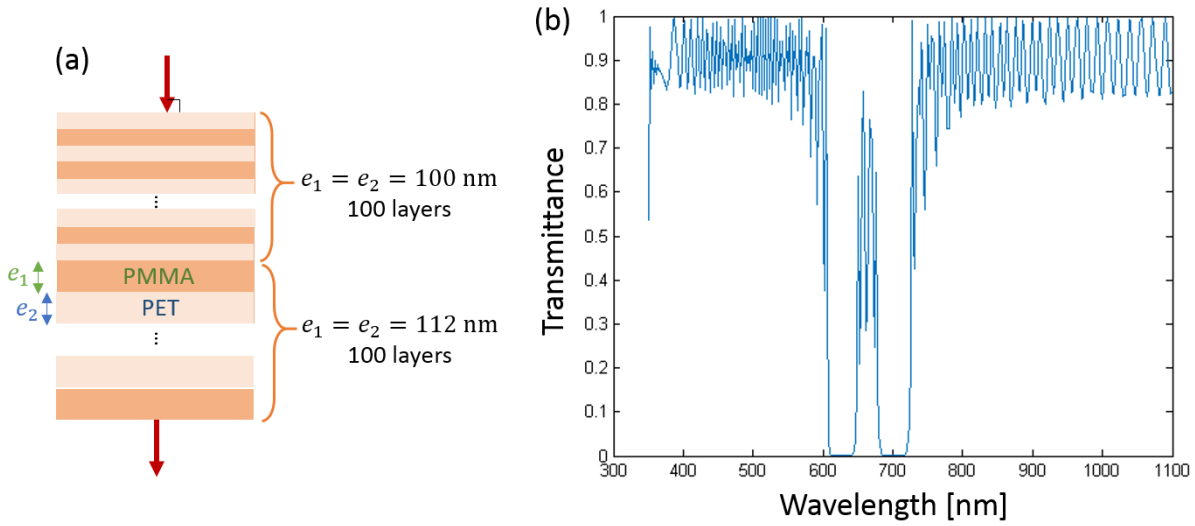

Figure 48: Schematic representation of two 1D photonic crystals stacked on top of each other, consisting of 100 layers of alternating PET and PMMA layers with a thickness of 100 nm for the top photonic crystal, and 112 nm for the bottom photonic crystal (a), and the corresponding calculated transmittance spectrum with a normally incident light (b).

2.5. Modeling of an opal photonic crystal

We have shown that the program implemented in this thesis can successfully simulate the optical behavior of a 1D photonic crystal. The next step is to model a 3D photonic crystal, which is the final structure that we want to model in this thesis. In this section we will study the possibility to model 3D nanostructured materials such as polymer opal photonic crystals using the numerical FMM method combined with a staircase approximation.

2.5.1. System presentation

The last step for our model validation is to properly model a 3D periodic opal photonic crystal. In order to do so, a non-compact structure is modelled here and comparisons between our numerical results with experimental results extracted from the literature [100] will be made, in terms of spectral reflectances. Polystyrene (PS) (refractive index $n_{PS} = 1.58$) spheres are ordered in a face centered cubic (fcc) structure and surrounded by a poly(ethyl acrylate) (PEA) (refractive index $n_{PEA} = 1.47$) matrix. A schematic representation of a (111) plane is shown in **Figure 49a** where values for sphere radius $r = 85.56$ nm and cell parameter $a = 318.2$ nm are also represented. The light is injected with an incidence angle θ relative to the normal to a (111) plane as shown in **Figure 49b**.

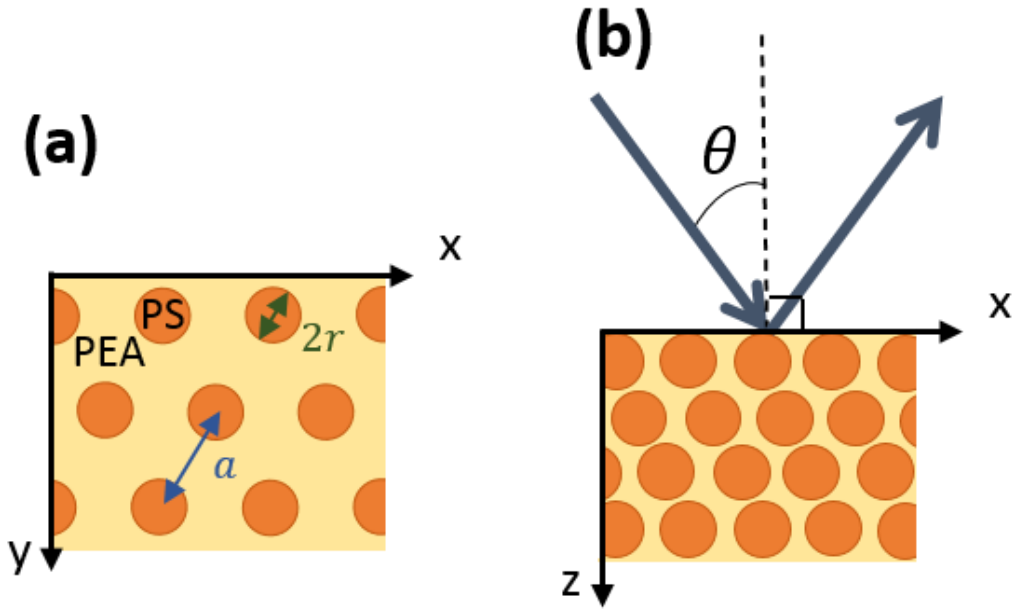

Figure 49: Schematic representation of a polymer opal photonic crystal consisting of PS spheres (diameter $2r = 171.1\ nm$) surrounded by a PEA medium, in an fcc structure (cell parameter $a = 318.2\ nm$), viewed from the top ((111) plane) (a) and from the side (perpendicularly to a (111) plane) (b). The light is incident with an angle θ relative to the normal to a (111) plane.

2.5.2. Influence of the number of periods along the depth direction

The material we are trying to model here is, in reality, very thick (typically a few hundred microns) [100]. However, from a certain number of periods along the depth direction z, the crystal behaves like an infinite crystal and it is thus not necessary to model such large film thicknesses. **Figure 50** shows the material reflectance spectra with a normally incident light ($\theta = 0$), for different numbers of periods in the [111] direction, for 7, 10, 15, 30 and 50 periods. The corresponding material thickness can be obtained through *Equation (2. 2)* and are respectively 3.9 µm, 5.5 µm, 8.3 µm, 16.5 µm, 28.6 µm. The material is transparent in the considered spectral region, so thin film interferences occur, visible as oscillations in the spectra. A reflectance peak linked to a PBG effect is observed around 560 nm. As the number of periods increases, the peak amplitude is increased, until it converges to what is obtained in the case of an infinite crystal. Note that thin film interferences depend on the material thickness, so the oscillations frequency and positions are dependent on the number of periods. Such oscillations wouldn't occur in an infinite crystal. Thus, for the convergence, only the average behavior of the material is considered on both sides of the PBG.

This convergence can be also seen in **Figure 51**, which represents the reflectance peak amplitude vs the number of periods in z direction used to model the crystal. The amplitude converges towards 1. It appears that a crystal consisting of 30 periods in the direction normal to the surface would have a similar optical behavior as an infinite 3D photonic crystal having the same materials and structural parameters. In order to mimic the behavior of an infinite crystal, 30 periods in the z direction are required, so unless specified differently, 30 periods will be modeled in the material depth in this section.

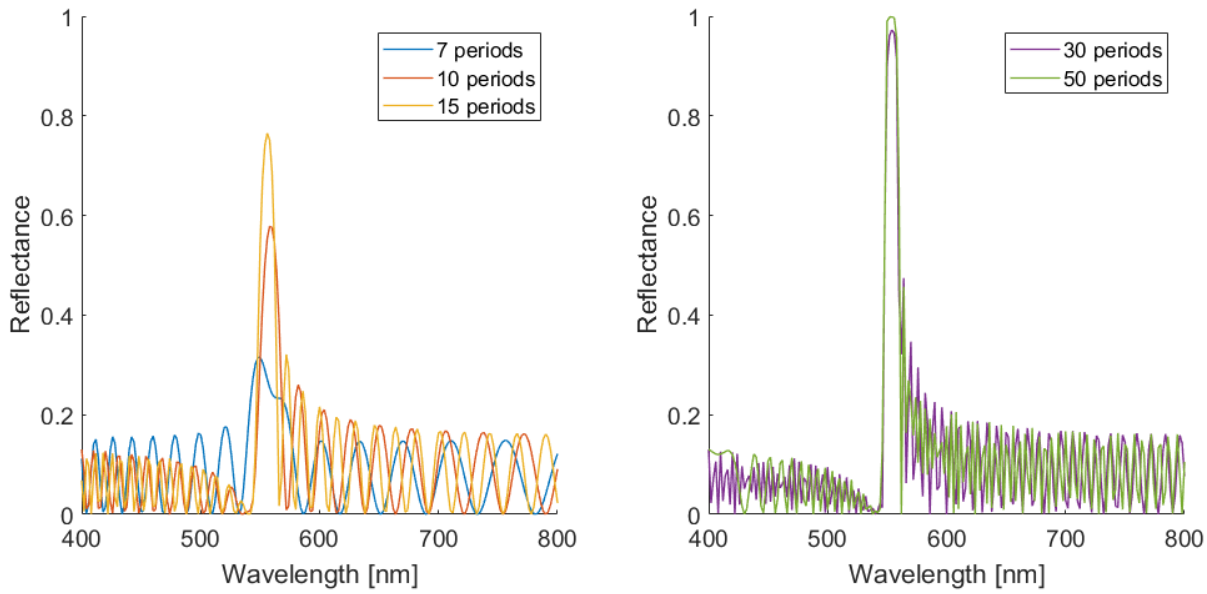

Figure 50: Reflectance spectra of a 3D photonic crystal consisting of PS spheres (radius r = 85.56 nm) in a PEA medium, in an fcc arrangement (parameter cell a = 318.2 nm), for different numbers of periods in the [111] direction (normal to the sample surface). The light is normally incident on the material surface.

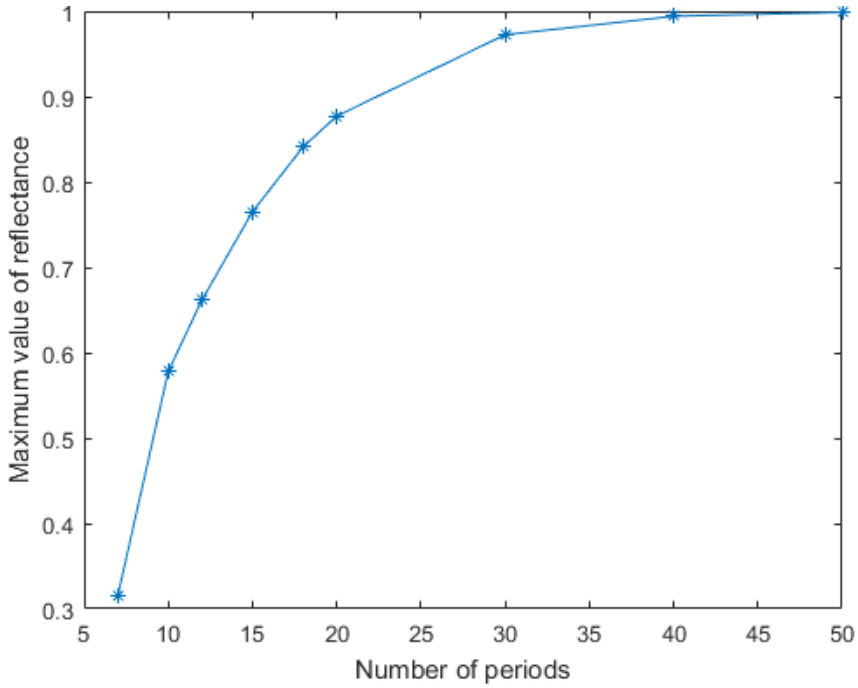

Figure 51: PBG reflectance peak amplitude as a function of the number of periods, for a 3D photonic crystal consisting of PS spheres (radius r = 85.56 nm) in a PEA medium, in an fcc arrangement (parameter cell a = 318.2 nm), for different numbers of periods in the [111] direction. The light is normally incident on the material surface.

2.5.3. Angle-dependent spectral reflectances comparisons

Angle-dependent reflectance spectra will be compared between our numerical simulations and the measurements presented for the Ogreen sample in [100]. Our FMM simulation results are presented in **Figure 52**, showing the angle-dependent reflectance spectra of this material for a non-polarized

incident light and an incidence angle from 0° (normal) to 80°. A reflectance peak is observed between 546 nm and 561 nm at normal incidence. This peak is linked to a PBG effect and is shifted towards lower wavelengths for higher incidence angles. PBG peaks shifting towards shorter wavelengths were also observed in other opal photonic crystals (for example [135]). Oscillations due to thin film interferences surround this peak.

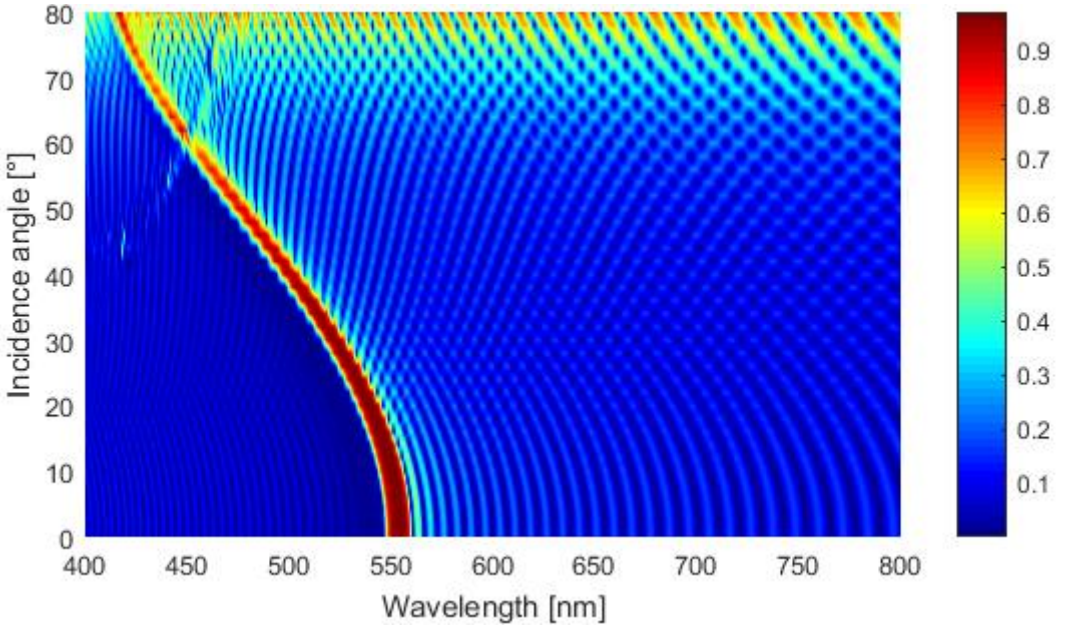

Figure 52: Angle-dependent reflectance spectra of a polymer opal consisting of PS spheres (radius r = 85.56 nm) in a PEA matrix with an fcc arrangement (cell parameter a = 318.2 nm), with a non-polarized incident light and 30 modelled periods in the [111] direction (normal to the sample surface).

Two values ($\theta = 0°$ and $\theta = 30°$) are extracted from these simulation results and compared with the experimental measurements of [100] in **Figure 53**. The peak position is about the same between our simulation and the experimental results from the literature. However, a few differences are observed between these two results. First of all, the larger PBG peak in the case of the measured reflectance may be due to internal defects in the real material, which are not currently considered in our model. A similar effect was observed in the case of a 1D photonic crystal in **Section 2.4.2**. However, the PBG peak position is not much influenced by these defects, so it remains the same between our simulation and the experimental results. Then, the absence of oscillations may be due to the sensor unable to detect high frequency oscillations. Indeed, the position of the m^{th} peak for normally incident light is given by

$$\lambda_m = \frac{2n_{eff}e}{m} \qquad (2.\ 7)$$

with n_{eff} the effective material refractive index and e the material thickness. The effective refractive index can be obtained through a Maxwell-Garnett approximation (see **Section 2.6.1**) considering PS spherical inclusions in a PEA matrix with a volume fraction of $f_{PS} = 0.3257$, resulting in $n_{eff} \approx 1.51$. The real material thickness being in a few hundred micrometers scale, this leads to an oscillations period in the visible spectral range of less than a nanometer (≈ 0.6 nm around $\lambda = 600$ nm for $e = 200$ µm). It is thus possible that such high frequencies are not detected by the sensor used in the experiment, resulting in an averaged value for these oscillations in the measured reflectance spectrum.

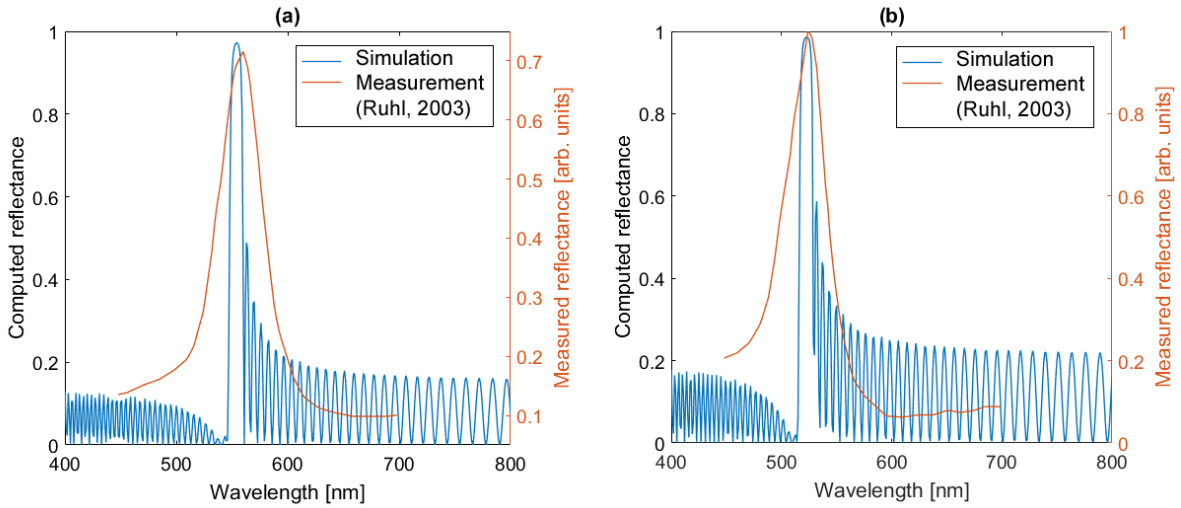

Figure 53: Reflectance spectra of a polymer opal consisting of PS spheres (radius r = 85.56 nm) in a PEA matrix with an fcc arrangement (cell parameter a = 318.2 nm), with a non-polarized light incident normally (a) and with a 30° angle relative to the normal to the sample surface (b). The incidence plane includes the [111] direction. Our simulation results are compared with measurement results extracted from [100].

This agreement between our numerical results and the experimental measurements extracted from the literature ensures that our model using the numerical FMM method combined with a staircase approximation can be used in order to model 3D periodic structures such as polymer opal photonic crystals, which is exactly the kind of structure considered in this thesis.

2.6. Effective behavior of the opal interstices

In this thesis, a polymer opal photonic crystal containing VO_2 nanoparticles in the interstices is modelled. In order to limit the model complexity, one idea is, instead of modelling each single VO_2 nanoparticle in the opal interstices, to rather consider an effective optical behavior for these interstices as represented in **Figure 54**. The interstitial spaces filled with dispersed VO_2 nanoparticles surrounded by a polymer P will be approximated by a homogeneous medium described by an effective refractive index derived from both VO_2 and P refractive indexes. In this section the accuracy of such approximation is investigated. Only a unique polymer is considered here, the spheres are thus made of polymer P and the interstices are a mix of the same polymer P and VO_2.

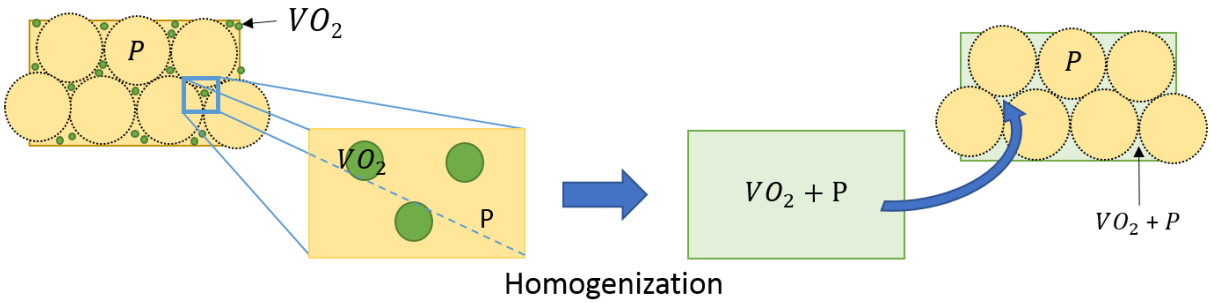

Figure 54: Schematic representation of the opal interstices homogenization process in the case of a unique polymer P.

2.6.1. Maxwell Garnett approximation and its validity

There are various models able to compute an effective optical behavior. Among the most commonly used, the Maxwell Garnett approximation [103,136] describes the optical behavior of small disperse spherical inclusions in a medium and will be used here due to its relative simplicity (effective refractive index directly obtained through a single formula). It introduces an effective refractive index n_{eff} based on the inclusions and medium refractive indexes, respectively denoted n_i and n_m. Maxwell-Garnett approximation gives:

$$n_{eff}^2 = n_m^2 \frac{1 + \frac{2}{3} f\alpha}{1 - \frac{1}{3} f\alpha} \qquad \text{with} \qquad \alpha = \frac{n_i^2 - n_m^2}{n_m^2 + \frac{1}{3}\left(n_i^2 - n_m^2\right)} \tag{2. 8}$$

with f the filling factor (volume ratio of the inclusions in the material).

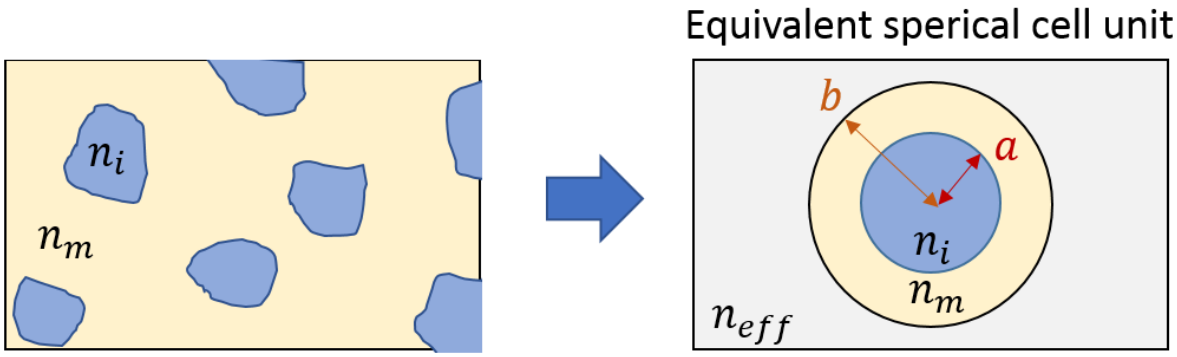

Figure 55: Separated grain structure with inclusion of refractive index n_i in a medium of refractive index n_m, equivalent to a spherical cell unit represented by a core-shell spherical particle with a core of material n_i and a shell of material n_m embed in a material of the effective refractive index n_{eff}. Reproduced from [137].

The mathematical origins of this approximation are detailed in [138]. The formula comes from modelling the system of dispersed inclusions by an equivalent spherical unit cell with a refractive index n_i coated with a material of refractive index n_m. A schematic representation is given in **Figure 55**. The spherical unit cell parameters are related to the filling factor by the following relationship:

$$f = \left(\frac{a}{b}\right)^3 \tag{2. 9}$$

with a and b the radii of the inner and outer spheres, respectively. The scattering amplitude of this coated sphere is a Taylor series in terms of b/λ with λ being the light wavelength in the effective medium. With small enough b/λ, the series can then be approximated to only its leading term. Note that as a is smaller than b, small values for b/λ implies also small values for a/λ. With no scattering event happening in a homogeneous medium, this leading term put to zero results in *Equation (2. 8)*. The accuracy of the Maxwell Garnett approximation depends on this b/λ term. Inaccuracies happen when b/λ becomes too large, meaning that either the spherical unit cell size or the light wave-vector become too big. In other words, the approximation becomes inaccurate when the spherical unit cell size becomes much larger than the wavelength in the surrounding medium. According to [138], the Maxwell-Garnett approximation will thus be accurate in the case of inclusions with a size smaller than the light wavelength, with no restriction on the value of the filling factor f.

However, Ruppin [139] showed that this criterion is insufficient near resonances of the dielectric constant of the inclusions. He derived two other criteria, which are reliable close to dielectric constant resonances:

$$| k_i R | \ll 1 \tag{2. 10}$$

$$\frac{(k_0 R)^2 [(\epsilon_1 + 2\epsilon_m)^2 + \epsilon_2]}{90 \epsilon_m} \ll 1 \tag{2. 11}$$

with k_i and k_0 the propagation constant respectively in the inclusions and the surrounding material, defined as:

$$k_i = \sqrt{\epsilon_i} \frac{2\pi}{\lambda} \tag{2. 12}$$

$$k_0 = \sqrt{\epsilon_m} \frac{2\pi}{\lambda} \tag{2. 13}$$

R is the spherical inclusions radius. $\epsilon_i = \epsilon_1 + i\epsilon_2$ and ϵ_m are the dielectric functions of the inclusions and the surrounding material respectively. The Equations (2. *10*) and (2. *11*) show that larger spheres having higher dielectric functions (both real and imaginary parts) contribute to inaccuracies in the Maxwell Garnett approximation. In particular, highly absorbing inclusions (high ϵ_2) may lead to inaccuracies.

Approximating our opal interstices by an effective index derived from the Maxwell Garnett theory may introduce inaccuracies due to large particles or the absorbing coefficients of the metallic VO_2 nanoparticles.

2.6.2. Ruppin criteria in the case of VO_2 nanoparticles dispersed in a polymer matrix

In order to evaluate the validity of a Maxwell Garnett approximation in the case of VO_2 nanoparticles dispersed in a polymer matrix, the criteria given by Ruppin (*Equations (2. 10) and (2. 11)*) are calculated in this case. The VO_2 dielectric function is extracted from [7]. The polymer refractive index is set to $n = 1.5$ as an average value for refractive indexes of polymers.

The particle size was chosen in order to be compatible with an opal polymer containing a few particles in the opal interstices. In a closed-packed face-centered cubic structure, there are two kinds of interstices: tetrahedral and octahedral interstices. The diameter of a tetrahedral interstice is:

$$d_{tetra} = \frac{a\sqrt{3}}{2} - R \tag{2. 14}$$

and the diameter of an octahedral interstice, slightly smaller, is:

$$d_{octa} = \frac{a}{2} - R \tag{2. 15}$$

with a the cell parameter and R the sphere radius. In the case of the smallest structure considered in this thesis ($a = 500$ nm), we can estimate the interstices size in our material: $d_{tetra} = 256.2$ nm and $d_{octa} = 73.2$ nm. To fill these interstices, in particular the tetrahedral interstices, we choose VO_2 particles of radius 100 nm.

Considering these parameters, the left terms of *Equations (2. 10)* and *(2. 11)* are calculated and represented in **Figure 56** as a function of the incident light wavelength.

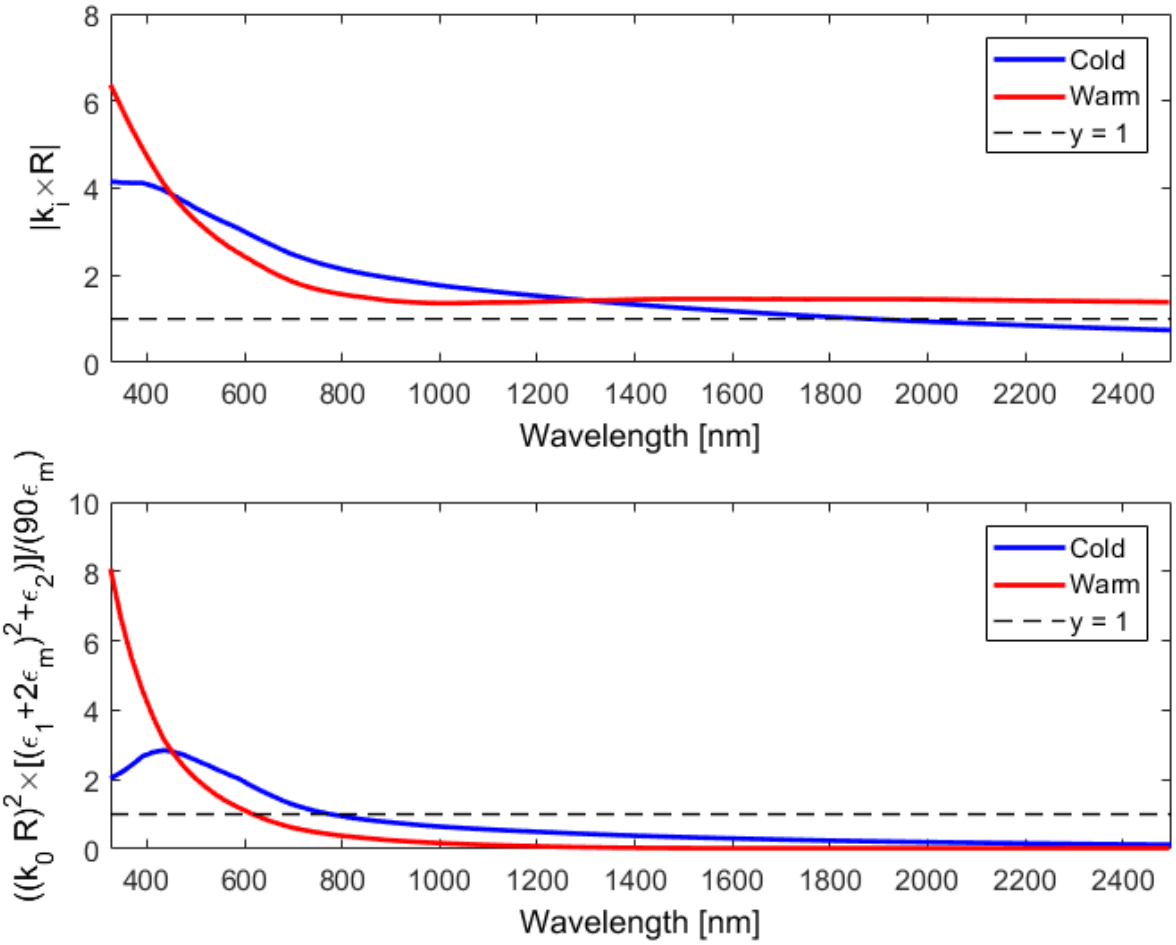

Figure 56: Left terms of the criteria given by Ruppin (Equations (2. 10) and (2. 11)), for VO_2 spherical nanoparticles, with a 100 nm radius, surrounded by a polymer matrix (n = 1.5) in cold (blue) and warm (red) conditions. For a valid Maxwell-Garnett homogenization, these values should be small compared to 1 (dashed lines).

When the represented value is small compared to 1, this corresponds to good conditions for a Maxwell-Garnett homogenization. Dashed lines representing the value of 1 are displayed on each graph to visualize in which conditions the Ruppin criteria are followed. For both criteria, it appears that the values generally decrease for increasing wavelengths. At shorter wavelengths, the values are much larger than 1, reaching up to 8 for the second criterion (bottom graph) in the warm conditions. This indicates that the homogenization may become wrong for these shorter wavelengths. For longer wavelengths, the first criterion (top graph) remains around 2, only decreasing slightly below 1 in the cold conditions. At a 2500 nm wavelength, it is equal to 0.74. The second criterion (bottom graph) shows much smaller values at longer wavelengths, reaching 1 at a 780 nm wavelength in the cold conditions and at a 630 nm wavelength in the warm conditions. Then it keeps decreasing, reaching at a 2500 nm wavelength, 0.12 in the cold conditions and 0.03 in the warm conditions.

According to these criteria, a Maxwell Garnett homogenization of our system may generate some inaccuracies, especially at shorter wavelengths, when considering VO_2 nanoparticles with a radius of 100 nm. Nevertheless, it can be noticed that considering VO_2 nanoparticles about 10 times smaller, both Ruppin criteria are perfectly verified for all wavelengths. Thus, a Maxwell-Garnett homogenization of the interstices will be valid in the case of VO_2 nanoparticles with a radius smaller

than 10 nm. Nevertheless, as fabricating such smaller VO_2 nanoparticles remains challenging, the next section will be dedicated to the evaluation of the error made on the material optical properties when using a Maxwell-Garnett homogenization in the case of VO_2 nanoparticles of radius 100 nm.

2.6.3. System description

In the following section, we will compare the optical behavior of dispersed VO_2 particles in a polymer medium of refractive index $n = 1.5$, with this of the homogenized material counterpart. The purpose is to evaluate the error introduced by the opal interstices homogenization in the case of VO_2 nanoparticles having a radius of 100 nm.

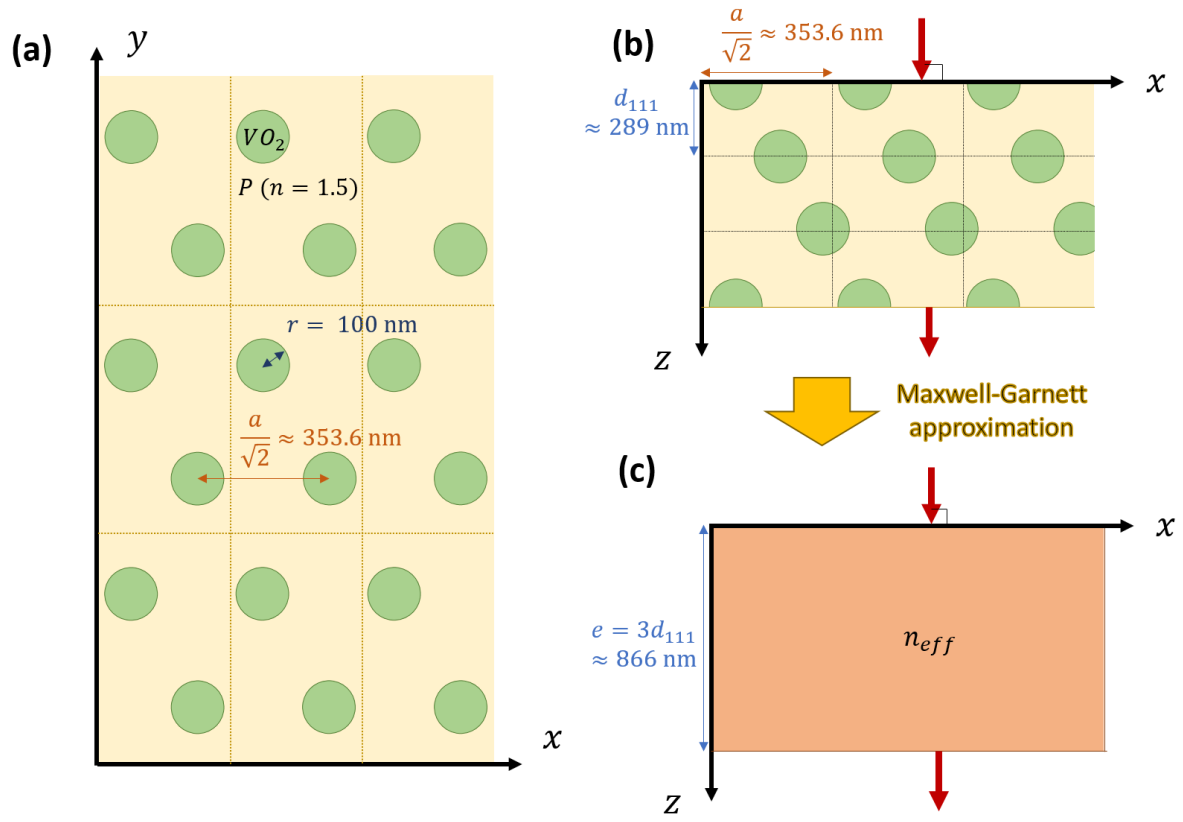

Figure 57: Top view (a) and side view (b) of 54 VO_2 nanoparticles (radius $r = 100$ nm) placed at the nodes of an fcc lattice with a cell parameter $a = 500$ nm, surrounded by a polymer matrix of refractive index $n = 1.5$, and its homogenized counterpart (c). The light is normally incident on a (111) plane. 3x3 primitive cells in the (111) plane and 1 primitive cell in the [111] direction are modelled.

The FMM program used to generate the polymer opal structure was adapted for this study in order to generate spherical VO_2 particles. A schematic representation of the system is given in **Figure 57a** and **Figure 57b**. VO_2 nanoparticles replace the polymer spheres in the opal photonic crystal, they are thus placed at each node of the fcc lattice. A cell parameter of $a = 500$ nm is chosen here. However, such representation introduces artificial structural ordering, leading to undesired effects. In order to reduce these effects, disorder is introduced by removing a certain number of particles randomly (cf **Figure 58**). Note that due to the periodic boundary conditions in x and y directions, the primitive cell is infinitely repeated in these directions: the material has thus a remaining periodicity, even when removing some particles in order to generate disorder.

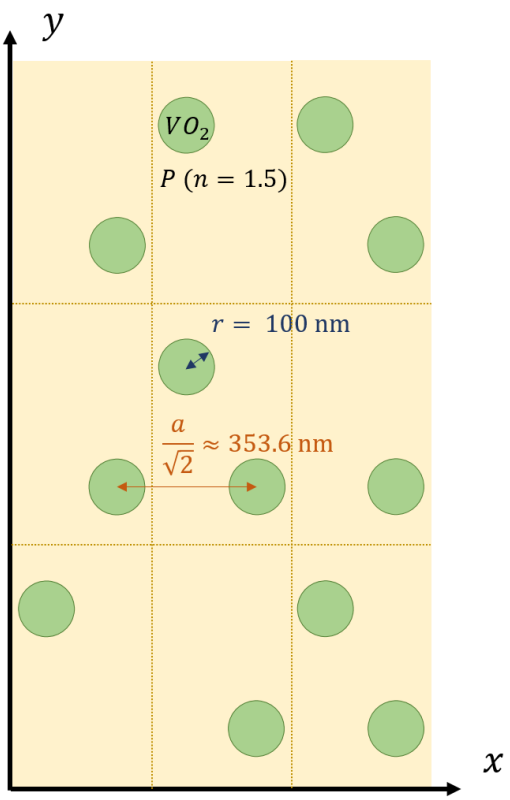

Figure 58: Top view of a certain number of VO_2 nanoparticles (radius $r = 100\ nm$) placed among the nodes of an fcc lattice with a cell parameter $a = 500\ nm$, surrounded by a polymer matrix of refractive index $n = 1.5$.

We chose to model here a grid consisting of 3x3 primitive cells in the (111) plane and one period along the direction normal to this plane. The material thickness is thus 866 nm. Since a primitive cell contains 6 particles as discussed earlier, the considered system primitive cell can thus contain a total of 54 VO_2 nanoparticles. Different numbers of VO_2 particles present in the primitive cell among the maximum 54 particles in the grid are considered, while keeping the particle size constant. Different VO_2 concentrations are thus generated. The considered cases are summed up in **Table 4** with the number of VO_2 particles in the system and the corresponding total VO_2 concentration.

Number of VO_2 nanoparticles	Total VO_2 concentration [vol%]
5	1.24
20	4.96
40	9.93
54	13.4

Table 4: Considered cases in the study: number of VO_2 particles and corresponding VO_2 concentrations.

2.6.4. Evaluation of the error introduced on the transmittance by the opal interstices homogenization in the case of VO_2 nanoparticles having a radius of 100 nm

2.6.4.1. Comparison of the transmittance spectra in the structured and homogenized cases

In this section, the differences in optical behaviors between 100 nm radius dispersed VO_2 nanoparticles in a polymer medium of refractive index 1.5 (**Figure 57ab** and **Figure 58**) and its corresponding

homogenized material (**Figure 57c**) are studied in order to estimate the error introduced on the material transmittance by the opal interstices homogenization.

Light is injected perpendicularly to the material surface, i.e. in the [111] direction. For the four different VO_2 concentrations listed above, spectral transmittances are calculated in the visible and near infrared regions. In the case of 5, 20 and 40 VO_2 nanoparticles, the particles positions are randomly drawn among the 54 possible positions in the system. Performing multiple draws for each case reduces the effect of one specific draw on the shape of the spectral transmittance. Therefore, four draws are performed for each of these three cases, and the averaged transmittance spectra are presented in **Figure 59**. Plain lines refer to the structured material, and dashed lines to the corresponding Maxwell-Garnett homogenized medium. Blue and red colors refer to the VO_2 cold and warm phases respectively.

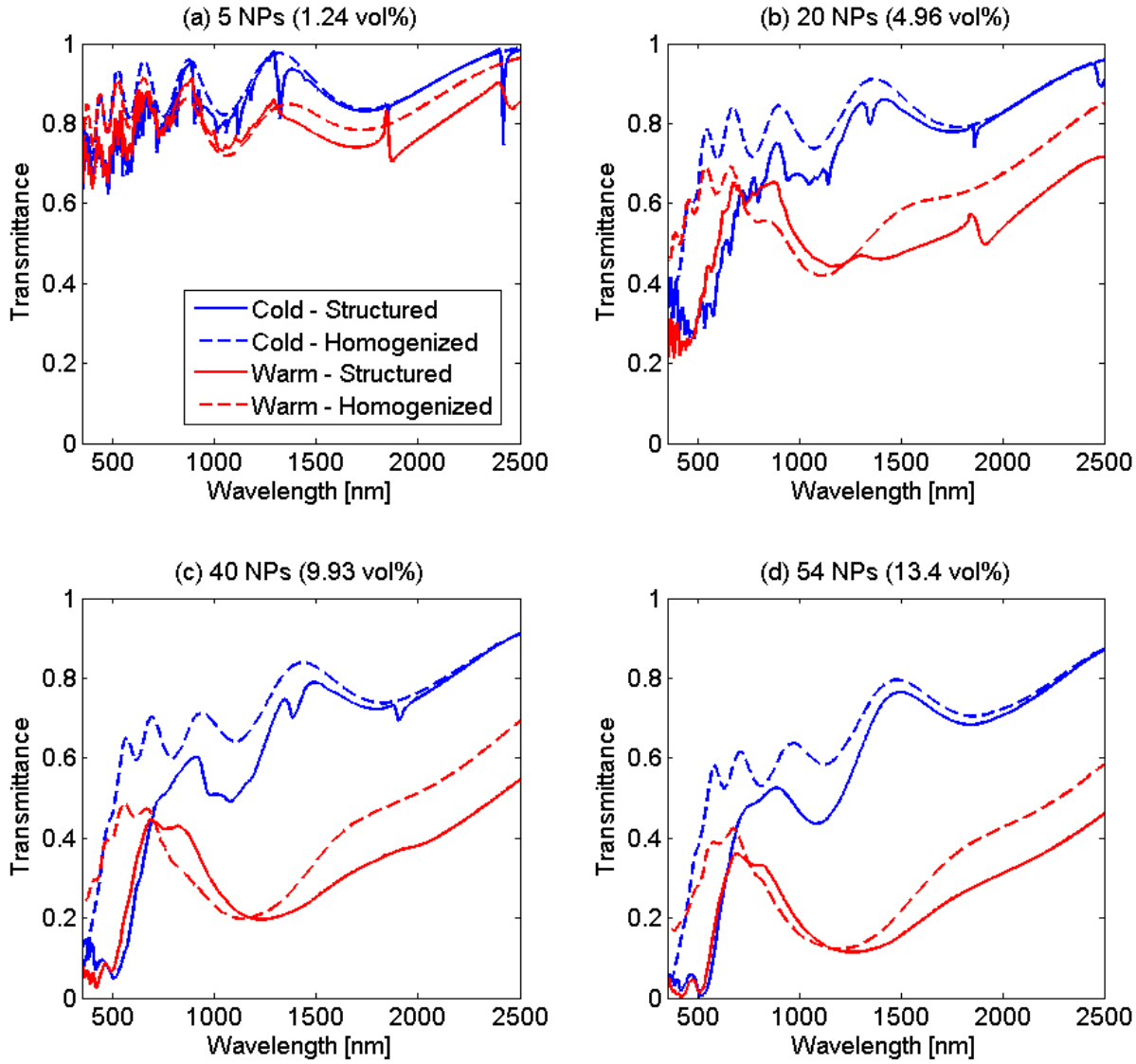

Figure 59: Calculated transmittance spectra of 5 (a), 20 (b) and 40 (c) VO_2 nanoparticles (NPs) placed at random positions at the nodes of 3x3 adjacent primitive cells of an fcc lattice surrounded by a polymer matrix having a refractive index $n=1.5$, in cold (blue) and warm (red) conditions, at normal incidence. Plain lines refer to the structured material, while dashed lines consider a homogenized material. Displayed results are averaged over four simulation results obtained by random particle positions. The unique non-random case with all nodes filled with VO_2 NPs is also represented (d).

Comparing plain and dashed lines in each case means comparing the spectral transmittance of a system having quite randomly dispersed VO_2 nanoparticles in a polymer matrix with its corresponding homogenized material calculated through the Maxwell Garnett approximation. While both curves have similar shapes, the observed differences may be due to various factors.

Due to the relatively thin thickness of the material (866 nm), the thin film interferences generate oscillations in the spectra, mostly when the layer is less absorbent, which is the case when the VO_2 concentration is lower and mostly in the case of semiconducting VO_2. The oscillations are indeed visible for the VO_2 warm phase only in the case of 5 nanoparticles, whereas they are visible for all numbers of nanoparticles in the cold case. When present, the oscillations are observed for both the homogenized and non-homogenized cases.

For wavelengths below about 750 nm, a more rapid decrease of the curves for the non-homogenized cases is observed, which is not present for homogenized cases. This decrease is less pronounced when the number of VO_2 particles decreases.

For the VO_2 cold phase, for the non-homogenized case, a valley around a wavelength of 1200 nm is observed, particularly in the case of 54 nanoparticles. This valley is less and less present when the number of VO_2 particles decreases. This is due to the periodic structure generating a bandgap effect. Indeed, according to Bragg's law (see *Equation (1. 38)*), such structure should generate a PBG around 952 nm. The valley position is slightly shifted compared to this value, probably due to the influence of the thin film interferences. This effect becomes weaker as the number of VO_2 particles is reduced. It is still slightly visible with 40 VO_2 nanoparticles (**Figure 59c**) and then much less with 20 VO_2 nanoparticles (**Figure 59b**). This is because structural disorder is introduced with decreasing number of VO_2 nanoparticles, which reduces the PBG effect occurring in periodic structures. This effect in an artifact in the present model, as we want to evaluate here the error induced by the interstices homogenization, but in the case of randomly placed VO_2 nanoparticles in the interstices. This effect is nevertheless limited as the modelled material has only one period in the [111] direction (see **Figure 57b**).

The valley is not observed for the VO_2 warm phase, which is certainly due to the higher absorption of the nanoparticles (higher imaginary part of the dielectric function, see **Figure 8**), which inhibits the PGB effect (see **Section 4.2.2**).

Looking for generally on the curve shapes, it can be observed that in the cold cases a higher discrepancy is observed between the structured and homogenized cases for small wavelengths, but the difference decreases with increasing wavelengths. In the warm cases, a higher discrepancy is also observed for small wavelengths, but after decreasing around 1200 nm, the discrepancy grows again for higher wavelengths. These observations are in good agreement with the Ruppin criteria (cf **Figure 56**), with a global improvement of the criteria in the cold case for increasing wavelengths, whereas in the warm case (particularly for the 1^{rst} criterion), a first decrease is observed for small wavelength, but the values then stagnate above 1.

2.6.4.2. Estimation of the error

In order to quantify the differences introduced by the interstices homogenization on the transmittance spectra, we introduce a relative error parameter defined as:

$$Error(\lambda) = \left| \frac{T_{struct}(\lambda) - T_{homo}(\lambda)}{T_{struct}(\lambda)} \right| \times 100 \qquad (2.\ 16)$$

with $T_{struct}(\lambda)$ and $T_{homo}(\lambda)$ the spectral transmittances respectively for the non-homogenized and homogenized cases at a wavelength λ. This parameter is calculated at each wavelength from 350 nm to 2500 nm with a 2 nm step. The total number of wavelength values is thus 1076. This relative error parameter is calculated in each considered case and results are shown in **Figure 60**.

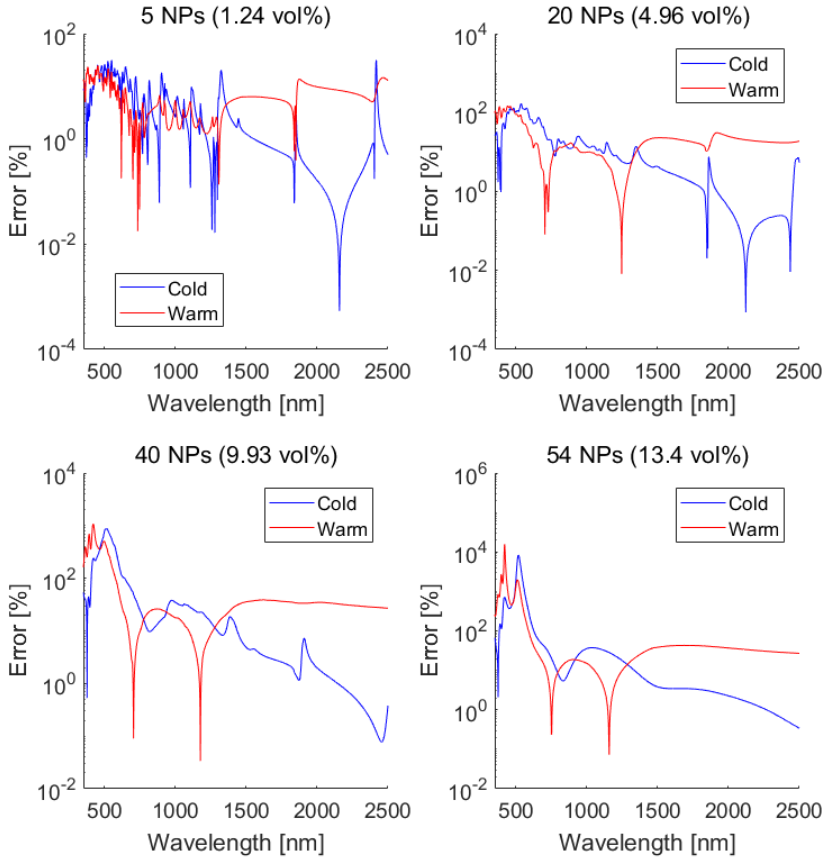

Figure 60: Calculated relative error between the spectral transmittances for the non-homogenized and homogenized cases in the cold and warm conditions as a function of the wavelength, for different VO_2 concentrations.

A few observations can be made from this figure. In all considered cases, the calculated error is relatively high, especially at shorter wavelengths (below 750 nm). A significant drop of the error occurs around this 750 nm wavelength in all four cases, in both cold and warm conditions. For example, below a 750 nm wavelength, the error is lower than 30% for 5 nanoparticles, and 150% for 20 nanoparticles. These values drop to much lower values at longer wavelengths: in the case of 5 nanoparticles, the error drops below 15%, while with 20 nanoparticles, it drops below 25%. In all cases, the error at these longer wavelengths remains below 35% in cold conditions, and 43% in warm conditions. It is worth noticing that while at shorter wavelengths, the behavior in cold and warm conditions is relatively similar, a difference is observed between the two states at longer wavelengths, as the error obtained in warm conditions is generally higher than in the cold conditions at these longer wavelengths. Finally, an increase of the error is also observed with increasing VO_2 concentrations.

To better visualize how much error is introduced by the interstices homogenization, a percentage of the total number of wavelengths corresponding to a given value of the relative error is calculated and

histograms representing them are given in **Figure 61**. The relative error values are split into bins having a width of 5%. The values for the relative error cover from 0% to 50%, higher values are counted in the last bin (most right), which is responsible for the higher peak observed in the cases of higher numbers of VO_2 nanoparticles.

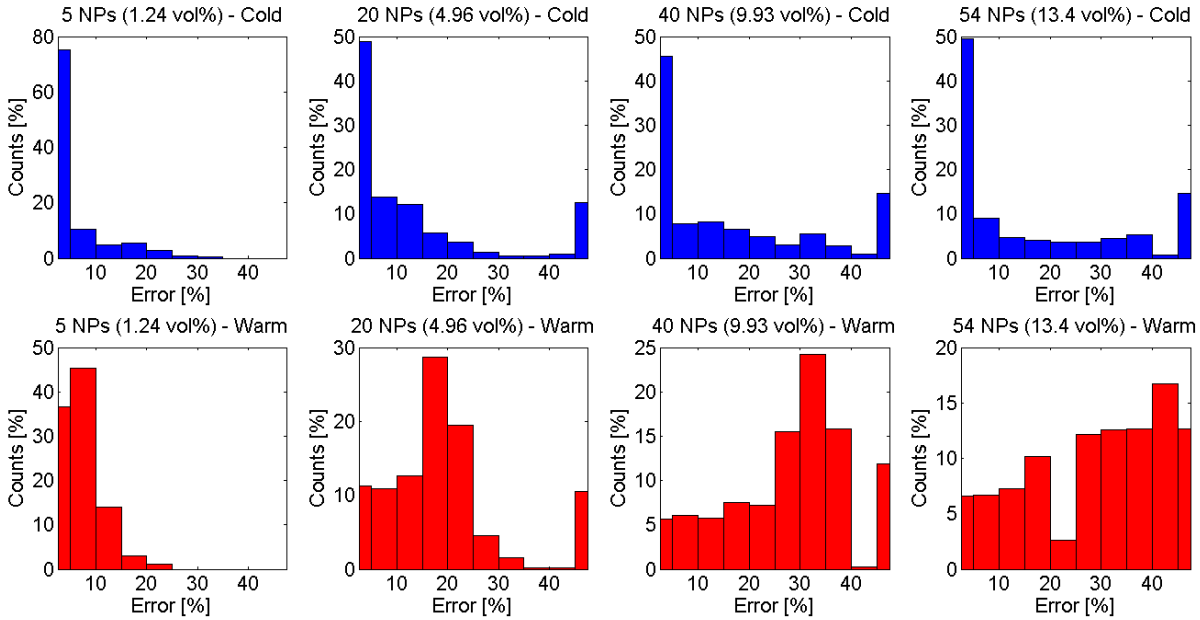

Figure 61: Histograms of the relative error between the spectral transmittances for the non-homogenized and homogenized cases in the cold (top) and warm (bottom) conditions, for different VO_2 concentrations. The counts are a percentage of the total number of wavelengths.

For a low number of VO_2 nanoparticles (5 nanoparticles) in the system, 85.4% of the transmittance spectrum has a relative error lower than 10% in the cold conditions. In the warm condition, only 81.8% of the spectrum has a relative error lower than 10%. The relative error increases with increasing number of VO_2 nanoparticles. With 20 nanoparticles, 62.7% of the transmittance spectrum has a relative error lower than 10% in the cold conditions, while in the corresponding warm case, 22.1% of the transmittance spectrum has an error lower than 10%. In general, higher errors are obtained in warm conditions.

2.6.5. Possible origin of the high discrepancy observed between structured and homogenized cases at smaller wavelengths

The more rapid decrease of the non-homogenized transmittances than the homogenized ones at wavelengths below 750 nm might be due to the nanoparticle scattering happening only without the material homogenization when the particles are well defined. With a 100 nm radius for the scattering particles, Rayleigh scattering can be used to explain this phenomenon. According to the Rayleigh scattering, the scattering efficiency Q_{sca} is related to the light wavelength λ by [57]:

$$Q_{sca} = \frac{8}{3}\left|\frac{m^2-1}{m^2+2}\right|^2 x^4 \qquad (2.\ 17)$$

with m the refractive index ratio between the scattering particle and its environment, and

$$x = \frac{2\pi\, n\, r}{\lambda} \qquad (2.\ 18)$$

with n the refractive index of the surrounding medium and r the particle radius. *Equation (2. 9)* shows that for small scattering particles, the scattering efficiency is proportional to λ^{-4}. This means that the scattering efficiency significantly increases for smaller wavelengths and such behavior is confirmed in **Figure 62**, which represents the scattering efficiency of a single VO_2 particle in cold and warm conditions, surrounded by a polymer of refractive index $n = 1.5$. This behavior is in agreement with the observed increased relative error between structured and homogenized cases (see **Figure 60**) at smaller wavelengths, since the scattering which occurs only in the heterogeneous material reduces the spectral transmittance, mostly at lower wavelengths.

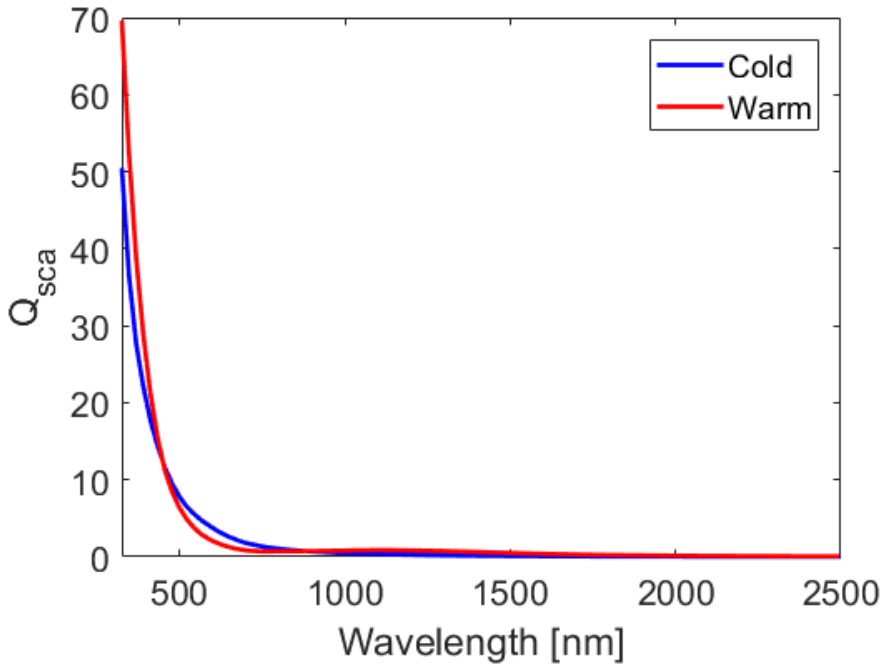

Figure 62: Calculated scattering efficiency Q_{sca} vs light wavelength, for a single VO_2 nanoparticle of radius $r = 100\ nm$ surrounded by a polymer of refractive index $n = 1.5$, in cold and warm conditions.

This calculation was done considering the Rayleigh scattering, usually valid for $x < 1$. However, at the lowest considered wavelength (350 nm), this parameter is equal to 2.7. Because of this, the calculated Q_{sca} may be overestimated at these shorter wavelengths. In this configuration, even if Q_{sca} does not exactly follow *Equation* (2. *17*) when λ is small (< 942 nm), Q_{sca} increases with increasing x, thus with decreasing wavelengths. The discussion here remains the same.

To conclude this study, the homogenization of the opal interstices using a Maxwell-Garnett approximation in the case of 100 nm radius VO_2 nanoparticles leads to high errors for wavelengths below 750 nm, which seems to be due to the loss of the scattering effect due to the VO_2 nanoparticles. Also, whereas for the cold VO_2 phase the relative error induced on the transmittance spectra by the interstices is below 35% for wavelengths higher than 750 nm, it can reach a value of 43% in the warm phase for a VO_2 concentration of 13.4 vol%. Warm metallic VO_2 has indeed a higher dielectric function imaginary part, which increases for wavelengths higher than 750 nm (see **Figure 8**). This leads to a worse respect of the Maxwell-Garnett homogenization validity criteria derived by Ruppin. It can also be noticed, that the higher the VO_2 concentration, the higher the error. Quite acceptable errors are

obtained at a VO_2 concentration of 1.24 vol% for all wavelengths and cold and warm phases, with more than 81.8% of the spectrum having a relative error below 10%.

2.7. Conclusion of this chapter

The purpose of this thesis is to model an opal photonic crystal containing VO_2 nanoparticles in the interstices. An FMM based program has been developed. This chapter presents the description of this program, as well as validations of the program on materials with increasing complexity: single interface, monolayer film, 1D photonic crystal and polymer opal. In the model used in this thesis, the opal interstices containing VO_2 nanoparticles are described by an effective refractive index computed through the Maxwell-Garnett formula. The validity of this approximation has been studied and it was shown that the scattering effect from the VO_2 nanoparticles is lost for particles with a radius of 100 nm. However, this approximation remains acceptable for a low VO_2 concentration of about 1.2 vol%. It is also acceptable for smaller nanoparticles: the Maxwell-Garnett homogenization validity criteria derived by Ruppin [139] are respected for nanoparticles with a radius smaller than 10 nm.

The material considered in the following chapters will thus be an opal photonic crystal made of polymer spheres surrounded by a material described by an effective refractive index derived from the Maxwell-Garnett approximation applied to a certain concentration of VO_2 nanoparticles in a polymer matrix. The optical properties of such material will be studied in the following chapters, with different focuses depending on the application considered for the material. Applications such as transparent smart glazing or tarpaulins for greenhouses will be considered in the next chapter, whereas the fourth one will be dedicated to opaque materials, dedicated for example to building roofs or walls or satellites coatings.

Chapter 3 Optical properties of the nanostructured thermochromic coating in the visible and near infrared spectral regions

The optical properties of a polymer opal photonic crystal containing VO_2 nanoparticles are studied. The system is illustrated in **Figure 63**. The opal spheres, denoted as P_s and of radius R, are surrounded by a mixture of VO_2 and a polymer P_i modelled by an effective refractive index derived from the Maxwell-Garnett approximation. The cell parameter is called a. The structure compacity is defined by:

$$C = \frac{4 \times \frac{4}{3}\pi R^3}{a^3} \tag{3. 1}$$

When the opal spheres are touching each other, the opal structure is compact and its compacity is equal to $C = 0.74$, which is its maximum value.

Light is injected with an incidence angle θ with respect to the perpendicular to the material surface. The material surface is a (111) crystallographic plane of the opal structure. The material is surrounded by air on both sides and its thickness is e. Due to the periodic conditions imposed by the Fourier Modal Method (FMM), the material is considered as infinite in both x and y directions.

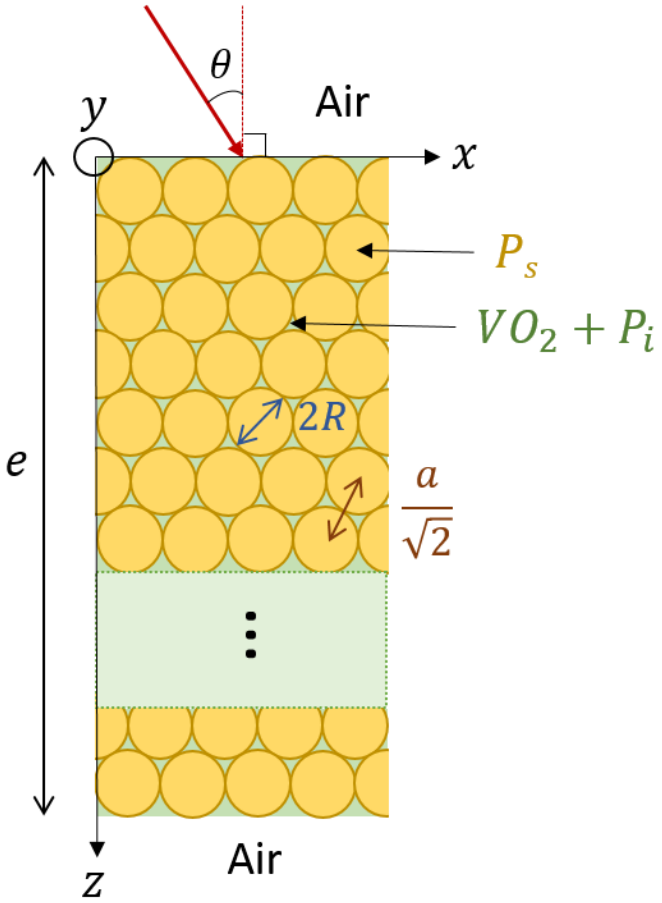

Figure 63: Schematic representation of the modelled system. Light is injected with an incidence angle θ with respect to the perpendicular to the surface of an opal photonic crystal consisting of P_s spheres of radius R, surrounded by a mixture of VO_2 nanoparticles and a polymer P_i modelled by an effective refractive index. The cell parameter is a and the material thickness is e.

The VO_2 refractive indexes used in this chapter in cold and warm conditions are presented in **Figure 64**. These refractive indexes correspond to the dielectric functions of Mlyuka et al presented in **Figure 8**, obtained by fitting reflectance and transmittance spectra measured on a 50 nm thick VO_2 film, using Fresnel equations.

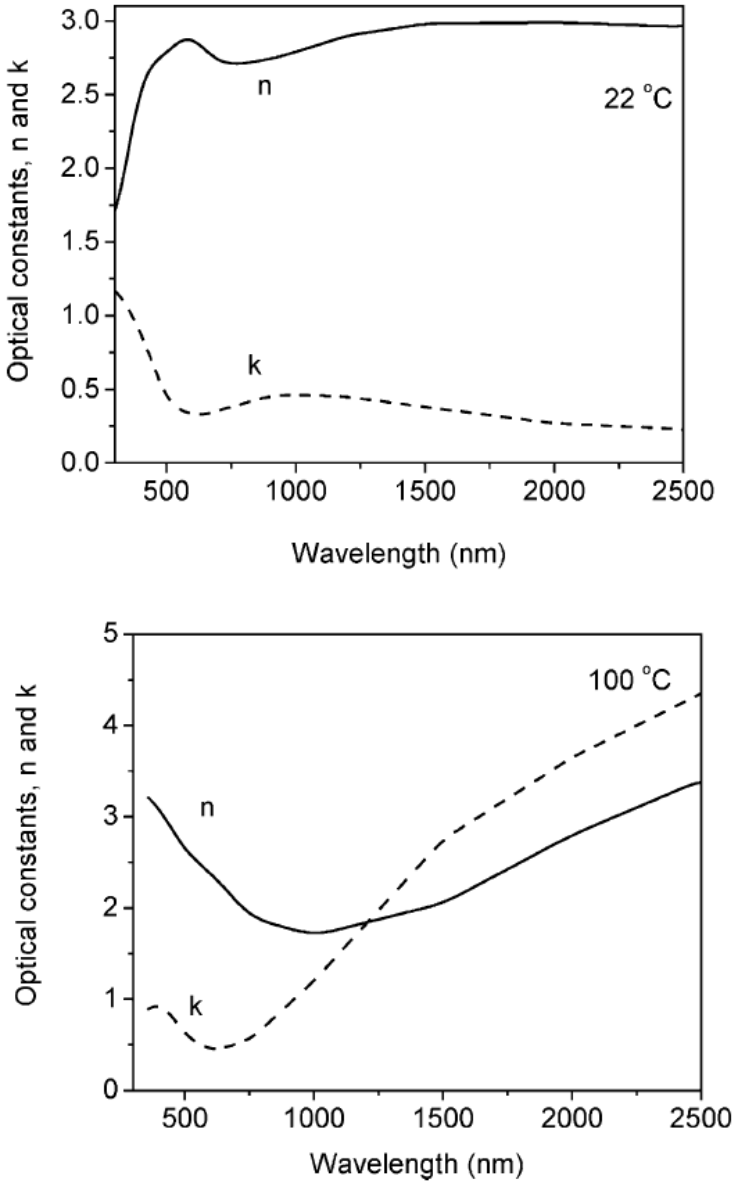

Figure 64: Real (n) and imaginary (k) parts of the VO_2 refractive indexes in the visible and near infrared spectral region in cold (top) and warm (bottom) states. Extracted from [7].

In this chapter the material optical behavior will be studied in the visible and near infrared spectral regions, which are of interest for applications such as energy efficient glazing coatings. For these applications two main quantities can be used to quantify the coating performances, the luminous transmittance T_{lum} and solar transmittance T_{sol}, defined as:

$$T_{lum} = \frac{\int_{380nm}^{780nm} V(\lambda)\, T(\lambda)\, d\lambda}{\int_{380nm}^{780nm} V(\lambda)\, d\lambda} \quad \text{and} \quad T_{sol} = \frac{\int_{350nm}^{2500nm} E_{\lambda}^{AM1.5}(\lambda)\, T(\lambda)\, d\lambda}{\int_{350nm}^{2500nm} E_{\lambda}^{AM1.5}(\lambda)\, d\lambda}, \qquad (3.\ 2)$$

with $T(\lambda)$ the material spectral transmittance, $V(\lambda)$ the CIE photopic luminosity function [14] and $E_{\lambda}^{AM1.5}(\lambda)$ the global AM1.5 spectral solar irradiance extracted from [13] (cf *Equations* (1. *18*) and (1.

20)). T_{lum} directly depends on the material transmittance in the visible spectral range, whereas T_{sol} depends on the material transmittance in the solar spectral range. As explained in **Section 1.1.3**, the solar transmittance is calculated from 350 nm to 2500 nm.

As the material undergoes a phase transition at a certain transition temperature τ_c due to the thermochromic nature of vanadium dioxide, T_{lum} and T_{sol} can be defined in both cold and warm cases as $T_{lum,cold}, T_{lum,warm}, T_{sol,cold}$ and $T_{sol,warm}$. The transmittance modulation at this transition temperature leads to a modulation of both luminance and solar transmittance values defined as the difference between the values at low temperatures and at high temperatures:

$$\Delta T_{lum} = T_{lum,cold} - T_{lum,warm} \quad \text{and} \quad \Delta T_{sol} = T_{sol,cold} - T_{sol,warm} \qquad (3.\ 3)$$

Applications as a glazing coating material require this coating to be transparent for the visible light, while having a significant impact on thermal solar energy [2]. It means that the material should have both high luminous transmittance T_{lum} (in both cold and warm states) and high solar transmittance modulation ΔT_{sol} .

In this chapter the influence of various structural parameters on the material performances in terms of luminous and solar transmittances are studied through numerical simulations. Based on the spectral ranges defined by the luminous and solar transmittances, we will focus on the visible and near infrared spectral regions.

3.1. Preliminary study: determining material thickness and VO_2 concentration

This preliminary study aims at determining material global parameter values, such as material thickness e and total VO_2 concentration f_t, which are compatible with acceptable values for T_{lum} and ΔT_{sol} for glazing coating applications. These parameters are indeed the main factors influencing the spectral transmittances of the material.

As a first approximation, the system considered here is a dispersion of VO_2 spherical nanoparticles in a polymer matrix of refractive index $n = 1.5$, chosen as an average value of refractive indexes for polymers. A schematic representation of such system is shown in **Figure 65**. This system can be described by an effective refractive index derived from the Maxwell-Garnett approximation, which estimates an effective optical behavior based on all implied refractive indexes and the inclusions volume ratio in the system. The effective refractive index is calculated for various VO_2 concentrations. A homogenized material is considered here instead of a structured one, as it is a more efficient method to explore a wide range of parameters without needing very high computation time.

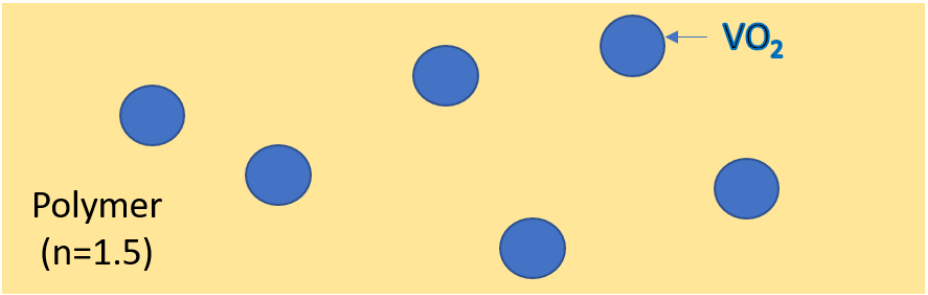

Figure 65: Dispersion of VO_2 nanoparticles in a polymer (n=1.5) matrix

With a normally incident light on this material surface, spectral transmittances in the visible and near infrared regions are calculated with our model. Then the luminous and solar transmittances are derived from *Equation* (3. *2*) and presented in **Figure 66**. In order to evaluate the material luminous transparency, keeping in mind that the metallic VO_2 is more absorbent than the semiconducting VO_2, studying the material luminous transparency in warm conditions seems more pertinent as it is the limiting factor. Based on this assumption, **Figure 66a** shows a 3D representation of the system luminous transmittance in warm conditions as a function of both material thickness (up to 25 µm) and VO_2 concentration (from 0 to 100 vol%). This map shows regions where the material is more or less transparent in the visible spectral range. As expected, it shows that with low concentrations of absorbing VO_2 nanoparticles or in the case of thinner layers, the material becomes more transparent. For a given VO_2 concentration, this map gives the acceptable values for the material thickness, to have acceptable values for $T_{lum,warm}$. **Section 1.2.3.1** gathers real materials having $T_{lum,cold}$ of about 40%, and since $T_{lum,warm} < T_{lum,cold}$, we decide that $T_{lum,warm}$ should be higher than 30%. For VO_2 concentrations higher than 10%, only thin materials (thickness below about 3 µm) have an acceptable luminous transmittance in the warm state of VO_2.

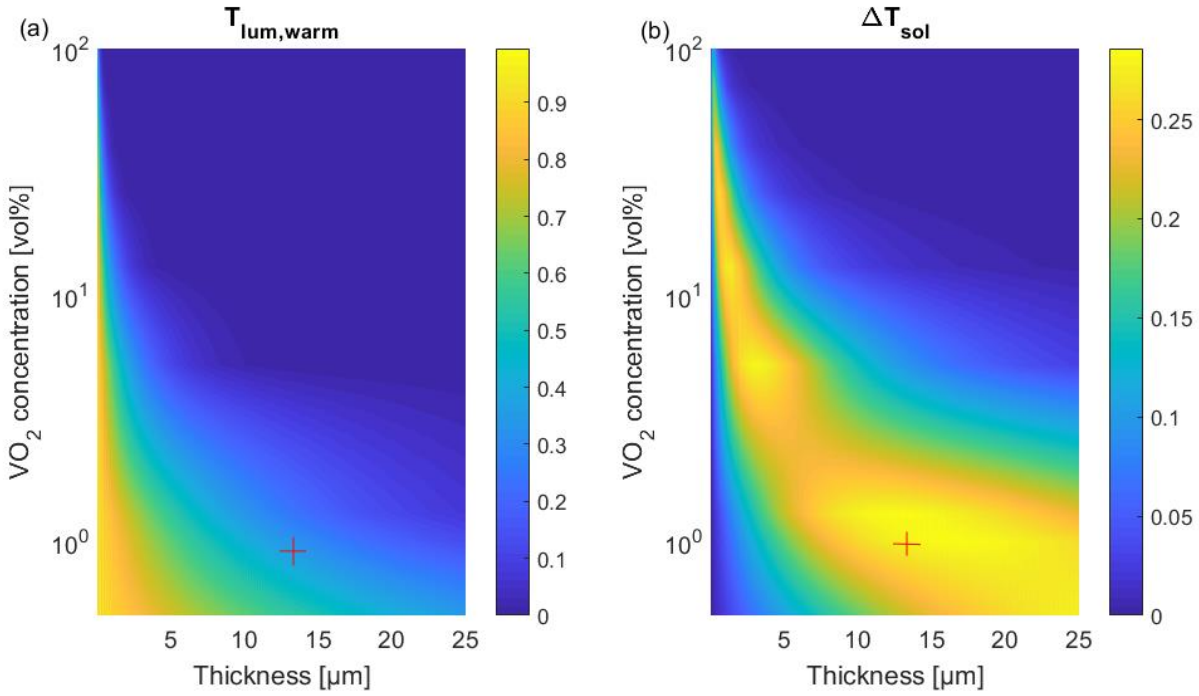

Figure 66: Luminous transmittance $T_{lum,warm}$ in warm state (a) and solar transmittance modulation ΔT_{sol} (b) for a homogenized material as a function of material thickness e and VO_2 concentration f_t with a normally incident light on the material surface. The red crosses represent the parameters selected for the future simulations.

For glazing applications, a high solar transmittance modulation is also desired. This value is obtained using *Equation* (3. *3*) from the material solar transmittances in cold and warm conditions. This solar transmittance modulation is mapped in **Figure 66b**, as a function of both material thickness and VO_2 concentration with the same ranges as **Figure 66a**. With not enough VO_2 in the system, cold and warm conditions have limited impact on the material transmittance. Thus, the solar transmittance modulation is lower when the quantity of VO_2 is low, that is for low VO_2 concentration or low material thickness. This explains the blueish region at the bottom left corner. On the other hand, with too much VO_2 in the system, the material becomes very absorbent and spectral transmittance is reduced. When in both cold and warm conditions, the transmittance is very low, then the solar transmittance modulation is also very low. A higher solar transmittance modulation is observed in between, when

the right amount of VO_2 is introduced in the system, enough to have a significant impact on the material optical properties while keeping it transparent enough.

In this chapter, we will focus on that region where the solar transmittance modulation is higher and with the highest possible luminous transmittance. This large region around $f_t = 1\ \mathrm{vol\%}$ going from $e = 8\ \mu m$ to $e = 25\ \mu m$ seems interesting. However, the luminous transmittance decreases significantly with increasing thickness while no increase is observed on the solar transmittance modulation. We will thus choose a spot close to the lower end of this layer thickness range. We choose a 13 µm thick material loaded with 1 vol% VO_2 nanoparticles. With a cell parameter $a = 500\ \mathrm{nm}$ in order to place the PBG peak around the visible and near infrared regions, such thickness represents 15 periods along the [111] direction (see *Equation* (2. *2*)). These parameters will be used in the following simulations of this chapter unless specified otherwise. This spot is located with the red cross on **Figure 66b**. The homogenized material with such parameters has a solar transmittance modulation of about 27% and a luminous transmittance in warm state of about 33% in warm state and 49% in cold state, comparable to VO_2-based coatings for glazing applications (see **Section 1.2.3.1**).

3.2. Optimization of the polymer refractive indexes in the case of a homogenized material

3.2.1. System description

In the previous section, a one-step homogenization process applied to dispersed VO_2 nanoparticles in a polymer matrix was employed to estimate the optimal material thickness and VO_2 concentration. In this section, we are now interested in new parameters, related to the polymers refractive indexes. This requires to introduce two polymers, one for the opal spheres P_s and one for the opal interstices P_i. The one-step homogenized system does not allow the study of these two polymers as it considers only a single polymer. We will thus use a two-step Maxwell-Garnett homogenization process here. This process is illustrated in **Figure 67**. First, homogenizing the opal interstices containing f_i vol% VO_2 spherical nanoparticles and P_i, and then homogenizing once again considering the polymer P_S spheres surrounded by the mixture of (VO_2 + P_i) described by the previously calculated refractive index. This representation allows a quick estimate of the evolution of the material optical properties as a function of both polymers refractive indexes.

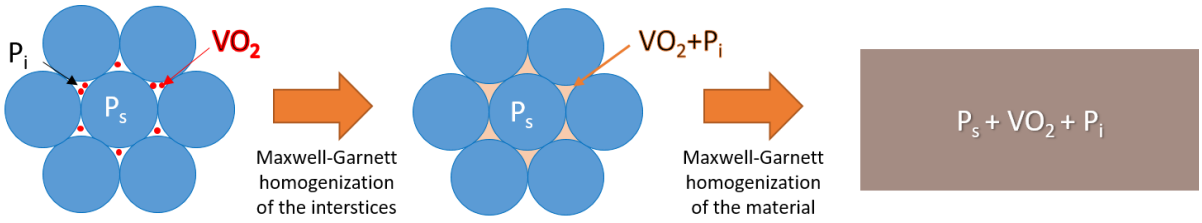

Figure 67: Equivalent material containing two polymers (Ps and Pi) and VO_2 nanoparticles, modelled by two successive Maxwell-Garnett homogenization processes.

In this section, we choose to consider a compact opal photonic crystal, meaning that all opal spheres are in contact. Keeping in mind that a closed-packed fcc structure has a compacity of 74%, this means

that the total volume of these spheres is 74% of the volume of the whole material. This property limits the maximum VO_2 concentration to 26%, as the VO_2 is only contained in the opal interstices.

3.2.2. Influence of the polymers refractive index

In this section, the influence of both P_s and P_i polymers refractive indexes on the material optical behavior is studied. Spectral transmittances are calculated for different polymers refractive indexes and presented in **Figure 68** with a normally incident light on the material surface and for both VO_2 phases. The study range is defined by the refractive indexes of common polymers, typically ranging from 1.3 to 1.7. From there, multiple combinations are possible for the refractive indexes of P_s and P_i, denoted $n(P_s)$ and $n(P_i)$ respectively. Among them, the ones considered in this study are listed in the two left columns of **Table 5**. Only the two extreme values of $n(P_i)$ are considered: $n(P_i) = 1.3$ (plain lines) and $n(P_i) = 1.7$ (dashed lines). For these two values, all values for $n(P_s)$ are considered inside the defined range, with a step of 0.1, represented in **Figure 68a** with colors from dark blue to cyan and **Figure 68b** from red to yellow with increasing indexes.

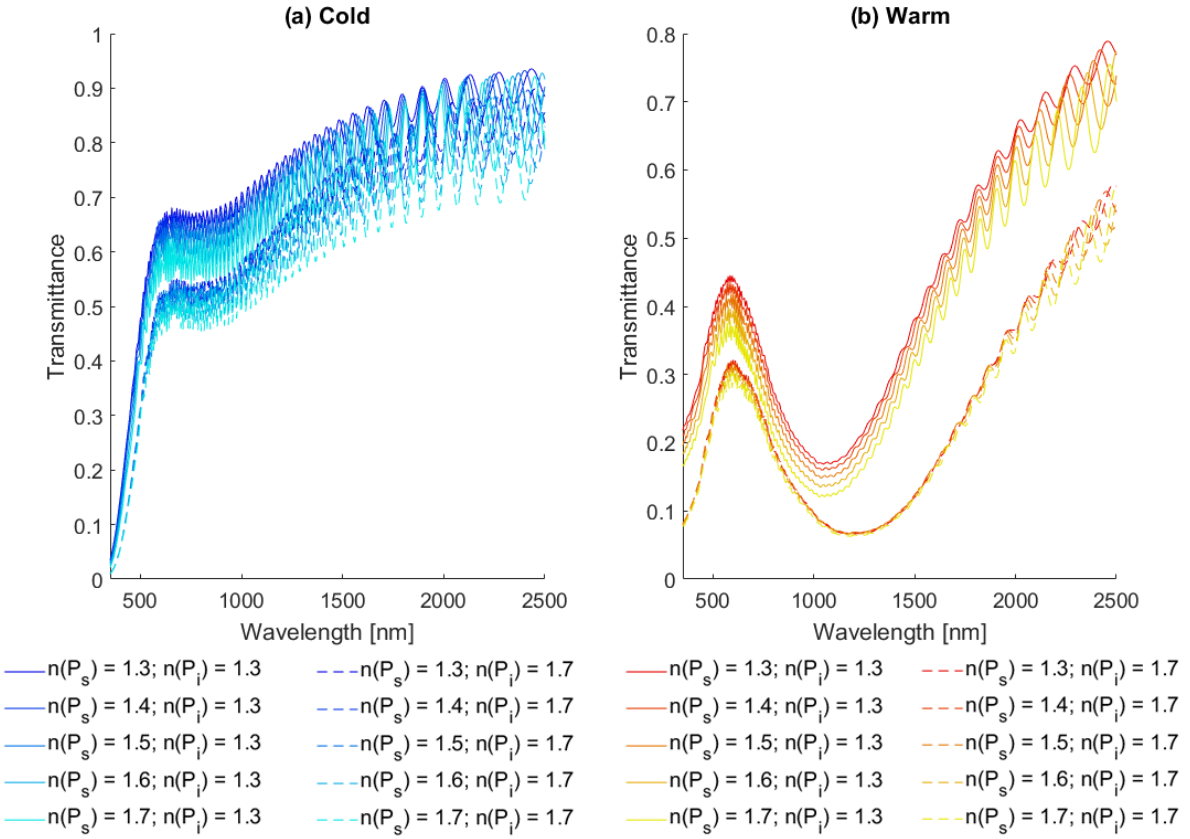

Figure 68: Transmittance spectra for normally incident light of a homogenized material composed of 1 vol% VO_2 nanoparticles dispersed in the interstices of a polymer opal with different polymer refractive indexes $n(P_s)$ for the spheres and $n(P_i)$ for the interstices in cold (a) and warm (b) conditions.

Comparing our results to other simulation results reported in the literature, similar shapes for the transmittance spectra of spherical VO_2 nanoparticles dispersed in a dielectric material were obtained by Li et al. [36] (see **Figure 69**). These transmittance spectra were calculated for various VO_2 nanoparticles shapes (defined by their aspect ratio m) dispersed in a matrix of refractive index $n = 1.5$, on a substrate having the same refractive index, using effective medium theories and Fresnel equations. We are here interested in the VO_2 nanospheres ($m = 1$). Compared to our system, there

are a few differences. First, our system is modelled by a two-step homogenization process (see **Figure 67**) which allows us to have two different refractive indexes for our two polymers (opal spheres and polymer in the opal interstices), while Li et al. modelled a suspension of VO_2 nanoparticles in a single dielectric material by an effective refractive index. The same Maxwell-Garnett equation was used in both models. Second, different refractive indexes were used for the dielectric materials. Finally, **Figure 69** considered a substrate with a refractive index $n = 1.5$ while our model considers a layer with no substrate (air on both sides). The presence of this substrate has a few noticeable effects on the transmittance spectra. Reducing the refractive index difference at the bottom interface between the film and the substrate globally increases the amount of transmitted light while also reducing the amplitude of the oscillations related to thin film interferences, clearly visible in **Figure 68** but not in **Figure 69**.

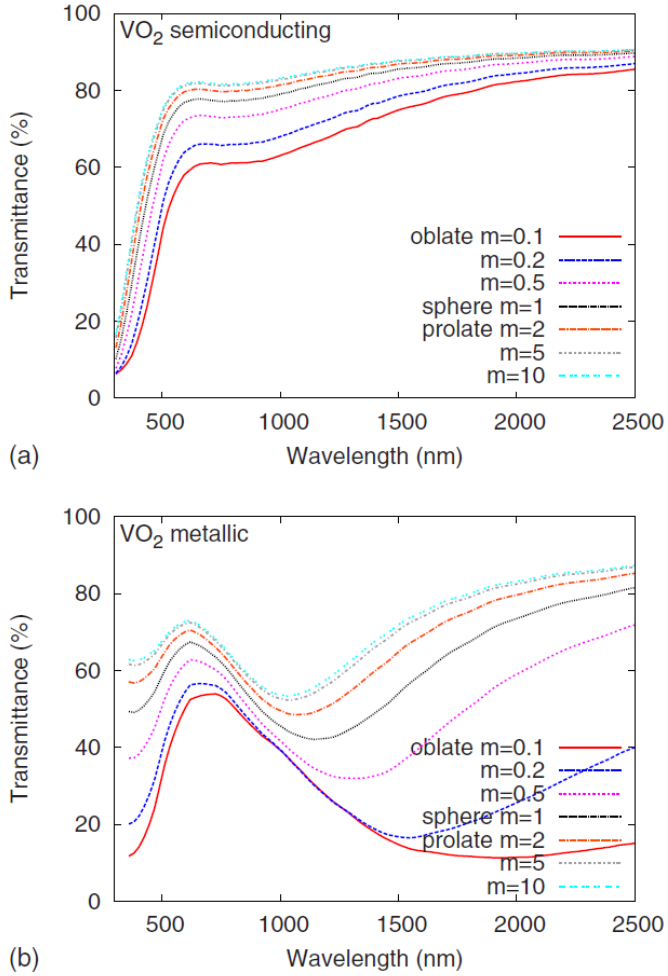

Figure 69: Calculated transmittance spectra of spheroidal VO_2 nanoparticles in cold (a) and warm (b) conditions dispersed in a dielectric material having a refractive index 1.5, on a substrate having the same refractive index. The parameter m is related to the VO_2 nanoparticle aspect ratio. The VO_2 volume filling factor is 0.01. Extracted from [36].

In the case of VO_2 metallic nanoparticles (**Figure 68b**), it is worth noting that for wavelengths from about 700 nm to 1500 nm, the spectral transmittance describes a valley due to the plasmon effect appearing for metallic nanoparticles [140]. Absorbing the incident light, the metal surface electrons vibrates and enter in resonance at a characteristic wavelength. This effect creates an absorption peak, thus leading to a reduced transmittance around this wavelength. It can also be observed on the material refractive index imaginary part (also called extinction coefficient): a peak in the extinction coefficient indicates an absorption peak. To illustrate this property, the extinction coefficient of the

modelled material placed in our opal interstices (homogenized mixture of dispersed VO_2 nanoparticles in a polymer matrix with refractive index $n(P_i)$) in warm conditions is shown in **Figure 70** for various values of $n(P_i)$. The VO_2 concentration used here is the VO_2 concentration in the opal interstices defined as:

$$f_i = \frac{f_t}{1 - C} \tag{3. 4}$$

with the parameters set in this study: a total VO_2 concentration $f_t = 1$ vol% and a structure compacity $C = 0.74$,this leads to $f_i = 3.8$ vol%.

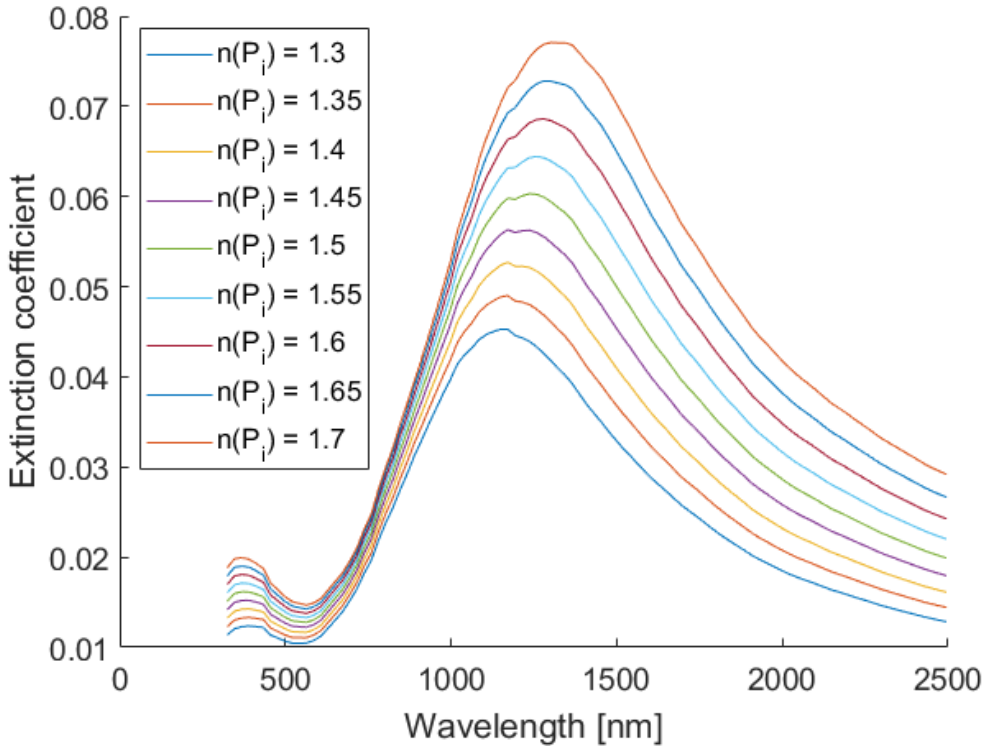

Figure 70: Effective extinction coefficient of 3.8 vol% dispersed metallic VO_2 particles in polymers with different refractive indexes $n(P_i)$.

The position of the extinction coefficient peak corresponds to an absorption peak in the material and confirms the valley observed in the transmittance spectra (**Figure 68b**). **Figure 70** also shows an increase of the extinction coefficient with increasing polymer refractive index, meaning that a higher polymer refractive index leads to slightly more absorbing materials. This is a global observation in the transmittance spectra for both cold and warm VO_2 phases (**Figure 68a and Figure 68b**): higher polymers refractive indexes result in lower spectral transmittances. And from *Equation* (3. *2*),lower spectral transmittances lead to both lower luminous and solar transmittances in cold and warm conditions.

These integrated transmittance values and their modulations are calculated using *Equation* (3. *2*) and summed up in **Table 5**.

$n(P_s)$	$n(P_i)$	Cold		Warm		ΔT_{lum}	ΔT_{sol}
		T_{lum}	T_{sol}	T_{lum}	T_{sol}		
1,3	1,3	0,59	0,61	0,42	0,33	0,17	0,28
1,4	1,3	0,58	0,60	0,41	0,32	0,17	0,28
1,5	1,3	0,56	0,58	0,40	0,31	0,17	0,27
1,6	1,3	0,54	0,56	0,37	0,29	0,16	0,27
1,7	1,3	0,51	0,54	0,35	0,27	0,16	0,27
1,3	1,7	0,44	0,49	0,29	0,20	0,15	0,28
1,4	1,7	0,44	0,48	0,29	0,20	0,15	0,28
1,5	1,7	0,43	0,48	0,29	0,20	0,15	0,27
1,6	1,7	0,42	0,47	0,28	0,20	0,14	0,27
1,7	1,7	0,41	0,45	0,27	0,19	0,14	0,26

Table 5: Luminous and solar transmittance for normally incident light of a homogenized compact opal photonic crystal containing 1vol% spherical VO_2 nanoparticles, and their modulations at the VO_2 phase transition, as a function of the polymer spheres ($n(P_s)$) and interstices ($n(P_i)$) refractive indexes.

For each considered combination of the polymer refractive indexes $n(P_s)$ and $n(P_i)$ listed on the left, the luminous and solar transmittances are given in cold and warm conditions. From there, the luminous and solar transmittance modulations are then calculated using *Equation* (3. *3*) and given in the two right columns. The cases are split in two, based on the two considered values of $n(P_i)$. For applications like energy-efficient coatings for windows, high T_{lum} and ΔT_{sol} are desired (see **Section 1.2.3.1**). So, we will choose here the polymers refractive indexes in order to maximize these values. Looking at ΔT_{sol} in **Table 5** in the two case groups, it seems that higher values are obtained for low values of $n(P_s)$. For this reason, we set $n(P_s) = 1.3$, for which ΔT_{sol} is maximized and equal to 0.28. The same is done for the value of $n(P_i)$. Since ΔT_{sol} varies very slightly between $n(P_i) = 1.3$ and $n(P_i) = 1.7$, we use the other criterion (high T_{lum} in both cold and warm conditions). Since $T_{lum,cold} = 0.59$ and $T_{lum,warm} = 0.42$ when $n(P_i) = 1.3$ while $T_{lum,cold} = 0.44$ and $T_{lum,warm} = 0.29$ when $n(P_i) = 1.7$, we decide to set $n(P_i)$ to 1.3. For the further simulations presented in this chapter, unless mentioned otherwise, a single polymer with refractive index $n(P_i) = n(P_s) = 1.3$ will be considered, for both the interstices and the spheres.

3.3. Transparent structured material (low VO_2 concentrations)

Now that the influence of the parameters which are not based on the structure have been studied on homogenized materials, the next step consists in introducing a structure in order to study the influence of structural parameters on the material transmittance properties, and in particular on T_{lum} and ΔT_{sol}.

3.3.1. System description

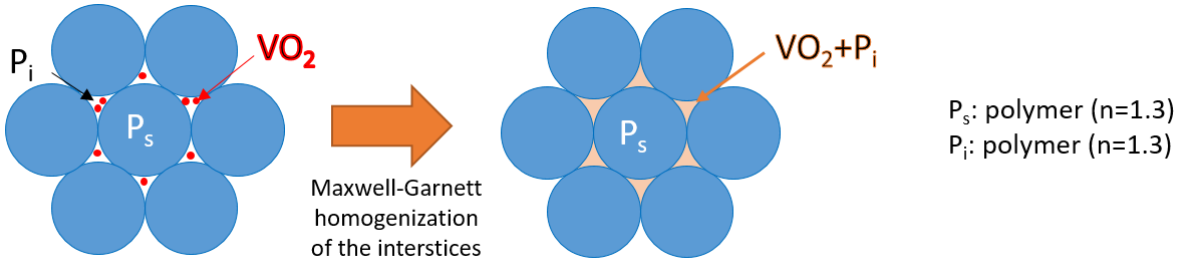

Figure 71: Polymer opal (n=1.3) loaded with VO_2 nanoparticles, with interstices modelled using a Maxwell-Garnett homogenization

In order to study parameters related to the material structure, the homogenized system used in the previous section cannot be used anymore. In this section, only the opal interstices are homogenized in our model, as illustrated in **Figure 71**. The selected parameters previously determined are maintained. The resulting system is an opal consisting of polymer P_S spheres of refractive index $n = 1.3$ surrounded by the homogenized interstices of VO_2 spherical nanoparticles dispersed in a polymer P_i of refractive index $n = 1.3$. The VO_2 total concentration f_t is still 1 vol% and the coating is 13 µm thick.

This new model allows the study of parameters such as the structure compacity C, which will be the main parameter studied in this section.

3.3.2. Setting the spatial resolution along the direction normal to the surface

As it was described in Chapter II, the model uses a FMM method combined with a staircase approximation to model spherical particles. Due to this approximation, it is required to set an appropriate spatial resolution along the z axis (the opal [111] crystallographic direction). A finer discretization results in more spherical particles, but to a higher computational time. The parameter of interest in this section is the number of layers used to model one period along the z axis. Examples for two different values for this parameter are given in **Figure 72**. In this figure, the illustration is limited to one period along the z axis, with only one sphere in each (111) plane. Perfect spheres are superposed with their corresponding stacked cylinders. More cylinders are used to define a sphere with the parameter used to define the spatial resolution increasing from 6 (**Figure 72a**) to 24 (**Figure 72b**).

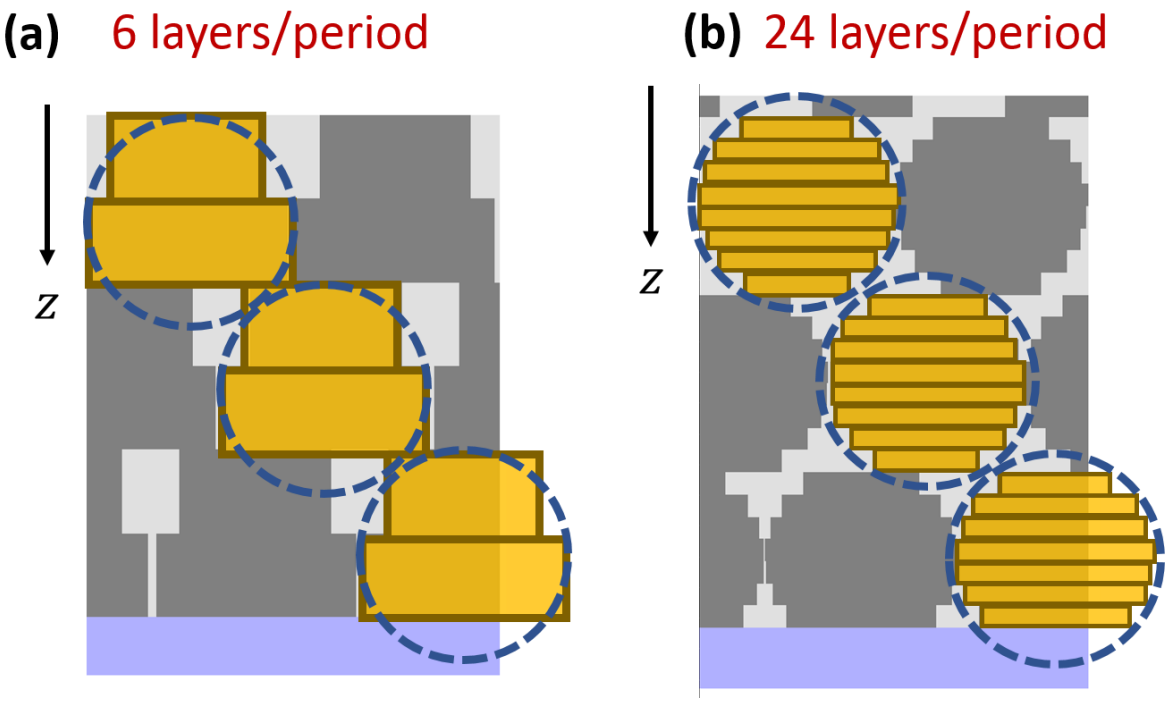

Figure 72: One opal period along the [111] direction (z axis) discretized into 6 layers (a) and 24 layers (b).

This preliminary section will focus on the influence of this spatial resolution on the calculated transmittance values. **Figure 73** shows the transmittance spectra for normally incident light on the material surface for different spatial resolutions. Insets are the same spectra zoomed around the PBG position (valley at about 750 nm visible in **Figure 73a**). As we increase the spatial resolution, the spectra converge towards a unique transmittance spectrum obtained when the system is very well discretized. However, even for lower resolutions, the transmittance spectrum remains close to this limit spectrum.

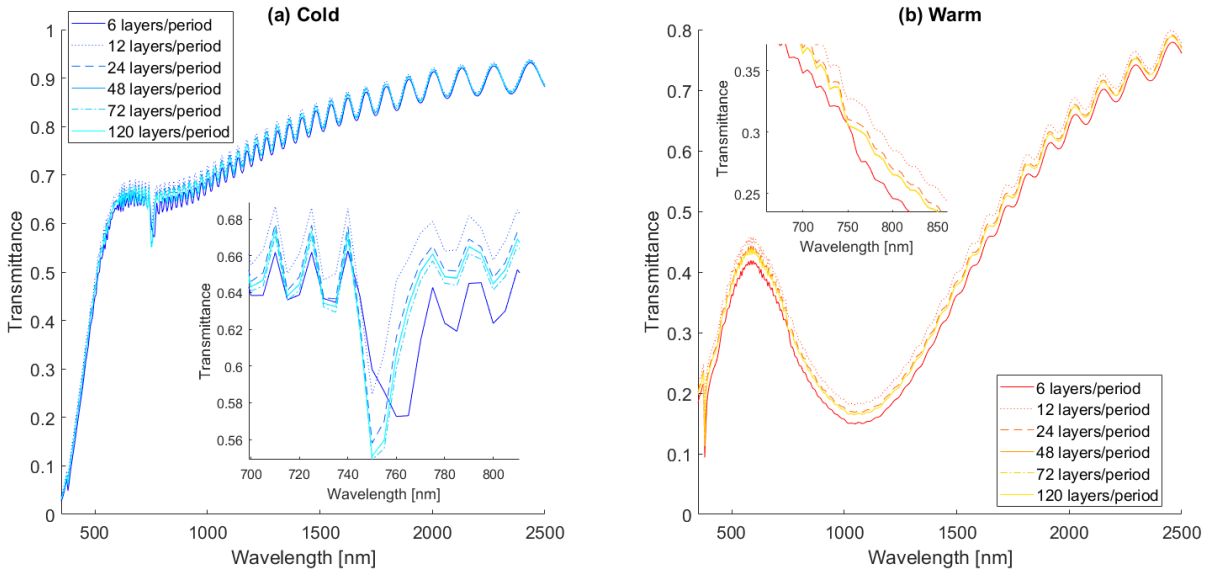

Figure 73: Transmittance spectra for normally incident light on a compact opal made of polymer spheres (n=1.3) surrounded by a mixture of VO_2 (total concentration f_t = 1 vol%) and the same polymer, in both cold (a) and warm (b) conditions. Each period of the opal in the [111] direction is modelled by a certain number of parallel layers. Insets are the same spectra zoomed around the PBG position (valley at about 750 nm visible in the cold case).

In order to quantify the deviation compared to our finest resolution (120 layers/period), the normalized root mean square δ of the difference between the considered transmittance spectrum and the transmittance spectrum for 120 layers/period has been computed:

$$\delta = \sqrt{\frac{1}{N-1}\sum_{i=1}^{N}(T(\lambda_i) - T_{120}(\lambda_i))^2}\,, \qquad (3.\ 5)$$

where λ_i is the i-th wavelength of the spectrum, $T(\lambda_i)$ is the considered transmittance spectrum value at the wavelength λ_i, $T_{120}(\lambda_i)$ is the 120 layers/period transmittance spectrum value at the wavelength λ_i and N is the total number of wavelengths.

The calculated values of δ are presented in **Table 6** and **Figure 74** as a function of the number of stacked layers used to model one period, in both VO_2 states.

Layers/period	Cold	Warm
6	0.0652	0.0325
12	0.0329	0.0186
24	0.0073	0.0042
48	5.66E-4	6.35E-4
72	0.0074	3.86E-4

Table 6: Root mean square difference δ as a function of the number of stacked layers used to model one period for both cold and warm VO_2 states.

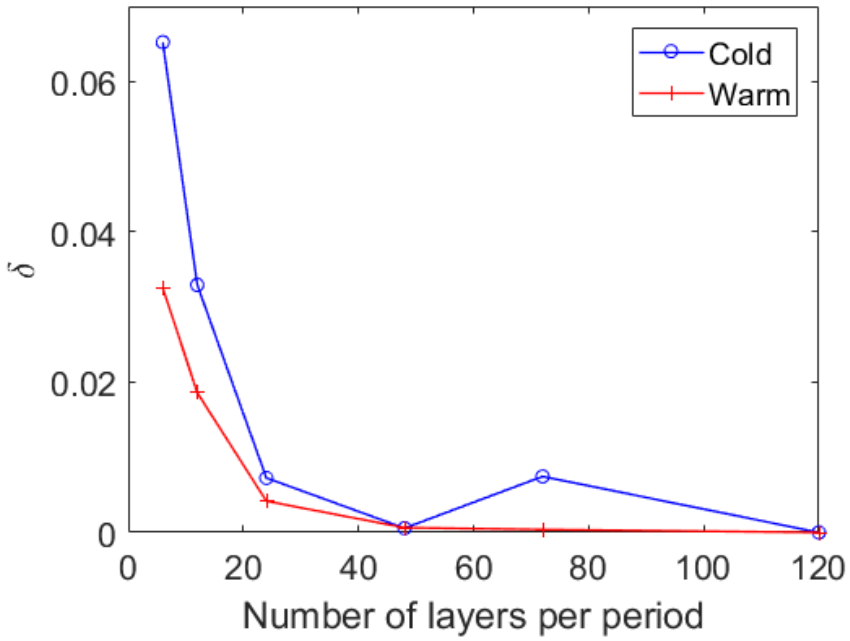

Figure 74: Root mean square difference δ as a function of the number of stacked layers used to model one period for both cold and warm VO_2 states.

As the number of layers/period increases, the transmittance spectrum converges towards the value obtained for our finest model with 120 layers/period. We decide that a value of δ lower than 0.01 is enough to correctly model the optical behavior of our material. 0.01 indeed corresponds to a relative variation of a few percent as average transmittance values over the considered wavelength range are about 0.5 (see **Figure 73**). Based on this criterion, we consider that it is unnecessary to use more than

24 layers to model one period along the z axis. So in this chapter, unless stated otherwise, 24 layers will be used in order to model one opal period along the [111] direction.

3.3.3. Influence of the structure compacity

In this section, the influence of the structure compacity on the material transmittance properties is studied. Varying the compacity is possible by varying the opal spheres radius for a given cell parameter (*Equation* (3. *1*)). For this study we set the cell parameter to $a = 500$ nm while varying the spheres radius R.

Other parameters are influenced by the structure compacity. This is the case of the VO_2 concentration. The total VO_2 concentration was set to $f_t = 1$ vol%, which results in a VO_2 concentration in the interstices of $f_i = 3.8$ vol% when the compacity is equal to 0.74 (*Equation (3. 4)*). If the same homogenized material is used here for the opal interstices, this will result in an increase of the total VO_2 concentration in the system as the compacity is reduced. This is due to the fact that smaller opal spheres lead to larger interstitial areas containing VO_2 nanoparticles, which results in higher VO_2 concentrations in the full system.

This study will thus be split into two parts: the first part will consider a constant f_i, which means that the interstice material will remain the same as the spheres size vary, while the second part will consider a constant f_t, which means that f_i is adjusted for each considered compacity value. We will here study in which case and how the structure compacity influences the material transmittance properties. In addition, in order to evaluate the influence of the material structuration, a comparison with an equivalent homogeneous layer modelled by a two-step homogenization process will be made.

3.3.3.1. At constant f_i

In this section, we set the VO_2 concentration in the interstices to f_i = 3.8 vol% and study the influence of the structure compacity on the material transmittance. The four considered cases are shown in **Figure 75**, covering the whole possible compacity range from C = 0.01 to 0.74. The compact structure is represented on the left, and smaller compacities are represented from left to right. The corresponding opal spheres diameters are also shown, along with the total VO_2 concentrations f_t. All sphere center positions are identical, only their sizes change. As the spheres get smaller, while f_i is kept constant, f_t increases as explained above.

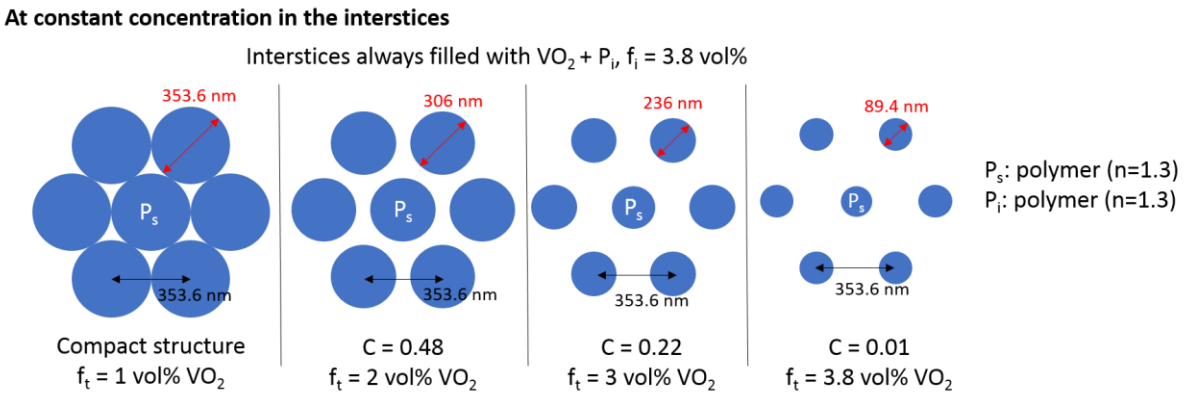

Figure 75: Top views of a (111) plane of the simulated opals at various structure compacities C with a constant VO_2 concentration in the opal interstices f_i.

Optical properties and performances of the material

The corresponding spectral transmittances are shown in **Figure 76**, for both VO_2 states and for normally incident light. In both cold (**Figure 76a**) and warm (**Figure 76b**) conditions, the spectral transmittance increases with increasing compacities. This is due to the fact that higher compacities lead to lower values for f_t. Since VO_2 is an absorbing material, lower VO_2 concentrations in the system result in a higher transmittance. Based on *Equation* (3. *2*), this increase in transmittance leads to an increase in both luminous and solar transmittances, for cold and warm conditions. This increase is visible in **Figure 77**, which show the calculated T_{lum}, T_{sol} and their modulation at the VO_2 phase transition as a function of C. While T_{lum} and T_{sol} increase as expected, their variations are not linear. These non-linear variations lead to non-monotonic variations of ΔT_{lum} and ΔT_{sol}.

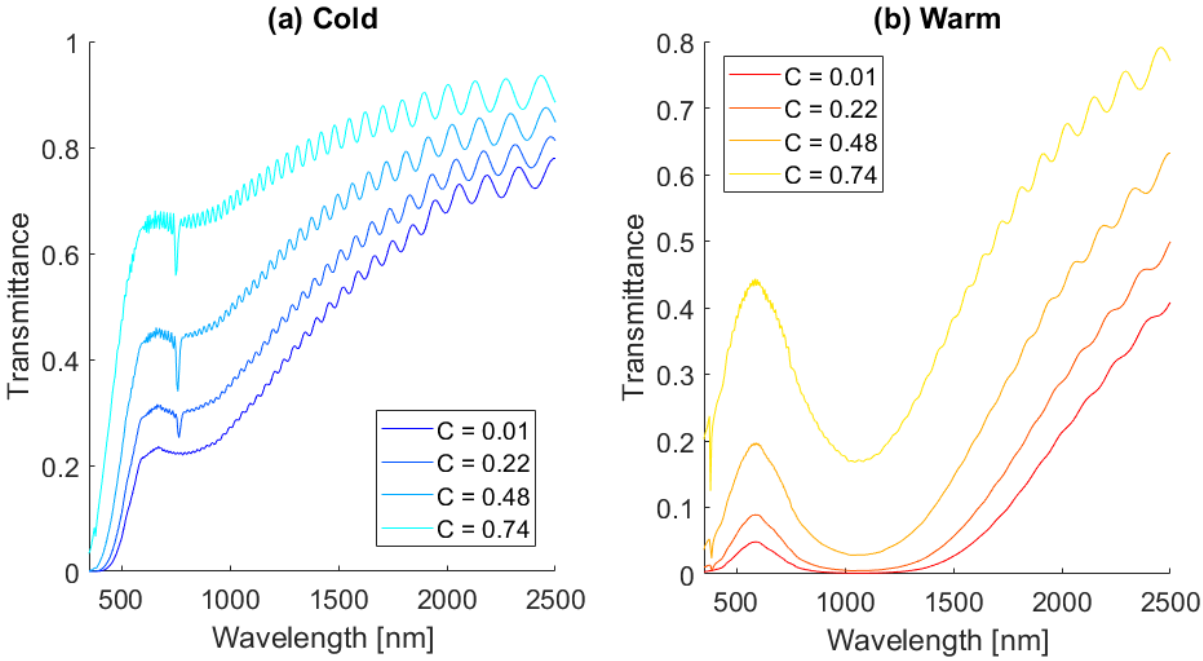

Figure 76: Transmittance spectra for normally incident light of an opal made of polymer (n=1.3) spheres and interstices filled with a mixture of f_i = 3.8 vol% VO_2 and that same polymer, for different compacities C, in VO_2 cold (a) and warm (b) phases.

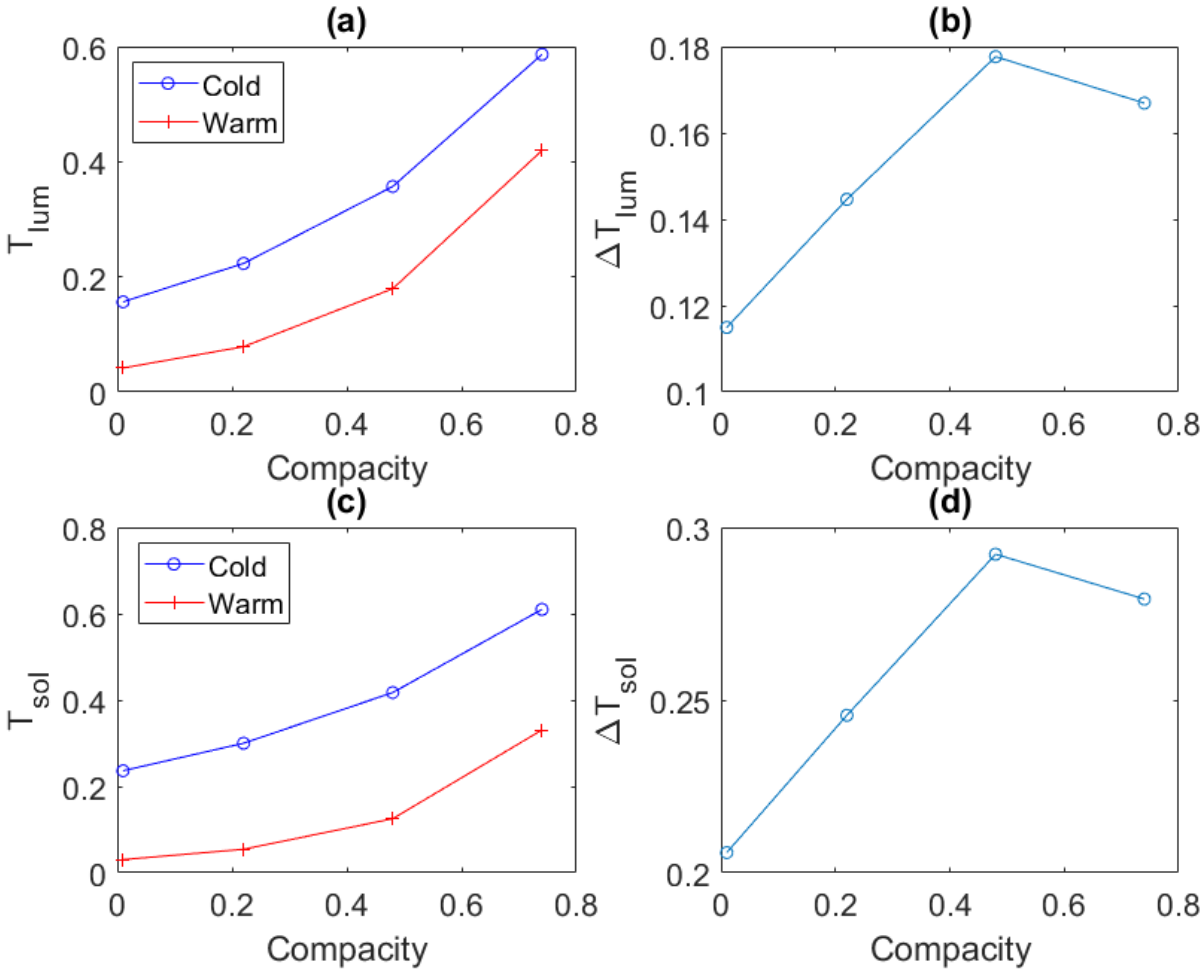

Figure 77: Luminous and solar transmittances in both VO_2 states, and their modulations, for normally incident light, for an opal made of polymer (n=1.3) spheres and a mixture of f_i = 3.8 vol% VO_2 and the same polymer, for different compacities.

Keeping in mind that applications such as energy-efficient window coatings require high values for T_{lum} and ΔT_{sol}, we are interested in the top left and bottom right graphs of **Figure 77**. While ΔT_{sol} seems to reach a maximum value at $C = 0.48$, T_{lum} keeps increasing significantly with increasing compacities. For this specific application, it may be interesting to set the compacity parameter to 0.48 or 0.74, depending on the importance of each criterion.

Influence of the structure on the optical properties

We will now study the impact of ordering on the material transmittance properties for the four different values of compacities considered here. **Figure 78** shows the same transmittance spectra as in **Figure 76** (plain lines) along with those of their corresponding homogeneous layer modelled by an effective refractive index derived from a two-step homogenization process using Maxwell-Garnett approximation (dashed lines). For each considered compacity, the spectral transmittance is very similar between the structured material and its homogenized counterpart. The only difference can be seen where the transmittance drops around the PBG position. In this case, with the considered parameters, this PBG is located around 760 nm. It is clearly visible in the cold conditions, but not in the warm conditions due to a conjugated effect of a very weak refractive index contrast between the interstices and the spheres and a more important absorption (see **Section 3.3.3.2**). The inset in **Figure 78a** is a zoomed view around this PBG position. The PBG peak seems thin, yet its amplitude increases with increasing compacities. This is because the spheres size decreases with the compacity (see **Figure 75**).

For example, when $C = 0.01$, the opal spheres have a diameter of 90 nm, and are thus small compared to the light wavelengths so the propagating light is not so affected by the material nanostructuration.

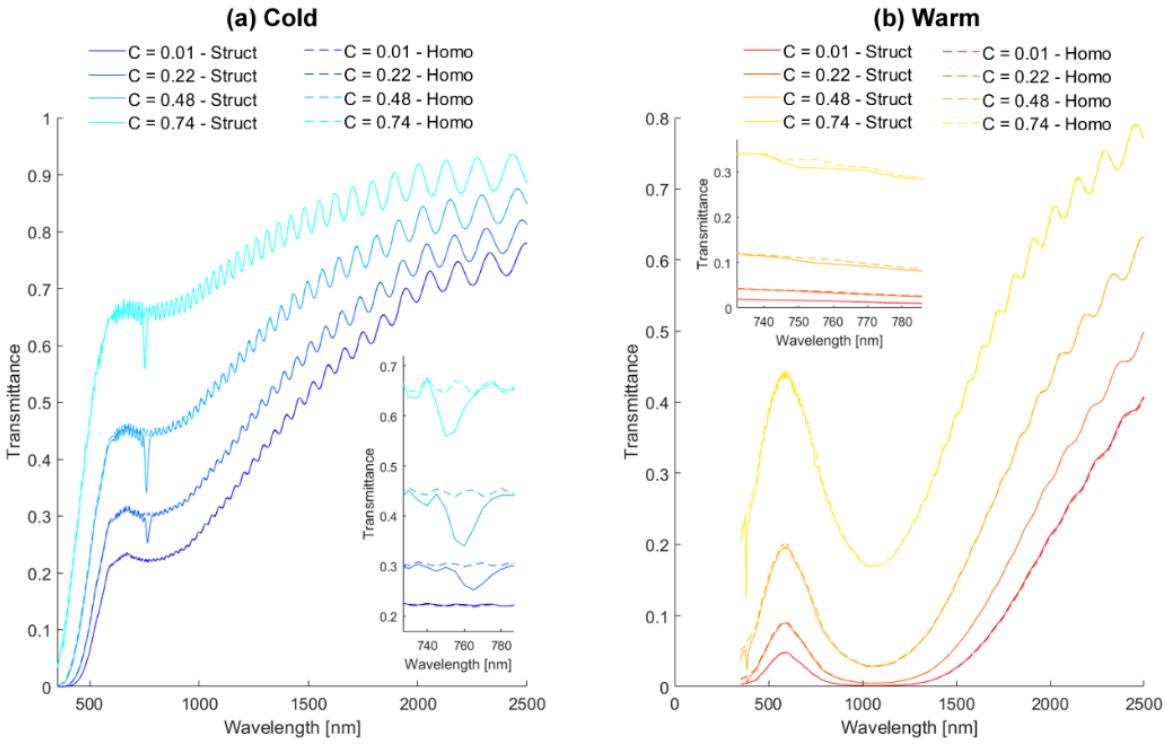

Figure 78: Transmittance spectra for normally incident light of an opal made of polymer (n=1.3) spheres and interstices filled with a mixture of f_i = 3.8 vol% VO_2 and that same polymer, for different compacities C, in cold (a) and warm (b) VO_2 phases, considering a structured material (solid lines) and a homogenized one (dashed lines). Insets are zoomed views around the PBG position.

T_{lum}, T_{sol}, ΔT_{lum} and ΔT_{sol} are calculated based on these spectral transmittances and represented in **Figure 79** as a function of the structure compacity, in both cold and warm conditions. Curves denoted by 'Struct' are the same as presented in **Figure 77**. The new results obtained for the homogenized material are quite similar to the previous results obtained for the structured material. It appears that in these conditions, ordering the material has a very negligible impact on the material integrated transmittance values. Thus, the influence of the compacity on the material transmittance presented in this section it not caused by the compacity itself, but by the change in total VO_2 concentration induced by the compacity modification.

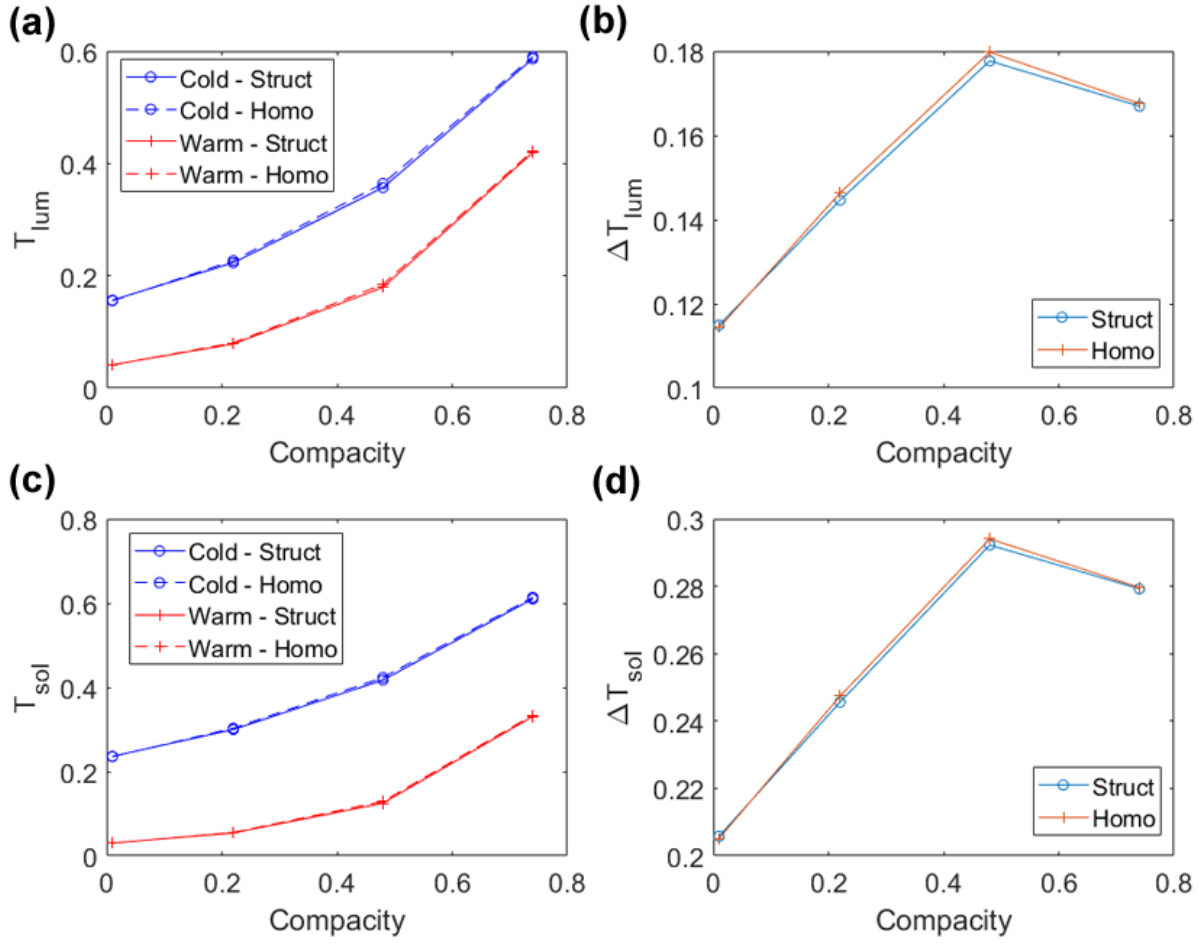

Figure 79: Luminous (a) and solar (c) transmittances in both VO_2 states, and their modulations (b,d), for normally incident light, for an opal made of polymer (n=1.3) spheres and a mixture of f_i = 3.8 vol% VO_2 and the same polymer, for different compacities, considering a structured material (solid lines) and a homogenized one (dashed lines).

3.3.3.2. At constant f_t

Keeping the total VO_2 concentration f_t constant, we now study how the structure compacity impacts the PBG and the material transmittance properties. Two different values for f_t are studied: 1 vol% and 3.8 vol%. While $f_t = 1$ vol% was the value selected earlier in this chapter, it might also be interesting to perform this study at another f_t to see a potential influence of the total VO_2 concentration on the PBG effect. A schematic representation of the structure is shown in **Figure 80**, with the parameters used in the case of f_t = 1 vol% in green and f_t = 3.8 vol% in orange. Four cases, each with different compacities C, are represented. To model these materials, f_i is adjusted so that f_t is kept constant.

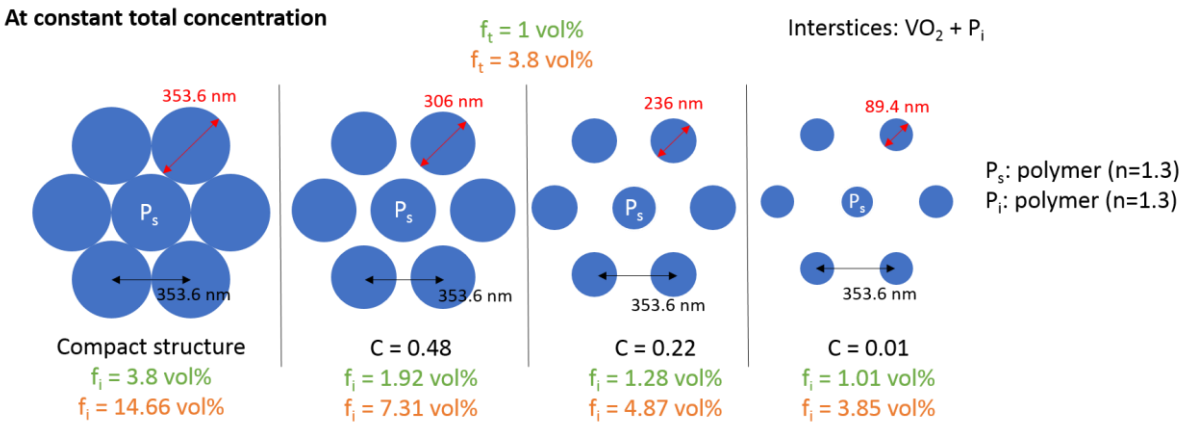

Figure 80: Top views of a (111) plane of the simulated opals at various structure compacities C with constant total VO_2 concentrations $f_t = 1$ vol% and $f_t = 3.8$ vol%.

At total VO_2 concentration $f_t = 1$ vol%

The case where $f_t = 1$ vol% is first considered. Spectral transmittances are calculated in each considered case at normal incidence and presented in **Figure 81**. Plotted alongside in dashed lines is the corresponding homogenized material. All considered cases share the same homogenized material, as the Maxwell Garnett approximation used for homogenization does not consider the sphere size as an input parameter, but only the volume ratio f_i and the materials refractive indexes. All curves are quite similar. The spectral transmittances vary as a function of the structure compacity only around the PBG position and for the VO_2 cold phase. Indeed, as described earlier, higher compacities lead to stronger PBG effects due to the growing size of the opal spheres. The opal structure has more impact on the incident light when the sphere size becomes comparable to the incident light wavelengths. No variations of the transmittance with the compacity are observed for the VO_2 warm phase, even close to the PBG position. The higher value of absorption and low interstices/spheres refractive index contrast for the warm VO_2 phase indeed inhibits the PBG effect. So, at constant f_t, the compacity has only an impact on the transmittance in the cold VO_2 state close to the PBG position, and almost no impact on the transmittance in the warm VO_2 state.

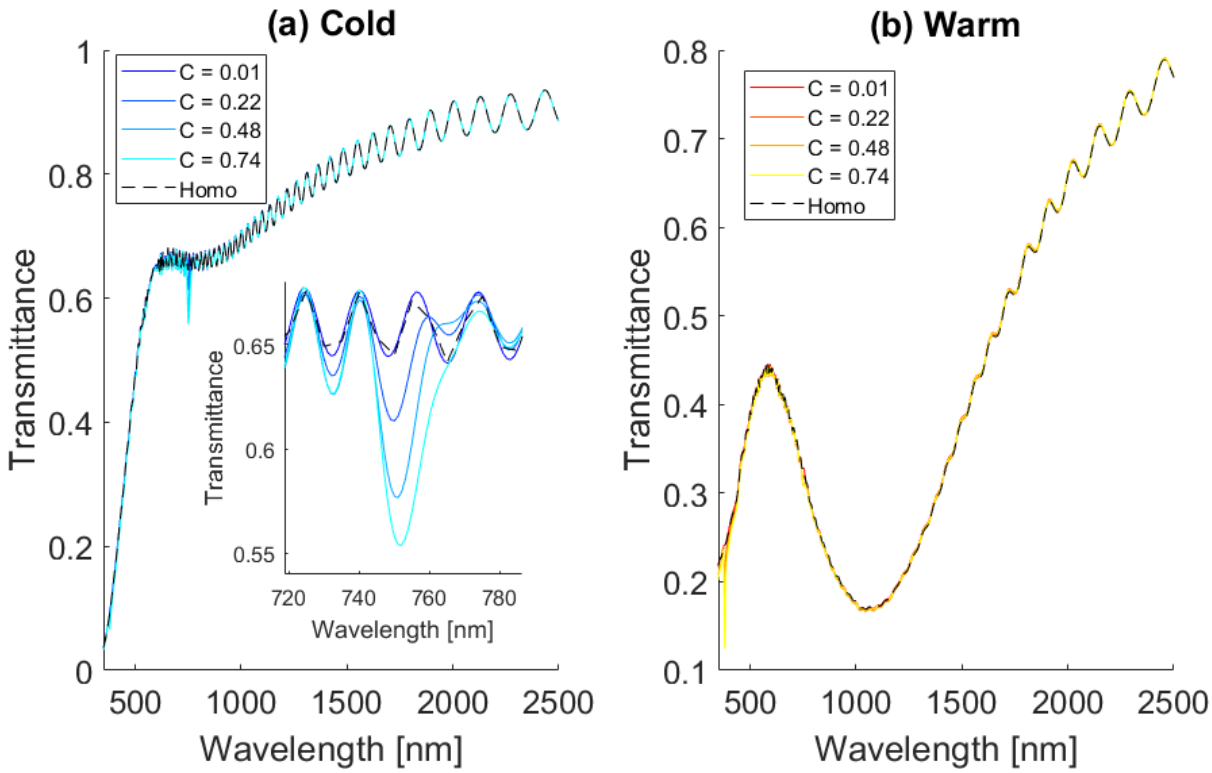

Figure 81: Transmittance spectra for normally incident light of an opal made of polymer (n=1.3) spheres and a mixture of VO_2 nanoparticles dispersed in the same polymer, for different structure compacities C and both VO_2 cold (a) and warm (b) phases, considering a structured material (solid lines) and a homogenized one (dashed lines). The total VO_2 concentration is set to ft = 1 vol%. The inset in the left figure is a zoom around the PBG position for the cold VO_2 phase.

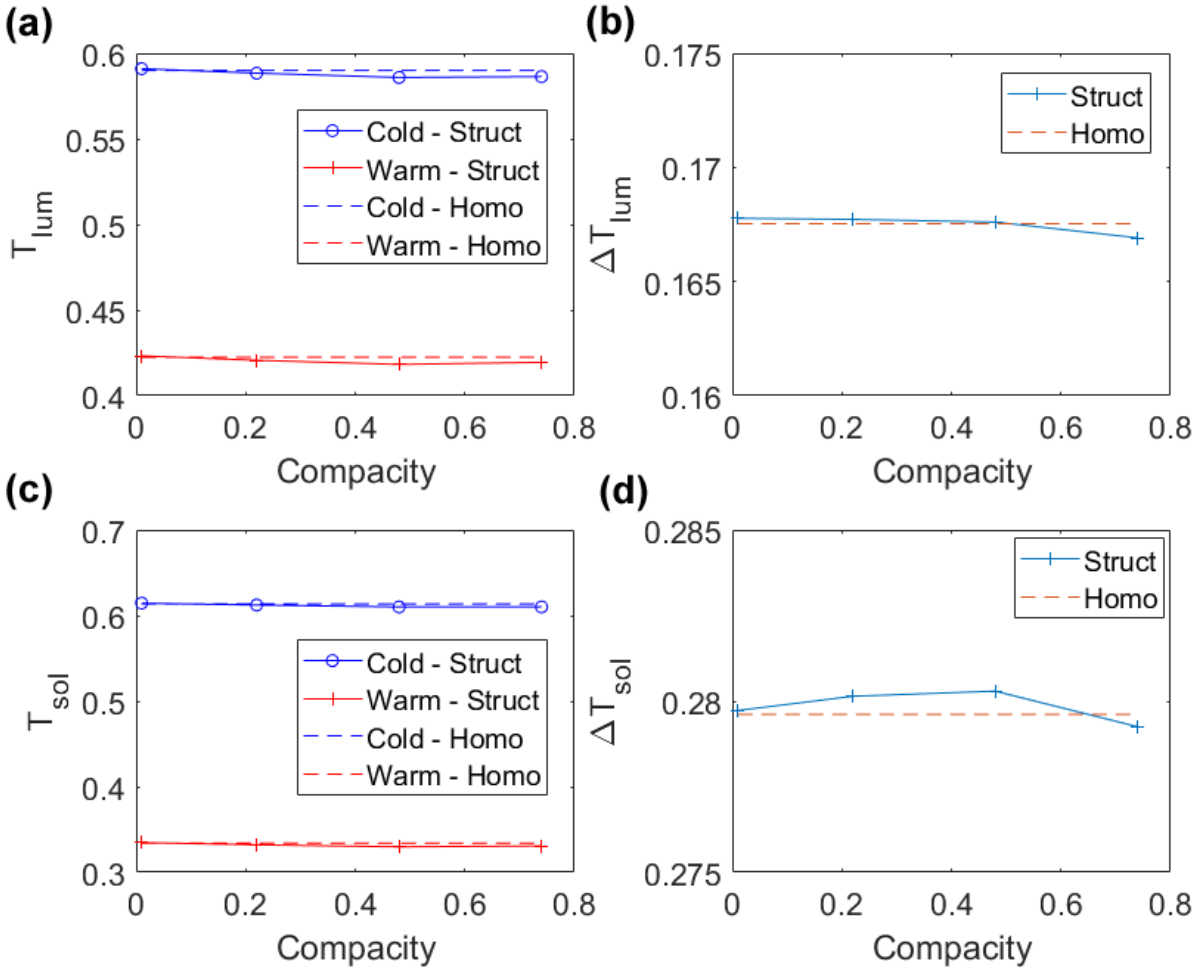

Figure 82: Luminous (a) and solar (c) transmittances in both VO_2 states, and their modulations (b,d), for normally incident light, of a polymer opal (n=1.3) loaded with f_t =1 vol% VO_2 nanoparticles (solid lines), and its homogenized counterpart (dashed lines), for different structure compacities.

Compacity	Sphere diameter [nm]	Cold		Warm		ΔT_{lum}	ΔT_{sol}
		T_{lum}	T_{sol}	T_{lum}	T_{sol}		
0,01	89,4	0,59	0,61	0,42	0,33	0,17	0,28
0,22	236	0,59	0,61	0,42	0,33	0,17	0,28
0,48	306	0,59	0,61	0,42	0,33	0,17	0,28
0,74	353,5	0,59	0,61	0,42	0,33	0,17	0,28
Homogenized		0.59	0.61	0.42	0.33	0.17	0.28

Table 7: Luminous and solar transmittances, in both VO_2 states, and their modulations, for normally incident light, in the case of a polymer opal (n=1.3) loaded with f_t = 1 vol% VO_2 nanoparticles, for different structure compacities. The last row is the case of the homogenized material.

This reduced spectral transmittance around the PBG position for the VO_2 cold phase when the compacity increases is not likely to reduce the luminous and solar transmittances as the PBG is very thin. To confirm this observation T_{lum}, T_{sol}, ΔT_{lum} and ΔT_{sol} are calculated and presented in **Figure 82** and **Table 7**. It confirms that the variations of the transmittance close to the PBG position for the cold VO_2 state does not significantly influence these integrated transmittance values, even for the highest compacity. With two significant digits, these integrated transmittance values are exactly the same when the compacity varies from 0.01 to 0.74 at constant $f_t = 1$ vol%. The PBG effect is indeed very weak, and it could be due to the relatively low refractive index contrast in the photonic crystal for

low VO_2 concentrations. Also, in the warm VO_2 phase, the absorption due to the absorbing VO_2 nanoparticles is too high to see any PBG effect. To emphasize these points, the refractive indexes used to model the opal interstices for the four different values of f_i indicated in **Figure 80** (case $f_t = 1$ vol%) are presented in **Figure 83.**

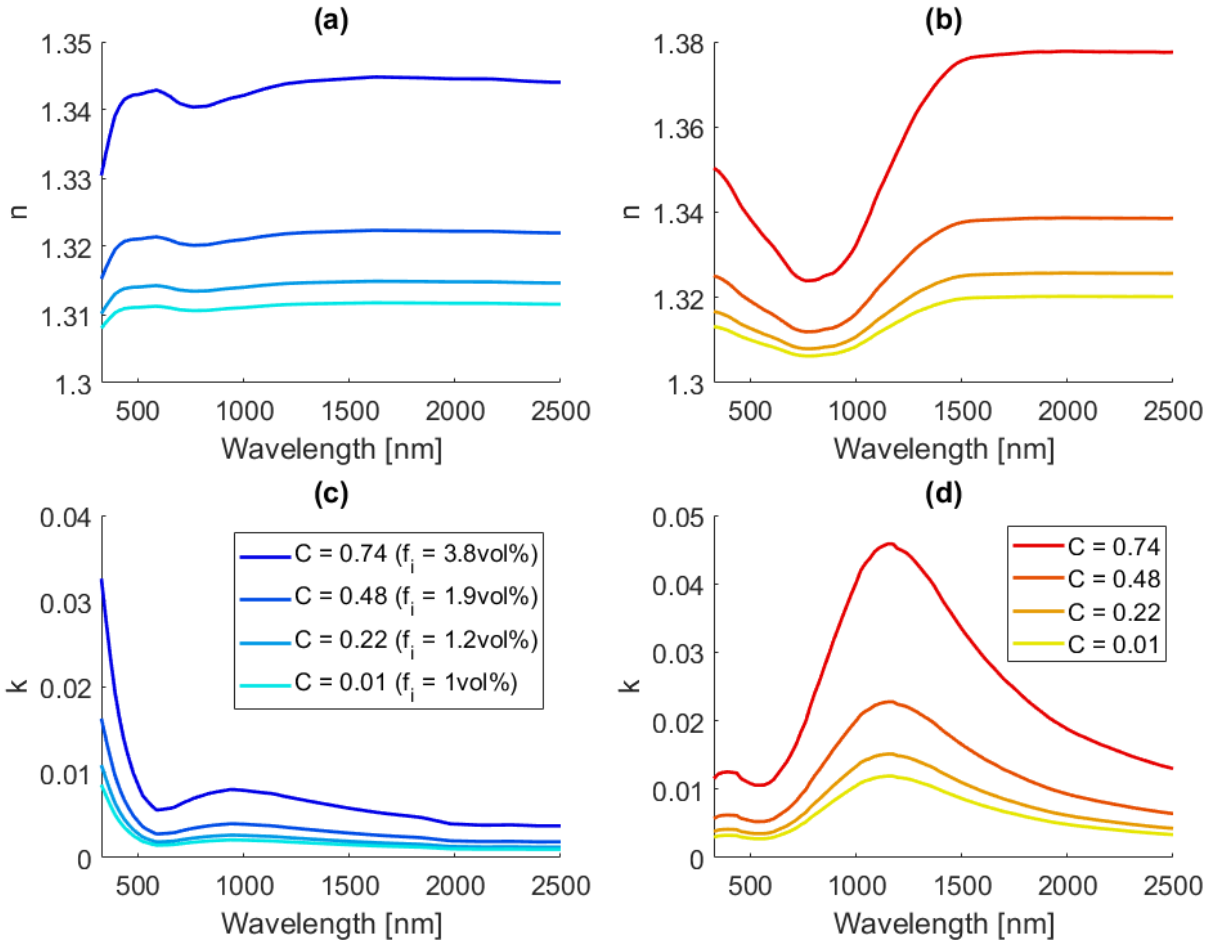

Figure 83: Real (a,b) and imaginary (c,d) part of the effective refractive indexes used to model the opal interstices consisting of a mixture of VO_2 spherical nanoparticles in a polymer matrix of refractive index 1.3 for different VO_2 concentrations f_i in cold (a,c) and warm (b,d) conditions.. These concentration values correspond to the concentrations used in the interstices of the different structures with compacities C to have a constant total VO_2 concentration of 1 vol%.

In all considered cases, the refractive index real and imaginary parts increase with increasing structure compacities. These variations are related to the variations of the VO_2 concentration in the interstices f_i. Indeed, on one hand, higher compacities lead to higher f_i at constant f_t (*Equation* (3. *4*)). On the other hand, keeping in mind that in the considered spectral region, the VO_2 refractive index real and imaginary parts (see **Figure 64**) are higher than the real and imaginary parts of the refractive index of the polymer medium surrounding the particles ($n = 1.3$), an increase of f_i results in an increase of the effective refractive index real and imaginary parts used to model the opal interstices.

Comparing the real part of the interstices refractive indexes to the spheres refractive index $n(P_s) = 1.3$, it seems that the refractive index contrast in the photonic crystal is quite limited. In the cold conditions, this contrast reaches up to 0.04, which is very low compared to the refractive indexes found in many manufactured artificial opal and inverse opal photonic crystals [141,142]. For example, a polymer opal photonic crystal manufactured by Ruhl et al. [100] has a refractive index contrast of 0.11. It seems that the refractive index contrast is not enough to produce a significant PBG effect in the system. It is also particularly the case in the warm phase, where the interstices refractive index real

part has a minimum around 760 nm, very close to the PBG position, leading to a maximum refractive index contrast at this wavelength of 0.02. In order to obtain a stronger PBG effect, the spheres/interstices refractive index contrast needs to be increased. This can be done by increasing the VO_2 concentration in the opal interstices.

Comparing the imaginary parts of the interstices refractive indexes for the cold and warm VO_2 phases close to the PBG position (that is around 750 nm), its value is twice as much in the warm condition than in the cold condition (for example, 0.02 in the warm and less than 0.01 in the cold condition, for $C = 0.74$). This, combined with the low refractive index contrast due to the minimum of the refractive index real part close to the PBG position explains the disappearance of the PGB effect for the warm VO_2 phase.

At total VO_2 concentration $f_t = 3.8$ vol%: transmittance properties

In order to see if the PBG effect could be increased, the VO_2 total concentration f_t has been increased to 3.8 vol%. The other parameters are the same as in the previous study. **Figure 84** shows the transmittance spectra in both VO_2 phases. The observations are similar to the previous study: higher compacities lead to larger PBG and only in the case of cold semi-conducting VO_2. With this higher VO_2 total concentration f_t, the amplitude of the PBG transmittance drops for $C = 0.74$ (deepest PBG) is increased to about 0.15 compared to 0.1 in the case of $f_t = 1$ vol%.

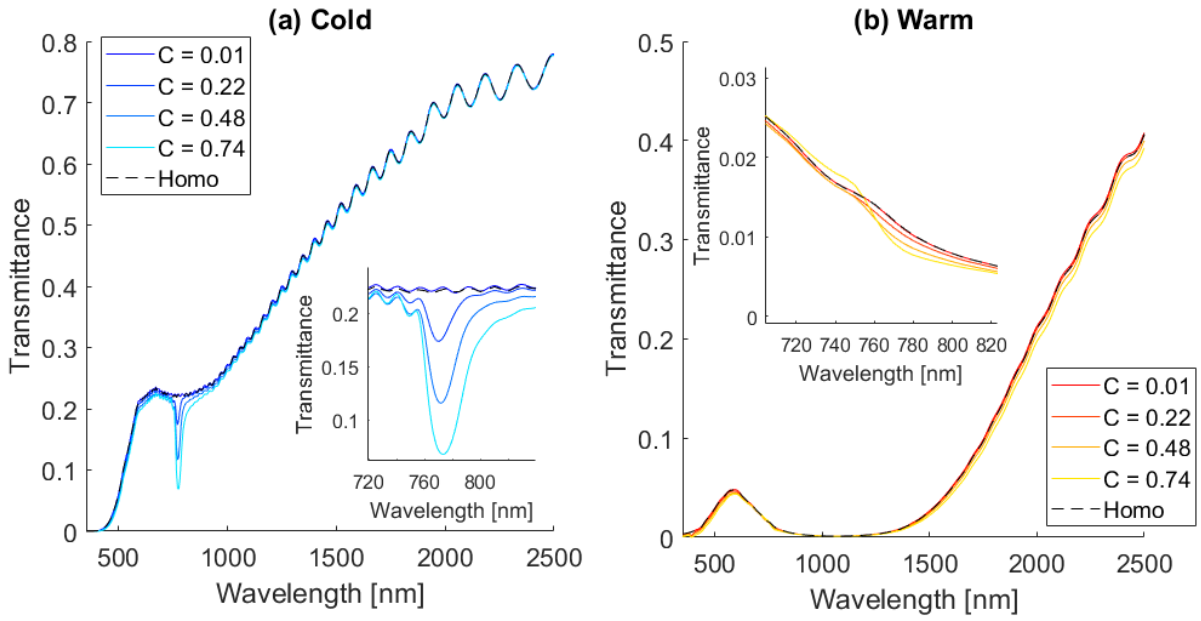

Figure 84: Transmittance spectra for normally incident light of an opal made of polymer (n=1.3) spheres and a mixture of VO_2 nanoparticles dispersed in the same polymer (solid lines), and its homogenized counterpart (dashed lines), for different structure compacities C and both cold (a) and warm (b) VO_2 phases. The total VO_2 concentration is set to $f_t = 3.8$ vol%. The insets are zooms around the PBG position.

However, once again, the variations of both luminous and solar transmittances as a function of the structure compacity are quite limited, even with a slightly higher total VO_2 concentration, as shown in **Figure 85** and **Table 8**.

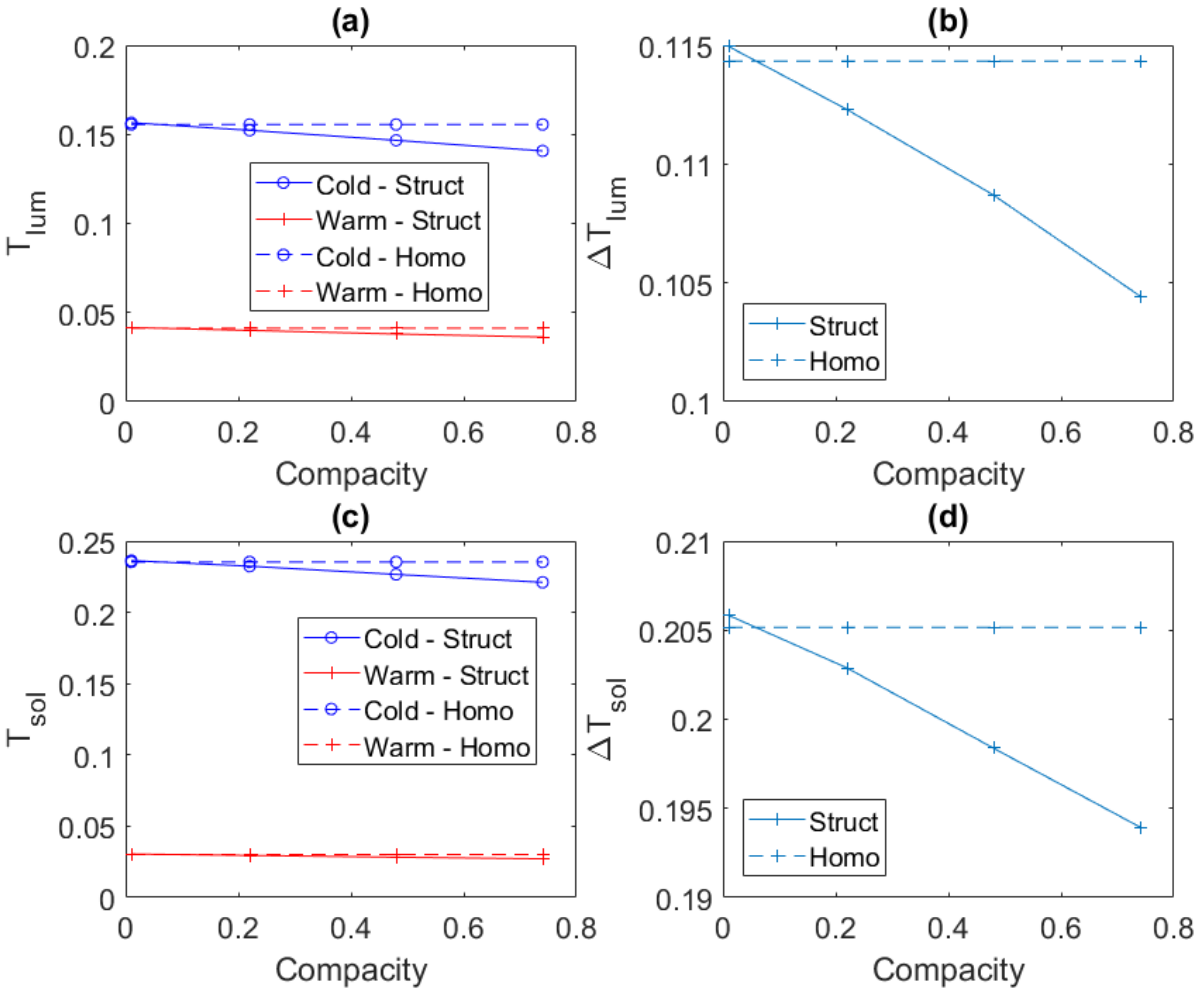

Figure 85: Luminous (a) and solar (c) transmittances, in both VO_2 states, and their modulations (b,d), for normally incident light, of a polymer opal (n=1.3) loaded with 3.8 vol% VO_2 nanoparticles (solid lines), and its homogenized counterpart (dashed lines), for different structure compacities.

Compacity	Sphere diameter [nm]	Cold		Warm		ΔT_{lum}	ΔT_{sol}
		T_{lum}	T_{sol}	T_{lum}	T_{sol}		
0.01	89.4	0.16	0.24	0.04	0.03	0.11	0.21
0.22	236	0.15	0.23	0.04	0.03	0.11	0.20
0.48	306	0.15	0.23	0.04	0.03	0.11	0.20
0.74	353.5	0.14	0.22	0.04	0.03	0.10	0.20
Homogenized		0.16	0.24	0.04	0.03	0.11	0.21

Table 8: Luminous and solar transmittances in both VO_2 states, and their modulations, for normally incident light, in the case of a polymer opal (n=1.3) loaded with ft = 3.8 vol% VO_2 nanoparticles, for different structure compacities. The last row is the case of the homogenized material.

Figure 85 and **Table 8** also show the case of the homogenized material. Comparing the integrated values obtained for a structured material to the homogenized layer, it appears that the material structure has little to no impact on the material luminous and solar transmittance properties. Comparing with the case $f_t = 1$ vol% ($T_{lum,warm} = 0.42, \Delta T_{sol} = 0.28$), it appears that an increase of the total VO_2 concentration from 1 vol% to 3.8 vol% leads to a significant decrease of the luminous transmittance (10 times lower, from 0.42 to 0.04). This very low value for the luminous transmittance is not acceptable for applications as an energy efficient coating for windows. For ΔT_{sol}, this increase

of f_t has a smaller impact as a 30% decrease is observed on ΔT_{sol}, from 0.28 to 0.2 when increasing the total VO_2 concentration.

The total VO_2 concentration was increased from $f_t = 1$ vol% to $f_t = 3.8$ vol%. This increase leads to an increase of the refractive index contrast in the opal photonic crystal from $\Delta n = 0.04$ to $\Delta n = 0.16$ in the cold conditions, around the PBG position (760 nm wavelength). The PBG slightly shifts (around 770 nm with $f_t = 3.8$ vol%) with the increase of the VO_2 concentration, but this shift is relatively small and Δn is not influenced. Even with this increased refractive index contrast, the PBG effect remains relatively low and does not have much impact on the integrated transmittance values and their modulations. Furthermore, despite $f_t = 3.8$ vol% is a relatively low concentration, the material becomes too absorbent to be used for glazing applications. Thus, according to the previous studies, having a structured material isn't interesting for applications requiring a transparent coating. The further point will be to check if structuring the material could be interesting to generate a reflectance modulation on an opaque material.

At total VO_2 concentration $f_t = 3.8$ vol%: reflectance properties

This section is a study of the PGB effect on the reflectance spectra, for the same material as studied previously. **Figure 86** shows the reflectance spectra in both cold and warm conditions for different structure compacities C at a total VO_2 concentration f_t = 3.8 vol% (same material as for **Figure 84**). At this slightly higher VO_2 concentration, the PBG peak is observed around 770 nm. Its amplitude and width increase with the compacity, and its amplitude is much higher than for the transmittance spectra, with a value of about 0.45 in the cold state and 0.14 in the warm state for $C = 0.74$. It is important to note that the PBG peak is clearly visible for the reflectance spectra in the warm condition, whereas it was totally inhibited by the bulk absorption for the transmittance spectra.

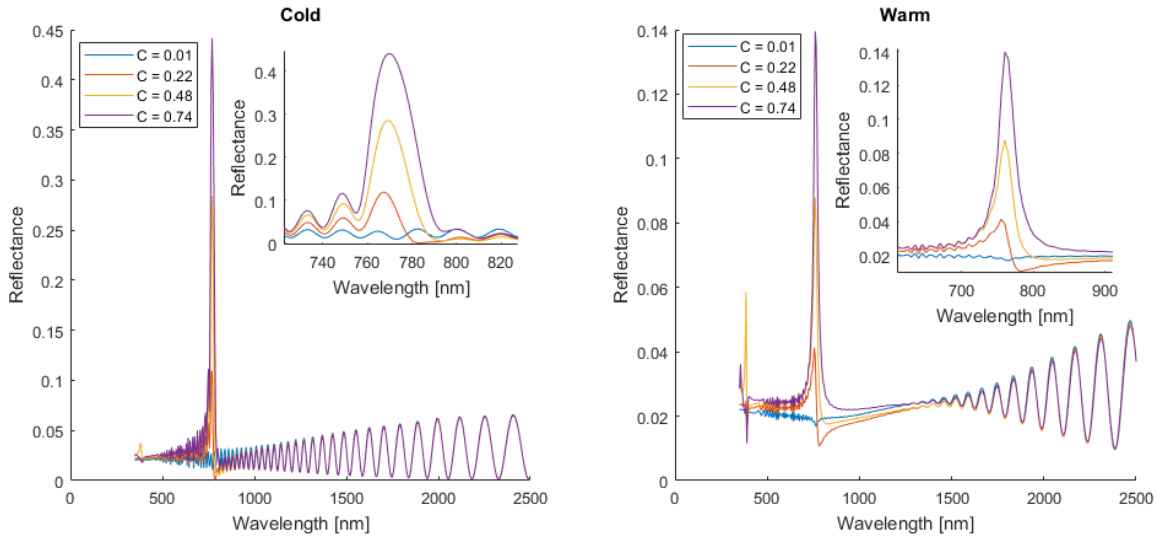

Figure 86: Reflectance spectra for normally incident light of an opal made of polymer (n=1.3) spheres and a mixture of VO_2 nanoparticles dispersed in the same polymer with n=1.3, for different structure compacities C and both VO_2 cold (left) and warm (right) phases, in the case where the material structure is taken into account. The total VO_2 concentration is set to f_t = 3.8 vol%. The insets are zooms around the PBG position.

The impact of the material structure is thus more important for the reflectance spectra than for the transmittance one. This point is encouraging for the interest of structuring the material to generate an impact on its reflectance. Furthermore, considering an opaque coating removes the transparency requirement. Without this condition, it is thus possible to investigate a wider range of VO_2 concentrations. Higher VO_2 concentrations may lead to larger refractive index contrasts, meaning stronger PBG effects.

3.3.4. Single- and double-step homogenization processes

In the previous sections we compared two different models: a structured material and its homogenized counterpart obtained by a two-step homogenization process (homogenization of the opal interstices and then of the whole material). However, the same polymer (that is the same refractive index $n = 1.3$) has been used for both the spheres and the interstices, so only two different materials are actually present in the system. In this case, a single-step homogenization process (like in **Section 3.2**) may have also been possible. In this section, this possibility is investigated by comparing the optical behavior of homogenized layers obtained by a single and a double-step homogenization process to the one of the structured material previously modelled. Both homogenization processes are illustrated in **Figure 87**. This section aims to choose which homogenization to apply when studying the influence of the material structure on the material optical properties. This will be done by comparing the spectral transmittance of a structured material with its two homogenized counterparts, and then choosing the homogenization leading to the minimum transmittance difference. Since we want to study the influence of the structure, the goal is to choose the homogenization leading to minimum influence of other possible effects. The study thus needs to be performed in a spectral range where the structure has no influence.

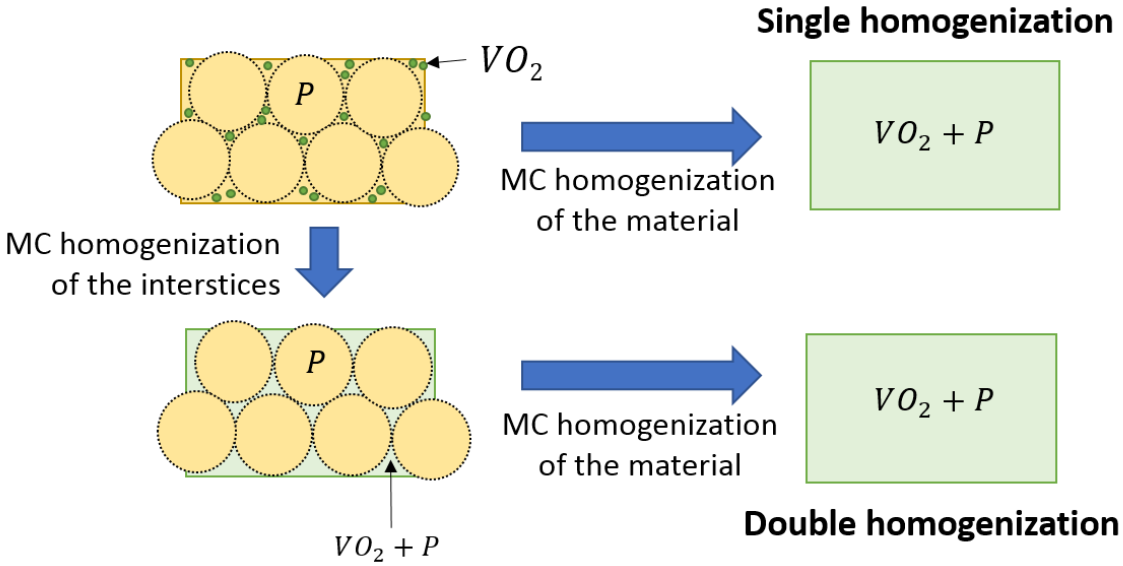

Figure 87: Illustration of the single and double homogenization processes. Arrows refer to homogenization processes. P designates both the spheres and interstices polymer.

The nanocomposite polymer opal that we want to model is represented at the top left corner of **Figure 87**. This material will then be homogenized through two different processes. The top one is obtained by a single step homogenization process: a Maxwell-Garnett approximation is applied to the dispersed

VO_2 nanoparticles in the polymer matrix (denoted P). The bottom one is obtained by a double-step homogenization process: the opal interstices are averaged with a first Maxwell-Garnett approximation (dispersed VO_2 nanoparticles in the polymer P), and then a second approximation is applied to the opal spheres (composed also of the polymer P) surrounded by the material obtained through that first homogenization. The validity of the interstices homogenization process has been studied in **Section 2.6**. The purpose here is to validate the double-step homogenization process used in the previous sections.

The system used for this study is a compact opal photonic crystal consisting of polymer spheres of refractive index $n = 1.5$. The opal interstices are filled with VO_2 spherical nanoparticles in a matrix of that same polymer. The cell parameter is set to $a = 500$ nm and the total VO_2 concentration is $f_t = 13.4$ vol%. This value corresponds to the highest concentration considered in **Section 2.6**. For this short study, a simple case with a single primitive cell is modelled, with one period along the [111] direction, which results in a total material thickness of about 866 nm. The light is normally incident on the (111) plane.

From there, the two homogenization processes are applied, leading to two homogenized layers modelled by their respective effective refractive indexes. The spectral transmittance of these three systems is calculated. Results are shown in **Figure 88** for both cold (**Figure 88a**) and warm conditions (**Figure 88b**). Plain lines refer to the opal photonic crystal with interstices modelled by an effective refractive index while dashed and dotted lines refer to the homogeneous counterparts, respectively obtained from single- and double-step homogenization processes.

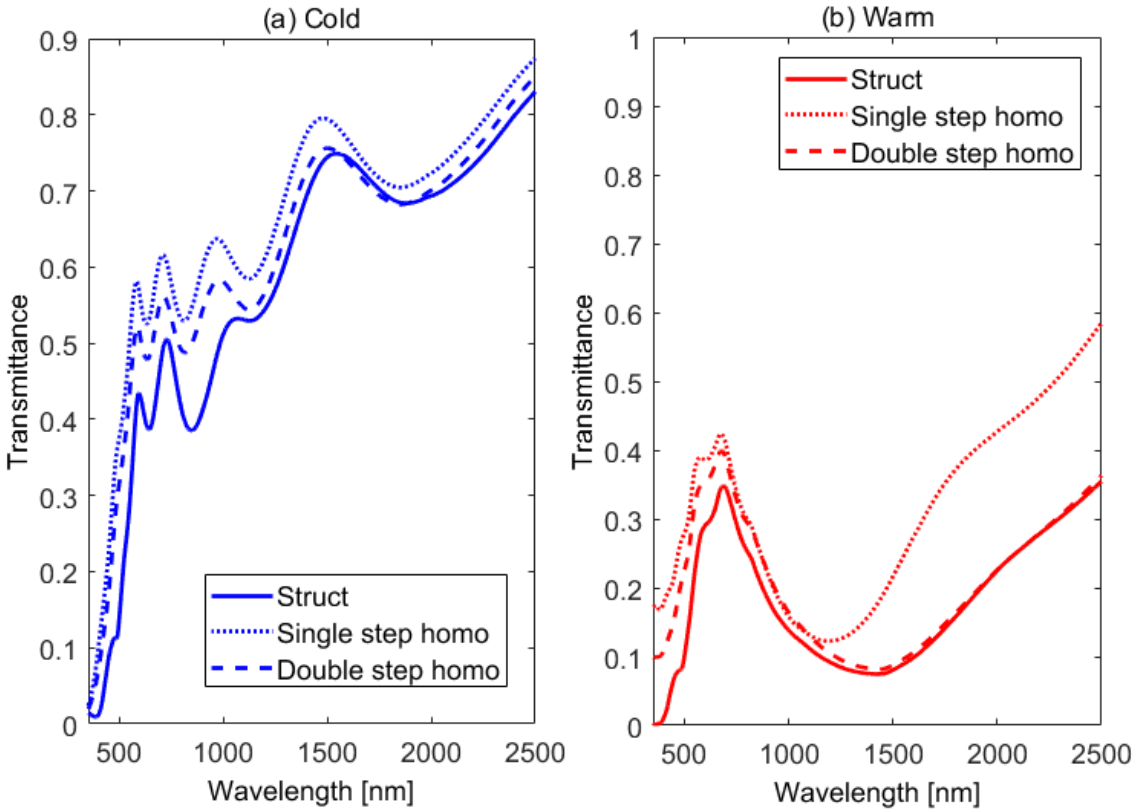

Figure 88: Transmittance spectra of an opal photonic crystal consisting of polymer spheres ($n = 1.5$) surrounded by a mixture of VO_2 nanoparticles and the same polymer, in cold (a) and warm (b) conditions (plain lines), and of it homogeneous counterparts modelled by an effective refractive index obtained through a single (dashed lines) and double (dotted lines) step homogenization process. The total VO_2 concentration is 13.4 vol%.

Comparing the structured case with the two homogenized layers cases, strong differences are observed. At shorter wavelengths (< 1000 nm), the spectral transmittances of both homogenized layers diverge from the structured material. While the shape remains quite similar, a small difference appears, especially in the case of the single-step homogenized layer, in both cold and warm conditions. At longer wavelengths, the single-step homogenized layer in the warm conditions (dotted line in **Figure 88b**) has a spectral transmittance significantly different than the two other curves.

From here, we could consider that a double-step homogenization process leads to a lower transmittance difference with the structured case. However, this comparison should rigorously be done in a spectral region where the structure has no influence, so that we can minimize the contributions of possible effects (other than the structure) by choosing the best homogenization process. In order to determine this spectral range, band diagrams are used.

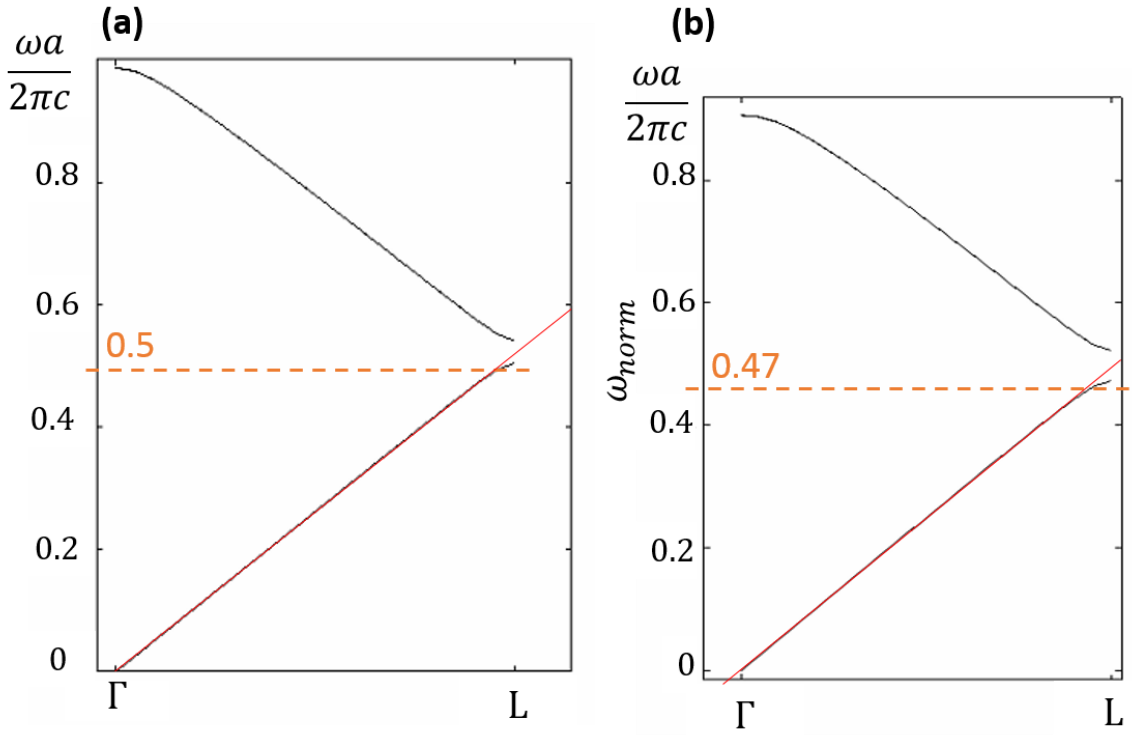

Figure 89: ΓL band diagrams of a compact opal photonic crystal consisting of polymer spheres ($n = 1.5$) surrounded by a material having a refractive index 2.1 (a) and 2.4. The linear dispersion relation is displayed as a red line. A dashed orange line gives the maximum frequency at which the first band follows this relation.

The ΓL band diagrams of the corresponding opal photonic crystals are calculated for real and non-dispersive refractive indexes. The mean effective refractive indexes of the interstices are used to compute these diagrams: $n_{eff} = 2.1$ in the cold conditions and $n_{eff} = 2.4$ in the warm conditions. These values are obtained through a Maxwell-Garnett approximation of the interstices consisting of VO_2 inclusions in a polymer matrix of refractive index 1.5, with a filling factor $f_i = 51.5$ vol%. Only the real component is considered. These effective refractive indexes are then averaged over the whole considered spectral range (from a wavelength of 350 to 2500 nm). The corresponding diagrams are represented in **Figure 89a** and **Figure 89b** respectively.

For low frequencies (below the orange dashed line), that is for high wavelengths, the dispersion relation giving the frequency ω as a function of the wavevector k is linear. We can thus write:

$$\omega = kv \qquad (3.\ 6)$$

with v the electromagnetic field group velocity inside the material. In our case, looking at **Figure 89**, this relation is correct for wavelengths longer than 1000 nm in the cold conditions, and 1064 nm in the warm conditions.

v can also be expressed relatively to the speed of light in vacuum c as:

$$v = \frac{c}{n_{eff}} \tag{3. 7}$$

with $n_{eff} \geq 1$. For these longer wavelengths, the material behavior is thus similar to a homogeneous material of refractive index n_{eff}.

When comparing the transmittance spectrum of the polymer opal composed of polymer spheres inside the homogenized interstices (plain lines of **Figure 88**) with the transmittance spectra obtained in the homogenized cases (dotted and dashed lines of **Figure 88**), if the homogenization process correctly predicts the material behavior, they should match for these high wavelengths. It can be observed in **Figure 88** that the double step homogenization process better matches with the structured case at high wavelengths, and it is particularly true in the warm case. Thus, the double step homogenization process correctly predicts the material behavior for wavelengths where the structure does not have an influence (or at least has an influence which can be modelled through a homogenization process) on the material optical properties. Thus, the bias that could be induced on the estimation of the influence of the structure by comparing the optical properties of a polymer opal composed of polymer spheres inside the homogenized interstices to these of the double-step homogenized material seems to be limited. Explaining the origin of the mismatch with the single-step homogenization process is beyond the scope of this section.

In the previous sections, the influence of the structure on the material optical properties was made by comparing the optical properties of a structured material and its homogenized counterparts modelled by an effective refractive index derived from a double-step homogenization process. We showed here that in the case of this double-step homogenization, the influence of possible effects other than the structure are limited, meaning that the differences between structured and double-step homogenized materials are only due to the material structure. The conclusions deduced from the comparisons in the previous sections are thus valid.

3.4. Non-transparent structured material (high VO_2 concentrations)

In this section, the refractive index contrast in a polymer opal photonic crystal containing VO_2 nanoparticles in the interstices will be studied, with no restriction on the maximum VO_2 concentration, as the transparency condition is removed. The system considered is a compact opal photonic crystal consisting of spheres of polymer P surrounded by a mixture of VO_2 nanoparticles in a matrix made of the same polymer P. The cell parameter is still set to $a = 500$ nm and the material thickness is $e = 13\ \mu m$.

In this case, the material refractive index contrast is defined as:

$$\Delta n = |\ \Re(n_{interstices}) - \Re(n_{spheres})\ | \tag{3. 8}$$

where $n_{interstices}$ is the effective refractive index of the opal interstices derived from the Maxwell-Garnett homogenization and $n_{spheres}$ is the refractive index of the polymer P. $\Re(z)$ is the real part of the complex number z.

From this definition and the Maxwell-Garnett homogenization model, it appears that Δn depends on the VO_2 concentration and the refractive index of the polymer P. These are the parameters of interest in this section. While the refractive index of the polymer P can range from 1.3 to 1.7, the total VO_2 concentration in the system can only range from 0 to 26 vol%. This is due to the fact that VO_2 is confined in the interstices of the compact opal photonic crystal (compacity $C = 0.74$). The maximum VO_2 concentration is reached when the interstices are filled with only VO_2, meaning $f_i = 100$ vol%, leading to $f_t = 26$ vol% (*Equation* (3. *4*)).

High refractive index contrasts lead to strong PBG [86]. We are thus looking for combinations of the polymer refractive index and VO_2 concentration leading to high refractive index contrasts. Since the VO_2 refractive index exhibits high variations with the wavelength, particularly in its warm state (see **Figure 64**) two different spectral regions will be considered. The first one considers an average VO_2 refractive index over the visible and near-IR spectral range (325 – 2500 nm), whereas the second one computes the VO_2 refractive index at the Bragg wavelength. In the first case both the influence of the polymer refractive index and total VO_2 concentration on the refractive index contrast are studied, whereas is the second case the polymer refractive index has been set to 1.3.

After a selection of the optimal polymer refractive index and total VO_2 concentration, the reflectance and transmittance spectra of the material will be computed, with a study of the impact of the structure on their integrated values over the visible and solar spectral ranges.

3.4.1. Optimization of the refractive index contrast for an average VO_2 refractive index in the visible and near infrared spectral regions (325 – 2500 nm)

First of all, the refractive index contrast is calculated when considering a VO_2 refractive index averaged over the whole visible and near infrared regions. **Figure 90** is a 3D plot of Δn for different total VO_2 concentrations f_t and polymer refractive indexes in their respective ranges specified above, in the cold (**Figure 90a**) and warm (**Figure 90b**) conditions.

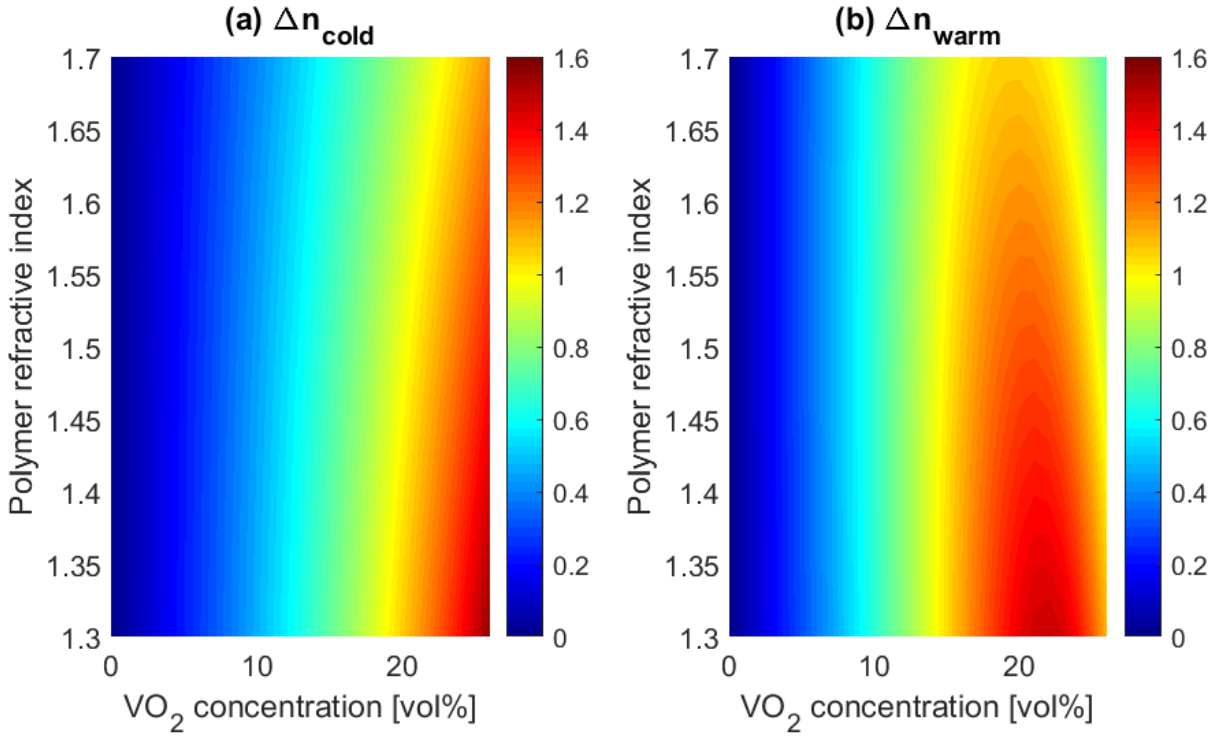

Figure 90: Contrast in refractive index between the spheres and the surrounding material, as a function of the total VO_2 concentration f_t and polymer refractive index, in cold (a) and warm (b) state, in the case where the VO_2 refractive index is averaged over wavelengths from 325 to 2500 nm.

It appears that in the cold condition, a maximum value of $\Delta n \approx 1.6$ is obtained for high VO_2 concentrations ($f_t = 26$ vol%) and low polymer refractive index. This means that an opal photonic crystal consisting of a polymer of refractive index $n = 1.3$ surrounded by pure VO_2 material has a relatively high Δn at low temperature. This result is explained by the high average value of the VO_2 refractive index in cold conditions ($n(VO_2(M)) \approx 3$) being higher than the refractive index of the polymer P ($n(P) = 1.3$). So higher VO_2 concentrations lead to an increase of the effective refractive index used to model the opal interstices, thus increasing its difference with the spheres refractive index $n(P)$, which thus has to be as small as possible ($n(P) = 1.3$). As the VO_2 concentration decreases or as the polymer refractive index increases, Δn progressively decreases.

For the warm condition, the maximum value of Δn is also reached at low polymer refractive index, but at a slightly lower VO_2 concentration ($f_t = 22$ vol%). Δn progressively decreases around this peak.

These results give a first estimate of the variations of Δn as a function of both VO_2 concentration and polymer refractive index.

However, as the VO_2 refractive index exhibits high variations with the wavelength, it could be interesting to compute Δn specifically at the PBG position rather than with an average of the VO_2 refractive index over a large spectral region.

3.4.2. Optimization of the refractive index contrast at Bragg wavelength

Instead of averaging the VO_2 refractive index in a large spectral region, in this section Δn is calculated at the specific Bragg wavelength λ_{Bragg}, given by Bragg's law (*Equation (1. 38)*). This wavelength gives

the position of the bandgap. Maximizing Δn at this particular wavelength leads to a maximum PBG effect in the material. Since λ_{Bragg} varies as a function of the materials refractive indexes, it has to be recalculated e every time the VO_2 concentration or the polymer refractive index varies. Since in the previous case Δn was always maximum when the polymer refractive index was low, we decided to set the polymer refractive index to $n(P) = 1.3$ here, so that the only remaining parameter is the total VO_2 concentration.

λ_{Bragg} is first calculated using *Equation (1. 38)*, as a function of the total VO_2 concentration, with a normally incident light. Since λ_{Bragg} is a real number, only the real part of the material effective refractive index n_{eff} is considered for the calculation. Moreover, since n_{eff} itself depends on the considered wavelength for dispersive materials like VO_2, an average of n_{eff} is performed over the whole spectral range from 325 to 2500 nm. n_{eff} is thus obtained as the spectral average of the real part of the effective refractive index derived from the Maxwell-Garnett approximation. This averaging may lead to small inaccuracies but still allows to calculate a good approximate value of λ_{Bragg}. λ_{Bragg} as a function of the VO_2 concentration in both cold and warm conditions, with a normally incident light, is represented in **Figure 91, top**. As mentioned previously, the opal cell parameter is $a = 500$ nm.

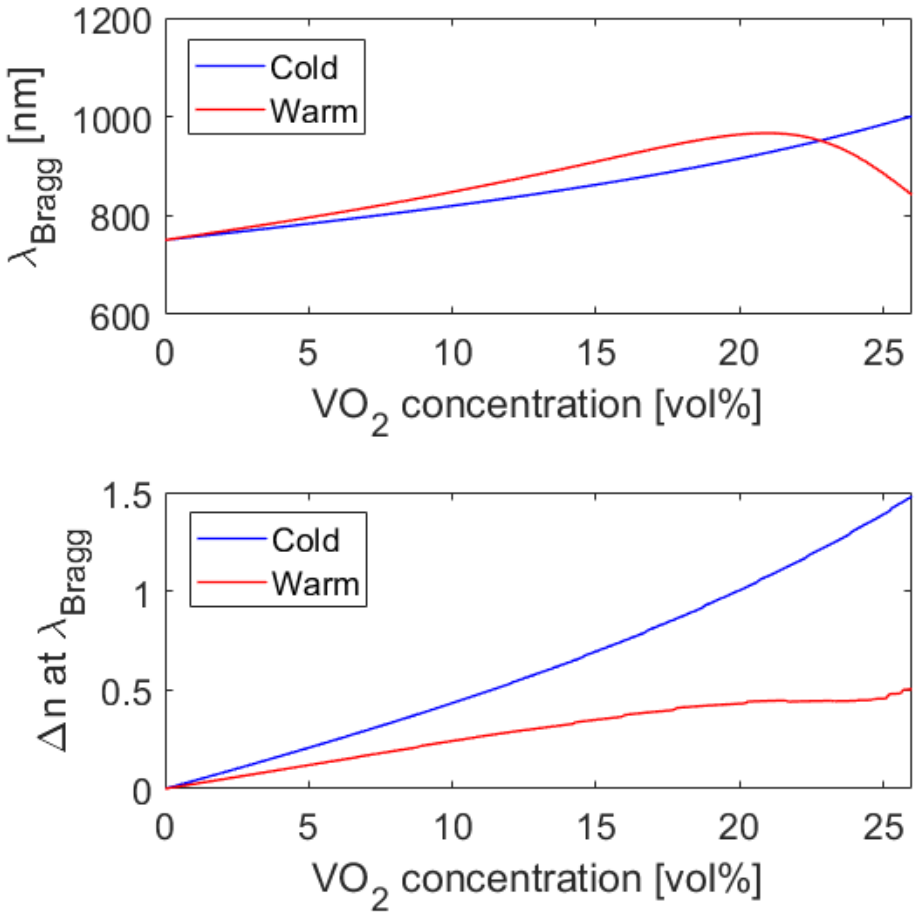

Figure 91: Bragg wavelength λ_{Bragg} (top) and refractive index contrast Δn at the Bragg wavelength (bottom) at normal incidence vs the total VO_2 concentration f_t in a compact opal photonic crystal (cell parameter $a = 500$ nm) with polymer spheres (n=1.3) surrounded by a mixture of VO_2 nanoparticles and the same polymer, in both VO_2 cold and warm states.

For the considered system, λ_{Bragg} varies in the near infrared region in both cold and warm conditions, and redshifts for increasing VO_2 concentrations due to an increase of n_{eff} for higher VO_2

concentrations (in this spectral region the VO_2 refractive index is higher than the polymer refractive index $n(P) = 1.3$).

The refractive index contrast is calculated at this Bragg wavelength for the different total VO_2 concentrations using *Equation* (1. *38*). Results are presented in **Figure 91, bottom**. It appears that for this system, Δn at λ_{Bragg} in both cold and warm conditions increases with increasing VO_2 concentrations, and that at λ_{Bragg}, Δn is higher in the cold condition than in the warm condition. It can also be noticed that in the warm condition the growth of Δn with f_t slows down for total VO_2 concentrations higher than 20 vol%.

For example, with $n(P) = 1.3$ and $f_t = 18$ vol%, we have:

$$\Delta n_{warm} = 0.41 \qquad \text{while} \qquad \Delta n_{cold} = 0.87 \tag{3. 9}$$

In this case, $\Delta n_{warm} < \Delta n_{cold}$. This should result in a stronger PBG effect in the cold than in the warm condition. This assumption will be confirmed in the following section by computing the spectral reflectance and transmittance of the corresponding polymer opal.

3.4.3. Impact of the material structure on the reflectance and transmittance spectra

The spectral reflectance and transmittance of a compact opal polymer consisting of polymer spheres with a refractive index $n(P) = 1.3$ surrounded by a mixture of VO_2 nanoparticles with a volume fraction $f_i = 69.2$ vol% (corresponding to a total VO_2 concentration $f_t = 18$ vol%) in a matrix made of the same polymer have been calculated in both cold and warm conditions. The light is normally incident on the material surface. Results are presented in **Figure 92a** and **Figure 92b**. Under the specified conditions (materials refractive indexes, structural parameters and illumination conditions), Bragg's law predicts 892.7 nm in cold conditions, and 946.6 nm in warm conditions, which corresponds to the reflectance peaks observed in **Figure 92a**. The observed peaks are due to PBG effects and their amplitudes and widths are related to the refractive index contrasts calculated above. As expected, the reflectance peak related to a PBG effect is bigger in the cold than in the warm conditions. Around this PBG wavelength position, the material is completely non-transparent ($T(\lambda) = 0$) so the PBG effect cannot be seen on the transmittance spectra (**Figure 92b**).

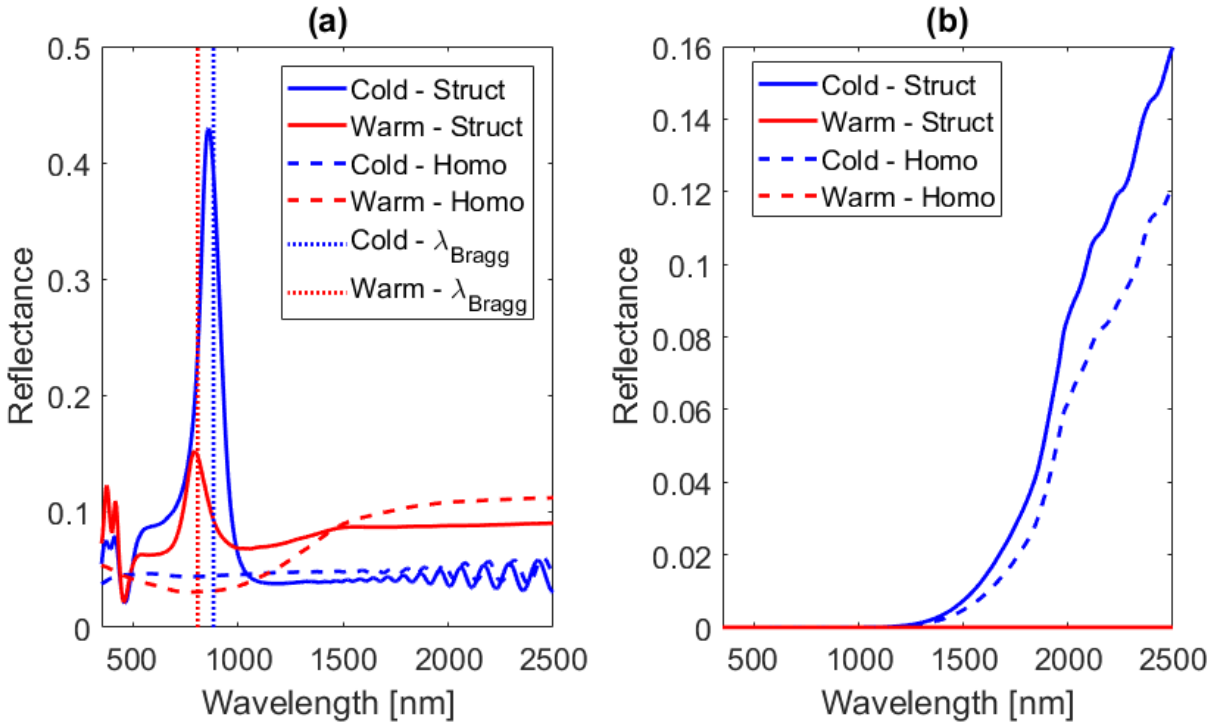

Figure 92: Normal incidence reflectance (a) and transmittance (b) spectra of a compact opal photonic crystal with polymer spheres (n=1.3) surrounded by a mixture of VO_2 nanoparticles and the same polymer (solid lines), and its homogenized counterpart (dashed lines), in both VO_2 cold and warm states. The corresponding calculated Bragg wavelength λ_{Bragg} is also represented in dotted lines. The total VO_2 concentration is $f_t = 18$ vol%.

A two-step Maxwell-Garnett homogenization process is performed on the material and for this homogenized layer, the spectral reflectance and transmittance properties are also calculated and presented as dashed lines in **Figure 92a** and **Figure 92b**. Dashed curves behave quite similar to their respective solid curves, except around the PBG peak which is not present in the homogenized material. Since the material is not transparent in this case, calculating the usual integrated values T_{lum} and T_{sol} does not really make sense here as they would be very close to zero. It may be more interesting to instead calculate the equivalent R_{lum} and R_{sol} defined similarly to T_{lum} and T_{sol}, as:

$$R_{lum} = \frac{\int_{380nm}^{780nm} V(\lambda)\, R(\lambda)\, d\lambda}{\int_{380nm}^{780nm} V(\lambda)\, d\lambda} \quad \text{and} \quad R_{sol} = \frac{\int_{350nm}^{2500nm} E_{\lambda}^{AM1.5}(\lambda)\, R(\lambda)\, d\lambda}{\int_{350nm}^{2500nm} E_{\lambda}^{AM1.5}(\lambda)\, d\lambda}, \qquad (3.\ 10)$$

with $R(\lambda)$ the material spectral reflectance, $V(\lambda)$ the CIE photopic luminosity function [14] and $E_{\lambda}^{AM1.5}(\lambda)$ the global AM1.5 spectral solar irradiance extracted from [13] (cf *Equations* (1. *19*) and (1. *21*)). We also define the luminous and solar reflectance modulations as:

$$\Delta R_{lum} = R_{lum,cold} - R_{lum,warm} \quad \text{and} \quad \Delta R_{sol} = R_{sol,cold} - R_{sol,warm} \qquad (3.\ 11)$$

Using these definitions, we obtain for this system the integrated values presented in **Table 9.**

	R_{lum}		R_{sol}		ΔR_{lum}	ΔR_{sol}
	Cold	**Warm**	**Cold**	**Warm**		
Structured	0.08	0.06	0.11	0.08	0.02	0.03
Homogenized	0.05	0.04	0.05	0.05	0.01	0

Table 9: Luminous and solar reflectances, in both VO_2 states, and their modulations, for normally incident light, of a polymer opal (n=1.3) loaded with f_t = 18 vol% VO_2 nanoparticles, and its homogenized counterpart.

Considering the position of the PBG peak in the near infrared region, R_{sol} is mostly impacted by the material structure, especially in the cold condition with an increase from 0.05 to 0.11 due to the PBG peak. The same observation is made in the warm condition with a smaller PBG peak, leading to an increase of the solar reflectance from 0.05 to 0.08. These variations lead to an increase of the solar reflectance modulation ΔR_{sol} from 0 to 0.03. For the luminous reflectance, smaller variations are observed as the reflectance increase due to the PBG starts at the edge of the visible spectral region. A similar behavior is thus observed for R_{lum} with a small increase brought by the material structure, mostly in the cold condition, resulting in a small increase of ΔR_{lum} from 0.01 to 0.02.

3.5. Conclusion of this chapter

In this chapter, the transmittance properties of a polymer opal photonic crystal containing VO_2 nanoparticles in the opal interstices were calculated in the visible and near infrared spectral regions. Luminous and solar transmittances were used to quantify the performances of such material for applications like energy efficient coating for windows. The influence of structural parameters on these integrated transmittance values was studied. This parametric study showed that a polymer opal photonic crystal consisting of polymer spheres of refractive index 1.3 surrounded by a mixture of VO_2 nanoparticles and that same polymer, with a total VO_2 concentration of 1 vol% and a total material thickness of 13 µm, seems promising for such applications. In this case, $T_{lum}^{cold} = 0.59$ and $\Delta T_{sol} = 0.28$, comparable with values obtained in the literature [3,7,8,55,56]. However, the transparency requirement related to the window coating application limits the range of VO_2 concentrations. Under these conditions, the impact of ordering is very limited. Removing this transparency condition enables situations where the PBG becomes stronger. For example, for a total VO_2 concentration of 18 vol%, the material is not transparent anymore. We are thus interested in the reflectance properties instead. In this case, the structure has a stronger impact on the material reflectance properties, with a 46% increase of R_{lum}^{cold} (from 0.05 to 0.08) and 50% increase of R_{lum}^{warm} (from 0.04 to 0.06). An increase of ΔR_{sol} is also observed from 0 to 0.03.

VO_2 is interesting for other applications which do not require transparent materials as camouflage or energy efficient coatings for buildings. The main parameter which has to be considered for these applications is the material mid-infrared emissivity. The next chapter will thus be dedicated to the optical properties of a polymer opal containing VO_2 nanoparticles in the mid-infrared spectral range.

Chapter 4 – Optical properties of a nanostructured thermochromic coating in the mid-infrared spectral region

In the previous chapter, the optical behavior of a polymer opal photonic crystal loaded with thermochromic VO_2 nanoparticles was studied in the visible and near infrared spectral regions. In this chapter the focus is made on the mid-infrared (mid-IR) region where the refractive index contrast in the material is larger, which should lead to a stronger PBG effect caused by the photonic crystal. The PBG effect will result in an increased reflectance in the mid-IR and thus in a decreased emissivity ϵ, and eventually in a decreased material surface temperature (see *Equation (1. 30)*). This smaller ϵ is desired in warm conditions for applications like camouflage (see **Section 1.2.2.3**), while it is desired in cold conditions for applications such as energy-efficient coatings for buildings and satellites (see **Section 1.2.3.2**). It may thus be interesting to increase the PBG effect in either cold or warm conditions, depending on the target application. In this chapter the material structural parameters will be adjusted in order to maximize the PBG impact on the material emissivity. The same material as in the previous chapter will be modelled, but all values for the structural parameters will be reset.

4.1. Preliminary study: setting the material parameters

4.1.1. Cell parameter for a PBG in the mid-IR region

The first step of this study is to choose the right PBG position in order to produce a maximum impact on the material emissivity. For applications as energy-efficient coating for buildings and satellites, an increased infrared reflectance is desired in the cold conditions, so this study is focused on the cold conditions.

According to the definition of ϵ (*Equation (1. 29)*), changing the material reflectance around the position of the blackbody emittance peak will influence the most ϵ. It is thus interesting to shift the PBG position to the position of this blackbody emittance peak. In order to find the right parameters leading to a superposition of these peaks, two laws will be combined in this section. On one hand, Bragg's law predicts the position of the reflectance peak λ_{Bragg} as a function of the d_{111} structural parameter (the spacing between the opal (111) planes):

$$\lambda_{Bragg} = 2\, d_{111} \sqrt{n_{eff}^2 - \sin^2 \theta_{inc}} \qquad (4.\ 1)$$

with n_{eff} the material effective refractive index and θ_{inc} the incidence angle with respect to the normal to the material surface. On the other hand, Wien's law predicts the position of the blackbody emittance peak λ_{Wien} as a function of the body temperature τ:

$$\lambda_{Wien} = \frac{2.89777291\,.10^{-3}}{\tau} \qquad (4.\ 2)$$

where the constant $2.89777291\,.10^{-3}$ is expressed is m.K. The superposition of these peaks means that λ_{Bragg} is equal to λ_{Wien}. Combining *Equations* (4. *1*) and (4. *2*), at normal incidence, this leads to a cell parameter of:

$$a = \frac{\sqrt{3}}{2} \times \frac{2.89777291.10^{-3}}{\tau \times n_{eff}} \quad (4.\ 3)$$

by using the relationship between a and d_{111} given by *Equation* (2. *1*). As a first approximation, we consider a polymer opal photonic crystal consisting of polymer spheres with a refractive index $n = 1.3$ surrounded by pure VO_2 material in cold conditions. For such material, the effective refractive index n_{eff} is calculated using a Maxwell-Garnett approximation and a single-step homogenization process considering polymer spheres inclusions in a matrix of pure VO_2. Keeping in mind that n_{eff} depends on the wavelength, we calculate it at $\lambda = \lambda_{Wien}$ where the two peaks are being superposed. For the material temperature, we use here the approximate temperature of the VO_2 phase transition $\tau = 70°C$. According to *Equation (4. 2),* this leads to $\lambda_{Wien} = 8.44$ µm. Using *Equation* (4. *3*), these parameters values result in a cell parameter of $a = 4.5$ µm. This value for the cell parameter will be used in this chapter in order to generate a reflectance peak in the mid-IR spectral region, where the influence on ϵ is maximum at the considered temperatures.

4.1.2. Setting the spheres refractive index

Once the PBG position is set, it is now interesting to maximize the refractive index contrast between the spheres and the interstices at this specific wavelength in order to maximize the PBG effect. In this section, the refractive indexes of the polymers composing the spheres (P_s) and the inclusions (P_i) will be set regarding this objective.

Considering that the only material present alongside the polymers is VO_2, we take a look at its refractive index. The real part of its refractive index in both cold and warm conditions is given in **Figure 93**. These mid-IR VO_2 refractive indexes are extracted from [6] and gathered with the visible and near infrared VO_2 refractive index extracted from [7], both measured on VO_2 films.

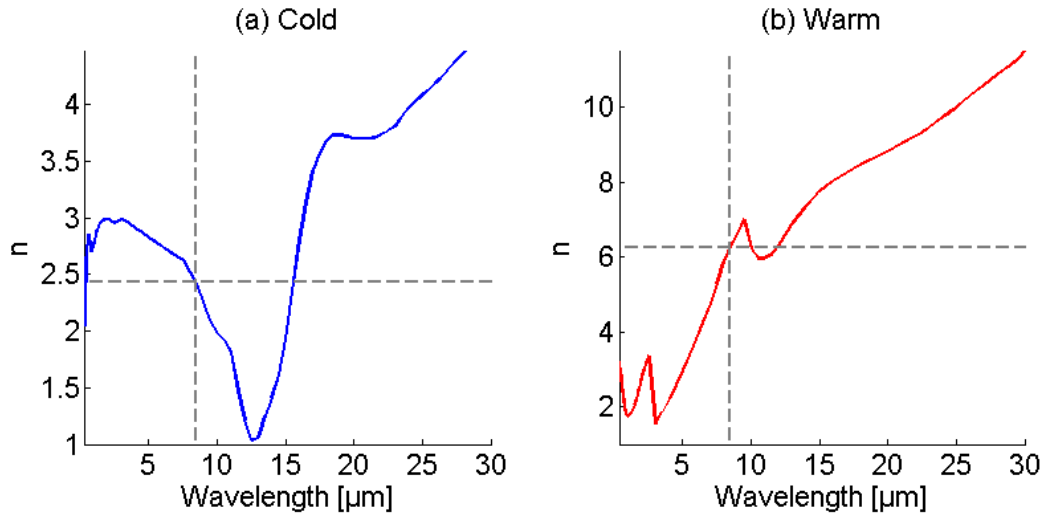

Figure 93: Real part of the refractive index of VO_2 in cold (a) and warm (b) conditions. Dashed lines indicate these indexes at a 8.44 µm wavelength. These values are extracted from [6,7].

At the PBG position calculated earlier ($\lambda = 8.44$ µm), the real part of the VO_2 refractive index is equal to 2.5 in cold conditions and 6.1 in warm conditions. Both of these values are higher than the range for common polymers refractive indexes (from 1.3 to 1.7), meaning that in order to maximize the refractive index contrast, the refractive index of the opal interstices where the VO_2 is located should

be maximized while the spheres refractive index should be minimized. Based on this assumption, we set the refractive indexes of the polymer spheres to $n(P_s) = 1.3$. For the polymer in the interstices, it can be set to $n(P_i) = 1.7$, but the maximum refractive index contrast in this system would be reached when the whole interstitial spaces are filled with pure VO_2 material.

4.2. Optical modelling of the nanostructured material

In this section, the spectral reflectance of an opal photonic crystal loaded with VO_2 nanoparticles is calculated and used to obtain the material emissivity in both cold and warm conditions. Keeping in mind that the main goal is to maximize the PBG effect in the material, the influence of parameters such as the VO_2 concentration and material thickness is studied. For the first studies, the material thickness is set to 117 µm. This value comes from 15 periods of the opal structure in the [111] direction, which is the same number of periods as in Chapter 3, with a cell parameter of $a = 4.5$ µm.

4.2.1. Setting the spatial resolution

As explained previously in Chapter 3, the model uses an FMM method combined with a staircase approximation. It is again required to optimize the spatial resolution in the [111] direction considering both computation time and correct modelling of the sphere shapes. For this study, the interstices are completely filled with vanadium dioxide and the spheres size is set so that the opal structure is compact (compacity $C = 0.74$). With $a = 4.5\ \mu m$, this results in a spheres diameter of 3.18 µm (*Equation* (3. *1*)).

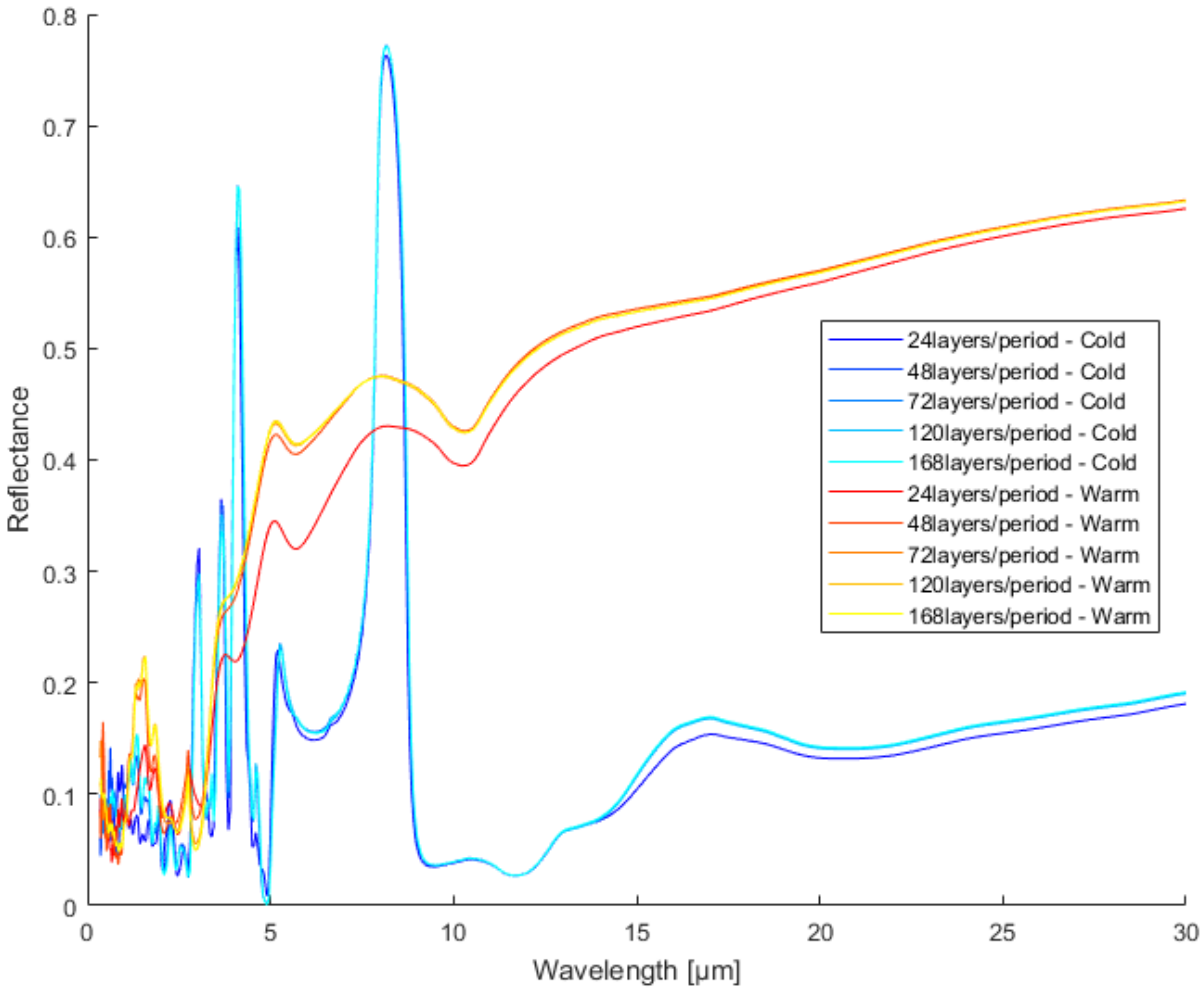

Figure 94: Reflectance spectra for normally incident light of an opal made of polymer spheres (n=1.3) surrounded by VO_2 in both cold and warm conditions, as a function of the model spatial resolution along the axis normal to the surface ([111] direction).

In order to determine if the same spatial resolution as in the previous chapter should be kept (24 layers were used to model one period along the [111] direction), models having 48, 72, 120 and 168 layers/period were considered and used to calculate the material spectral reflectance for normally incident light. Results are shown in **Figure 94**. A visible difference is observed on the reflectance spectra associated with 24 and 48 layers/period. Note that the PBG peak (rightmost peak) is observed in the cold conditions. The position of this peak (8.2 µm) is comparable to the predicted position of 8.44 µm. For the warm conditions, such a large reflectance peak does not appear. To understand why, Bragg's law was used to estimate the peak position, based on the real part of the refractive index of the warm metallic VO_2 ($n = 6.1$). In the [111] direction, this peak should be around a wavelength of 15.3 µm. At this wavelength, no reflectance peak is observed in **Figure 94**. This is possibly due to the high absorption coefficient of the metallic VO_2 warm phase (see **Figure 10**).

To quantify the differences between each of these curves compared to the curve obtained when the resolution is the highest, we compute, as previously explained in Chapter 3 (*Equation* (3. *5*)), the normalized root mean square of the difference between the considered reflectance spectrum and the reflectance spectrum for 168 layers/period. **Figure 95** is a representation of this root mean square difference as a function of the spatial resolution in both cold and warm conditions.

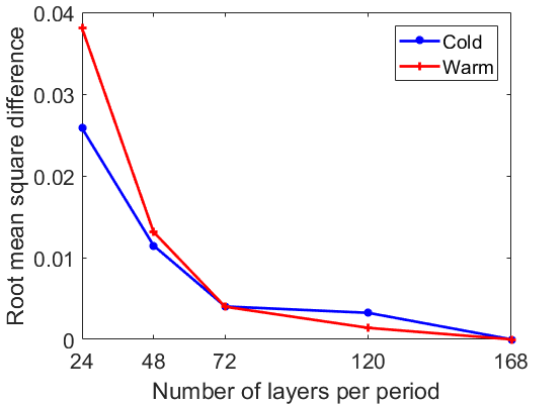

Figure 95: Root mean square difference compared to our finest model (168 layers/period), as a function of the model spatial resolution along the axis normal to the surface ([111] direction), for both cold and warm conditions.

As the model becomes finer, which means the spheres are more spherical, the material optical properties converge towards the values obtained in our finest model. The root mean square difference quickly decreases as the number of layers used to describe a period in the direction normal to the surface ([111] direction) increases from 24 layers/period to 72 layers/period. It is below 0.01 for cold and warm conditions when 72 stacked layers are used to model a period. From there, the root mean square difference decreases more slightly. It seems thus acceptable to use a model with at least 72 layers to describe a period. We decide from here to use a resolution of 120 layers/period in the [111] direction.

4.2.2. Setting the material thickness

Now that the model spatial resolution is set, the next parameter to consider is the material thickness. In this section, the same system is used: a compact opal photonic crystal consisting of polymer spheres with a refractive index $n = 1.3$ surrounded by pure VO_2 material. The light is injected along the [111] crystallographic direction, normal to the material surface. The material thickness is thus defined as the number of periods along this [111] direction times the thickness of a single period, which is equal to $3\ d_{111} = a\sqrt{3}$. For this study, five values are considered for the number of periods: 1, 3, 5, 7 and 15. These correspond to a material thickness of respectively 7.79 µm, 23.4 µm, 39 µm, 54.6 µm and 117 µm. Spectral reflectances are calculated for each of these cases, in both cold and warm conditions, and results are presented in **Figure 96**.

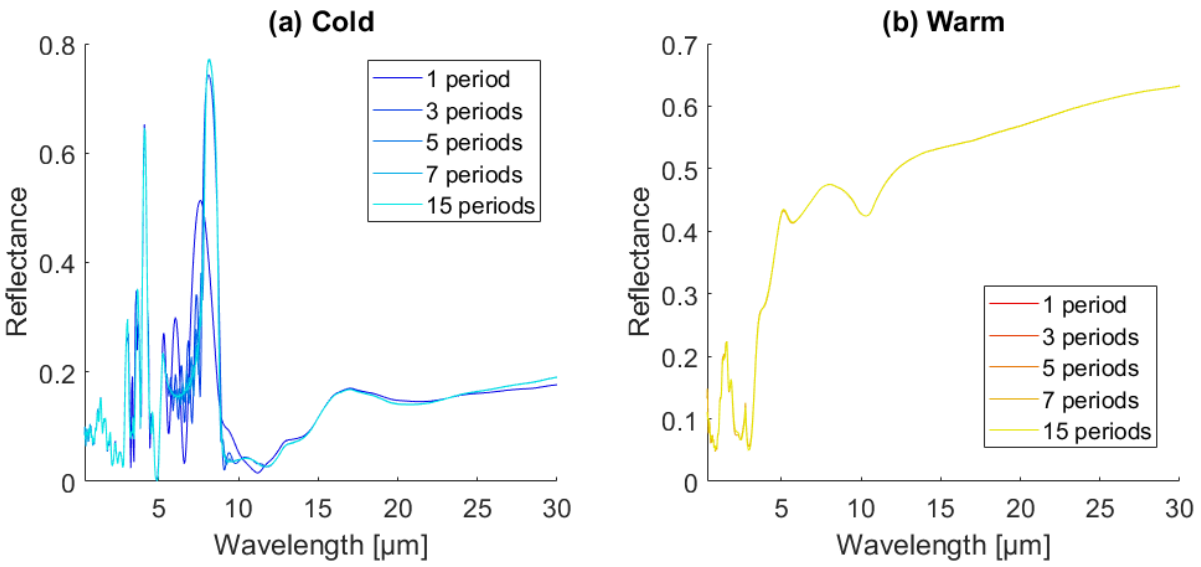

Figure 96: Reflectance spectra of a compact opal photonic crystal consisting of polymer spheres (n=1.3) surrounded by pure VO_2 material in cold (a) and warm (b) conditions, at normal incidence, for different numbers of periods in the direction normal to the material surface ([111] direction).

In the cold conditions (**Figure 96a**), the main variation of the spectral reflectance due to a variation of the number of periods along the [111] direction (and thus the material thickness) is observed at the PBG peak. In the case of a single period, the crystal is not rigorously periodic in all three directions anymore. The PBG peak remains but its amplitude is limited. As the number of periods increases, the optical behavior of the material should get closer to the behavior of an infinite crystal which has a perfect photonic bandgap (no light entering the material, which corresponds to a value of 1 for the reflectance). The closer to this infinite crystal the material gets, the more well-defined the PBG becomes, with a maximum reflectance amplitude. However, in this case, except for the case of a single period, the reflectance variations related to variations of the number of periods are limited. This may be due to the fact that the irradiance decreases as the light travels through the deeper layers. Indeed, using Equation (1. *13*) and the extinction coefficient of the homogenized layer modelled by an effective refractive index derived from a Maxwell-Garnett approximation considering the polymer ($n = 1.3$) inclusions surrounded by a pure VO_2 matrix in cold conditions, around an 8 µm wavelength (near the PBG peak position), about 74% of the incident irradiance reaches the bottom of the first period. While 41% reaches the bottom of the third period, only 23% of it remains after propagating through 5 periods.

This effect is clearly observed in the warm conditions (**Figure 96b**) as the light barely goes inside the material because of the highly absorbing metallic VO_2. In this case, all reflectance spectra are very alike for each number of periods. From this study, we could model a very thin material with for example three periods along the [111] direction, as the reflectance spectra barely changes with higher number of periods. However, we would like to later consider lower VO_2 concentrations. Reducing the VO_2 concentration may lead to a more transparent material, meaning that the light would then be able to reach deeper layers, thus increasing the influence of these deeper layers. A higher number of periods may then be required.

We decide to perform the same study at a lower VO_2 concentration, for example $f_t = 1$ vol% as it was the concentration used in Chapter 3. Spectral reflectances are calculated once again for the same considered numbers of periods along the [111] direction. Results are presented in **Figure 97** where small arrows indicate the height of the PBG peak for each curve. The labelled number indicate the number of periods.

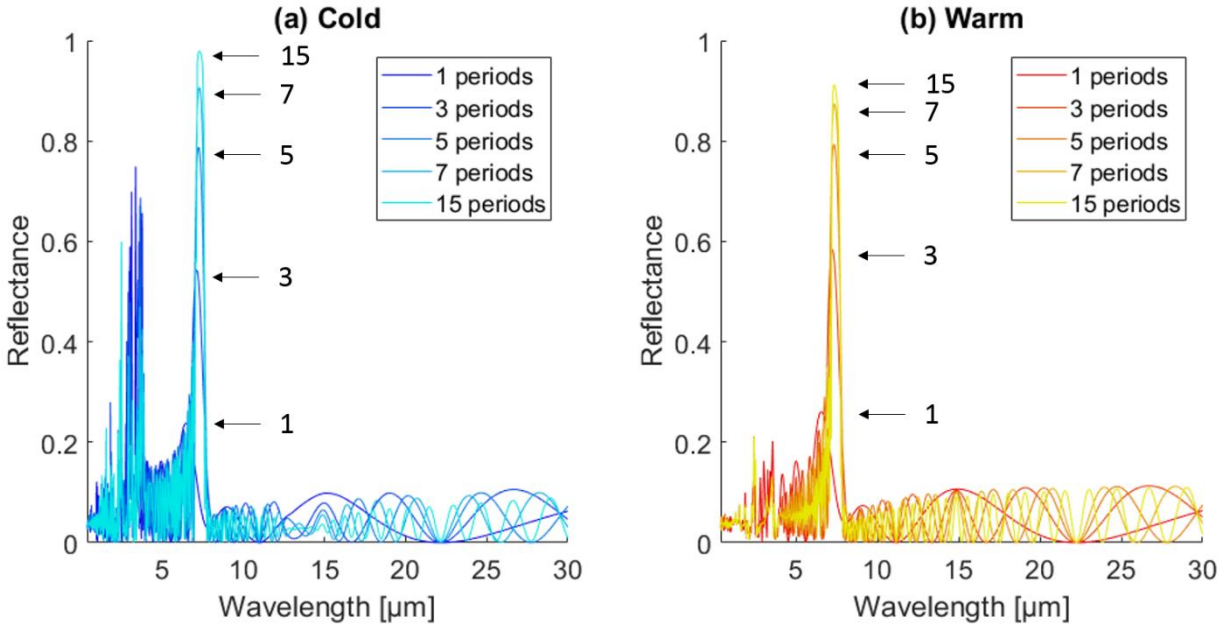

Figure 97: Reflectance spectra of a compact opal photonic crystal consisting of polymer spheres (n=1.3) surrounded by a mixture of VO_2 nanoparticles and another polymer (n=1.7) in cold (a) and warm (b) conditions, at normal incidence, for different number of periods in the direction normal to the material surface ([111] direction). The total VO_2 concentration is set to $f_t = 1$ vol%. Arrows indicate the height of the PBG peak for each number of periods.

Unlike the previous case (VO_2 concentration of $f_t = 26$ vol%), the case $f_t = 1$ vol% presented here shows that the PBG peak keeps increasing when the number of periods in the [111] direction increases from 1 to 15, in both cold and warm conditions. This is due to the light reaching deeper layers and thus letting them have an influence on the material reflectance properties. For the future simulations, in order to correctly model the optical behavior of this opal photonic crystal, we decide to use 15 periods along the [111] direction, which represent a total material thickness of 117 µm.

It is worth noting the appearance of oscillations in all reflectance spectra presented in **Figure 97**, which were not visible in **Figure 96**. These oscillations, mostly visible at longer wavelengths (from about 10 to 30 µm) are due to thin film interferences and appear here because the material is now transparent. Their frequency depends on the material thickness: thicker materials generate oscillations with a higher frequency. This is observed here with increasing number of periods leading to oscillations having higher frequencies (see *Equation* (5. *10*)). For these calculations, two different steps in wavelength are used in order to discretize these oscillations: in the visible and mid infrared regions ($\lambda < 2500$ nm), a 5 nm step is used, while it is set to 50 nm in the mid infrared region ($\lambda \geq 2500$ nm).

4.2.3. Influence of the VO_2 concentration

In this section, the influence of the total VO_2 concentration on the material optical and thermal properties is studied. This study will be split into two parts (see **Figure 98**): the first one will consider higher concentrations due to opal interstices completely filled with pure VO_2 material. The VO_2 total concentration will then be increased by reducing the opal spheres size, leading thus to a non-compact opal. The second part will then consider lower VO_2 concentrations, in a compact opal. These lower VO_2 concentrations are obtained by introducing another polymer in the interstices. As announced earlier

in the section related to the polymer refractive indexes (4.1.2), the refractive index of this polymer in the interstices is set to $n(P_i) = 1.7$.

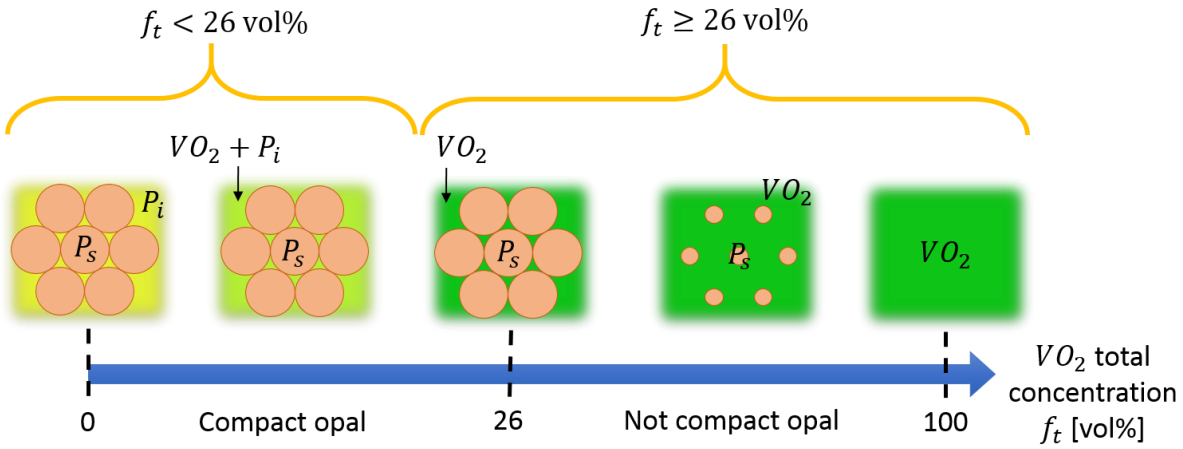

Figure 98: Schematic representation of the considered systems in the study of the influence of VO_2 total concentration.

4.2.3.1. High VO_2 concentrations (≥ 26 vol%)

In this first part, the opal interstices are filled with pure VO_2. From the compact opal structure containing 26 vol% of VO_2, the opal spheres size is reduced in order to allow higher VO_2 concentrations. Four cases are considered with concentrations from 26 to 99 vol%. These cases and their parameters (spheres size, cell parameter a, structure compacity C, VO_2 concentration f_t) are illustrated in **Figure 99**.

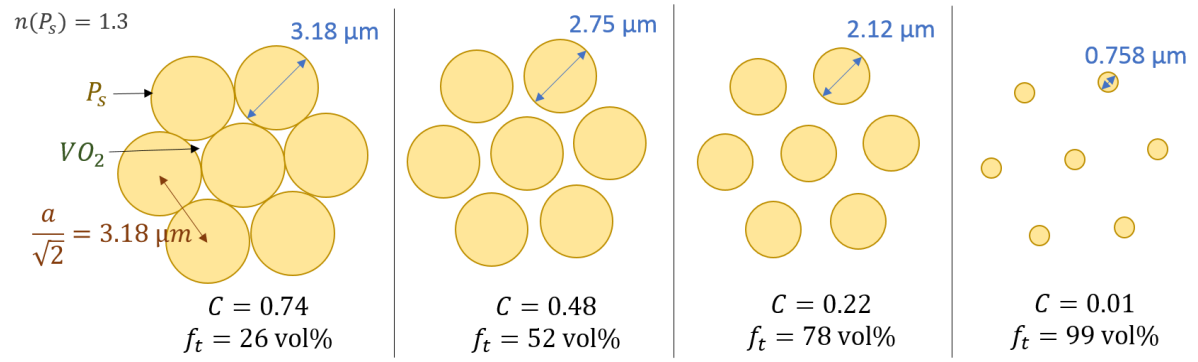

Figure 99: Top views of a (111) plane of opal photonic crystals consisting of polymer spheres of refractive index 1.3 surrounded by pure VO_2, with different total VO_2 concentrations f_t. The corresponding sphere sizes and compacities C are also shown.

Optical properties and performances of the material

Spectral reflectances are calculated in the four considered cases and results are shown in **Figure 100** for a normally incident light in both cold and warm conditions. The compact structure is shown in dark blue in the cold conditions and red in the warm conditions. Lighter colors refer to smaller spheres, and thus higher VO_2 concentrations.

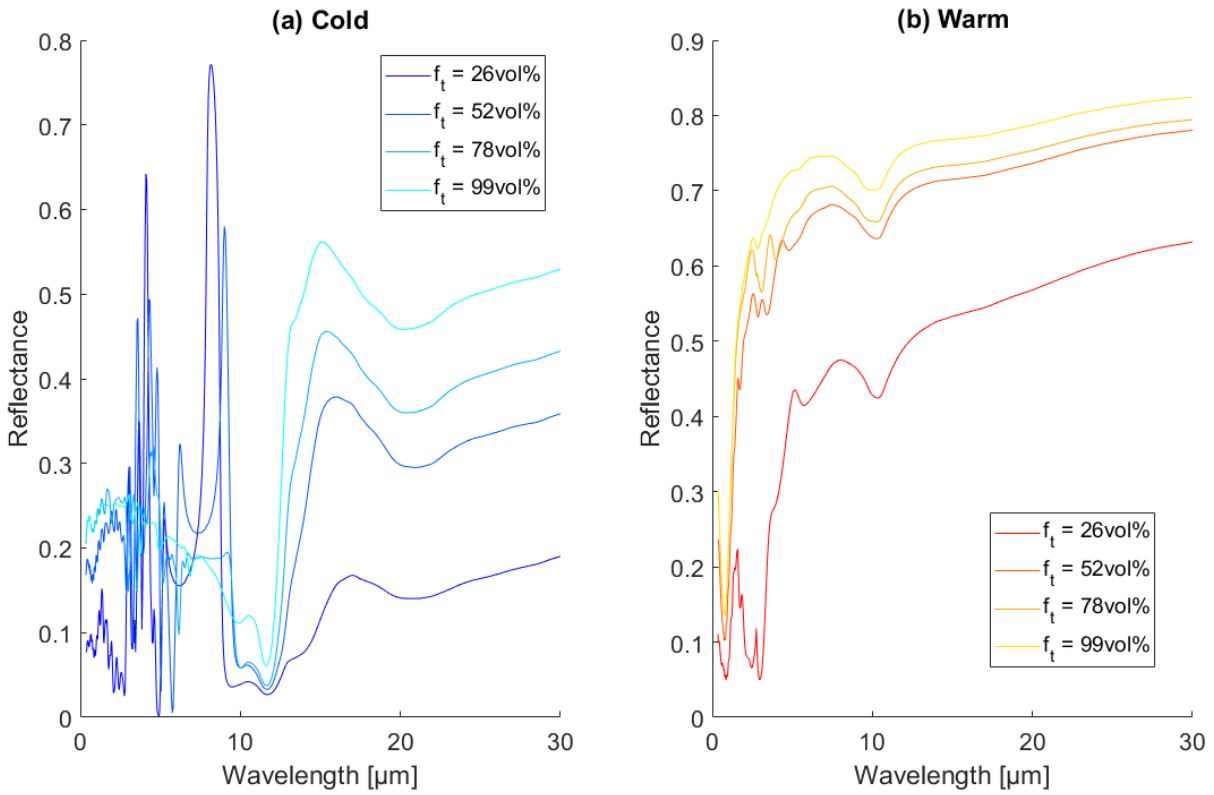

Figure 100: Reflectance spectra of a polymer opal photonic crystal consisting of polymer spheres (n=1.3) surrounded by VO_2 with a cell parameter a=4.5 µm, at normal incidence, in both cold (a) and warm (b) conditions, as a function of the total VO_2 concentration f_t from 26 vol% to 99 vol%.

As a global observation, the spectral reflectance for both cold and warm conditions decreases with decreasing VO_2 concentrations. This is due to the high reflectivity of VO_2 in its warm metallic state (high extinction coefficient, see **Figure 10**). This explanation is applicable also for the cold state, for wavelengths higher than 12 µm, where the VO_2 cold state refractive index has a high imaginary part. In the warm conditions, no PBG effect is observed due to a highly absorbing material. Indeed, using *Equation (1. 13)* in the case having the lowest VO_2 concentration ($f_t = 26$ vol%) around the PBG peak estimated using Bragg's law (*Equation* (1. *38*)) ($\lambda_{Bragg} = 11.2$ µm), the irradiance is ten times reduced after a propagation of 740 nm inside the material. Since one period is over 7 µm thick, this means that almost no light reaches this depth. The structure has thus no influence on the material optical properties.

In the cold condition, the PBG peak is clearly influenced by the VO_2 concentration. First, a displacement of the peak is observed, with a redshift when the VO_2 concentration increases. This is due to the change of the material effective refractive index. Indeed, with increasing VO_2 concentrations, the material effective refractive index increases, as the semiconducting VO_2 refractive index real part is higher than the polymer refractive index around the PBG position. According to Bragg's law, higher effective refractive indexes lead to a peak shifting towards longer wavelengths. This is observed here. For example, the reflectance peak is observed at a wavelength of 8.2 µm when the VO_2 concentration is 26 vol%, while it shifts to 9 µm when the VO_2 concentration doubles to 52 vol%.

In the cold condition, the PBG peak intensity also decreases as the VO_2 concentration increases. This is due partly to the increased material absorption with the VO_2 concentration. This absorption effect is relatively limited as the semiconducting VO_2 extinction coefficient around this spectral region is around 0.08. This leads to a light intensity reaching the other end of the material in the order of 10^{-7}.

At the same time, as it was explained in the previous chapter, when the polymer spheres get smaller, the material is more likely to be seen as homogeneous by the incoming light, thus leading to a reduced impact of the structure. The PBG effect is thus reduced as the structure compacity decreases. In order to maximize the PBG effect, it is thus more interesting to consider a compact structure.

Regarding the coating performances for the considered applications, values such as material emissivity and surface temperatures were calculated for these systems. For example, an energy-efficient coating for buildings and satellites requires a low emissivity modulation $\Delta\epsilon$ defined as the emissivity difference between cold and warm conditions (*Equation* (1. *33*)).

In order to solve the thermal balance and obtain the material surface temperature T_{surf}, both solar reflectance R_{sol} and material emissivity ϵ are required (see *Equation* (1. *30*)). These parameters are calculated from the material spectral reflectance through a weighted integration over the solar spectral irradiance and the blackbody spectral emittance, respectively *Equations (1. 19)* and (1. *29*). **Figure 101** presents the evolution of R_{sol}, ϵ and T_{surf} as a function of the total VO_2 concentration in both cold and warm conditions. T_{surf} is computed considering *Equation (1. 30)* corresponding to a horizontal surface illuminated by the sun, with an ambient air temperature of 25 °C, a sky temperature of 11 °C and a convection coefficient of 5 W/(m².K). The material is thus heated only by the sun light. The purpose is here to estimate what would be the temperature of a surface in these conditions if this surface had the same optical properties (i.e. same R_{sol} and ϵ) as our polymer opal composite either in its cold or warm phase. In particular, no compatibility of the surface temperature with the VO_2 state is taken into account: for example, the surface temperature could be lower than 68 °C and the material supposed to be in its warm state. The best thermal performance for an energy efficient coating is thus obtained with the highest possible T_{surf} in the cold state and the lowest possible T_{surf} in the warm state.

The modulations of R_{sol}, ϵ and T_{surf} are defined as:

$$\Delta R_{sol} = R_{sol,cold} - R_{sol,warm} \tag{4. 4}$$

$$\Delta\epsilon = \epsilon_{cold} - \epsilon_{warm} \tag{4. 5}$$

$$\Delta T_{surf} = T_{surf,cold} - T_{surf,warm} \tag{4. 6}$$

and are also represented in **Figure 101**.

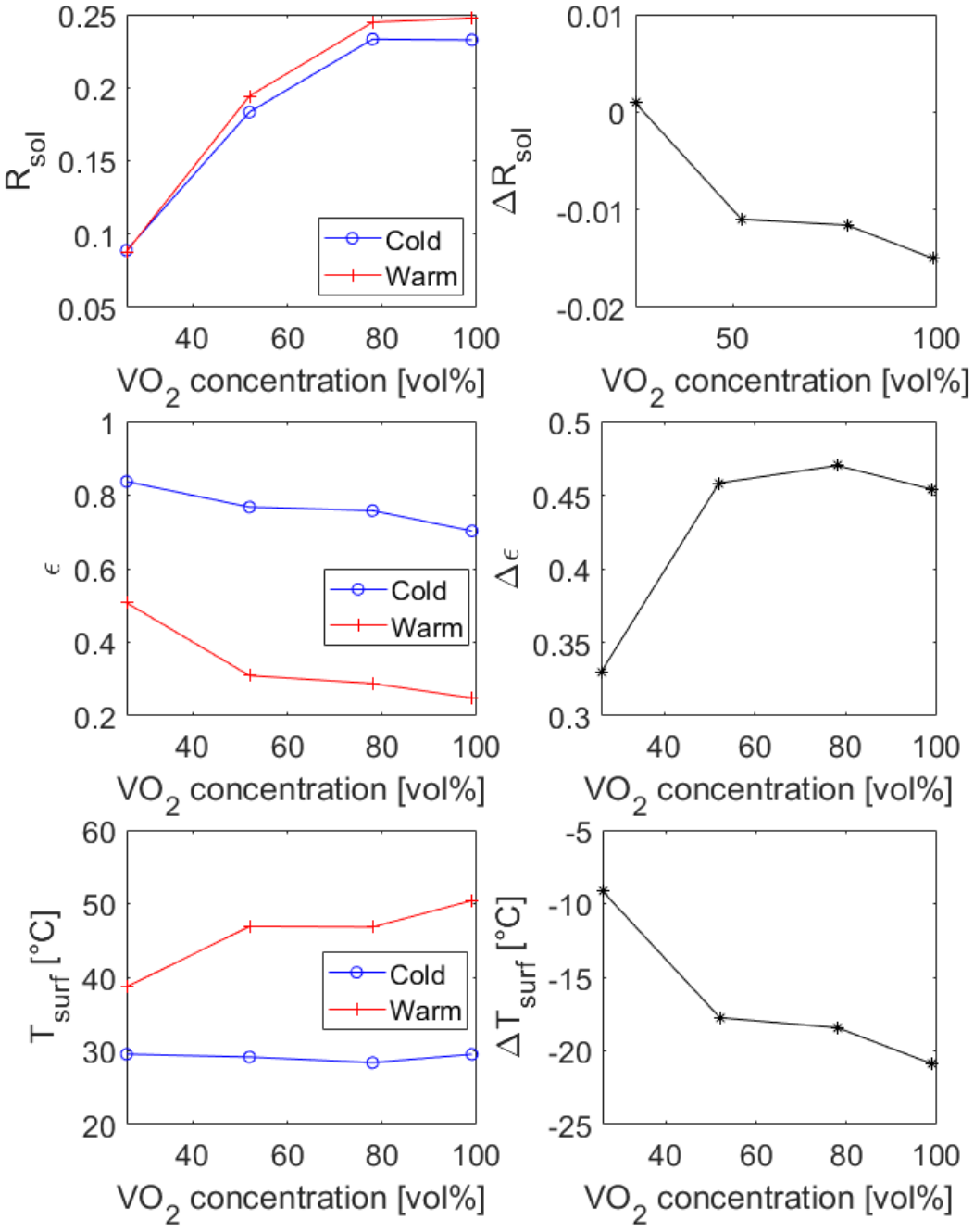

Figure 101: Calculated solar reflectance R_{sol}, emissivity ϵ and surface temperature T_{surf} of an opal photonic crystal consisting of polymer spheres (n=1.3) surrounded by VO_2 as a function of VO_2 total concentration in both cold and warm conditions. The incident light is normal to the material surface. The modulations ΔR_{sol}, $\Delta\epsilon$ and ΔT_{surf} are also represented.

Solar reflectances are calculated from the spectral reflectance, in the visible and near infrared spectral regions (wavelength range [350 nm – 2500 nm]). **Figure 100** shows an increase of the reflectance in this region with increasing VO_2 concentrations, for both VO_2 cold and warm phases. This is translated into an increase of the solar reflectance with increasing VO_2 concentrations. The energy used to increase the material surface temperature comes from the solar energy which is not initially reflected, so this increased reflectance should contribute in lower surface temperatures. Nevertheless, this is not the case, with $T_{surf,cold} = 29.5\ °C$ and $T_{surf,warm} = 38.7\ °C$ for a VO_2 concentration of 26 vol%, and $T_{surf,cold} = 29.5\ °C$ and $T_{surf,warm} = 50.4\ °C$ for a VO_2 concentration of 99 vol%. This is explained by the fact that the material emissivity decreases with the VO_2 concentration, due to the global increase of the material reflectance with the VO_2 concentration in the mid-IR wavelength range.

Let us have a look on the modulations ΔR_{sol}, $\Delta\epsilon$ and ΔT_{surf}. The similar values and variations of R_{sol} for cold and warm conditions lead to a low and slightly varying ΔR_{sol}, with absolute values below 0.02. Considering $\Delta\epsilon$, a clear difference is observed for a VO_2 concentration of 26 vol% with a value of 0.33, whereas for other VO_2 concentration $\Delta\epsilon$ is about 0.46. This particular value for a VO_2 concentration of 26 vol% has to be linked to the strong PBG effect observed in this case for the reflectance spectrum in the VO_2 cold phase. Also, while ΔT_{surf} is about -20 °C for all VO_2 concentrations besides 26 vol%, it jumps to -9°C at 26 vol%, in accordance with the variations of $\Delta\epsilon$.

Study of the influence of the structure

In order to confirm the impact of the structure on the material emissivity and temperature, the same study is performed with a homogenized layer modelled by a two-step homogenization process using two successive Maxwell-Garnett approximations (see **Section 3.2.1**). In such homogenized material, the optical effect due to the material structure is removed.

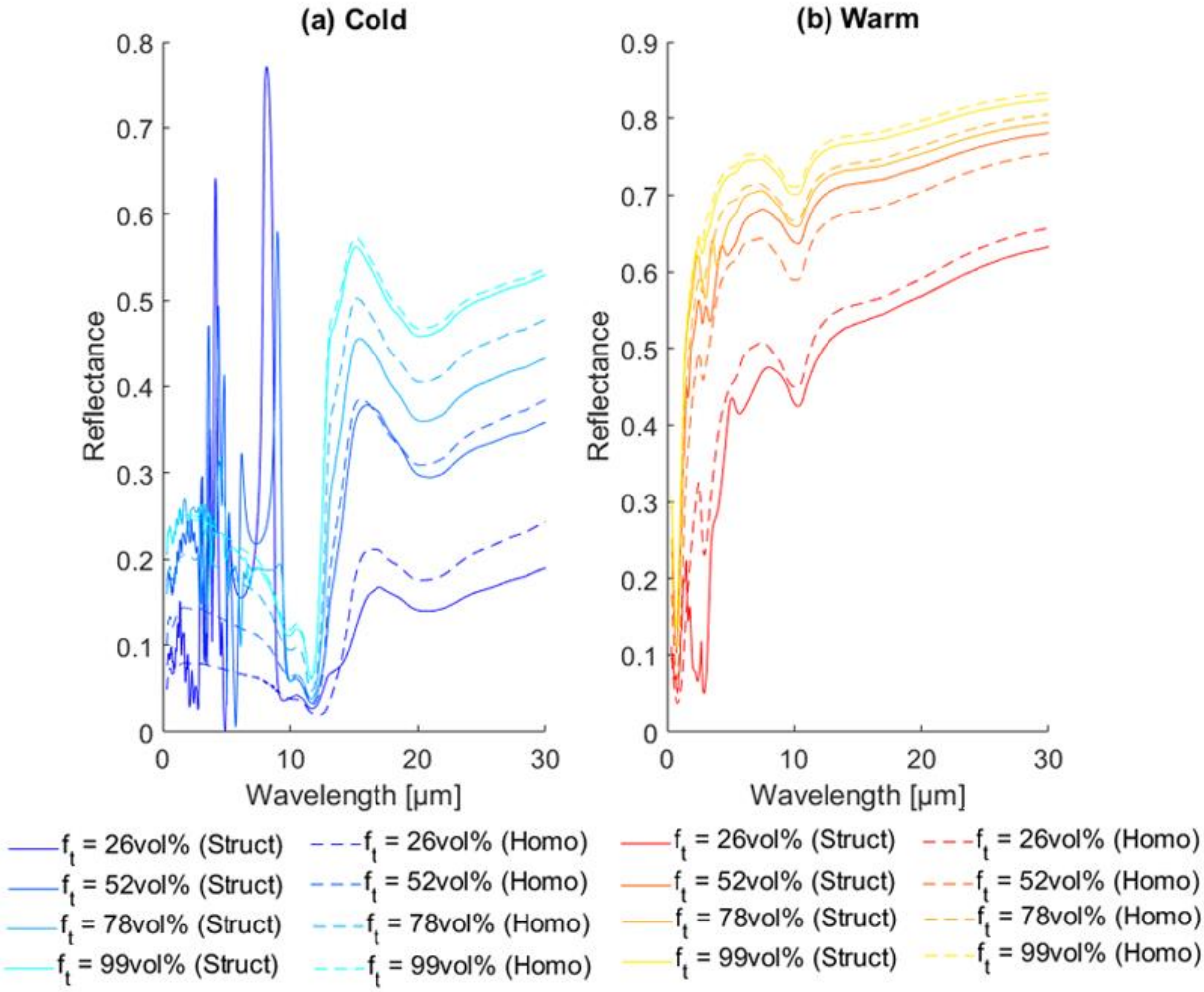

Figure 102: Reflectance spectra of a polymer opal photonic crystal consisting of polymer spheres (n=1.3) surrounded by VO_2 with a cell parameter a=4.5 µm (solid lines) and of the corresponding homogenized material (dashed lines), at normal incidence, in both cold (left) and warm (right) conditions, as a function of the total VO_2 concentration f_t.

Spectral reflectances for the four homogenized materials corresponding to the four previously considered systems are calculated and shown as dashed lines in **Figure 102**, along with the previously computed reflectance spectra. Comparing each system and its corresponding homogenized layer, the main difference can be seen on the PBG effect in cold conditions, present only when the material

structure is taken into account (solid lines), but not in the case of the homogenized layer (dashed lines). This observation is then translated in terms of thermal performances in **Figure 103**, by computing R_{sol}, ϵ and T_{surf} and their modulations ΔR_{sol}, $\Delta\epsilon$ and ΔT_{surf} for the homogenized material and the structured one.

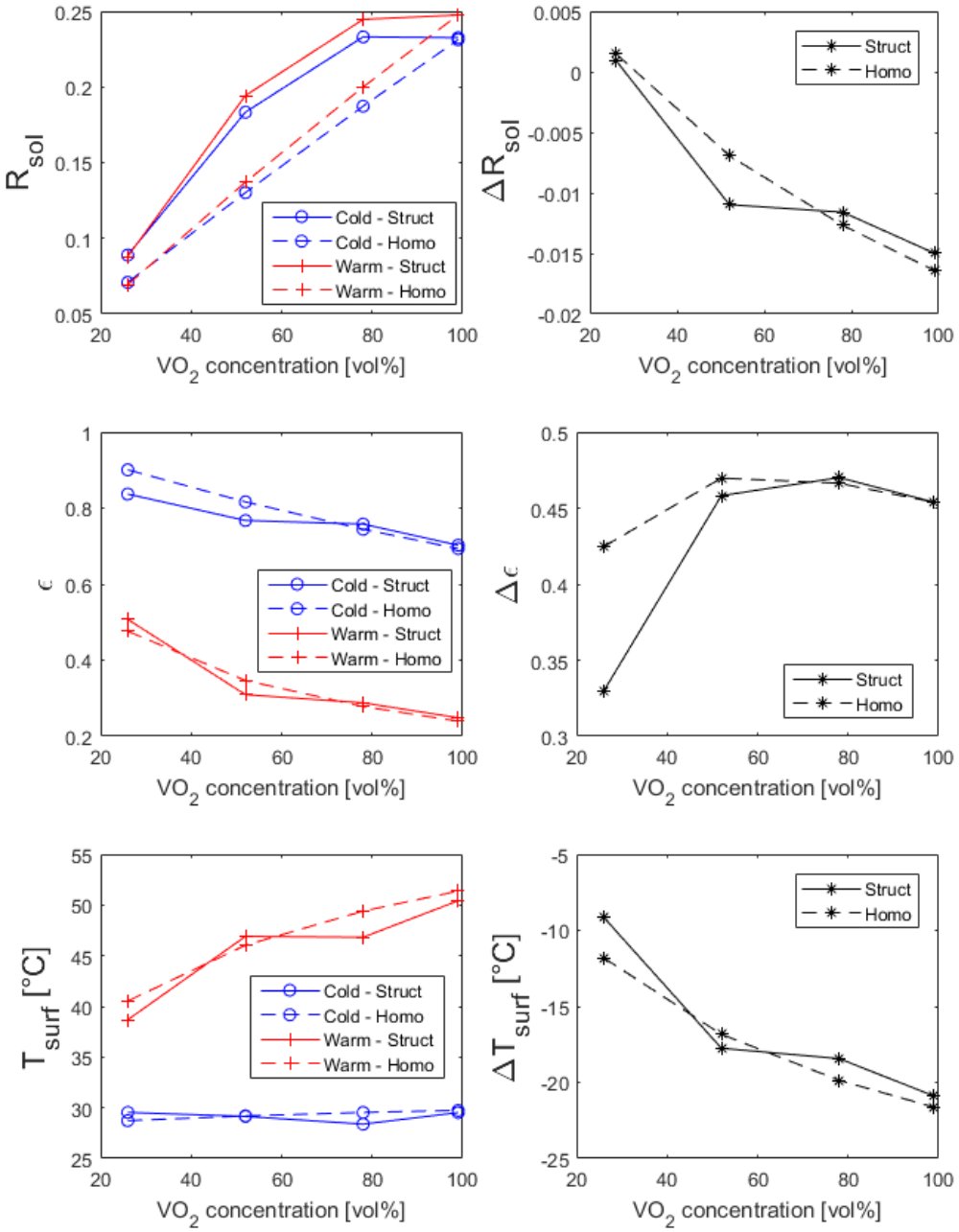

Figure 103: Calculated solar reflectance R_{sol}, emissivity ϵ and surface temperature T_{surf} of an opal photonic crystal consisting of polymer spheres (n=1.3) surrounded by VO_2 (solid lines), and of its corresponding homogenized layer (dashed lines), as a function of VO_2 total concentration in both cold and warm conditions. The incident light is normal to the material surface. The modulations ΔR_{sol}, $\Delta\epsilon$ and ΔT_{surf} are also represented for the structured material (solid lines) and the homogenized one (dashed lines).

Observing R_{sol} as a function of the total VO_2 concentration, a clear influence of the structure is observed, with lower values for R_{sol} for the homogenized material compared to the structured one. This is due to the effect of higher frequency peaks linked to the photonic band structure of the

material, which increase the material reflectance for wavelengths below the photonic bandgap (see **Section 4.2.4**).

Observing ϵ as a function of the total VO_2 concentration in the warm condition, the results obtained for the homogenized layer seem comparable to the results obtained for the structured material, with a highest variation of 12% at the VO_2 concentration of 52 vol%. In the cold condition, the highest variation (7.6%) is observed at the lowest considered VO_2 concentration ($f_t = 26$ vol%), which is the case where our system is a compact structure leading to the strongest PBG effect. Considering T_{surf}, with the combined influence of R_{sol} and ϵ, this effect is less pronounced. It can nevertheless be noticed that for $f_t = 26$ vol% an improvement of the material performance by the structure is observed, with a higher value for T_{surf}^{cold} and a lower value for T_{surf}^{warm} in the structured case than in the homogenized one.

Looking at the modulations ΔR_{sol}, $\Delta\epsilon$ and ΔT_{surf}, the main impact of the structure is observed for ΔR_{sol} at a VO_2 concentration $f_t = 52$ vol% with a decrease of 36% compared to the homogenized case. For $\Delta\epsilon$, the structure is responsible for a significant decrease from 0.42 to 0.33 (27%) at a VO_2 concentration of 26 vol%. Such reduced $\Delta\epsilon$ corresponds to an increase of ΔT_{surf} from -11.8°C to -9.1°C improving the material thermal performance.

4.2.3.2. Low VO_2 concentrations (up to 26 vol%)

The other part of the VO_2 concentrations range is studied in this subsection. Lower VO_2 concentrations are introduced by mixing the VO_2 with another polymer in the opal interstitial spaces, instead of considering interstices filled with pure VO_2 material. A compact structure is considered for this study, as such structure leads to stronger PBG effects.

In order to model the opal interstices, an effective refractive index derived from a Maxwell-Garnett approximation is used, considering the VO_2 concentration in the interstices f_i, related to the total VO_2 concentration in the system f_t by:

$$f_i = \frac{f_t}{1 - C} \quad with\ C = \frac{4 \times \frac{4}{3}\pi R^3}{a^3} \tag{4. 7}$$

Six cases related to six different VO_2 concentrations are modelled. These cases are listed in **Table 10**.

f_t [vol%]	f_i [vol%]
1	3.8
5	19.2
10	38.5
15	57.7
20	77.0
26	100

Table 10: Considered values of total VO_2 concentrations f_t and their corresponding VO_2 concentration in the interstices f_i in a compact opal photonic crystal.

Optical properties and performances of the material

For each case, the spectral reflectance and transmittance are calculated, with an incoming light normally incident on the material surface, in both cold and warm conditions. Results are presented in

Figure 104. The reduced VO_2 concentration is followed by a reduced absorption in the material. This leads to two main observations: the first one is that at low enough concentrations and at certain wavelengths, the material becomes partially transparent. This can be seen on the transmittance spectra, but also in the presence of oscillations in the reflectance spectra due to thin film interferences, as the light reaches the backside of the material. The second observation is that the PBG reflectance peak can now be observed in the warm conditions as the absorption is weak enough to have an influence of the structure on the material optical properties. The PBG reflectance peak corresponds to a transmittance hole, which is particularly visible for low VO_2 concentrations where the material is transparent enough. In both cold and warm conditions, as the VO_2 concentration increases, the PBG reflectance peak amplitude decreases and the peak position shifts towards longer wavelengths. The first effect is due to the material higher absorption coefficient (with a stronger decrease in the warm condition due to higher absorption of the warm VO_2 phase compared to the cold one), while the second effect is due to a higher effective refractive index for the material, which according to Bragg's law, leads to a red-shift of the peak. This shift of the PBG position might be responsible for smaller effect on ϵ as the cell parameter a was set so that $\lambda_{Bragg} = \lambda_{Wien}$ in the case where $f_t = 26$ vol%. With a varying λ_{Bragg}, a should be adjusted in order to keep $\lambda_{Bragg} = \lambda_{Wien}$ for a maximum impact on ϵ. However, we consider the peak shift in this case (about 0.65 nm between $f_t = 1$ vol% and $f_i = 20$ vol%) to be small enough to have a negligible impact on ϵ.

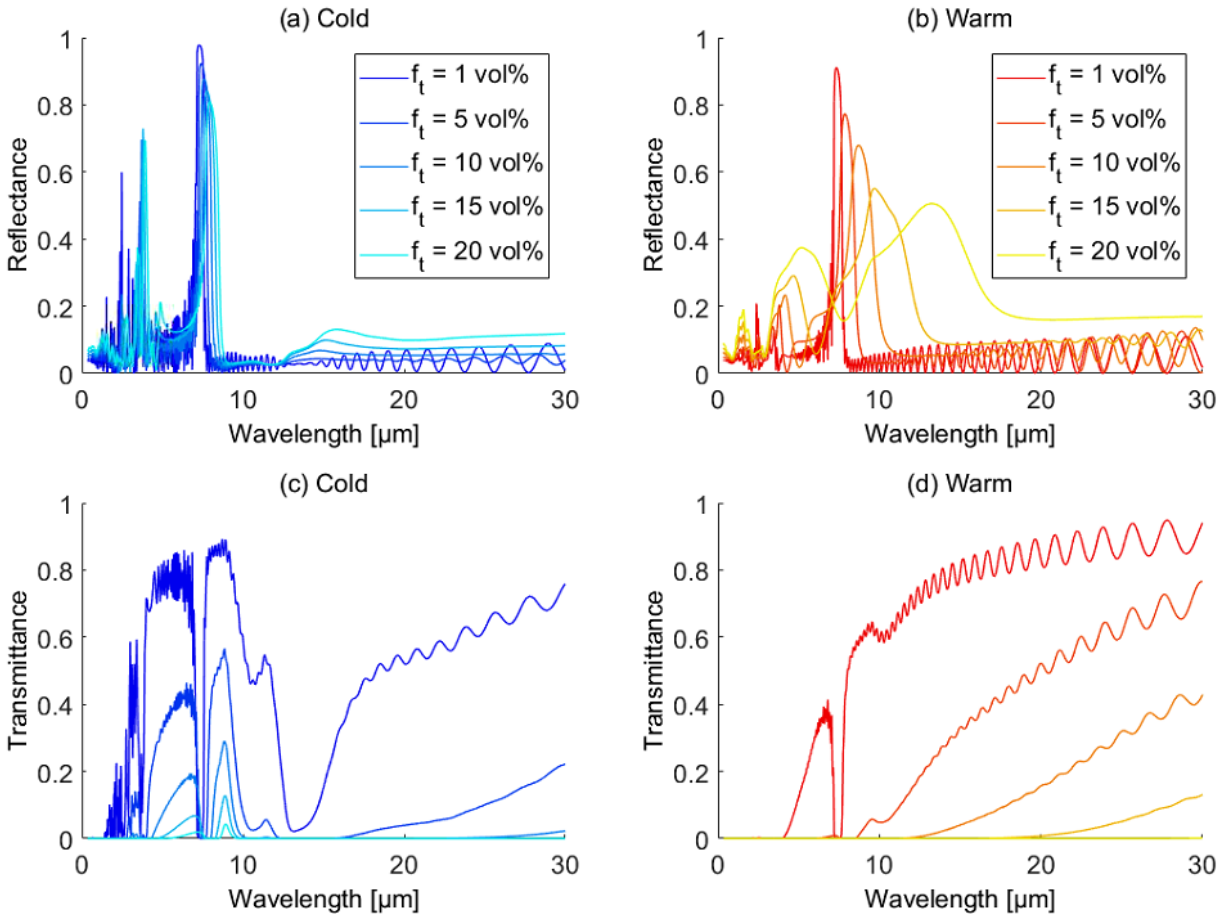

Figure 104: Reflectance (a,b) and transmittance (c,d) spectra of a polymer compact opal photonic crystal consisting of polymer spheres (n=1.3) surrounded by a mixture of VO_2 and another polymer (n=1.7), with a cell parameter a=4.5 µm, at normal incidence, in both cold (a,c) and warm (b,d) conditions, as a function of the total VO_2 concentration f_t from 1 vol% to 20 vol%.

Based on these spectral reflectances and transmittances, the solar reflectance R_{sol}, emissivity ϵ and surface temperature T_{surf}, and their modulations respectively ΔR_{sol}, $\Delta\epsilon$ and ΔT_{surf}, are calculated for VO_2 concentrations f_t from 0 to 20 vol%. Results are presented in **Figure 105**. The values related to $f_t = 26$ vol% are taken from the previous section and added in the figure.

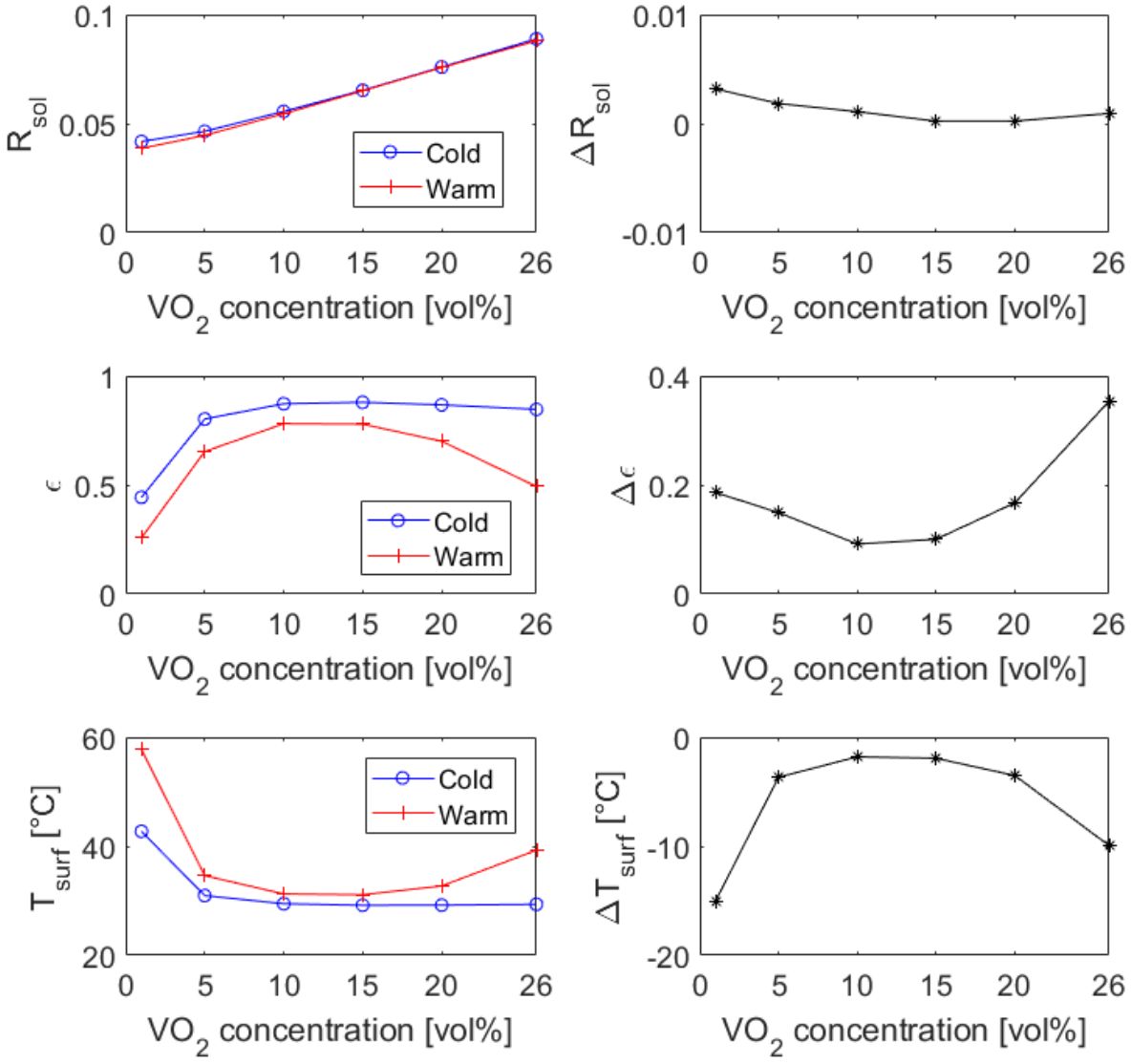

Figure 105 : Calculated solar reflectance R_{sol}, emissivity ϵ and surface temperature T_{surf} of an opal photonic crystal consisting of polymer spheres (n=1.3) surrounded by VO_2 as a function of VO_2 total concentration in both cold and warm conditions. The incident light is normal to the material surface. The modulations ΔR_{sol}, $\Delta\epsilon$ and ΔT_{surf} are also represented.

The solar reflectance R_{sol} increases for increasing VO_2 concentrations in both cold and warm conditions due to an increase of the spectral reflectance in the visible and near infrared spectral regions. However, there is no clear difference on R_{sol} between these two states, leading to a very little ΔR_{sol} with barely no variation with the VO_2 concentration.

Unlike in the previous section where the material emissivity was calculated based on the spectral reflectance only, here the material is now transparent (see **Figure 104c** and **Figure 104d**) so that the energy which can be used to increase its temperature is now related to the spectral absorptance $1 - R - T$ with R the material reflectance and T its transmittance (see *Equation* (1. *29*)). **Figure 106** represents this spectral absorptance for different VO_2 concentrations f_t in cold and warm conditions. Keeping in mind that the material emissivity is obtained by the absorptance integration weighted by

the blackbody radiance at a temperature of 70°C (represented in dotted lines in **Figure 106**), the strongest contribution of the material absorptance is located where the blackbody radiance is maximum. It appears that around the blackbody radiance peak, the lowest values of $1 - R - T$ are obtained for lower VO_2 concentrations, especially in the cold conditions. In the warm conditions, while $1 - R - T$ increases from $f_t = 1$ vol% to $f_t = 10$ vol%, a decrease is observed from $f_t = 15$ vol% to $f_t = 26$ vol% accompanied by a change of the curves shape, linked to the vanishing of the transmittance due to higher absorption. This tendency leads to lower emissivities for lower VO_2 concentrations, except at higher VO_2 concentrations in the warm conditions where the emissivity has the opposite tendency, as observed in **Figure 105**. The emissivity difference between cold and warm conditions lead to a positive $\Delta\epsilon$ ($\epsilon_{cold} > \epsilon_{warm}$) with a minimum value of about 0.09 obtained for $f_t = 10$ vol%.

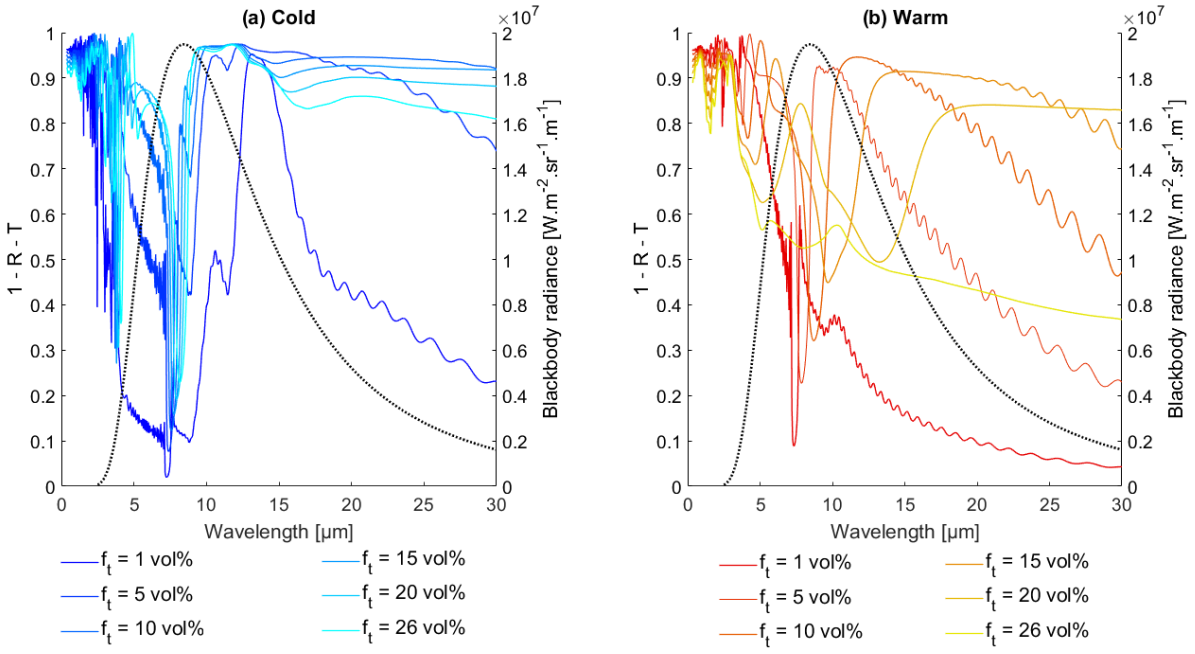

Figure 106: Absorptance spectra of a polymer compact opal photonic crystal consisting of polymer spheres (n=1.3) surrounded by a mixture of VO_2 and another polymer (n=1.7), with a cell parameter a=4.5 µm, at normal incidence, in both cold (a) and warm (b) conditions, as a function of the total VO_2 concentration f_t from 1 vol% to 26 vol%. The blackbody radiance at a temperature of 70°C is also represented in black dotted lines.

Both solar reflectance and emissivity are then used to calculate the material surface temperature T_{surf}. Combining the variations of R_{sol} and ϵ as a function of the VO_2 concentration leads to the variations of T_{surf}, which globally follow the variations of ϵ due to the small variations of R_{sol} (**Figure 105**). While $T_{surf,cold}$ and $T_{surf,warm}$ seem quite similar (about 30 °C) for VO_2 concentrations from 5 to 20 vol%, the curves split for extreme values of the VO_2 concentration. At $f_t = 1$ vol%, $T_{surf,cold} = 42.7\ °C$ while $T_{surf,warm} = 57.8\ °C$. These differences are represented as ΔT_{surf} which remains negative because $T_{surf,cold}$ is always lower than $T_{surf,warm}$. ΔT_{surf} has a maximum value of -1.8 °C observed at $f_t = 10$ vol% corresponding to the minimum value of $\Delta\epsilon$. This maximum value of ΔT_{surf} is interesting for applications as energy-efficient coating for buildings and satellites.

<u>Study of the influence of the structure</u>

Now in order to study the impact of the material structure on its optical and thermal properties, a two-step Maxwell-Garnett homogenization process is performed on the opal photonic crystal for the considered VO_2 concentrations from 1 to 26 vol%. The spectral reflectances and transmittances are

calculated for these homogenized layers and results are presented as dashed lines in **Figure 107**, along with the spectral reflectances and transmittances presented in **Figure 104** obtained for the structured material.

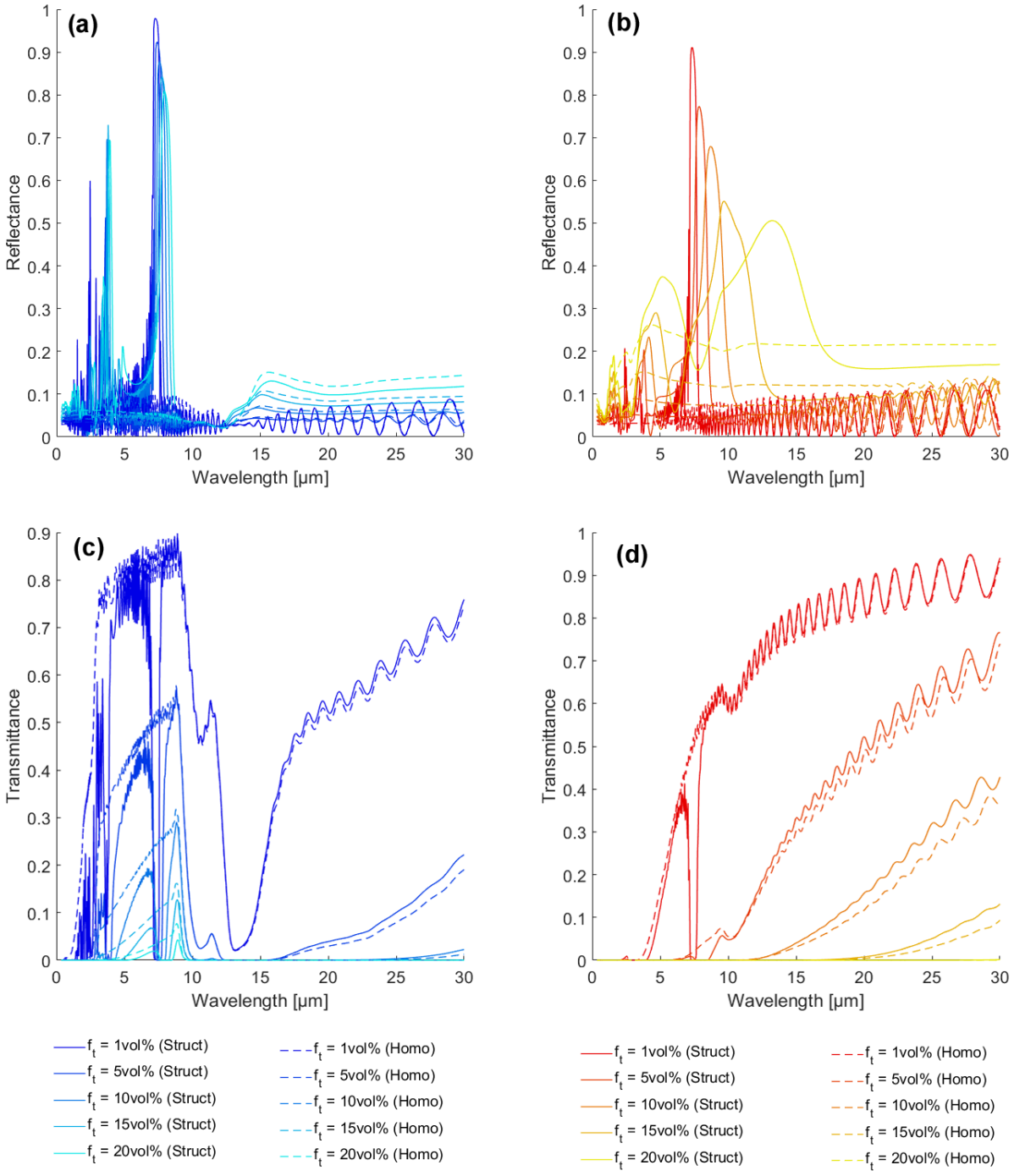

Figure 107: Reflectance (a,b) and transmittance (c,d) spectra of a polymer compact opal photonic crystal consisting of polymer spheres (n=1.3) surrounded by a mixture of VO_2 and another polymer (n=1.7) (solid lines), and its homogenized layer (dashed lines), with a cell parameter a=4.5 μm, at normal incidence, in both cold (a,c) and warm (b,d) conditions, as a function of the total VO_2 concentration f_t from 1 vol% to 20 vol%.

Comparing the spectral reflectances and transmittances between the structured material (solid lines) and its homogenized counterpart (dashed lines), the main difference is located at the PBG reflectance peaks (or transmittance holes in the cases were the material is transparent enough to have significant

transmittance values). In the cold conditions, the PBG peak position is 7.3 µm at a VO_2 concentration of $f_t = 1$ vol%. As the concentration increases, this peak shifts to 8 µm at $f_t = 20$ vol%. In the warm conditions, the peak both shifts and enlarges, changing from a sharper peak centered in 7.3 µm when $f_t = 1$ vol% to a smoother peak extending from 8 to 15 µm, with a maximum value at a 7.2 µm wavelength when $f_t = 20$ vol%. The disappearance of these peaks or holes for the homogenized material confirms that they are due to the material structure.

These spectral reflectances and transmittances are once again used to calculate the integrated values R_{sol}, ϵ and T_{surf}, and their modulation ΔR_{sol}, $\Delta\epsilon$ and ΔT_{surf}. Results are presented in **Figure 108**.

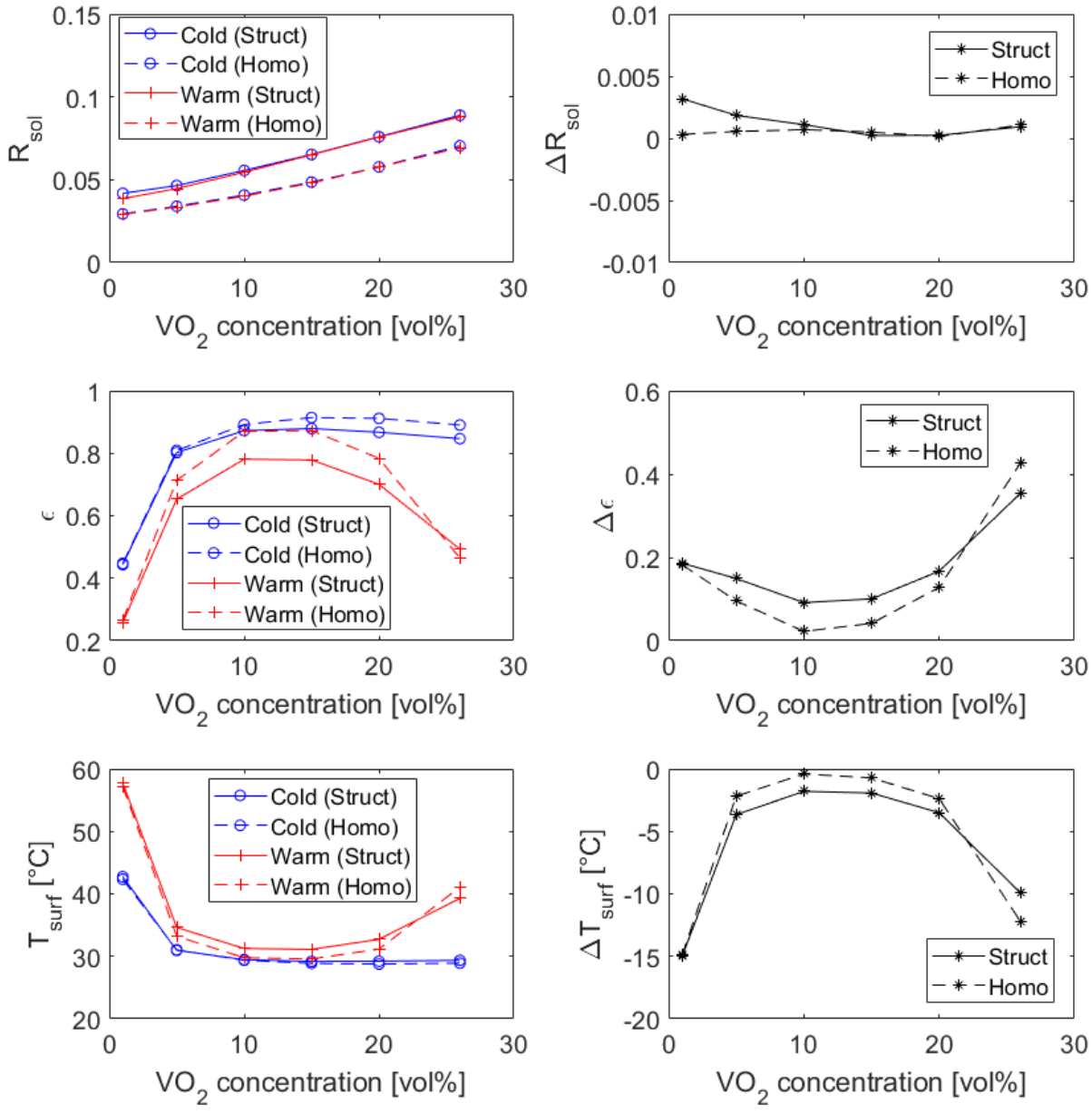

Figure 108: Calculated solar reflectance R_{sol}, emissivity ϵ and surface temperature T_{surf} of a compact opal photonic crystal consisting of polymer spheres (n=1.3) surrounded by VO_2 (solid lines), and of its homogenized counterpart (dashed lines), as a function of VO_2 total concentration in both cold and warm conditions. The incident light is normal to the material surface. The modulations ΔR_{sol}, $\Delta\epsilon$ and ΔT_{surf} are also represented for the structured material (solid lines) and the homogenized one (dashed lines).

Increased values of R_{sol} are observed when the material is structured, due to reflectance peaks observed at shorter wavelengths linked to the photonic band structure (see **Section 4.2.4**). The structure also causes reduced values of ϵ_{cold} due to the PBG effect. At a VO_2 concentration of 26 vol%, a 5.2% decrease is observed due to the structure. However, at lower concentrations, the structure has less impact on ϵ_{cold}. Noticing that the PBG has a very strong influence on the reflectance at these lower VO_2 concentrations (see **Figure 107a**), the material emissivity should be strongly influenced by the material structure. It is not the case because ϵ is calculated based on the spectral absorptance $1 - R(\lambda) - T(\lambda)$ and not only on $1 - R(\lambda)$. Where the PBG is located, a reflectance peak corresponds to a transmittance valley. At the end, an increase of $R(\lambda)$ is compensated by a decrease of $T(\lambda)$, leading to an almost unchanged emissivity. To better visualize it, the absorptance spectra in the case of $f_t = 1$ vol% is represented in **Figure 109**.

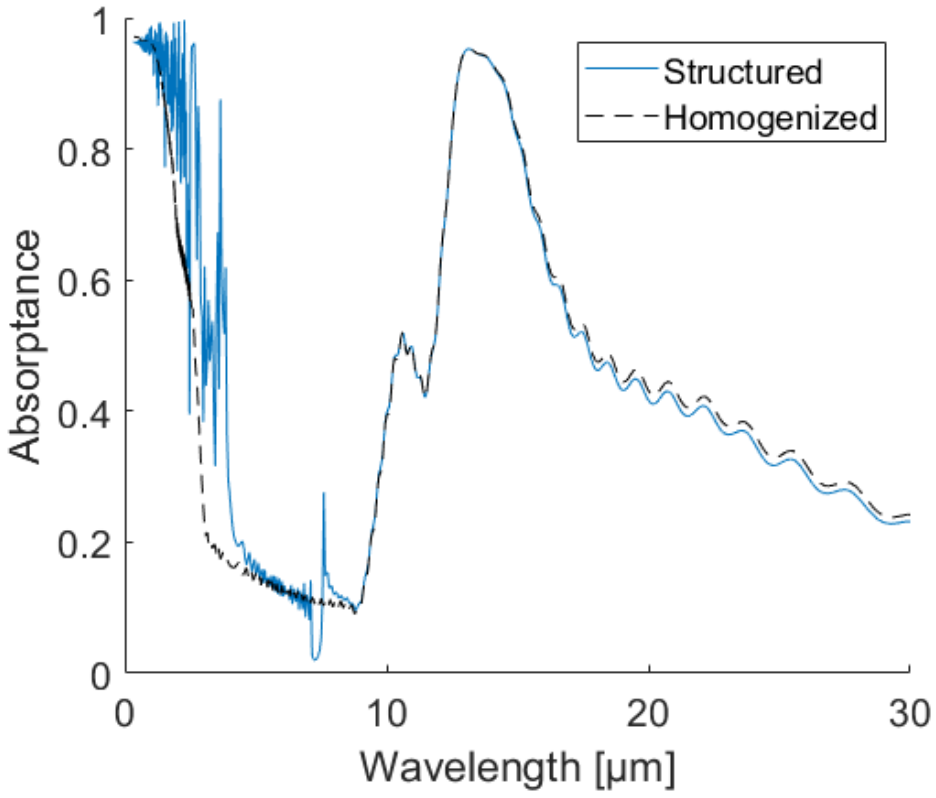

Figure 109: Absorptance spectra of a polymer compact opal photonic crystal consisting of polymer spheres (n=1.3) surrounded by a mixture of VO_2 and another polymer (n=1.7) (solid lines), and its homogenized counterpart (dashed lines), with a cell parameter a=4.5 µm, at normal incidence, in cold conditions. The VO_2 total concentration is 1 vol%.

Little variations are observed between the structured and homogenized cases. The structure generates a small valley around a wavelength of 7.3 µm corresponding to the PBG position but its influence on ϵ_{cold} remains very little. In this case, no major change on ϵ_{cold} is observed (**Figure 108**).

For ϵ_{warm}, the difference between structured and homogenized materials is maximum when the VO_2 total concentration is equal to 15 vol% with a 12% decrease due to the structure. This 15 vol% concentration corresponds to a limit where the material absorption is high enough to cancel the effect of the transmittance hole on the emissivity and low enough to have a significant PBG reflectance peak. Note that also the VO_2 refractive index real part may have an influence on the position of this limit, as

the PBG peak exhibits a high shift towards the higher wavelengths at higher VO_2 concentrations and is not anymore aligned with the blackbody emittance maximum.

T_{surf} combines the effects of both R_{sol} and ϵ. The structure has a little influence in the cold case, a maximum effect is observed at the highest considered VO_2 concentration with an increase of about 0.5 °C. In the warm case, the structure leads to an increase of T_{surf}^{warm} with a maximum difference of 1.5 °C at a VO_2 concentration of 15 vol%.

ΔR_{sol} is barely influenced by the structure with a maximum influence at a 1 vol% VO_2 concentration with a negligible 0.003 variation between the structured and homogenized materials. $\Delta\epsilon$ is higher when the material is structured for VO_2 concentrations from 1 vol% to 20 vol%. At 26 vol%, this tendency is reverted. The maximum influence of the structure is obtained when $f_t = 10\ \mathrm{vol\%}$. In this case the structure leads to an increase of the material emissivity modulation of 0.07. Finally, in accordance with $\Delta\epsilon$, ΔT_{surf} is higher in the case of the structured material, compared to the homogenized layer, when the VO_2 concentration is between 1 vol% and 20 vol%. This tendency is reverted for higher concentrations. The structure has a maximum influence on ΔT_{surf} at a VO_2 total concentration of 5 vol% with a 1.5 °C decrease due to the structure.

4.2.3.3. Gathering all VO_2 concentrations from 1 to 100 vol%

This short subsection gathers the data calculated in the two previous subsections in order to have VO_2 concentrations ranging from 1 vol% to 100 vol%. The solar reflectance, emissivity and surface temperature, and their modulations, are presented in **Figure 110** for these VO_2 concentrations. It gathers data already presented in **Figure 103** and **Figure 108**.

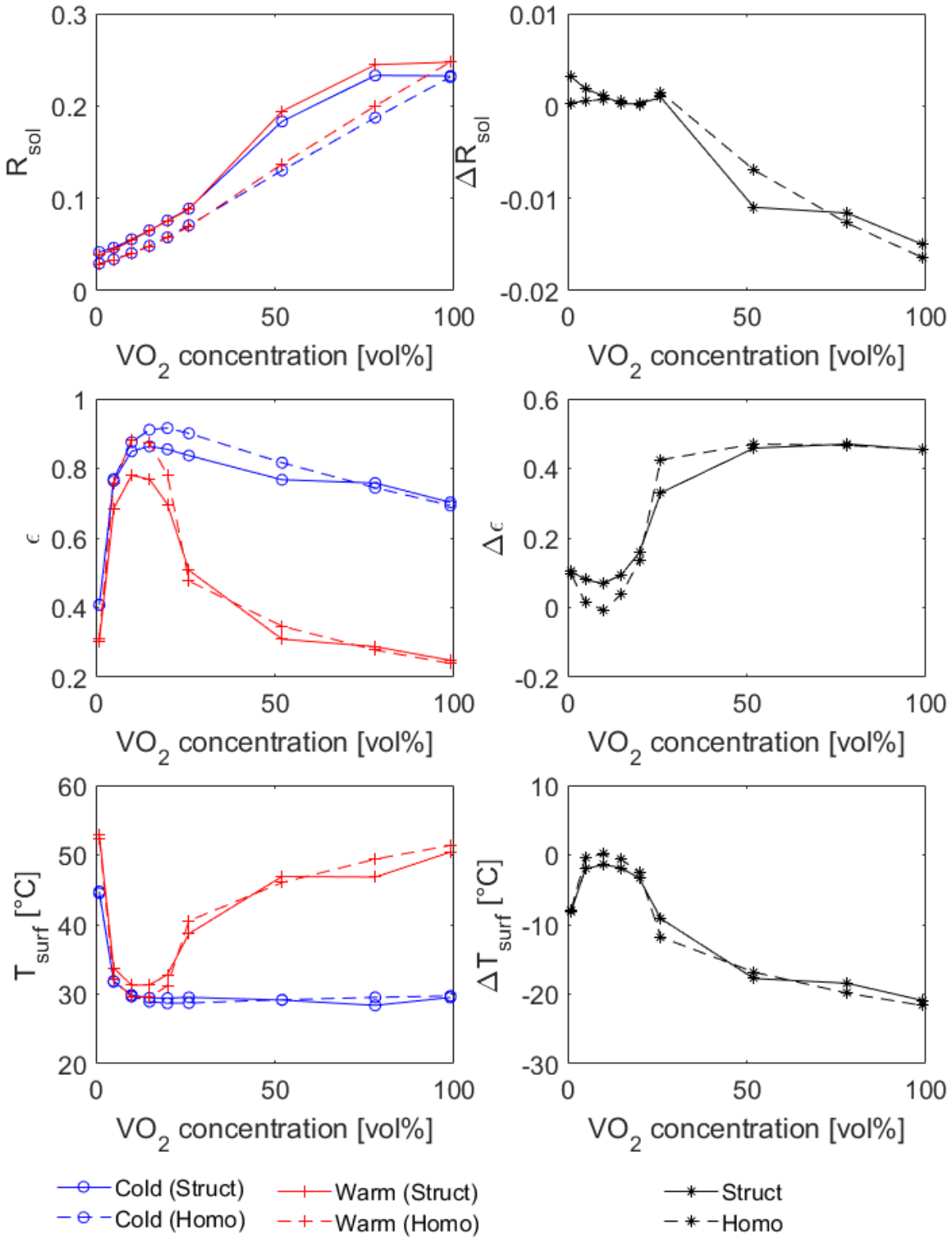

Figure 110: Calculated solar reflectance R_{sol}, emissivity ϵ, surface temperature T_{surf} and their modulations ΔR_{sol}, $\Delta\epsilon$ and ΔT_{surf} for a compact opal photonic crystal consisting of polymer spheres (n=1.3) surrounded by a mixture of VO_2 and another polymer (n=1.7) (solid lines), and its homogenized counterpart (dashed lines), as a function of the total VO_2 concentration f_t in cold and warm conditions. From $f_t = 26$ vol%, higher concentrations are obtained by filling the interstices of pure VO_2 and reducing the opal compacity.

Regarding the applications, different applications require different optimized parameters. For energy-efficient coating for buildings and satellites, a lowest possible $\Delta\epsilon$ is desired. According to **Figure 110**, this is obtained for a VO_2 concentration of 10 vol%, for which $\Delta\epsilon = -0.01$ in the homogenized layer. In this case, the structure decreases the performance as $\Delta\epsilon$ increases with the structure to $\Delta\epsilon = 0.07$. A case where the structure benefits the material performances for this target application is for $f_t = 26\ \mathrm{vol}\%$, in which case $\Delta\epsilon$ decreases from 0.42 to 0.33.

If considering a camouflage application for the material, the best performance is obtained for the highest $\Delta\epsilon$, which is obtained at higher VO_2 concentrations where no particular improvement is obtained by the material structuration. We can note that the $f_t = 100\ \mathrm{vol}\%$ case corresponds to a 117 µm-thick pure VO_2 film layer. In this case, $\Delta\epsilon = 0.45$, comparable with $\Delta\epsilon$ values in the order of 0.4 measured on pure VO_2 films by Dillon et al. [4]. On the other hand, if lower VO_2 concentrations are used, increased $\Delta\epsilon$ values can be obtained with a material structuration.

4.2.4. Trying to improve the material performance by using the effect of reflectance peaks at lower wavelengths

4.2.4.1. Origin of the reflectance peaks: band diagrams

Reflectance peaks at lower wavelengths than the principal PBG can be seen on the material reflectance spectra in cold conditions (see **Figure 94** for example). These peaks seem to be due to the material structure as they do not appear for a homogenized material (see **Figure 102a** for example). To understand their origin, let us have a look on the crystal photonic band structure. The band diagram of a compact opal photonic crystal consisting of polymer spheres with a refractive index $n = 1.3$ surrounded by pure semiconducting VO_2 is calculated. The calculation method (PWE) does not allow dispersive materials, so to model the VO_2 material, a constant refractive index is required.

Due to the dispersive property of VO_2, the band diagrams presented in this section are all wavelength-dependent. This means that each diagram is only valid for a certain range of wavelengths where the refractive index variations can be neglected. Depending on how fast the VO_2 refractive index varies around a certain wavelength, this region of validity may vary in size.

Position of the PBG peak on the band diagram

We will first look at the previously studied PBG reflectance peak observed around a wavelength of 8.3 µm and identify its position on the band diagram. At this wavelength, the real part of the semiconducting cold VO_2 refractive index is about 2.42. Using this value, the crystal band diagram is calculated and represented in **Figure 111**.

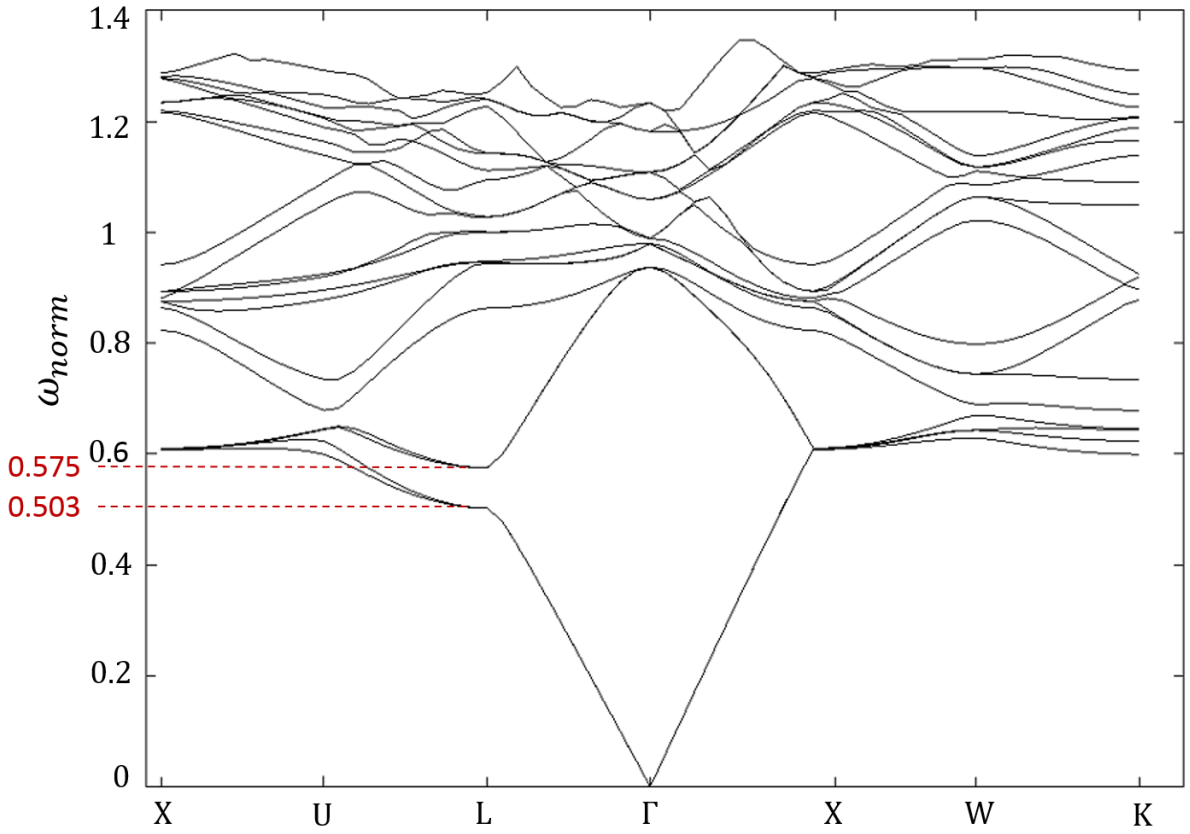

Figure 111: Complete band diagram of a compact opal photonic crystal consisting of polymer spheres (n=1.3) surrounded by pure VO_2 in cold conditions. The VO_2 refractive index is set to a real constant value of 2.42. The red dashed lines highlight the position of the PBG in the ΓL direction.

Figure 111 also displays in red dashed lines, the first PBG located between the normalized frequencies 0.503 and 0.575. These frequencies can be translated in terms of wavelengths using *Equation* (1. *37*)). The corresponding wavelengths give the PBG range from 7.82 µm to 8.95 µm. These values can be compared to the PBG position observed in **Figure 94**. At half maximum, this strongest reflectance peak is located between 7.75 µm to 8.75 µm. The similarity between these values is confirmed in **Figure 112** by aligning the reflectance spectrum of a compact polymer opal consisting of polymer spheres ($n = 1.3$) surrounded by pure VO_2 in cold conditions, modelled by its dispersive complex refractive index with a normally incident light, with the band diagram of the structure. Only the ΓL direction is presented on the band diagram, which corresponds to light normally incident on an opal having a surface cut in the [111] crystallographic direction.

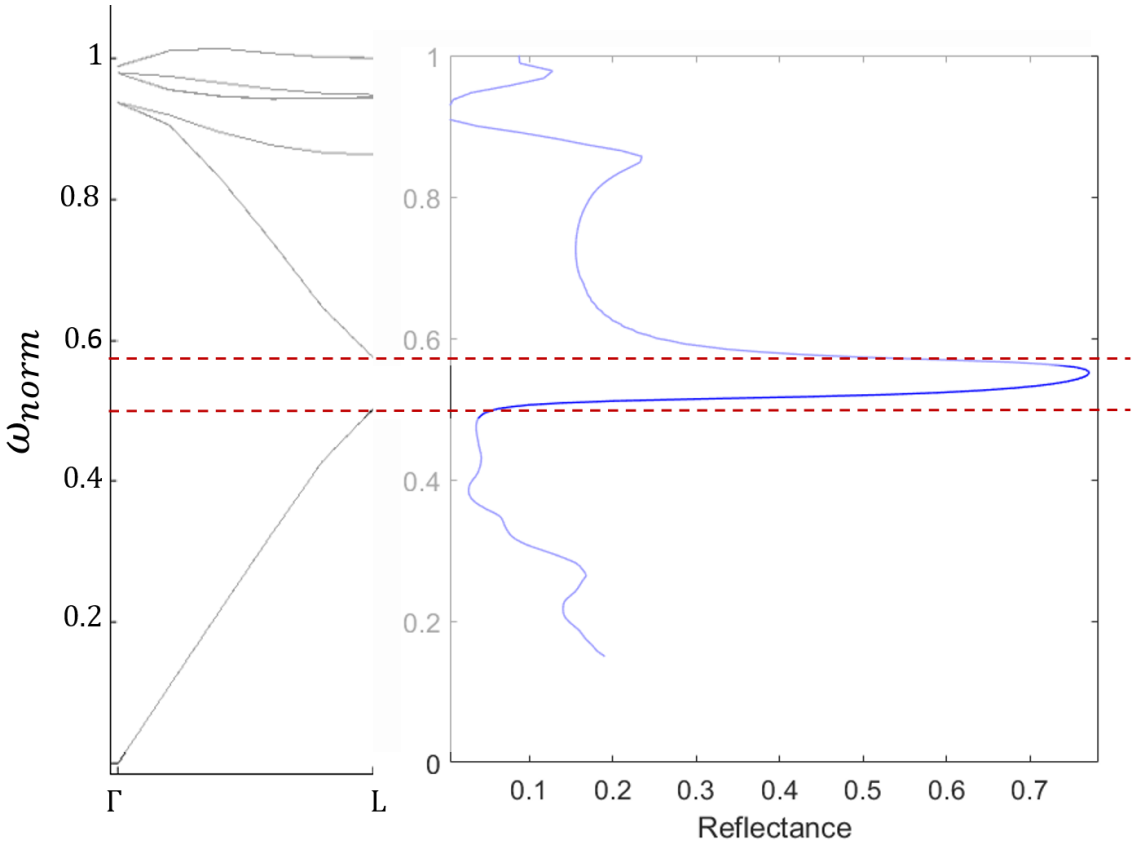

Figure 112: ΓL band diagram of a compact opal photonic crystal consisting of polymer spheres (n=1.3) surrounded by pure semiconducting VO_2 modelled by a refractive index 2.42 (left). (Right) Spectral reflectance of a compact polymer opal photonic crystal consisting of polymer spheres (n=1.3) surrounded by pure semiconducting VO_2. The normalized frequency ω_{norm} is aligned for both plots, which allows to highlight the PBG between the red dashed lines. The figures are cut considering a 2% variation of the VO_2 refractive index around 2.4.

As no band (no electromagnetic mode can propagate inside the material) is observed on the band diagram in the area delimited by the red dotted lines, this reflectance peak is thus due to a PBG effect.

In order to choose a validity range around the considered refractive index used to model the dispersive VO_2, we consider that the variation in refractive index should have a limited impact on the PBG peak position. For example, a 2% variation around $n = 2.42$ gives a refractive index range from 2.37 to 2.47. Using Bragg's law, a compact opal photonic crystal consisting of polymer spheres ($n = 1.3$) surrounded by a material having these refractive indexes has a peak at a wavelength of respectively 8.26 µm and 8.41 µm. This result means that a 2% variation on the refractive index of 2.42 shifts the Bragg peak position in about a 0.15 µm range. This range is only 15% of the total peak width (1 µm). We can thus consider that the peak position is barely impacted by this small refractive index variation. A 2% validity range is used in this study. Converting the edges of this validity range in terms of normalized frequencies ω_{norm}, we obtain a range from 0.521 to 0.545. This validity domain is displayed on **Figure 112** as shaded areas outside of this domain. We can observe that the size of this validity domain is very limited near the peak.

Identification of the lower wavelength reflectance peaks on the band diagram

To understand the material reflectance at lower wavelengths (i.e. higher frequencies), the refractive index of the opal interstices is set to the real part of the semiconducting VO_2 refractive index at a wavelength of 4 µm (corresponding to $\omega_{norm} \approx 1.1$) where another strong reflectance peak is

observed (see **Figure 94**). At this wavelength, this refractive index real part is equal to 2.9. The band diagram is calculated using this new refractive index and results are shown in **Figure 113**, alongside with the spectral reflectance at normal incidence in the same spectral range. Unlike the band diagram, this reflectance spectrum is calculated for VO_2 modelled by its dispersive complex refractive index.

Considering an acceptable refractive index variation of 2% around this constant value of $n = 2.9$, the VO_2 refractive index variations remain acceptable for wavelengths from 3.4 µm to 4.8 µm, which is equivalent to normalized frequencies from 0.94 to 1.88. To visualize this domain of validity, the graphs of **Figure 113** have been shaded off outside of the validity domain.

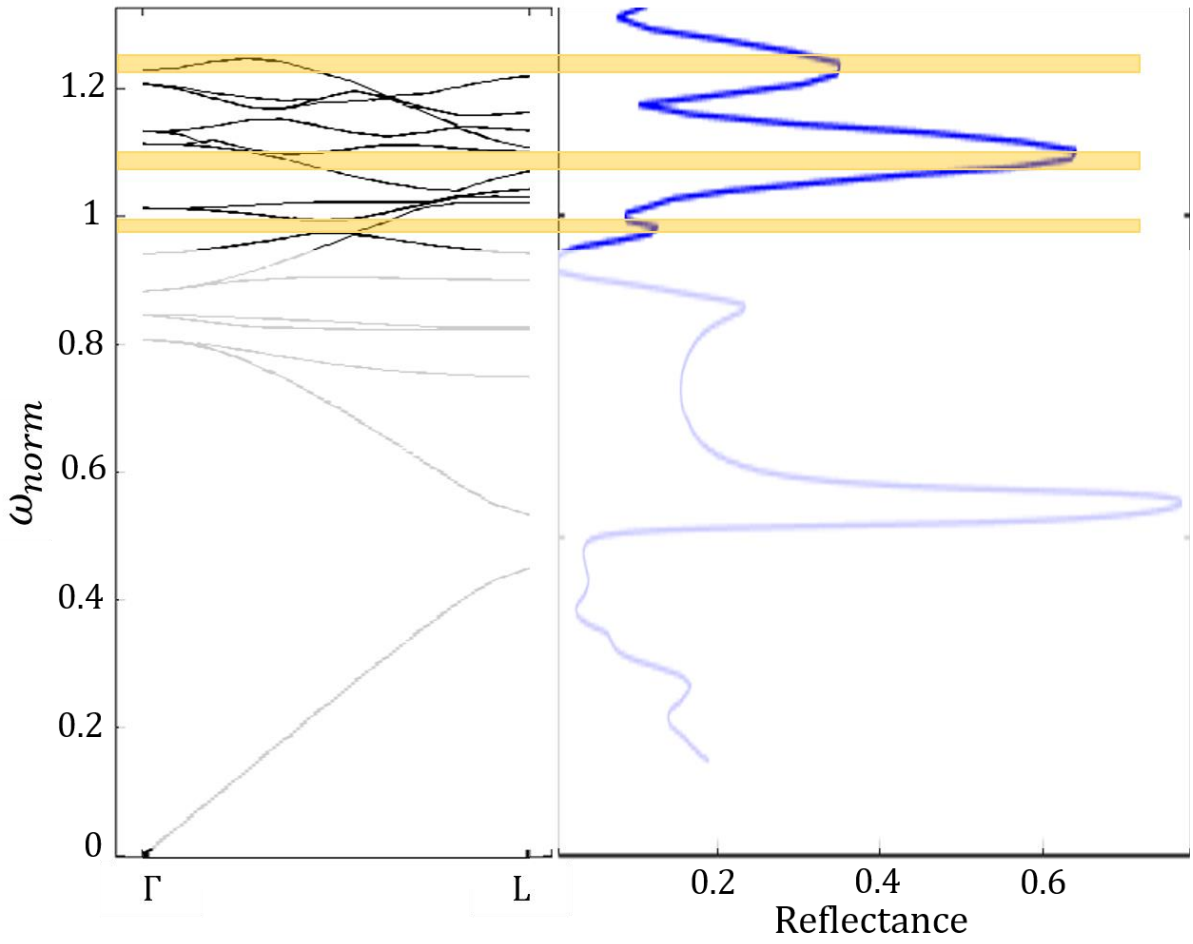

Figure 113: ΓL band diagram of a compact opal photonic crystal consisting of polymer spheres (n=1.3) surrounded by pure semiconducting VO_2 modelled by a refractive index 2.9 (left). (Right) Reflectance spectrum of a compact opal photonic crystal consisting of polymer spheres (n=1.3) surrounded by pure semiconducting VO_2. The normalized frequency ω_{norm} is aligned for both plots, which allows to highlight the position of higher frequency reflectance peaks. The figures are cut considering a 2% variation of the VO_2 refractive index around 2.9. The yellow areas correspond to areas were only one single mode can propagate in the material.

Looking at the band diagram at frequencies close to the reflectance peaks, it can be observed that close to each reflectance peak an area where only one single mode propagates in the material can be delimited. These areas are highlighted by yellow rectangles in **Figure 113**. Outside of these areas, higher numbers of modes can propagate, leading to a decrease of the reflectance and thus generating reflectance peaks on the single mode areas. These reflectance peaks are thus not linked to a PBG effect, but to a decrease of the number of propagating modes.

It is worth noting that the PBG peak observed previously in **Figure 111** and **Figure 112** is no longer aligned between the band diagram and the reflectance spectrum. This is due to the fact that at the PBG frequency, the VO_2 refractive index is different from the one used for the calculation of the band diagram presented in **Figure 113** (it is 2.42 instead of 2.9 which corresponds to a variation of 17%). A significant shift is observed: the bands seem to shift towards lower frequencies with the increase of the refractive index used in the crystal interstices. This is a clear observation of the importance of the validity domain.

We have here investigated the origins of the peaks observed in the material reflectance spectrum. While the first peak ($\lambda = 8.2\ \mu m$) is related to a PBG effect, the lower wavelengths peaks cannot be considered as bandgaps but may still be related to a band structure effect. As a result, their position may also be shifted with variations of the material structural parameters.

4.2.4.2. Influence of the reflectance peaks shifting

Shifting these lower wavelengths reflectance peaks closer to the position λ_{Wien} of the blackbody emittance peak could increase their contributions to the material emissivity, and potentially have more impact on the emissivity than only aligning the position of the main PBG with λ_{Wien}. This shift can be done by increasing the cell parameter a, which according to Bragg's law, results in a shift of the main PBG towards longer wavelengths, and thus also of these lower wavelengths peaks. However, shifting them also results in shifting the PBG away from the blackbody emittance peak. Because of this, the shift should not be too large, as the contribution of the main PBG would be reduced. In this section, various values for a are used in order to perform different shifts and the influence of these shifts on the material emissivity is studied.

The system used in this section is a compact opal photonic crystal consisting of polymer spheres ($n = 1.3$) surrounded by pure VO_2 . The total VO_2 concentration is thus $f_t = 26\ \mathrm{vol}\%$. It has 15 periods along the [111] direction. The material thickness thus varies as a function of a. Four parameters a are considered in this study: 4.5 µm (previously used), 5 µm, 6 µm and 7 µm, which correspond to thicknesses of respectively 117 µm, 130 µm, 156 µm and 182 µm. Spectral reflectances are calculated in cold and warm conditions with an incident light normal to the material surface. Results are shown in **Figure 114**. For a better comprehension of these spectra, the real and imaginary parts of the VO_2 refractive index is plotted alongside for both cold and warm conditions.

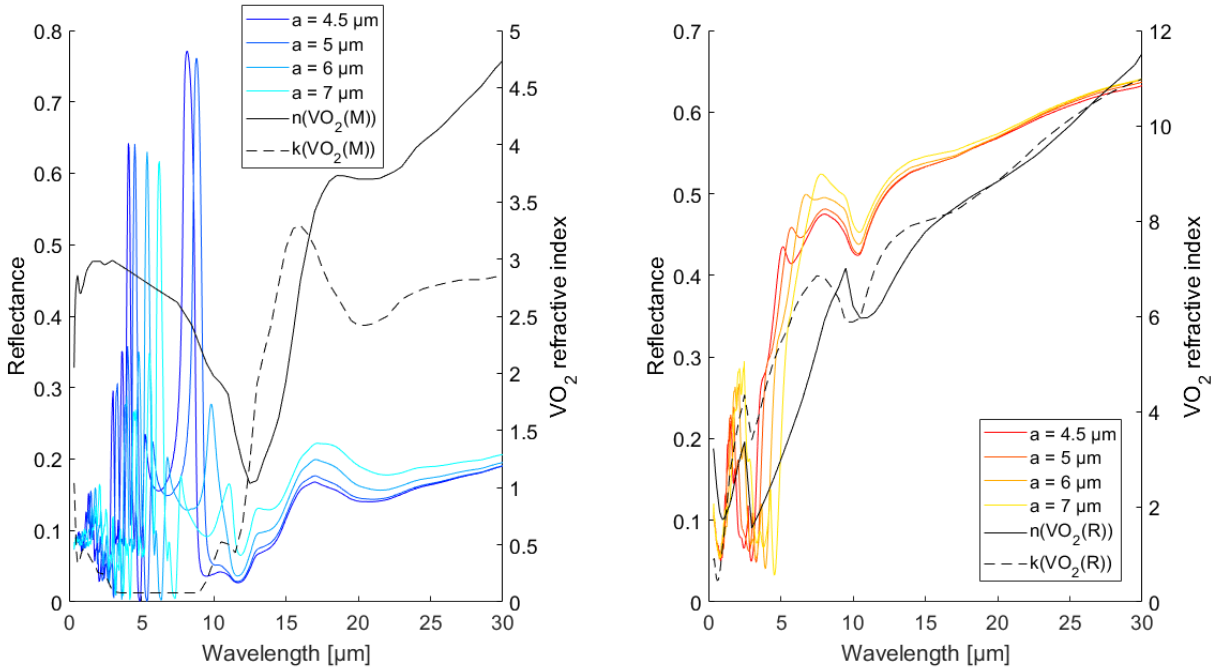

Figure 114: Reflectance spectra of a compact opal made of polymer spheres (n=1.3) surrounded by VO_2 in cold (left) and warm (right) conditions, for different cell parameters a, for normally incident light. The system has 15 periods along the [111] direction. The real (black solid lines) and imaginary (black dashed lines) parts of the VO_2 refractive index is also represented in both cold ($VO_2(M)$) and warm ($VO_2(R)$) conditions.

The variation of the cell parameter does not have much influence on the reflectance spectra in warm condition. Nevertheless, shifts of a peak situated in the [1 µm – 3 µm] wavelength range and of a smooth peak in the [5 µm – 10 µm] wavelength range are observed. Due to the high imaginary part of the refractive index of the warm VO_2 phase, these peaks are attenuated.

In the cold condition, as the cell parameter increases, all reflectance peaks are shifted towards longer wavelengths. The higher the cell parameter is, the lower the amplitude of the main PBG peak is. This is related to the variations of the VO_2 refractive index in the [8 µm – 12 µm] wavelength range. Indeed, in the cold conditions, the real part of the VO_2 refractive index decreases around these wavelengths as shown as the black solid line of **Figure 114, left**, making it closer to the spheres refractive index, and thus reducing the refractive index contrast in the crystal, resulting in a weaker PBG effect. In the wavelength range [4 µm – 6.5 µm] the refractive index contrast remains high, leading to an almost constant value of the amplitude of the lower wavelengths reflectance peaks.

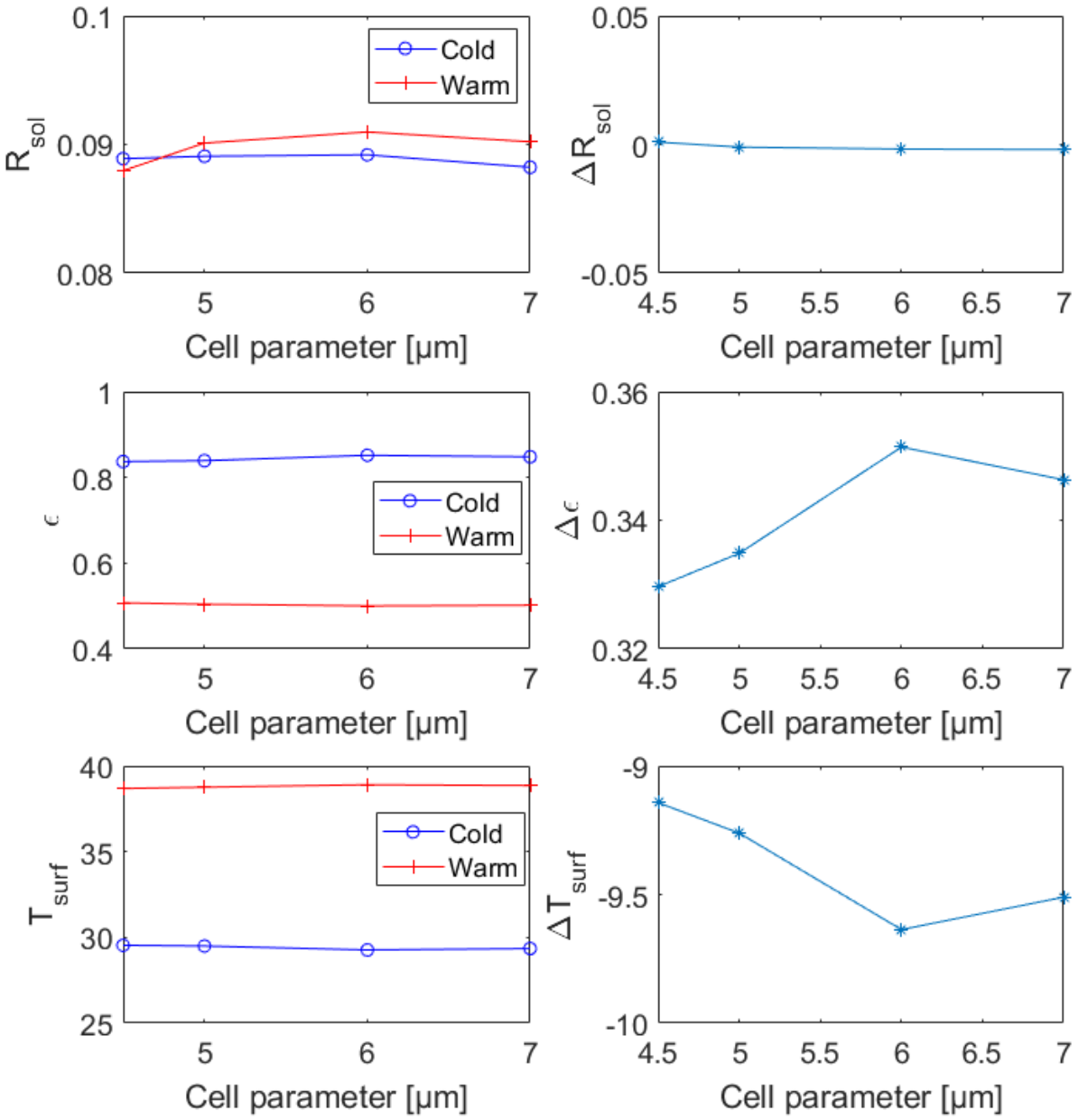

Figure 115: Solar reflectance (R_{sol}), emissivity (ϵ), material surface temperature (T_{surf}) as a function of the crystal cell parameter for a compact opal having spheres made of a polymer (n=1.3) surrounded by VO_2 in both phases. The incident light is normal to the material surface. The modulations ΔR_{sol}, $\Delta\epsilon$ and ΔT_{surf} are also represented on the 3 graphs on the right.

Using these spectral reflectances, $R_{sol}, \epsilon, T_{surf}$ and their modulations are calculated. Results are presented in **Figure 115**. Nevertheless, no significant impact of the cell parameter on R_{sol}, ϵ and T_{surf} is observed. ΔR_{sol} exhibits important relative variations (relative variations between the cases $a = 4.5\ \mu m$ and $a = 7\ \mu m$ of 60%), but due to the low values of ΔR_{sol}, these variations are not significant. ΔT_{surf} exhibits a slight decrease (-0.5 °C) for cell parameters from 4.5 µm to 6 µm, in accordance with a slight increase of $\Delta\epsilon$ (+0.2). Increasing the cell parameter thus does not improve the material thermal performance. This result shows that the contribution from the higher orders reflectance peaks is not enough to compensate the first order PBG not being correctly aligned with the blackbody emittance peak anymore and experiencing an amplitude decrease due to the reduced refractive index contrast at higher wavelengths. In this regard, it seems that shifting the PBG peak reduces the influence of the structure on the material emissivity.

4.3. Conclusion of this chapter

In this chapter, the optical and thermal properties of a polymer opal photonic crystal containing VO_2 in the opal interstices are studied. Structural parameters were chosen in order to maximize the impact of the PBG on the material emissivity. With a cell parameter $a = 4.5\ \mu m$ and 15 periods in the [111] direction a strong PBG effect occurs in the mid-IR, where the blackbody emittance peak at a temperature of $\tau = 70°C$ (approximate temperature of the VO_2 phase transition) is located. This reflectance peak leads to reduced emissivities in the cold conditions, which results in decreased values of $\Delta\epsilon = \epsilon_{cold} - \epsilon_{warm}$and thus increased values of $\Delta T_{surf} = T_{surf,cold} - T_{surf,warm}$, interesting for applications like energy-efficient coatings for buildings and satellites. Based on our simulation results (see **Figure 110**), an optimized case for this application would be for a VO_2 concentration of 10 vol% for which $\Delta T_{surf} = 0.1\ °C$ when considering a homogenized layer. However, the structure seems to have a negative impact in this case, as it tends to reduce ΔT_{surf}. On the other hand, in the case of a compact polymer opal photonic crystal consisting of polymer spheres of low refractive index ($n = 1.3$) surrounded by pure VO_2, the structure has a beneficial effect. Indeed, the strong PBG observed in this case reduces the material emissivity in the cold conditions from $\epsilon_{cold} = 0.90$ to $\epsilon_{cold} = 0.84$, resulting in a reduced emissivity modulation from $\Delta\epsilon = 0.42$ to $\Delta\epsilon = 0.33$ and an increase of the material surface temperature modulation from $\Delta T_{surf} = -11.8°C$ in the homogeneous case to $\Delta T_{surf} = -9.2°C$ in the structured material. In any case, ΔT_{surf} remains negative, which is not desired for such application.

For the camouflage application where a strong $\Delta\epsilon$ is desired, it seems that the optimized cases are obtained for high VO_2 concentrations. For a VO_2 total concentration higher than 52 vol%, $\Delta\epsilon$ varies around values from 0.45 to 0.47. This is comparable to the $\Delta\epsilon = 0.46$ measured on VO_2 nanopowder pellets by Ji et al. [5]. At these high VO_2 concentrations, the structure does not have much effect on the material emissivity as the material is more absorbent, which reduces the PBG amplitude.

It is important to notice that all these conclusions are based on simulations with assumptions which need to be checked by comparisons to experimental measurements. First, the interstices refractive index is computed through a Maxwell-Garnett homogenizing process, and thus a potential diffusion process by the VO_2 nanoparticles is not taken into account. Also, the structured material is supposed to be perfectly periodic, which is hardly the case for an experimental sample. Moreover, the estimation of the influence of the structure on the material performances is based on a comparison with a two-step Maxwell-Garnett homogenized material, which could lead to a bias depending on the way the material is homogenized. This bias has been nevertheless limited by the choice of this two-step Maxwell-Garnett homogenized process. It exhibited indeed the best agreement between the simulations of the structured material and of the homogenized one on wavelengths where the photonic band diagram of the structure showed a limited influence of the structure.

The next chapter will be dedicated to the comparison of the simulations with experimental data. As difficulties occurred in the fabrication of a polymer opal containing VO_2 nanoparticles, the comparison will be made on another structure, which can be assimilated as a disordered 2D photonic crystal over a metallic substrate.

Chapter 5 – Introduction of structural disorder

The simulations presented previously in this thesis were considering perfectly ordered structures. However, real opal photonic crystals made from self-assembly techniques often have undesired structural disorder [9,143,144]. Common kinds of structural disorders in opal photonic crystals include stacking faults (broken sequence ABCABC in the fcc structure), spheres radius variations or position variation from the perfect lattice sites.

In order to model more accurately real materials, artificial structural disorder related to the opal spheres position and size is introduced in the model used in this thesis. The goal is to show that our model can correctly describe materials having such structural disorders. In order to do so, a comparison between simulations results and experimental measurements is desired. However, no opal photonic crystal is available in our laboratory, while alumina 2D photonic crystals can be locally manufactured. For this practical reason the system chosen for this chapter is an alumina 2D photonic crystal.

The real material will first be described and an estimation of its structural parameters will be extracted using microscopy techniques. These parameters can then be introduced in our program in order to model the material optical behavior. In order to reach this final comparison between simulation results and experimental measurements, we will start from a similar material (a perfectly ordered porous alumina 2D photonic crystal) described in the literature [145] and progressively adjust its parameters. This slow process allows us to identify potential issues related to modelling structural disorder using a model which usually considers only perfectly ordered structures.

5.1. Description of the real material

5.1.1. Material synthesis

The studied sample is an anodized aluminum sample. The raw material is a 99.9% commercial aluminum plate with a size of 4 cm x 3 cm. The aluminum plate is submitted to a mechanical polishing process using a 1 µm polishing solution as a final step. The sample is then etched in a 15 vol% H_3PO_4 solution for 1h at 20°C. The anodizing process is a two step anodizing process, in a 0.3 M $(HCOO)_2$ solution. The first anodizing step is performed at a solution temperature of 5°C for 1h30 at an imposed current density of 30 mA/cm^2. The anodizing voltage is about 70 V during the process. After this first anodizing step, the sample is etched for 2h in an H_3PO_4 (6 wt%)/Cr_2O_3 (1.8 wt%) solution. The second anodizing step is performed at a solution temperature of 20°C for 3h40 at an imposed current density of 60 mA/cm^2. The anodizing voltage goes from about 16 V at the beginning of the process to about 100 V at its end.

Figure 116: Photography of the experimental sample placed on a sample holder, next to a color chart.

5.1.2. Structural characterizations

The material is observed through Scanning Electron Microscopy (SEM) using a MEB-FEG 6500F from JEOL. SEM micrographs are presented in **Figure 117**. **Figure 117a** shows the surface of the material. The oxide layer is porous, with air holes visible as dark areas, surrounded by lighter areas being the alumina material. These holes generally extend as cylinders until the substrate, but they might not be completely straight. The holes size and position are randomly dispersed, but seem to keep a short distance order, with a relatively constant distance between one hole and its six nearest neighbors.

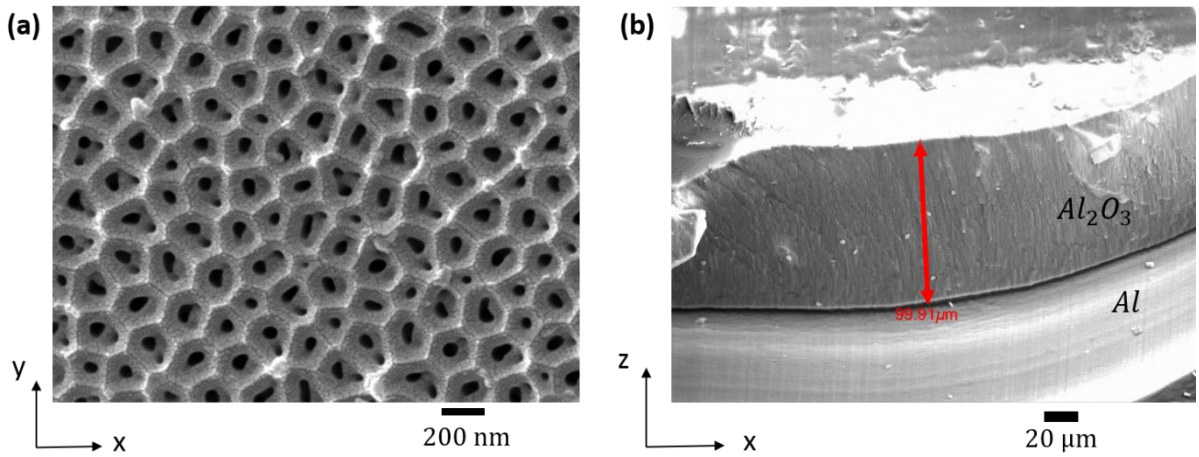

Figure 117: Top view (a) and side view (b) of the anodized aluminum material. The value indicated in red in the subfigure (b) is the oxide layer thickness, equal to 99.91 µm.

The oxide layer thickness is about 100 µm (**Figure 117b**). Note that in **Figure 117b** a gap is observed between the oxide layer and the metal: this is due to the fact that, when cutting the sample in order to have a side view, the oxide layer has been slightly peeled off.

5.1.3. Estimation of the cylinders size and lattice cell parameter

In order to evaluate the material pores size and position, image processing techniques were used on **Figure 117a**. After converting the picture to a grayscale image and adjusting the image contrast levels, a threshold is defined and adjusted so that most holes are split from the surrounding alumina. This is shown on the binarized picture in **Figure 118a**. The holes are represented as white areas in **Figure 118a**. These holes having various shapes, they are approximated by circular shapes, while keeping the same area. A total of 94 detected pores have been represented as red circles in **Figure 118b**.

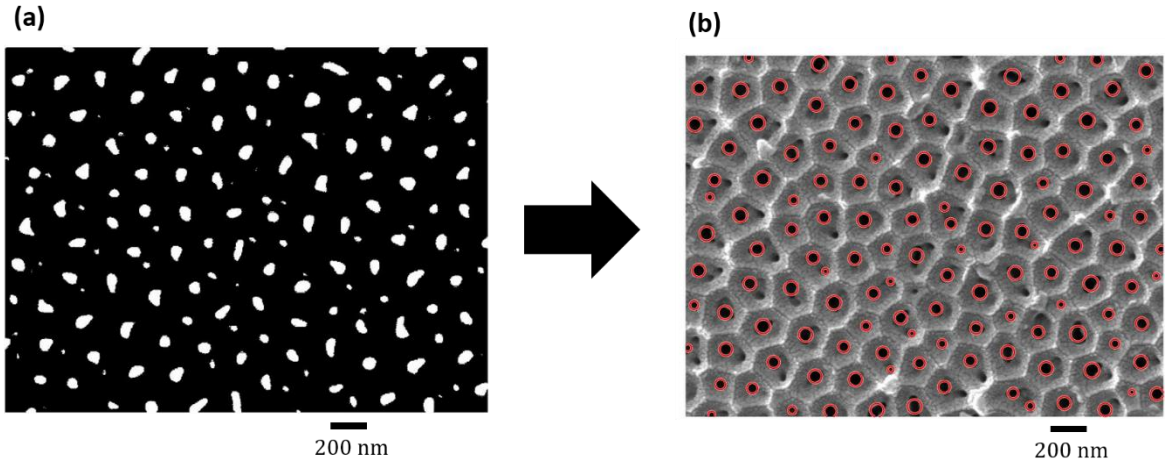

*Figure 118: Binarized picture from **Figure 117a** (a) and detected pores made circular while keeping the same area (red circles) superposed with the original picture (b).*

From there, each cylinder radius is extracted and the distribution of the cylinders radii on this image is given in **Figure 119b**. It appears that the histogram shows a slightly peaked distribution of the cylinders radii, with a mean radius of about $\mu_r = 30$ nm with a standard deviation of about $\sigma_r = 3$ nm. Knowing the coordinates of the centers of all the detected holes, the distance between the six nearest neighbors is also obtained by calculating the distance between a cylinder with all other cylinders, then sorting them in increasing distances and keeping the six shortest distances. The corresponding distribution for these six nearest neighbor distances is shown in **Figure 119a**. The histogram shows a peaked distribution, confirming the short distance order of the structure. The distribution has a mean of $\mu_a = 190$ nm and a standard deviation of $\sigma_a = 10$ nm. Keeping in mind that the structure is close to a triangular lattice, the distance between six closest neighbors corresponds to the cell parameter.

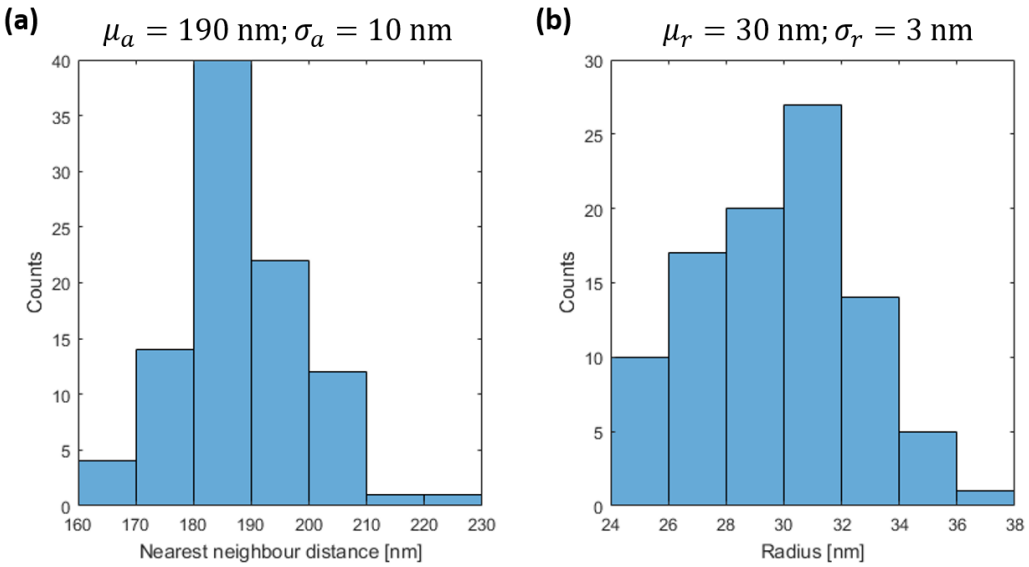

Figure 119: Histograms of the six nearest neighbor distance between cylinders (a) and of the cylinders radii (b) measured on ***Figure 117a****. Mean values and standard deviations of the distributions are also given.*

5.1.4. Optical properties measurements

The material spectral reflectance was measured using an X-Rite Ci 7800 spectrophotometer. **Figure 120** shows the specular (blue round markers) and total reflectance (green cross markers) which were measured in the visible range with an 8° incidence angle and non-polarized incident light. The wavelength resolution of the spectrophotometer is 10 nm. The illuminated area on the sample has a diameter of 17 mm.

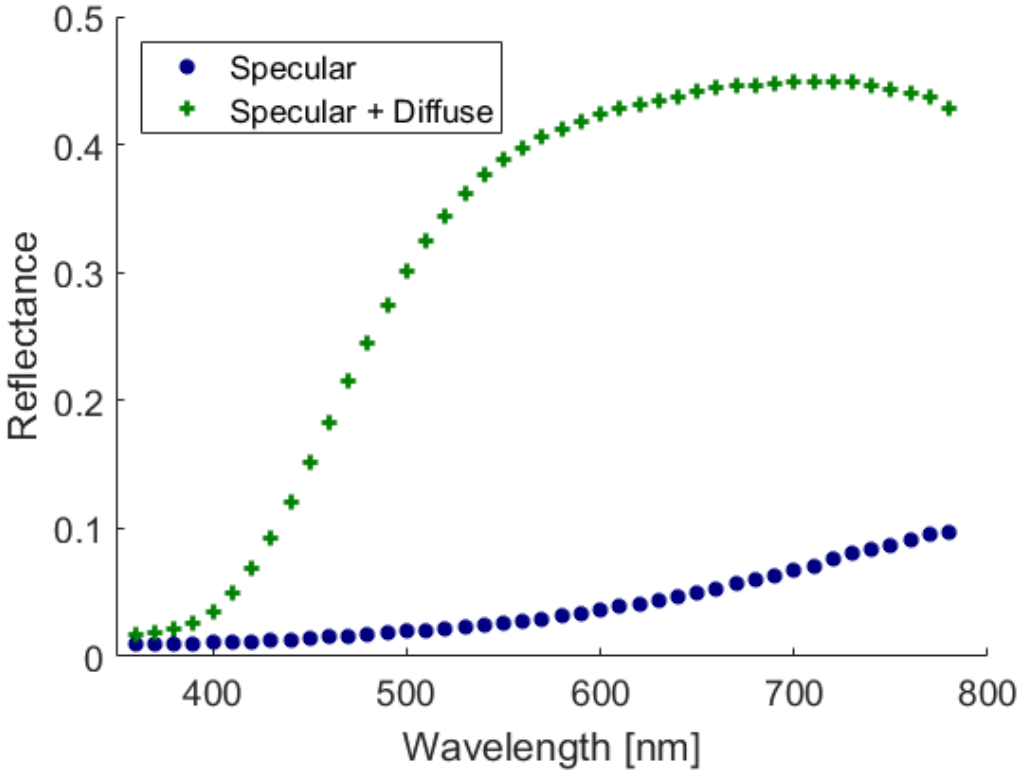

Figure 120: Measured specular and total reflectance spectra of the anodized aluminum sample with an 8° incidence angle and non-polarized incident light.

It appears that the reflected light is mostly scattered in directions different from the specular 8° direction, particularly for wavelengths longer than 400 nm. This may be explained by the surface roughness of the material (see **Figure 117a**) but a more detailed study of the material roughness should be done to confirm and quantify this phenomenon. Also, pores inhomogeneities could lead to scattering.

In our model, the material surface is considered perfectly flat, meaning there is no surface roughness involved. In addition, the model calculates the specular reflectance only. The scattering effect due to the surface is thus not modelled, so the material total reflectance will mainly correspond to the material specular reflectance. The simulation results will thus be compared to the measured total reflectance spectrum. Note that scattering from the material bulk can lead to a non-specular signal, which will be included in the measured total reflectance, but not in the simulation.

5.2. Perfectly ordered porous alumina photonic crystal: comparison with literature results

In this chapter, the goal is to prove that our model is able to correctly describe materials having structural disorder by comparing simulation results to experimental measurements in the case of a disordered alumina 2D photonic crystal. We start this study by modelling a perfectly ordered material presented in the literature by Kral et al. ([145]). This material is a porous alumina 2D photonic crystal described as air cylinders arranged in a triangular lattice and surrounded by pure alumina (Al_2O_3). From

there, after having verified the good agreement between our simulation results and literature results for a perfectly ordered material, structural disorder will be introduced.

5.2.1. Material description

In order to model a perfectly ordered 2D photonic crystal with cylinders arranged in a triangular lattice, a primitive cell containing two cylinders is used. The center positions (x_1, y_1) and (x_2, y_2) of these two cylinders, expressed as ratios to the cell periods in x and y directions, are:

$$\begin{pmatrix} x_1 \\ y_1 \end{pmatrix} = \begin{pmatrix} 1/4 \\ 3/4 \end{pmatrix} \quad \text{and} \quad \begin{pmatrix} x_2 \\ y_2 \end{pmatrix} = \begin{pmatrix} 3/4 \\ 1/4 \end{pmatrix}.$$

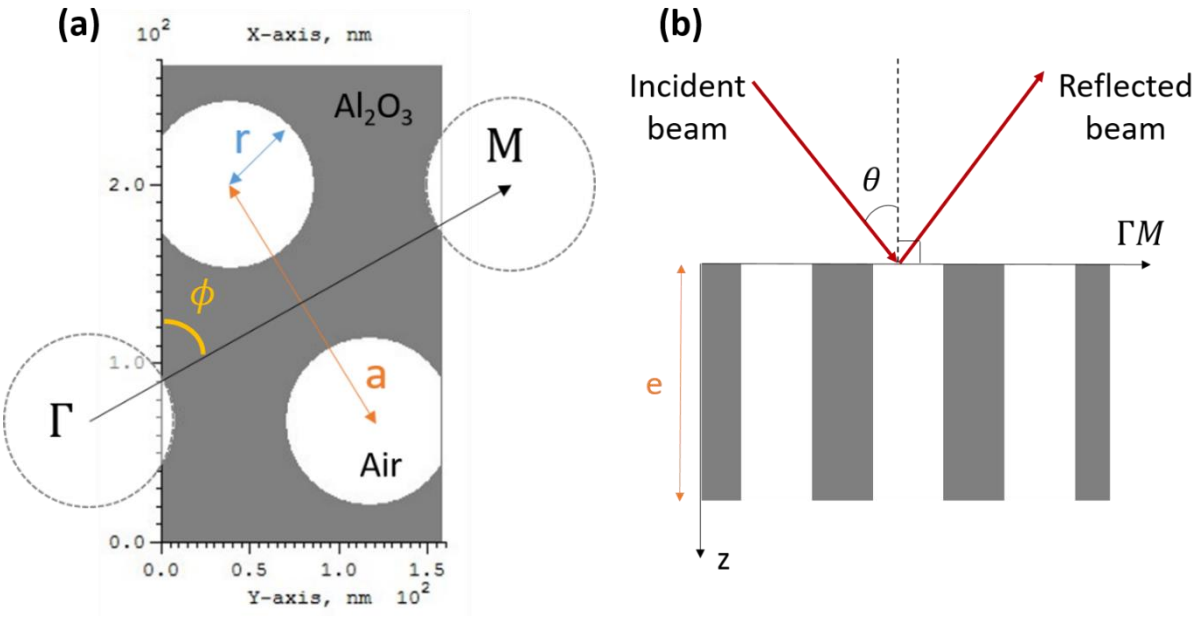

Figure 121: Top (a) and side (b) view of a porous alumina 2D photonic crystal having a triangular lattice. The ΓM direction, included in the xy plane with an angle $\phi = 60°$ with respect to the x-axis, is represented by adding two cylinders surrounding the primitive cell. r is the cylinder radius, a the cell parameter and e the material thickness. The light is incident with an angle θ relatively to the normal of the material surface (z-axis). The incidence plane contains both z and ΓM directions.

A top-view of the material primitive cell is represented in **Figure 121a** along with the considered parameters. Two surrounding cylinders are added to define the crystal ΓM direction. In order to fit the parameters given in [145], the cylinders radius is set to $r = 47$ nm, and the cell parameter is set to $a = 157$ nm. The material is surrounded by air on both sides. The incidence plane is defined by the normal to the surface and the crystal ΓM direction as indicated in **Figure 121b**. In order to include this ΓM direction into the incidence plane, the angle parameter ϕ (angle between the incidence plane and the x-axis) is set to 60°. θ is the incidence angle relatively to the normal of the material surface. Alumina is modelled by the refractive index given by the MC Grating catalog. This index is shown in **Figure 122**. The material thickness parameter e in the z direction is made vary between 1 and 10 µm.

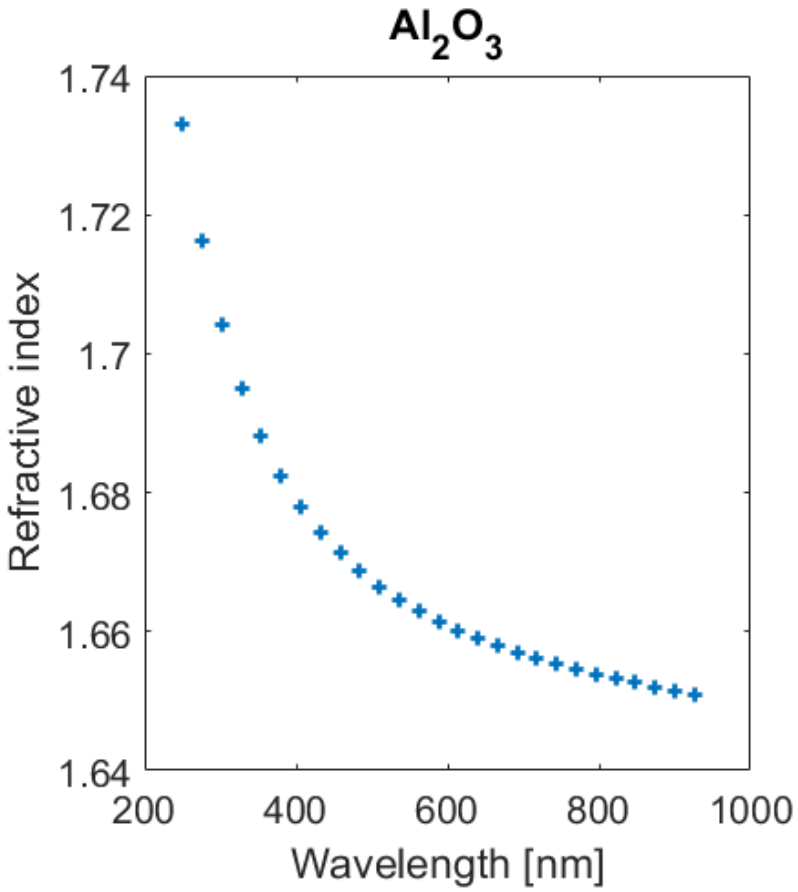

Figure 122: Alumina refractive index extracted from the MC Grating catalog. The refractive index imaginary part is zero.

5.2.2. Comparisons of simulated reflectances with Kral et al. results

Angular-dependent reflectance spectra have been calculated and presented in **Figure 124** for two different thicknesses ($e = 300$ nm and $e = 900$ nm) for TE polarized incident light. For both thicknesses, a band with high reflectance can be observed at normalized frequencies between about 0.53 and 0.58 (equivalent to a wavelength range from 271 nm to 296 nm, so in the UV region) at $\theta = 80°$. This band shifts to higher frequencies as the incidence angle decreases. This peak is linked to the band structure. Oscillations due to thin film interferences are also observed, and their frequency increases for thicker materials, as predicted by the positions ω_m of the local minima:

$$\omega_m = \frac{a\, m}{2\, n_{eff}\, e \cos(\theta_r)} \tag{5. 1}$$

with a the cell parameter, n_{eff} the material effective refractive index, e the material thickness, m a positive non-zero integer and θ_r the angle of the refracted light inside the film represented in **Figure 123**. n_{eff} is computed through the Maxwell-Garnett formula, taking into account the volume fraction of air due to the air cylinders which is 0.33.

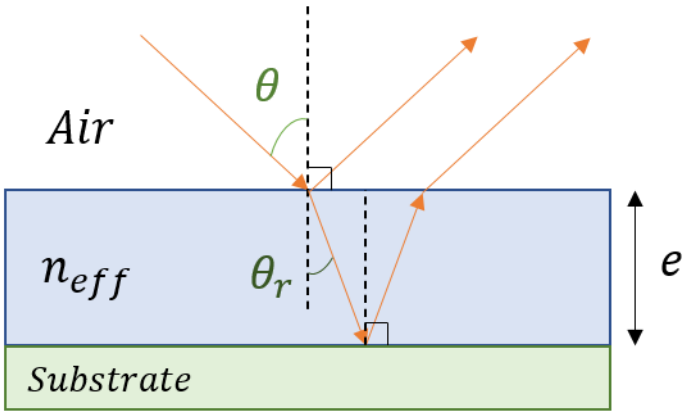

Figure 123: Illustration of the two principal optical paths leading to thin film interferences.

Using this equation, ω_m values were calculated at an incidence angle of $\theta = 15°$. It is worth noting that since the alumina has a slightly dispersive refractive index, n_{eff} varies with the frequency, so does ω_m. Two values for the alumina refractive index were used: 1.67 and 1.73, for respectively lower and higher frequencies. The resulting ω_m are marked on **Figure 124**, with respectively yellow and magenta markers, highlighting the positions of the oscillations minima.

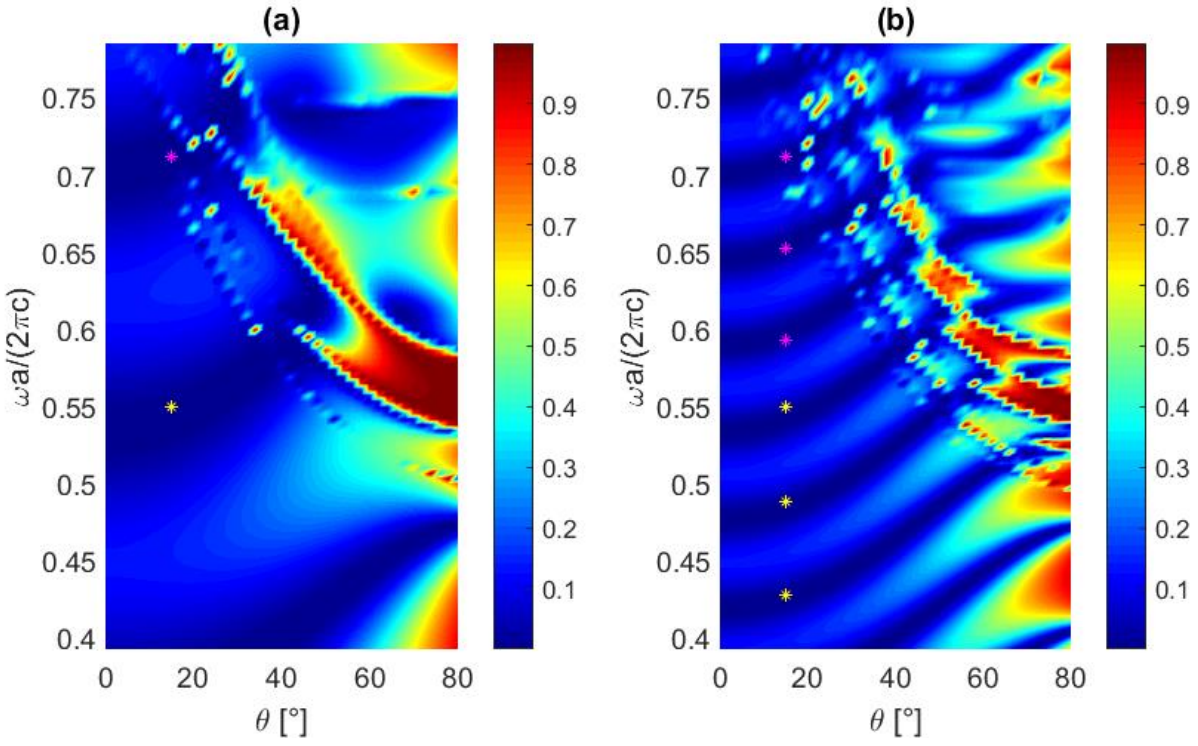

Figure 124: 2D maps of the calculated reflectance spectra of a perfectly ordered porous alumina triangular photonic crystal (i.e. air cylinders arranged in a triangular lattice) as a function of the incidence angle θ and the normalized frequency, for TE polarized incident light. The material thickness is set to 300 nm (a) and 900 nm (b). The yellow and magenta markers indicate the positions of the thin film interferences minima ω_m at $\theta = 15°$ computed respectively for $n_{eff} = 1.67$ and $n_{eff} = 1.73$.

The same spectral reflectances were observed by Kral et al. [145]. **Figure 125** shows a map of the reflectance spectra of such material for different thicknesses e (300 nm and 900 nm), as a function of both incidence angle θ and normalized frequency $\omega a/(2\pi c)$, for TE polarized incident light. The band diagram for TE polarization is also represented in white lines. As in **Figure 124**, a reflectance band is observed in both thickness cases, following the shape of the first band of the band diagram.

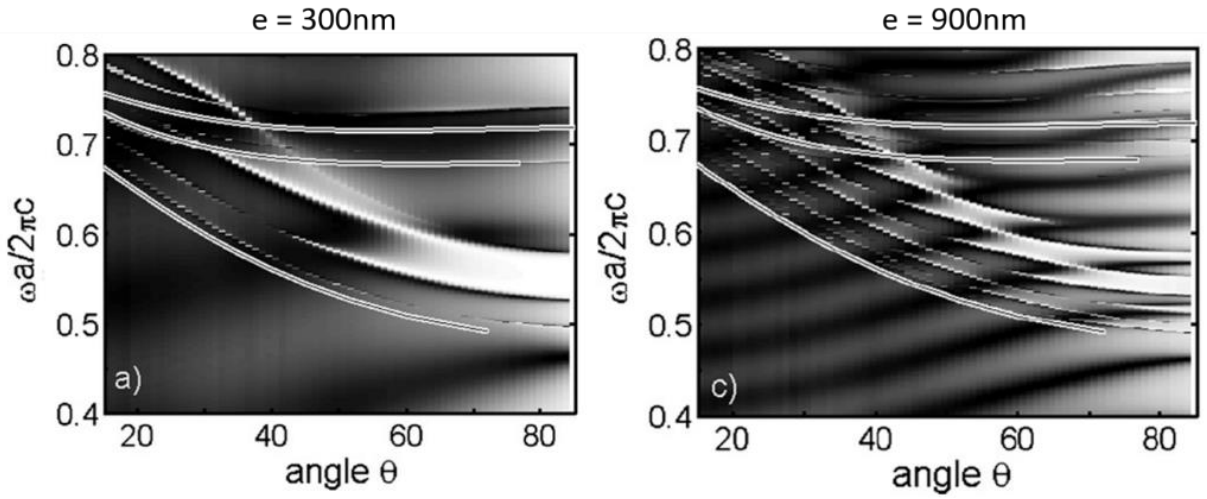

Figure 125: 2D maps of the calculated angular-dependent reflectance spectra of a perfectly ordered porous alumina triangular photonic crystal of thickness e = 300 nm (left) and 900 nm (right), as a function of the incidence angle θ and the normalized frequency, for TE polarized incident light. The three white bands correspond to the first 3 bands of the band diagram of the structure (considered having an infinite thickness). Both graphs are extracted from [145].

Figure 124 and **Figure 125** are compared in **Figure 126**, where the figures sizes are rescaled in order to be perfectly superposed. Our simulation results (in colors) have a larger frequency and incidence angle range, leading to a wider window. For the shared values of frequency and incidence angle, the comparison between the reflectance shapes shows that our simulation using the FMM method and the simulation results using the S-matrix obtained by Kral et al [145] are in good agreement.

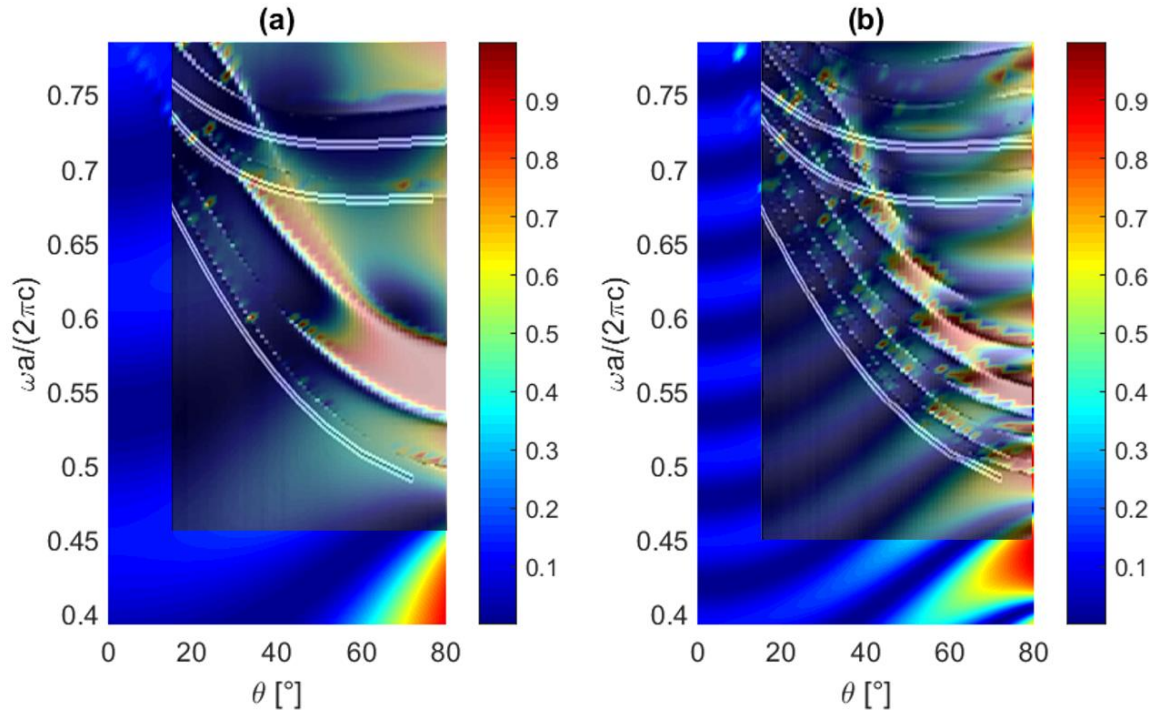

Figure 126: Superposition of 2D maps of the spectral reflectance of a perfectly ordered porous alumina triangular photonic crystal as a function of incidence angle and normalized frequency, for TE polarized incident light, for different material thicknesses: 300 nm (a) and 900 nm (b). The three white bands correspond to the first 3 bands of the band diagram of the structure (considered having an infinite thickness). Comparison between this work (colors) and simulation results extracted from [145] *(grayscale).*

5.3. Introduction of disorder in an alumina 2D photonic crystal

From this perfectly ordered alumina 2D photonic crystal, structural disorder is introduced by slight variations of the cylinders position and size, in order to better model a real material containing these structural defects. In this section, a description of the process is made, along with a study of its effect on the material spectral reflectance properties.

5.3.1. Disorder parameters definition

Each cylinder is defined by its center position and radius (its height is set by the material thickness). We define a property vector for each cylinder k:

$$P_k = \begin{pmatrix} x_k \\ y_k \\ r_k \end{pmatrix} \tag{5. 2}$$

with x_k, y_k being the 2D coordinates of its center position and r_k its radius. In the case of the perfectly ordered crystal, these parameters are denoted x_k^0, y_k^0 and r_k^0. In this chapter, two kinds of structural disorder are introduced: one related to the cylinder position, and one to its size. This means that in the first case, the first two parameters are slightly changed, while in the second, the last parameter is changed.

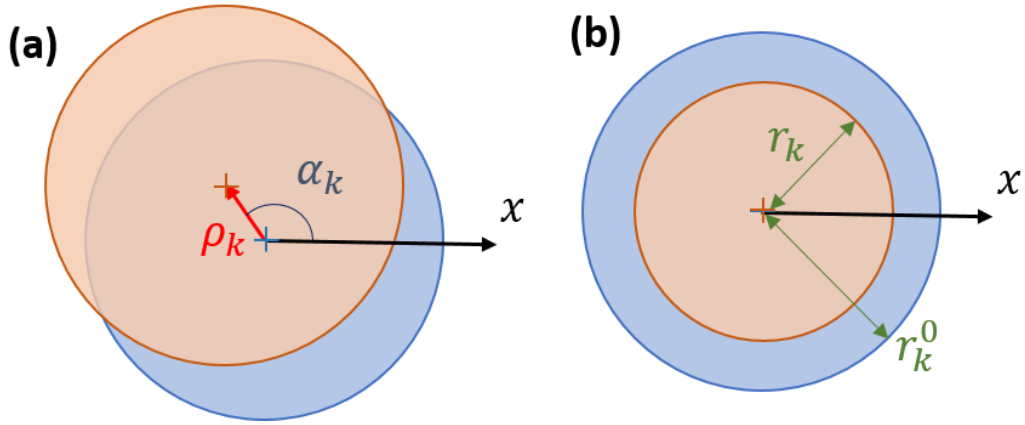

Figure 127: Schematic representation of a cylinder before (blue) and after (orange) applying a center position shifting defined by a distance ρ_k and an angle α_k relative to the x-axis (a), and a radius variation from r_k^0 to r_k (b) .

The variation in the k-th cylinder position (see **Figure 127a**) is defined by:

- a distance ρ_k between the center position before and after shifting obtained through a standard normal distribution centered in 0 with a standard deviation σ_a. This normal distribution probability density is:

$$f(\rho_k) = \frac{1}{\sigma_a\sqrt{2\pi}}\, e^{-\frac{{\rho_k}^2}{2\sigma_a^2}} \tag{5. 3}$$

  From this distribution, an array ρ related to the distance shift for each cylinder is computed.

- an angle α_k to indicate the direction in which the shift is done, with respect to the x-axis. Since the distance can take both positive and negative values, in order to cover all possible new positions, this angle is defined by a uniform distribution from 0 to 180°.

The variations of the cylinder radii (see **Figure 127b**) are defined with a normal distribution of the parameter r_k, centered in r_k^0 and with a standard deviation σ_r:

$$g(r_k) = \frac{1}{\sigma_r\sqrt{2\pi}}\, e^{\frac{-(r_k - r_k^0)^2}{2\sigma_r^2}} \tag{5. 4}$$

From this distribution, an array r related to the radius of each cylinder is computed.

Applying both position and size variations on a cylinder k, the new vector related to its parameters is:

$$P_k = \begin{pmatrix} x_k^0 + \rho_k \cos(\alpha_k) \\ y_k^0 + \rho_k \sin(\alpha_k) \\ r_k \end{pmatrix} \tag{5. 5}$$

In order to define these two types of structural disorders, two parameters are required: the standard deviation for each normal distribution σ_a and σ_r respectively for the shift in the cylinder position and size.

As a short comment, all these parameters can also be used in the case of a 3D opal photonic crystal, replacing cylinders with spheres, each having their index k. The property vector P_k (*Equation* (5. *2*)) thus has an extra component z_k and *Equation (5. 5)* becomes:

$$P_k = \begin{pmatrix} x_k^0 + \rho_k \cos(\alpha_k)\sin(\beta_k) \\ y_k^0 + \rho_k \sin(\alpha_k)\sin(\beta_k) \\ z_k^0 + \rho_k \cos(\beta_k) \\ r_k \end{pmatrix} \tag{5. 6}$$

with β_k the angle defining the direction in which the shift is done, with respect to the z-axis (see **Figure 128**). This angle is drawn from an uniform distribution from 0 to 360°.

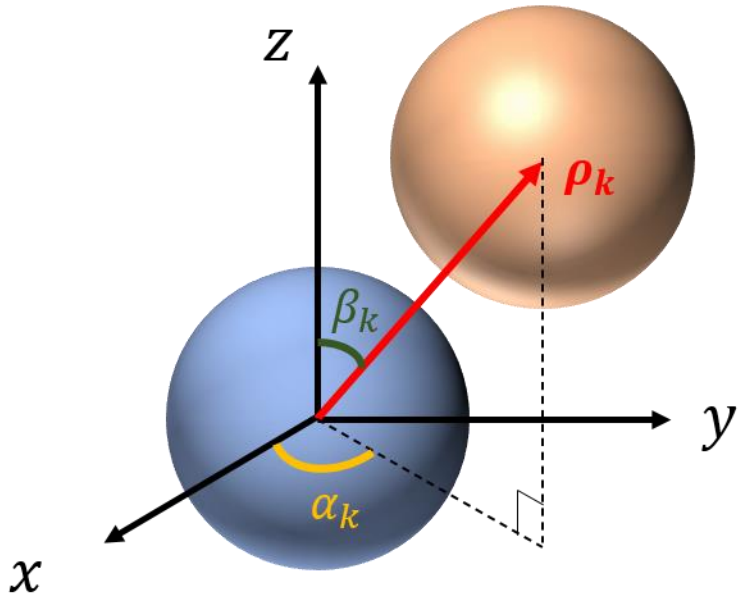

Figure 128: Schematic representation of a sphere before (blue) and after (orange) applying a center position shifting defined by a distance ρ_k and two angles α_k relative to the x-axis and β_k relative to the z-axis.

No disordered 3D structure is shown in this chapter as it is focused on an alumina 2D photonic crystal, but the program is implemented and ready for use.

5.3.2. Influence of the size of the primitive cell on the disorder simulation

In order to introduce structural disorder, the cylinders radius or position will be moved from their "perfect" values. However, considering a primitive cell with only two cylinders does not allow to introduce much disorder, as the FMM method assumes periodic boundary conditions (see **Figure 129a**). A bigger primitive cell containing more cylinders is thus required. An example of this supercell is represented in **Figure 129b** with a primitive 2x2 supercell composed of 4 adjacent 2-cylinders primitive cells (two cells in the x direction and two cells in the y direction).

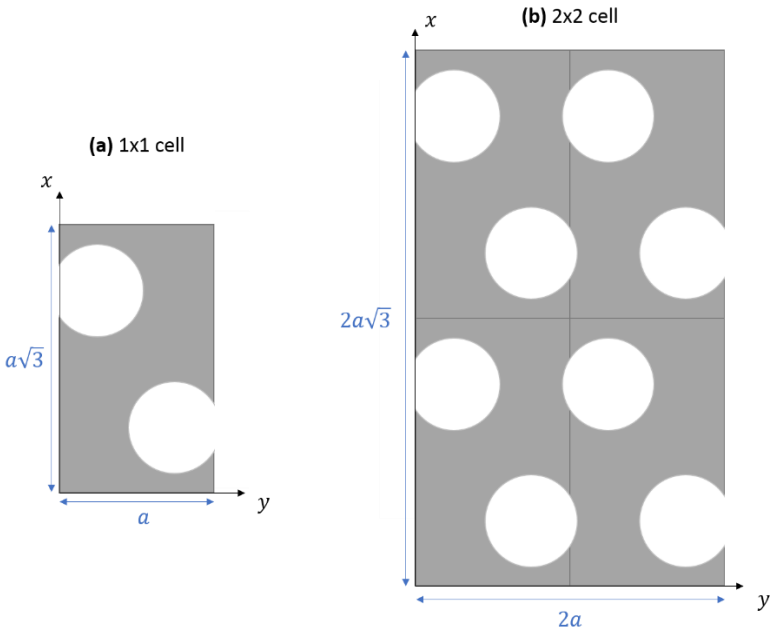

Figure 129: Representation of a 2-cylinder primitive cell (a) and of a primitive 2x2 supercell composed of 4 adjacent 2-cylinder primitive cells (b). The cylinders are arranged in a triangular lattice.

To illustrate the importance of increasing the supercell size, four draws are performed for four different supercells of 1x1, 2x2, 3x3 and 4x4 adjacent 2-cylinder primitive cells using the mean and standard deviation parameters from **Figure 119**. In each case, different parameters ρ_k and r_k are drawn according to the description given in *Equations* (5. *3*) and (5. *4*) ($\sigma_a = 10\,\mathrm{nm}$ and $r_k^0 = 30\,\mathrm{nm}$; $\sigma_r = 3\,\mathrm{nm}$). The resulting histograms for these two parameters are given in **Figure 130**. On each row, the supercell size is labelled on the left. The left histograms are associated with the distance ρ_k between the center position of the k-th cylinder before and after position shifting, while the right histograms are associated with the k-th cylinder radius r_k. The bins widths are respectively 10 nm and 2nm for ρ_k and r_k. For each histogram, the mean and standard deviation values recalculated after drawing the values are also displayed. These recalculated means and standard deviations are denoted $\tilde{\mu}_a, \tilde{\sigma}_a$ respectively for the cylinder position and $\tilde{\mu}_r, \tilde{\sigma}_r$ respectively for the cylinder radius.

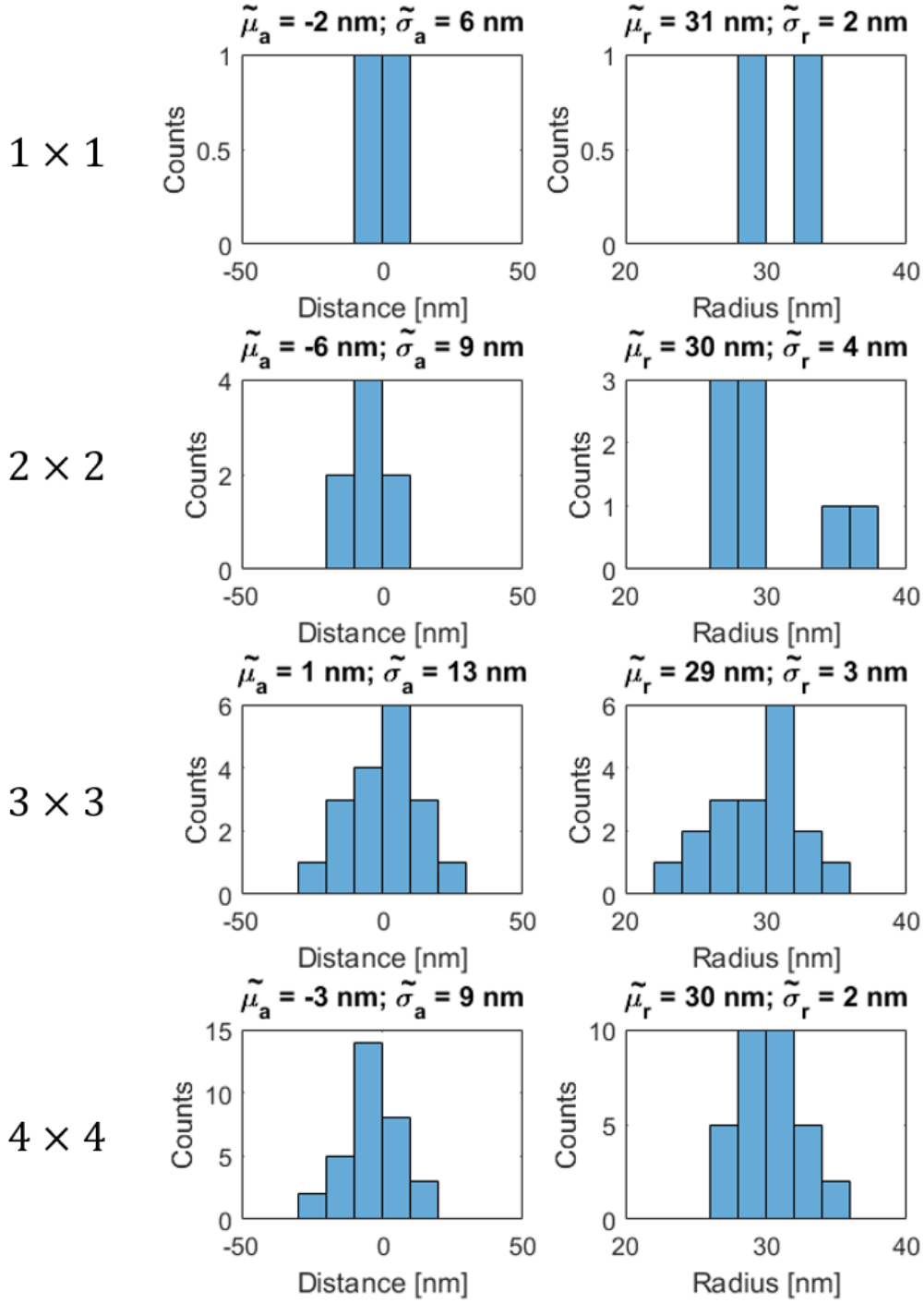

Figure 130: Histograms of the center position shift ρ_k (left) and the cylinder radius r_k (right) for different primitive supercell sizes 1x1, 2x2, 3x3 and 4x4 from top to bottom. The bin sizes are 10 nm for the center position shifts and 2 nm for the radii. The associated mean $\tilde{\mu}$ and standard deviation $\tilde{\sigma}$ values recalculated after drawing the values are also displayed.

On the top most row, associated with a single 2-cylinder primitive cell (denoted as 1x1), only two cylinders are modelled. As the supercell size increases, more cylinders are modelled and the distributions for ρ_k and r_k tend to visually become closer to the normal distribution used. An infinite number of cylinders would lead to this normal distribution, but in practice we need to choose a finite cell size. Looking at these histograms, it seems that the 3x3 supercell case shows a histogram close enough to a normal distribution. The mean and standard deviation values recalculated from the drawn values are quite similar to those used to define them. Taking also into account computation time which

grows with the primitive cell size, for the future calculations, we thus decide to limit the supercell size to a 3x3 supercell composed of 9 adjacent 2-cylinder primitive cells. In this case, a total of 18 cylinders are modelled.

5.3.3. Adaptation of the simulation number of modes for primitive supercells

Results obtained with a 2-cylinder primitive cell have to be the same as with a bigger primitive supercell in the case of a perfectly ordered material. Based on this fact, the simulation parameters in the case of a primitive supercell will be adapted to have a correct simulation of the material optical properties. Spectral reflectances for both cases are calculated in the UV region [200 nm – 400 nm] at various incidence angles θ from normal incidence ($\theta = 0°$) to $\theta = 60°$ with a step of 20°. For this study four different sizes of primitive supercells were considered: 2x2 (**Figure 129b**), 3x3 and 4x4 primitive supercells.

With increasing the primitive cell size, the required number of modes of the Fourier series decomposition (see **Section 1.4.3**) required to perform correctly the FMM calculation increases. For example, in the case of 3x3 primitive supercell, the number of modes used in the previous section (15 modes in the x direction and 7 in the y direction) do not lead to a good agreement with the reflectance spectra obtained for a 2-cylinder primitive cell, particularly for non-normally incident light. **Figure 131** shows the comparison between these two cases, for different number of modes in the x and y directions, listed in **Table 11**.

Number of modes in the…	
x direction	**y direction**
15	7
15	15
20	15

Table 11: List of the number of modes used to compute the angular-dependent spectral reflectance.

For each considered incidence angle θ, the reflectance spectra related to these different pairs of numbers of modes are compared to the spectral reflectance in the case of the 2-cylinder primitive cell. In order to identify more accurately which curves diverge from this reference reflectance, zoomed views are given in the insets of **Figure 131**. It appears that differences are observed for the yellow and orange curves, related to number of modes in the x and y directions of respectively 15 and 7, and 15 and 15, whereas the violet curve related to 20 modes in the x direction and 15 in the y direction seems quite similar to the blue curve used as the reference reflectance. From these results, we consider that 20 modes in the x direction and 15 modes in the y direction are required for a 3x3 primitive supercell.

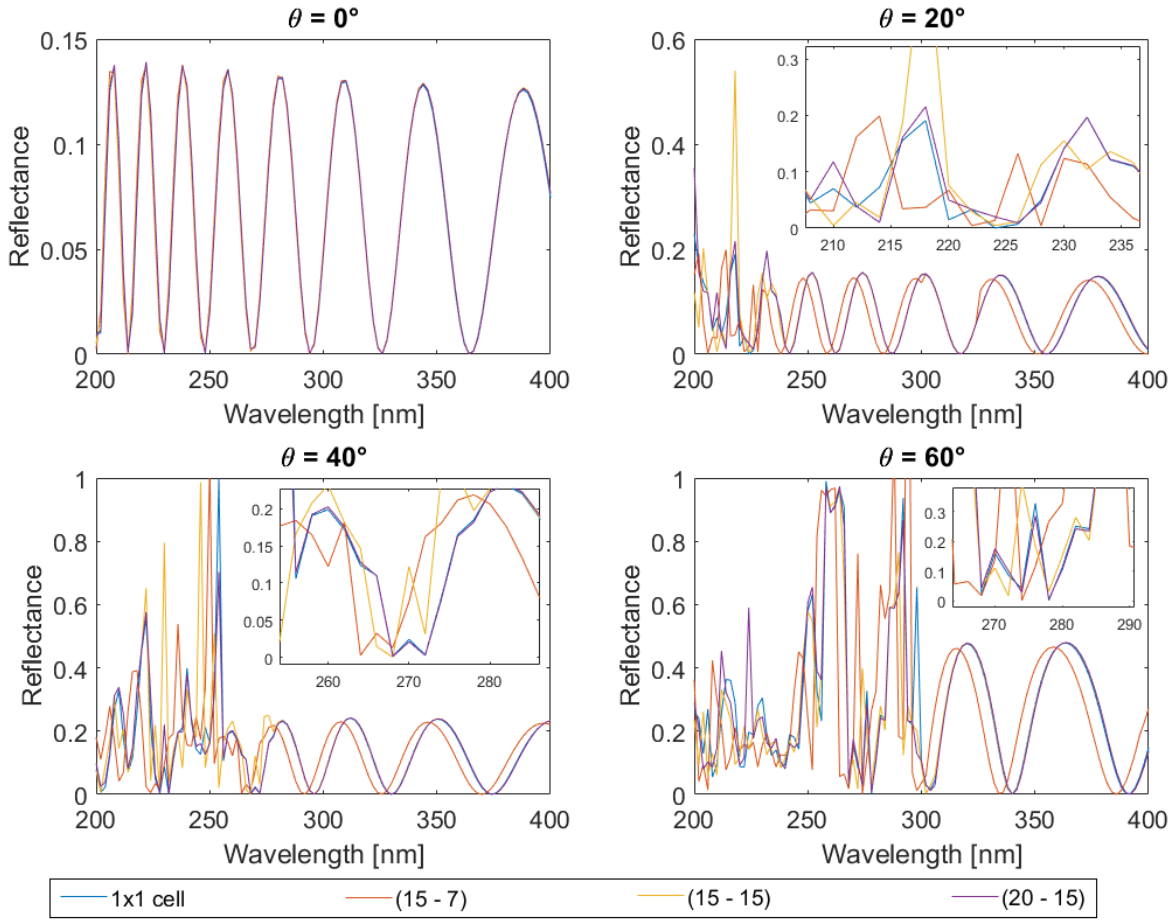

Figure 131: Reflectance spectra of a perfectly ordered porous alumina triangular photonic crystal (thickness $e = 1\ \mu m$) for different incidence angles θ (0°, 20°, 40° and 60°), for TE polarized incident light, in the case of a 2-cylinder primitive cell (blue curves, denoted as 1x1 cell) and for a 3x3 primitive supercell with different numbers of modes. The number of modes is denoted as ($m_x - m_y$) with m_x the number of modes in the x direction and m_y the number of modes in the y direction. Insets are zoomed views on parts of the curves. The number of modes in the case of the 2-cylinder primitive cell is 15-7.

Applying this method of adjusting the number of modes to the size of the primitive supercell, spectral reflectances are calculated for the different primitive supercells for different incidence angles. The number of modes used to calculate the 1x1, 2x2, 3x3 and 4x4 cells are respectively (15 - 7), (15 - 7), (20 - 15), (25 - 15). Results are presented in **Figure 132**.

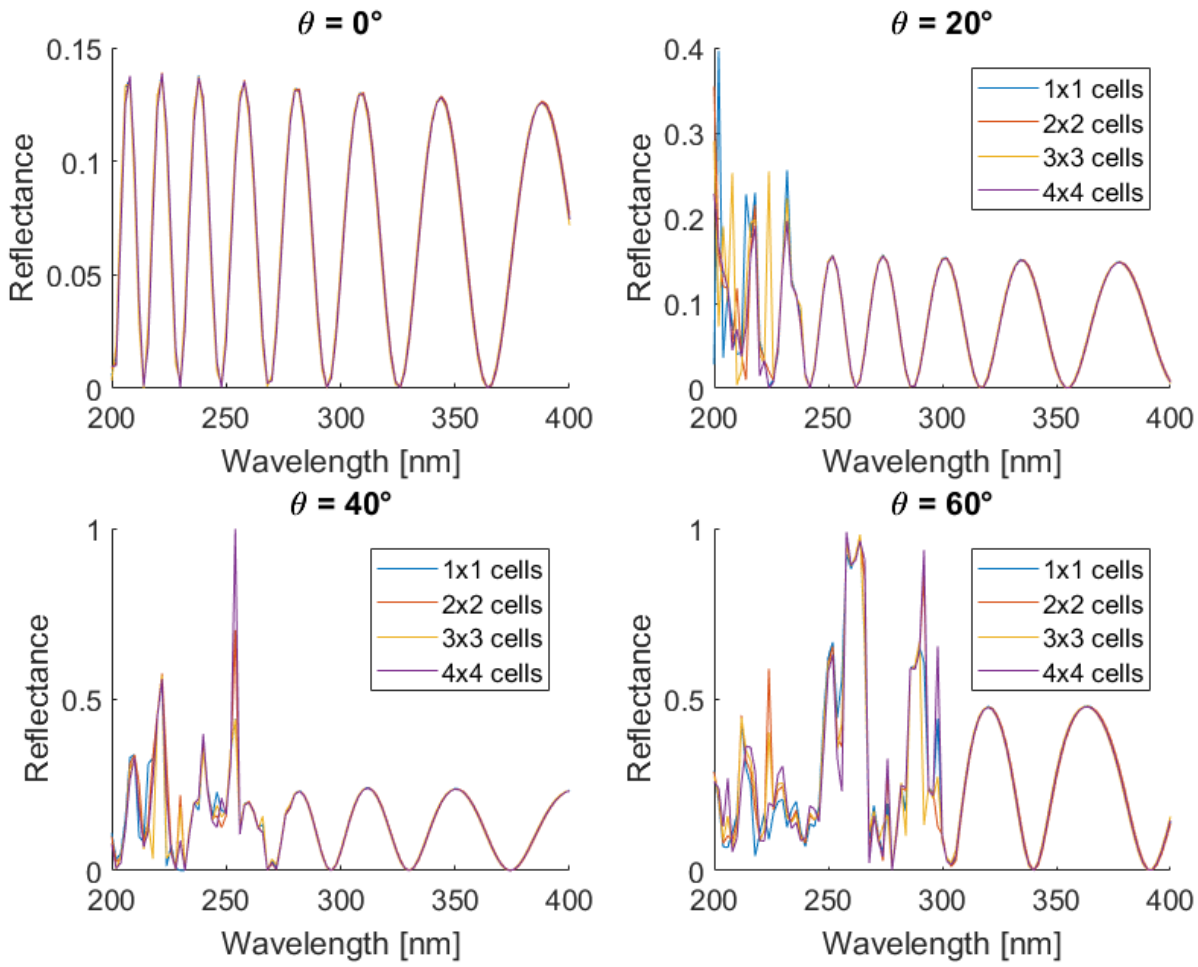

Figure 132: Reflectance spectra of a perfectly ordered porous alumina triangular photonic crystal (thickness $e = 1$ μm) for different incidence angles θ (0°, 20°, 40° and 60°), for TE polarized incident light, in the case of a 2-cylinder primitive cell (blue curves, denoted as 1x1 cell) and for 2x2, 3x3 and 4x4 primitive supercells. The numbers of modes are respectively (15-7), (15-7), (20-15) and (25-15) for the 2-cylinder primitive cell, the 2x2, 3x3 and 4x4 supercells.

With a normal incident light, all reflectance spectra are exactly the same, whatever the primitive cell size. Oscillations due to thin film interferences dominate. As the incidence angle increases, the high reflectance band observed earlier (cf. **Figure 124**) at high incidence angles starts to appear. For each incidence angle considered, the four curves are quite superposed, which means that the simulation results are independent of the primitive cell size when the number of orders is chosen adequately.

After this verification, we can now introduce structural disorder in the system with a big primitive supercell. In the following the 3x3 primitive supercell composed of 18 cylinders is modelled. For the calculations, 20 modes in the x direction and 15 modes in the y direction are used, as these values lead to results comparable with the case of a 2-cylinder primitive cell.

5.3.4. Influence of structural disorder

In this section, structural disorder is introduced in the material in order to study its influence on the material optical properties. First, only a disorder related to the cylinder position is introduced, and then only one related to cylinders size.

5.3.4.1. Cylinder position shift

In this section, only a shift in the cylinder center position is considered, with the parameter σ_a equal to different values (5, 10 and 20 nm) comparable to the σ_a from **Figure 119**, in order to evaluate the impact of this kind of structural disorder on the material optical properties. The cylinders radius is kept constant at a value of $r = 47$ nm. A total of 18 cylinders (3x3 primitive supercell) is considered and the top-view of the three generated structures is represented in **Figure 133**, along with the case of the perfectly ordered structure.

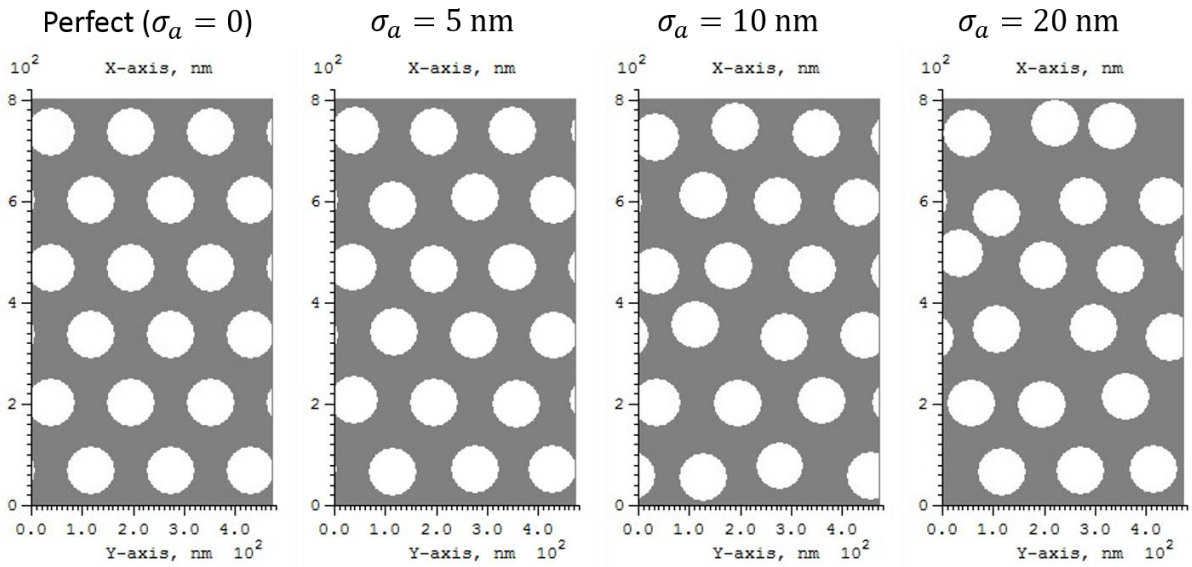

Figure 133: Top view of air cylinders almost arranged in a triangular lattice, as their center position varies with different standard deviations σ_a. The surrounding matrix is pure alumina.

For these four structures, angular dependent spectral reflectances are calculated at different incidence angles θ from 0° to 80°. Results are shown in **Figure 134**.

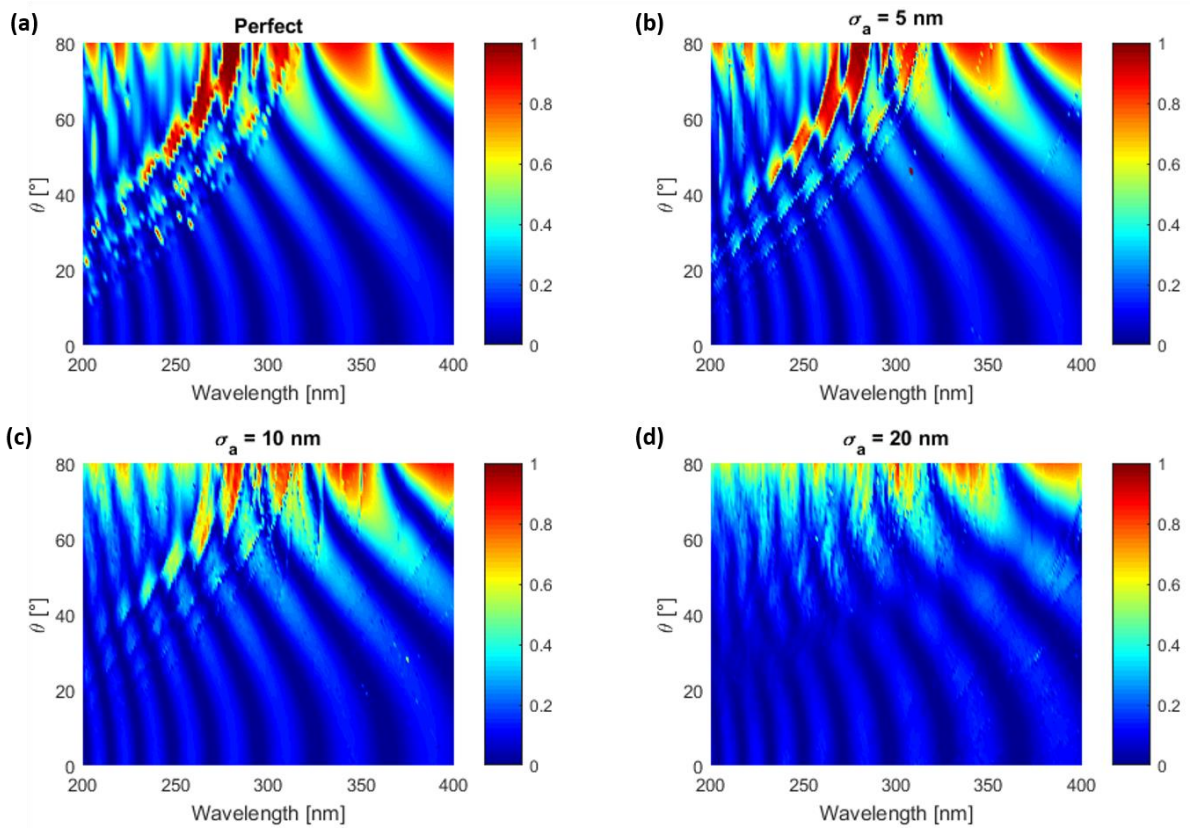

Figure 134: 2D maps of the angular-dependent reflectance spectra of air cylinders, surrounded by alumina, arranged in a triangular lattice (a), with a slight variation of their center position with different standard deviations σ_a of 5 nm (b), 10 nm (c) and 20 nm (d), with a TE-polarized light incident with an angle θ on the material surface. The material thickness is $e = 1\ \mu m$.

The oscillations due to thin film interferences are not influenced by the introduction of disorder, as they mainly depend on the effective refractive index and the layer thickness, which are both unchanged here. The noticeable change due to this kind of disorder is about the high reflectance band observed at oblique incidences. As disorder is introduced into the model, the band observed around 280 nm at an 80° incidence angle gradually disappears due to the loss of coherence of the system. With a less periodic structure, the effect due to the material structure decreases.

5.3.4.2. Cylinders size variations

In this section, the influence of the variations in the cylinders size on the material optical properties is studied. The cell parameter is kept constant here ($a = 157$ nm). The cylinders size varies with a normal distribution having a mean value $\mu_r = 47$ nm and various cases for the standard deviation σ_r: 0 (not disordered case), 5, 10 and 20 nm. The values of σ_r are higher than the experimental value obtained in **Figure 119** in order to clearly identify the impact of σ_r on the optical properties. The generated structures are represented in **Figure 135**.

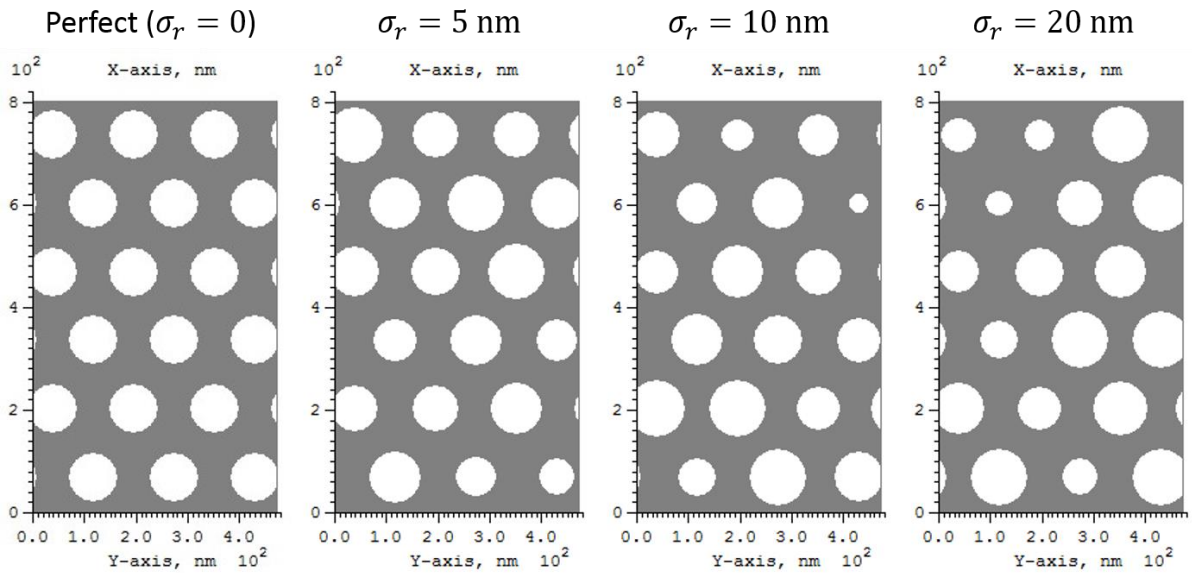

Figure 135: Air cylinders arranged in a triangular lattice, surrounded by alumina, with various sizes defined by a normal distribution on the cylinders radii, having a standard deviation σ_r.

Spectral reflectances are calculated in each case for different incidence angles θ from 0° (normal incidence) to 60°. Results are presented in **Figure 136**. The high reflectance band observed at high incidence angles (see **Figure 134a**) is visible in these reflectance spectra at oblique angles ($\theta = 60°$, see **Figure 136d**), especially in the perfectly ordered material (blue curve) around a wavelength of 260 nm. The same observation as with the study of the disorder related to the cylinders position (previous section) is made: when structural disorder is introduced, the amplitude of this reflectance band due to the material ordered structure decreases. A shift of the thin film interferences is observed, depending on the value of σ_r, particularly for small incidence angles. This is due to the fact that the effective refractive index of the material is dependent on the air volume fraction, which varies with the cylinders radii. As the cylinders radii are randomly drawn, the effective refractive index is not a monotonic function of σ_r, which for example explains that the interferences are more shifted from the perfect case for $\sigma_r = 10$ nm than for $\sigma_r = 20$ nm.

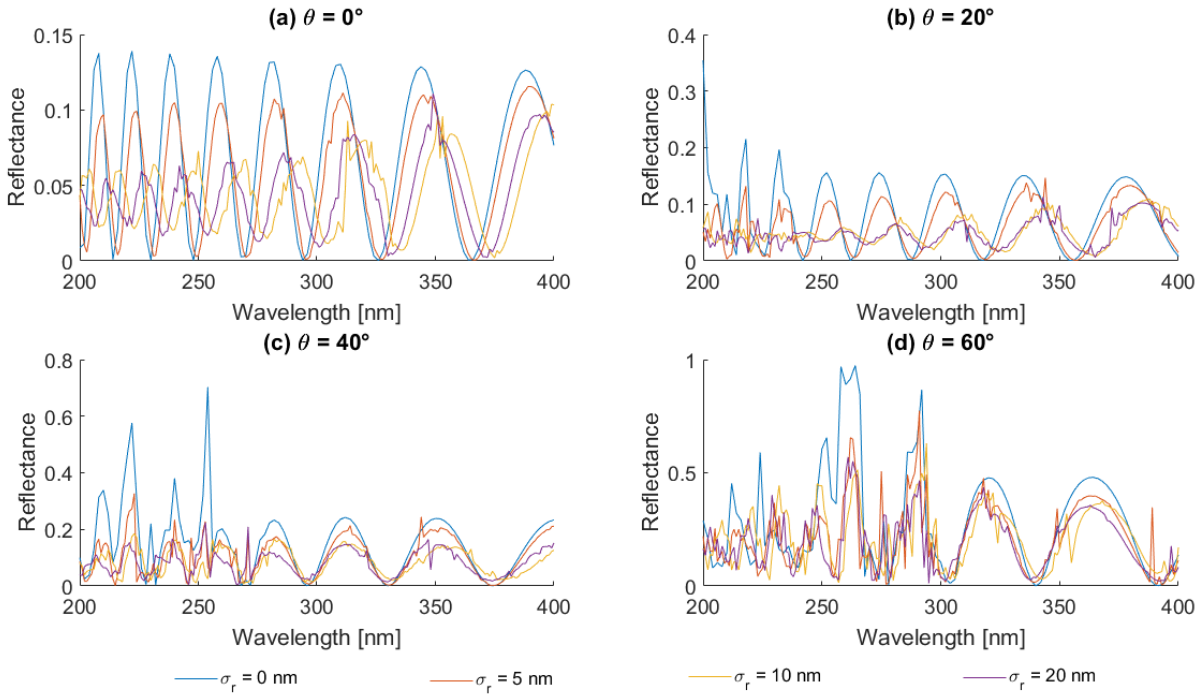

Figure 136: Reflectance spectra of air cylinders arranged in a triangular lattice, surrounded by alumina, with a cylinders radii variation defined by a standard deviation σ_r , at different incidence angles θ. The incident light is TE polarized and the material thickness is 1 µm.

5.3.5. Rotation of the incidence plane

The initial periodic structure before introducing disorder is highly anisotropic. In order to smoothen a residual anisotropy of the material after introducing disorder, the results obtained for incidence planes with various directions are averaged. The idea is to consider multiple values for ϕ, the angle between the incident plane and the x-axis, and average the resulting reflectances.

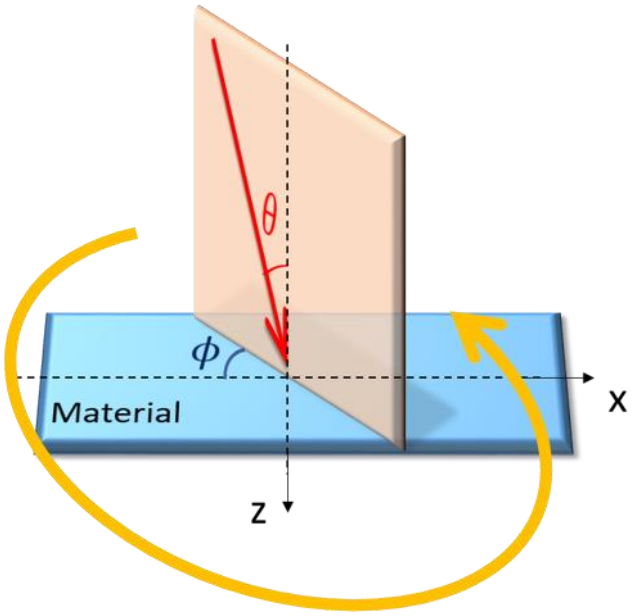

Figure 137: Rotation of the incidence plane around the z-axis, associated with a variation of the parameter ϕ.

Spectral reflectances are calculated for different incidence planes defined by different angles ϕ from 0° to 180° with a 1° step, with the same incidence angle $\theta = 45°$ (see **Figure 137**) for each disordered structure considered in **Figure 133** (variation of the cylinder positions only). Results are shown in **Figure 138**. The case of the perfectly ordered structure is also represented in **Figure 138a**.

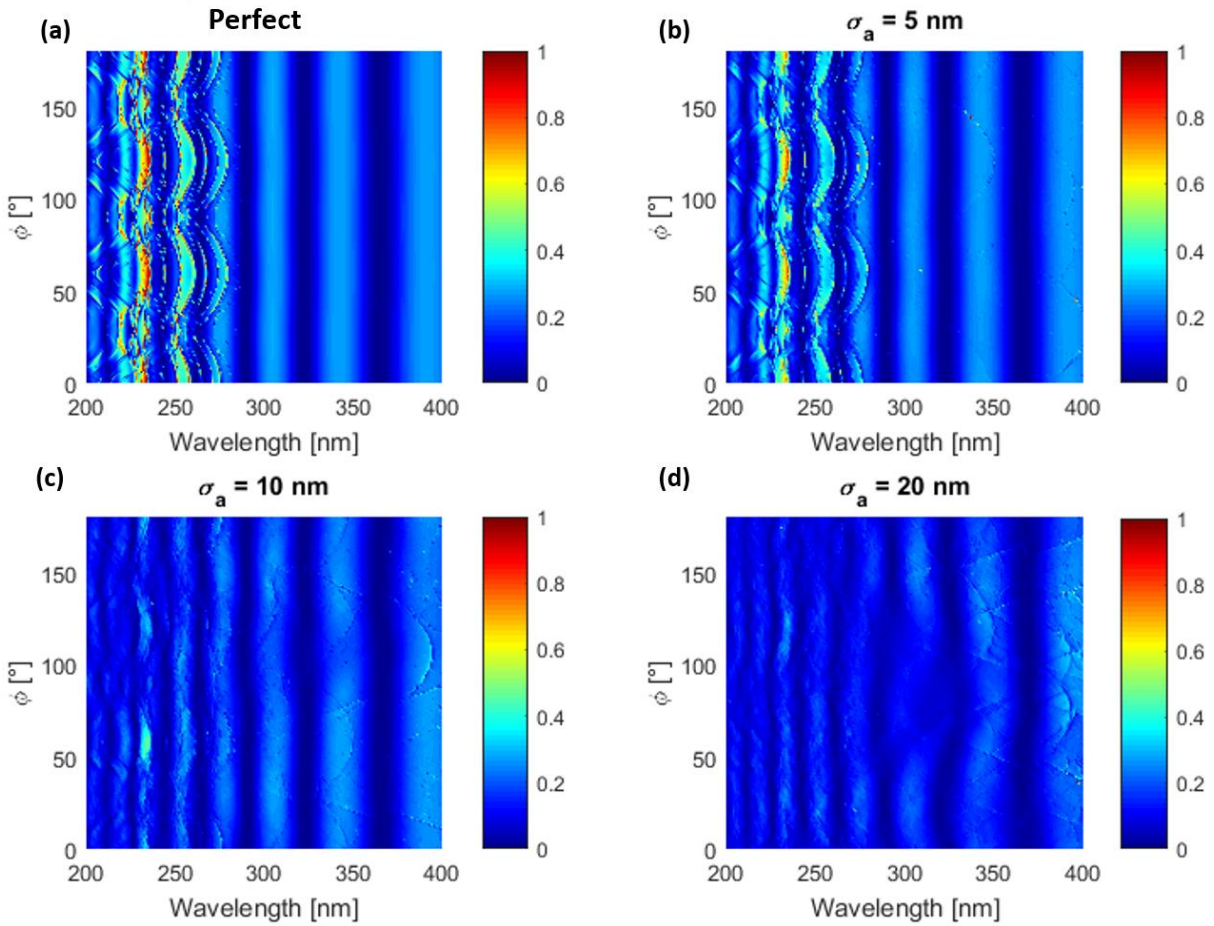

Figure 138: 2D maps of the reflectance spectra of air cylinders, surrounded by alumina, arranged in a triangular lattice (a) with a slight variation of their centers positions with different standard deviations σ_a of 5 nm (b), 10 nm (c) and 20 nm (d), with a TE-polarized light incident with a $\theta = 45°$ angle in the incidence plane which direction is defined by ϕ with respect to the x-axis.

Looking at the case of the perfect structure (**Figure 138a**), at wavelengths higher than 280 nm, the incident light does not "see" the details of the material structure, so only oscillations due to thin film interferences are observed. At lower wavelengths, these details interact with the incident light, resulting in the observed variations of the spectral reflectance at these wavelengths. A periodicity in ϕ is also observed, with a period of 60°. This is due to the fact that a 60° rotation around the z-axis leads to the same structure. This assumption is not verified anymore as soon as the cylinders are not placed perfectly periodically. This is the reason why when cylinders are randomly shifted, the spectral reflectance does not describe this periodic behavior at lower wavelengths. In fact, the effect due to the structure progressively disappears with stronger disorders. For stronger disorders, an impact is also visible on the interference fringes, with a more anisotropic behavior of the width of the fringes. It is particularly the case for $\sigma_r = 20$ nm around a wavelength of 300 nm. Averaging the reflectance spectra over all values of ϕ will thus smoothen this remaining anisotropy, which is due to the fact that the disorder is generated in the simulation only on a primitive cell with limited size and periodic boundary conditions.

In order to estimate the minimum required step $d\phi$ for the angle ϕ, for a correct average over the incidence plane directions, we will compare reflectance averages with larger steps to the smallest calculated 1° step which will be considered as a reference. This comparison will be preformed on the reflectance spectra presented in **Figure 138c** obtained for $\sigma_a = 10$ nm (same as **Figure 119**). To quantify the variations relative to this "exact" $d\phi = 1°$ value, a relative error is defined as:

$$\delta = \frac{1}{N}\sum_{\lambda}\left|\frac{R_{d\phi}(\lambda) - R_1(\lambda)}{R_1(\lambda)}\right| \times 100 \qquad (5.\ 7)$$

with $R_{d\phi}(\lambda)$ the averaged spectral reflectance considering a step $d\phi$, $R_1(\lambda)$ the averaged spectral reflectance with a 1° step on ϕ and N the considered number of wavelengths ($N = 201$, with a calculation from $\lambda = 200$ nm to $\lambda = 400$ nm with a 1 nm step). This quantity is calculated in the **Figure 138c** for different values of $d\phi$ from 1° to 180° with a 10° step. Results are shown in **Figure 139**.

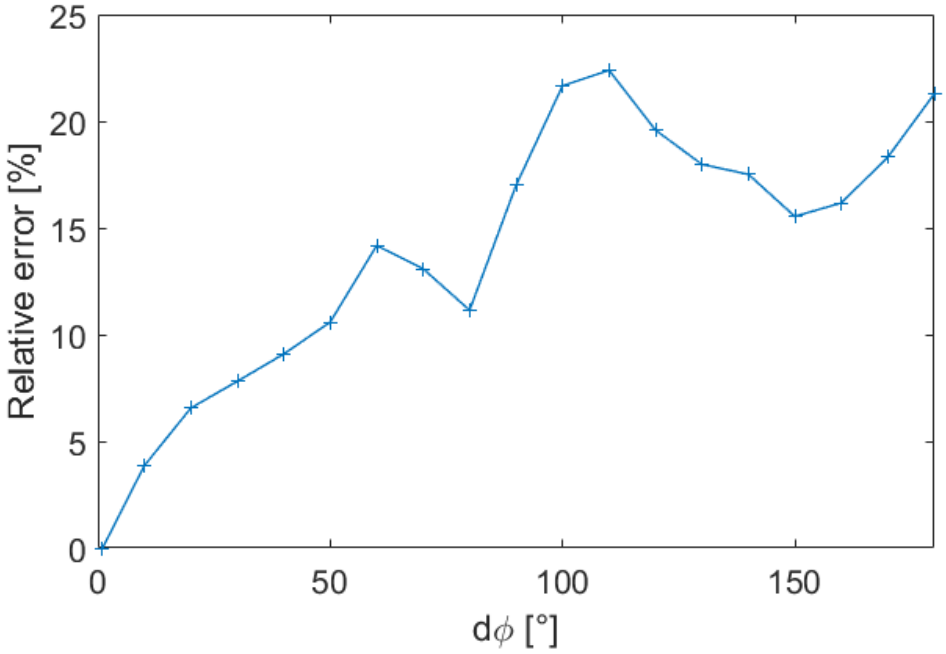

Figure 139: Relative error on the averaged spectral reflectance, related to the step in rotation angle ϕ denoted dϕ.

The case where $d\phi = 1°$ has a relative error of 0% as it is chosen as reference. As $d\phi$ increases, the error globally increases as the number of reflectance spectra used for the average decreases. From $d\phi = 100°$ to $d\phi = 180°$, only one single calculation is used and no average on ϕ is performed. We decide that an error lower than 5% is acceptable for the future calculations. According to this result, this means that a step of $d\phi = 10°$ is required. We will thus use this 10° step when rotating the incidence plane and averaging the result.

5.3.6. Simulating an unpolarized light

Up until now, simulations have been performed with a TE-polarized light. However, the light used experimentally is not polarized. This unpolarized light will be reproduced in our simulations by averaging the results obtained with a TE- and a TM-polarized light:

$$R(\lambda) = \frac{R_{TE}(\lambda) + R_{TM}(\lambda)}{2} \qquad (5.\ 8)$$

with $R_{TE}(\lambda)$ and $R_{TM}(\lambda)$ the spectral reflectance with a TE and a TM polarized light respectively. From here unless otherwise stated, results will be presented for a non polarized light.

5.4. Towards the optical properties of the experimental material

The purpose of this section is to simulate the optical behavior of the anodized aluminum substrate presented in **Section 5.1**. Compared to the previous simulations, there are two main differences. First, the nanoporous alumina structure is no longer surrounded by air on both sides but it is superposed on an aluminum substrate. Such aluminum substrate is modelled by the refractive index presented in **Figure 144**. The second difference is related to the structural parameters (cell parameter and cylinder size), as well as their respective disorder parameter σ_a and σ_r. All these adjustments are progressively made in this section in order to better model the optical behavior of the experimental material.

However, it is worth noting that the experimental material used here is very complex, with strong structural disorder. The goal in this section is not to perfectly model the optical behavior of such material, which would require further analysis of this real sample, but rather study how introducing structural disorder in the model can lead to a calculated optical behavior closer to the one of a real material.

5.4.1. Preliminary studies

A few preliminary studies are made in this section. For these first studies, the material is considered perfectly ordered. This section aims at setting a few global parameters before introducing structural disorder in a future section.

5.4.1.1. Estimation of the spectral resolution and problem related to thick materials

We will first list what is technically required for the optical simulations. We saw in **Sections 5.3.2** and **5.3.3** that a 3x3 supercell primitive cell containing 18 pores was necessary to introduce structural disorder in the material. To compute the spectral reflectance of such supercell primitive cell, 20 modes in the x direction and 15 in the y direction are required. An average over the ϕ angles (see **Section 5.3.5**) and the polarization (**Section 5.3.6**) are also required. Performing the average over the ϕ angles requires all ϕ angles from 0° to 180° with a 10° step, which represent a total of 19 points. The considered spectral range (λ from 350 nm to 800 nm) has a width of 450 nm. Considering these parameters, with our current resources, about five days are required to compute this 2D simulation for a 1 nm step on the wavelengths, for example. A smaller spectral step will thus lead to a longer computation time. This section aims at adjusting the correct spectral discretization to use in the calculation. Considering the oscillations present in the reflectance spectra, the spectral discretization depends on the frequency of the oscillations due to thin film interferences. We will thus estimate this frequency.

According to *Equation* (5. *1*), the oscillations minima positions λ_m depend on the effective refractive index n_{eff}, the material thickness e, the refracted angle θ_r and the order m. Using the average parameters $\mu_a = 190\ \text{nm}$ and $\mu_r = 30\ \text{nm}$ (**Figure 119**), we obtain $n_{eff} = 1.61$ from a Maxwell-Garnett approximation. For the material thickness, **Figure 117b** gives $e = 100\ \mu\text{m}$. Then the refracted angle θ_r is obtained from the Snell-Descartes equation with an incidence angle $\theta = 8°$ and the effective refractive index n_{eff}. Finally, higher orders m are linked to shorter λ_m.

From *Equation* (5. *1*), the local minima λ_m are located at:

$$\lambda_m = \frac{2\, n_{eff}\, e \cos(\theta_r)}{m} \tag{5. 9}$$

with $\theta_r = \sin^{-1}(\sin(\theta)/n_{eff})$ the angle of the refracted light inside the material, when the sample has no substrate. The experimental material having a metallic aluminum substrate, these positions are not exactly those predicted by this equation, but all peaks and valleys are shifted by a constant value [146]. The oscillations period thus remains unchanged and it is equal to:

$$\lambda_m - \lambda_{m+1} = \frac{2\, n_{eff}\, e \cos(\theta_r)}{m\,(m+1)} \tag{5. 10}$$

This equation shows that the period decreases for higher orders. In other words, the oscillations frequency increases at shorter wavelengths. In order to correctly discretize the calculations, we need to make sure to have a good enough discretization where the oscillations frequency is maximum, so at the shortest wavelength used in our calculation. Since our goal is to compare with the experimental measurement (see **Figure 120**) which is from 360 nm to 780 nm, we will compute from 350 nm to 800 nm. Around a wavelength of 350 nm, the oscillations period is about 0.4 nm. If we consider that the wavelength step used in the calculations should be much smaller than the oscillations period and decide that ten points are required to discretize the curve, then we would need a step of 0.04 nm, which is very small. Such small step would probably lead to many weeks of full calculations. An idea to avoid such long calculations is to remember that the spectrophotometer has a 10 nm spectral window in which the measured spectral reflectance is averaged. A moving average filter will thus be applied on the calculated reflectance to mimic this spectrophotometer measuring window.

The measuring window does not allow to see the very thin oscillations on the measured reflectance. Considering this fact, the thin spectral resolution required to visualize them may not actually be necessary. We only need the averaged result to be correct. We will now look for a method to reduce the spectral discretization step without altering the optical simulations results.

Effect of a bad spectral discretization

Investigating if this averaged final result remains the same when the discretization becomes worse, the spectral reflectance of a 100 µm thick porous alumina photonic crystal is calculated for different step on the wavelengths, with an unpolarized light arriving with an 8° incidence angle on the material surface. Considering these parameters, a step $d\lambda = 0.04\ \mathrm{nm}$ is required to correctly discretize the oscillations around $\lambda = 350\ \mathrm{nm}$ (Equation (5. *10*)). The cell parameter $\mu_a = 190\ \mathrm{nm}$ and the cylinders radius $\mu_r = 30\ \mathrm{nm}$ are used to fit the parameters of the experimental material. The angle ϕ is set so that the ΓM direction is included in the incidence plane. For this short study, the structure is perfectly ordered, so only a primitive cell containing two cylinders is necessary. The number of modes used for the calculations is also adjusted to 15 modes in the x direction and 7 in the y direction. Results are presented in **Figure 140**.

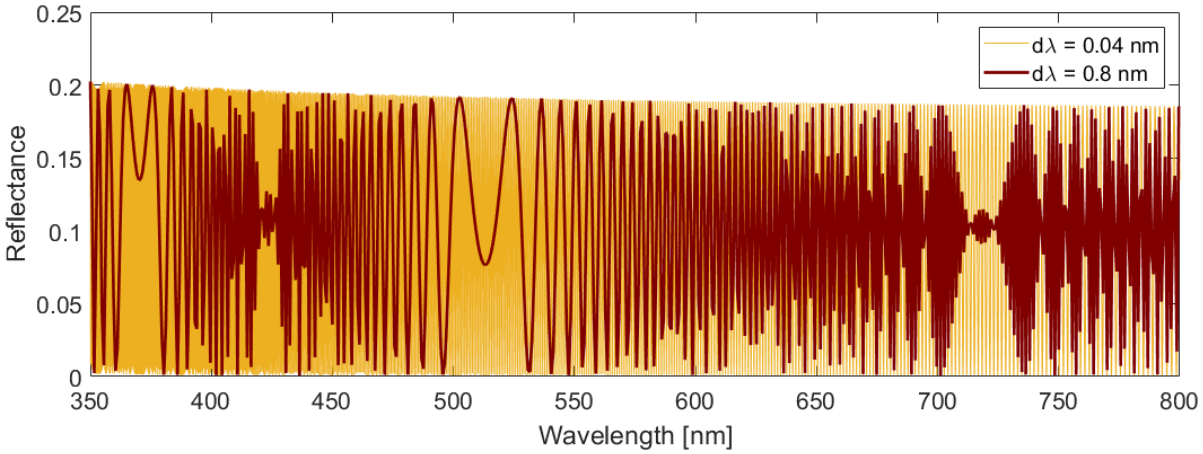

Figure 140: Reflectance spectra of a porous alumina 2D photonic crystal with different spectral discretizations $d\lambda$. The incident light is unpolarized. The incidence angle is 8° and the direction ΓM is included in the incidence plane. The material thickness is 100 µm. The structure is perfectly ordered.

The yellow curve is obtained with a step $d\lambda = 0.04$ nm, which should be enough to correctly discretize the oscillations in this 100 µm thick material, while the red curve is obtained with a larger step $d\lambda = 0.8$ nm. It appears that the spectral discretization is not accurate enough in the second case as a clear difference is observed between the two curves. In each period, only a few points are used to represent the red reflectance spectrum, leading to a different shape. The oscillations are not correctly discretized anymore, with regions where the reflectance is in general higher than the average, for example around 370 nm and from 500 nm to 535 nm. There are also regions where the oscillations amplitude significantly decreases, for example around a wavelength of 720 nm.

We will now investigate if these differences can be ignored after applying a moving average filter. The size of this moving average filter is set so that it contains one oscillations period where it is the largest in the considered spectral range. In our case, this is obtained at the largest wavelength $\lambda = 800$ nm, where the oscillations period is about 1.5 nm, with the considered parameters ($e = 100$ µm and $\theta = 8°$). So the window size is set to 1.6 nm as an integer number of points is required for the filter. Indeed, a 1.5 nm window contains 37.5 points considering the $d\lambda = 0.04$ nm step, while a 1.6 nm window contains 40 points. Also a 1.6 nm window contains 2 points for $d\lambda = 0.8$ nm. Applying this moving average filter on both reflectance spectra shown previously, the resulting filtered spectral reflectances are presented in **Figure 141**.

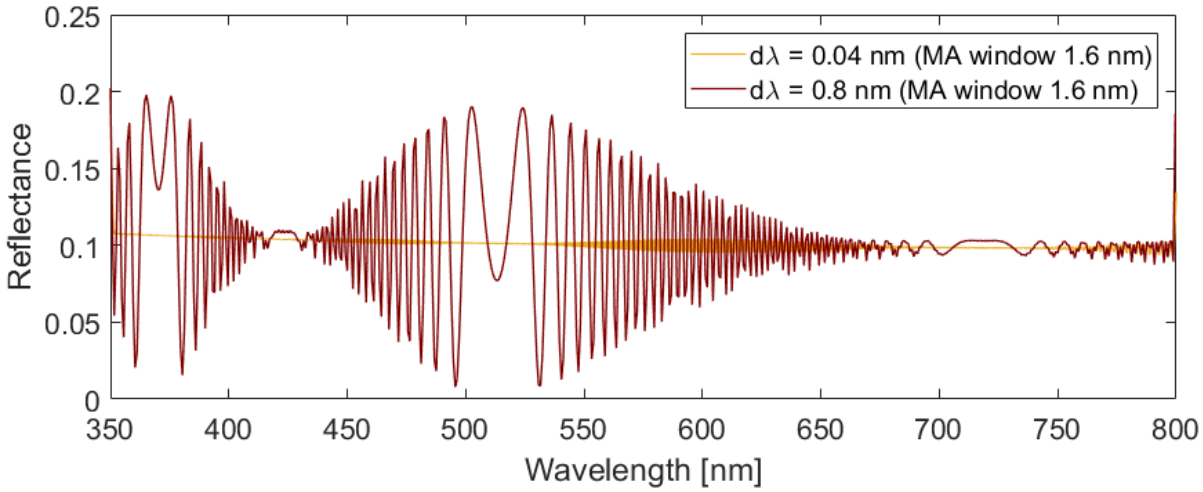

Figure 141: Reflectance spectra of a porous alumina 2D photonic crystal with different spectral discretizations $d\lambda$ filtered with a moving average (MA) filter having a window size of 1.6 nm. The incident light is unpolarized. The incidence angle is 8° and the direction ΓM is included in the incidence plane. The material thickness is 100 µm. The structure is perfectly ordered.

The colors refer to the same curves as in **Figure 140**. It appears that regions with higher reflectance remain, like around a wavelength of 370 nm. Regions where the oscillations frequency was artificially lower in **Figure 140** (for example from 500 nm to 535 nm) are unchanged after filtering as the filter size is relatively small compared to these oscillations period.

The differences between the two curves observed in **Figure 140** remain visible after filtering. It seems that a bad spectral discretization lead to wrong results. However, the same step $d\lambda$ can lead to both a good and a bad discretization of the oscillations, depending on their period. This period can be adjusted by the material thickness (Equation (5. *10*)). We will now investigate if the same averaged result can be obtained with a good discretization but for two different material thicknesses.

Effect of the material thickness

In order to compare the results obtained for $e = 100\ \mu\text{m}$ to another smaller thickness, the spectral reflectance of a 10 µm thick porous alumina 2D photonic crystal is calculated. All structural and illumination parameters are unchanged. The required discretization for this 10 µm thick material is 0.4 nm, so this is the step $d\lambda$ used here. Both reflectance spectra are represented in **Figure 142**.

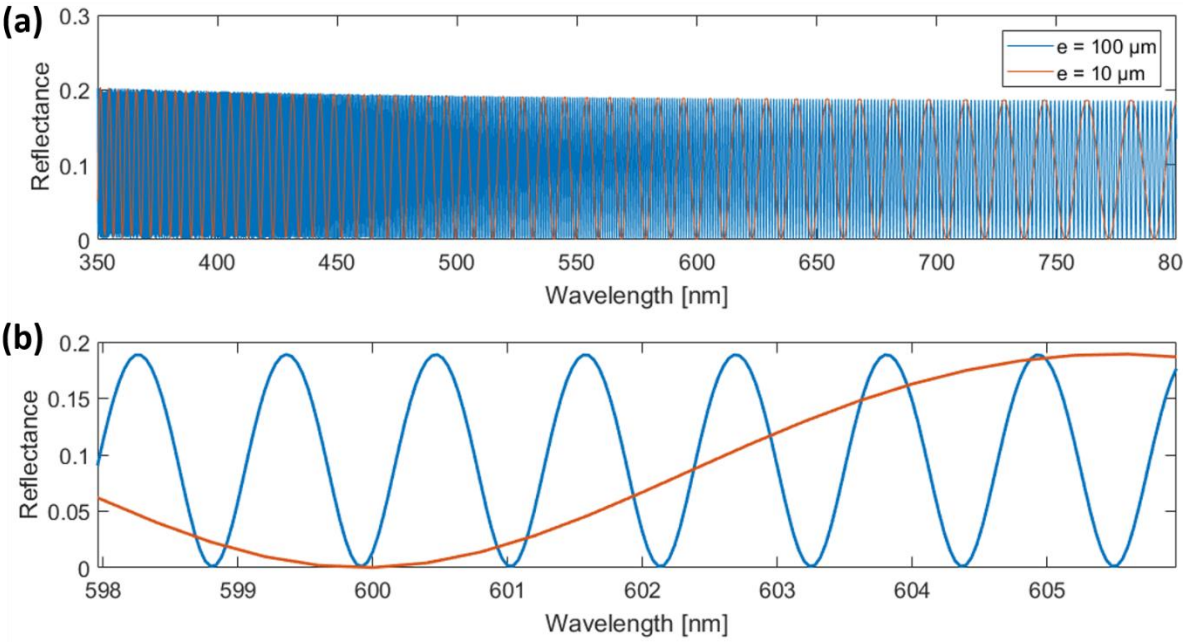

Figure 142: Reflectance spectra of a porous alumina 2D photonic crystal with different thicknesses e (a) zoomed on a shorter wavelength range (b), with an unpolarized light incident with an 8° angle on the material surface. The structure is perfectly ordered. The primitive cell contains two cylinders. The direction ΓM is included in the incidence plane. The spectral discretization step is $d\lambda = 0.04$ nm in the case $e = 100$ µm and $d\lambda = 0.4$ nm in the case $e = 10$ µm.

Figure 142a represents the reflectance spectra of both materials with their respective thickness $e = 100$ µm (blue line) and $e = 10$ µm (orange line) in the spectral range of interest (from 350 nm to 800 nm). While both spectra look similar, the only difference is the oscillations frequency. The blue curve related to the thicker material has higher oscillations frequency, as predicted by Equation (5. *10*). These oscillations become less visible on the figure, so a zoom on these curves is also displayed on **Figure 142b**. We also note that the oscillations are correctly discretized as they are clearly visible.

A moving average filter is applied, with its size depending on the largest oscillation period observed. In the case of $e = 10$ µm, the filter size is set to 16 nm, while it stays at 1.6 nm for $e = 100$ µm. The filtered spectra are represented in **Figure 143**.

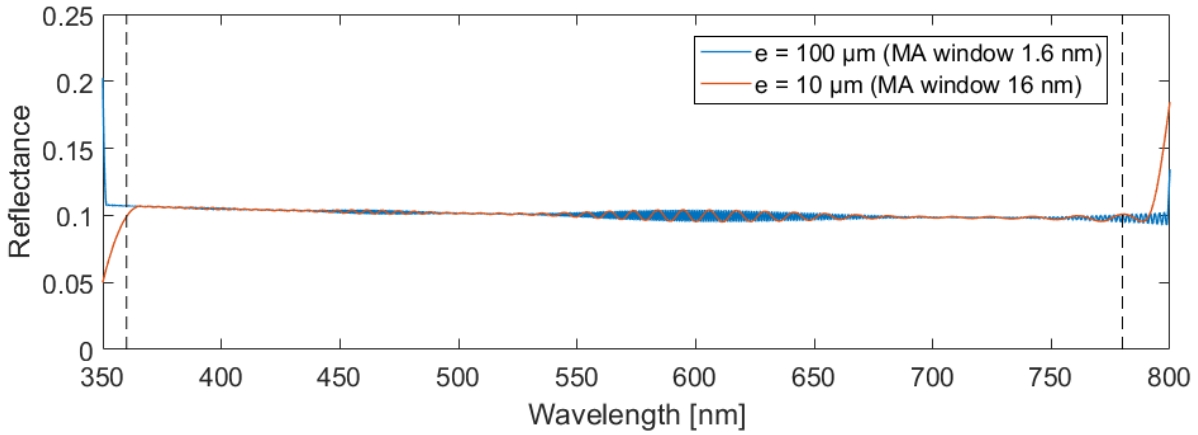

Figure 143: Reflectance spectra of a porous alumina 2D photonic crystal with different thicknesses e filtered with a moving average (MA) filter having a window size of 1.6 nm (blue line) and 16 nm (orange line). The incident light is unpolarized and the incidence angle is 8°. The ΓM direction is included in the incidence plane. The structure is perfectly ordered and the primitive cell contains two cylinders. The two dashed lines indicate the wavelengths of 360 nm and 780 nm.

Comparing both curves, they look quite similar. A few differences are however observed as the oscillations do not completely disappear after applying the moving average filter, but their amplitude is considerably reduced. This difference between the two filtered reflectance spectra are however small compared to the bias introduced in our simplified model material compared to the real one.

It is worth noting that the curves diverge at the borders, around wavelengths of 350 nm and 800 nm, especially in the case of a larger window size (orange curve). This is due to the edge effect. Consider for example the orange curve. When the filter is centered at 358 nm, its left edge is exactly located at 350 nm which is the edge of the available values. Now to calculate the values at lower wavelengths, less points are included in the filter window. Depending on how the oscillations vary around these edges, the resulting filtered spectrum may go to higher or lower values near these edges. This effect is reduced when the filter window becomes smaller as the window reaches one edge at a later value. This is the case for the blue curve. This effect is less an issue as the calculations are performed on a slightly larger spectral range (from 350 nm to 800 nm) than the experimental measurement (from 360 nm to 780 nm). These edges are displayed on Figure 143 as the two black dashed lines. Between these two lines, the edges effect disappears.

We conclude that materials having different thicknesses have the same averaged reflectance spectrum. So, if our final goal is to compare both averaged results between the measured and calculated reflectance, it is not necessary to set a high material thickness which would lead to a thin spectral discretization and thus high computational resources. We thus reduce the thickness in order to allow a larger spectral step and limit the required calculation time. In future calculations, the material thickness is set to $e = 1\ \mu\mathrm{m}$. While the minimum spectral resolution for the considered parameters is 4 nm, we decide to set $d\lambda = 1\ \mathrm{nm}$.

5.4.1.2. Adding an aluminum substrate

In this part, the material is considered perfectly ordered, meaning that all cylinders share the same size (radius $r = 47\ \mathrm{nm}$) and are arranged in a triangular lattice. Two cases are compared, one where the porous alumina triangular photonic crystal is surrounded by air (case studied in the previous simulations) and one where it is superposed on an aluminum substrate. The aluminum material is modelled by a refractive index extracted from [147], represented in the spectral range of interest in **Figure 144**.

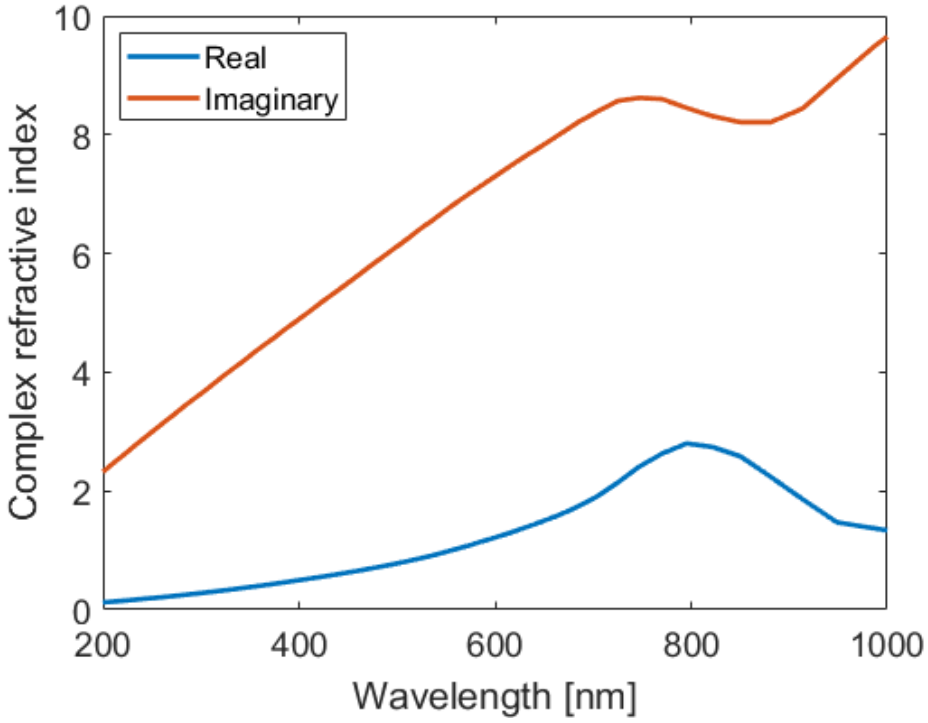

Figure 144: Real (blue) and imaginary (orange) parts of the aluminum refractive index extracted from [147].

The material thickness is 1 µm. The spectral reflectances for an incidence angle $\theta = 8°$ (and still $\phi = 60°$ to have a direction of the incidence plane in the ΓM direction of the photonic crystal) are calculated for an unpolarized light for the material without (**Figure 145a**) and with (**Figure 145b**) the aluminum substrate. The primitive cell is a 3x3 supercell.

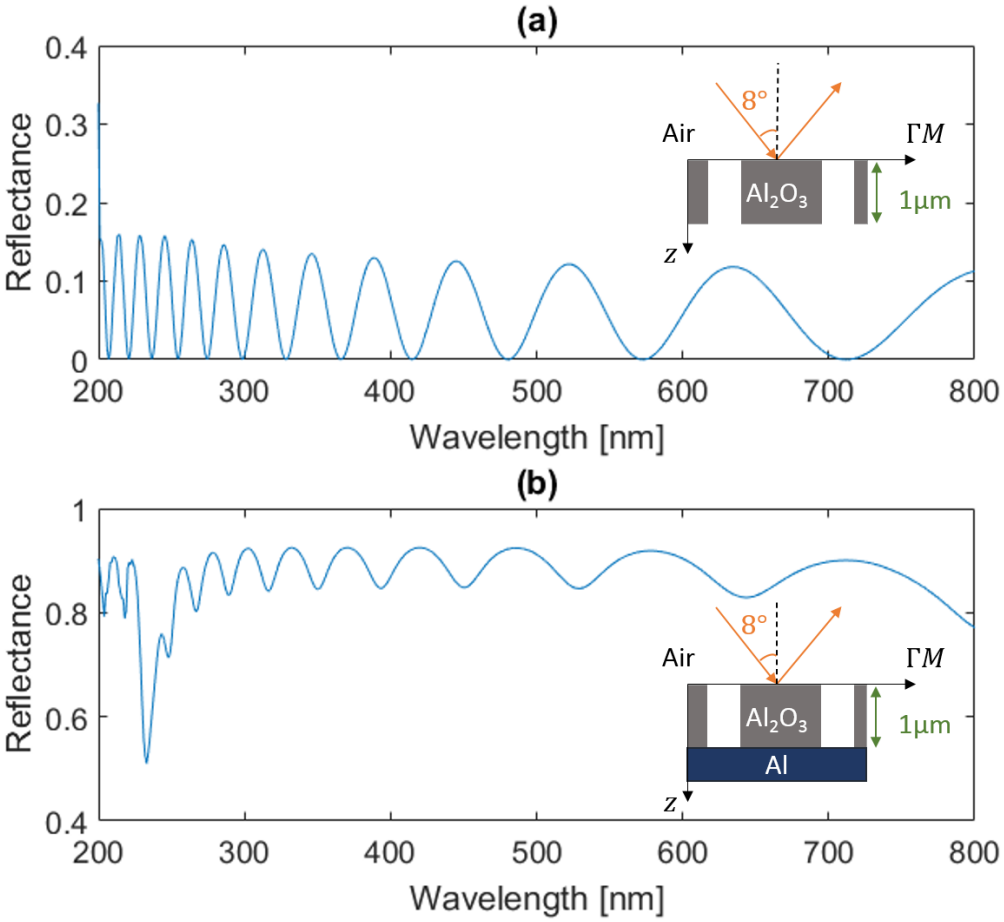

Figure 145: Reflectance spectra of air cylinders in alumina arranged in a triangular lattice, surrounded by air (a) and with an aluminum substrate (b). The light is incident with an 8° angle on the material surface and is unpolarized. The incidence plane is in the ΓM direction. Insets are schematic representations of the corresponding systems. The material thickness is 1 µm.

Adding the aluminum substrate highly increases the material reflectance due to the highly reflective aluminum material. The null absorbance of Al_2O_3 (its refractive index imaginary part is null in the model) allows the light to reach the substrate and be reflected. The thin film interferences thus generate the observed oscillations. At an 8° incidence angle, the UV high reflectance peaks do not appear (see **Figure 134a**).

5.4.1.3. Cylinder position and size adjustment

Another difference with the previously made simulations is related to the cell parameter and the average radius of the cylinders. The average cylinder radius and cell parameter extracted from **Figure 117a** are respectively $\mu_r = 30$ nm and $\mu_a = 190$ nm. These parameters were $r = 47$ nm and $a = 157$ nm in the previous simulations to be able to compare with Kral et aL. [145] results. These new parameters are implemented in the model and the primitive cell corresponding to the structure is represented in **Figure 146**. A perfectly periodic structure is used here, but the number of cylinders remains 18 cylinders (i.e. a primitive 3x3 supercell is used), ready for the introduction of disorder.

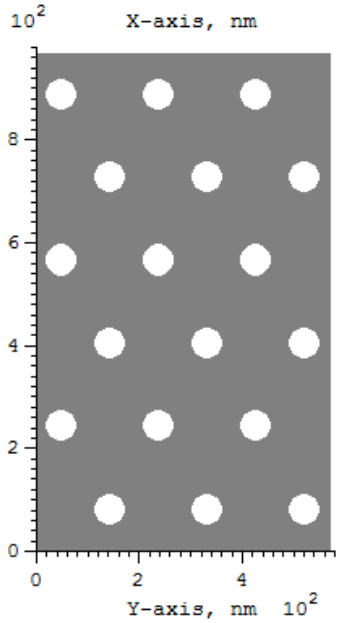

Figure 146: Representation of 18 air cylinders arranged in a triangular lattice (3x3 primitive supercell) surrounded by alumina, with a cylinder radius $\mu_r = 30\ nm$ and a cell parameter $\mu_a = 190\ nm$.

The spectral reflectances of a porous alumina triangular photonic crystal on top of an Al substrate are calculated for the two sets of parameters (r, a) and (μ_r, μ_a). The incidence angle is $\theta = 8°$, the incidence plane is in the ΓM direction and the incident light is not polarized. The spectra are shown in **Figure 147**.

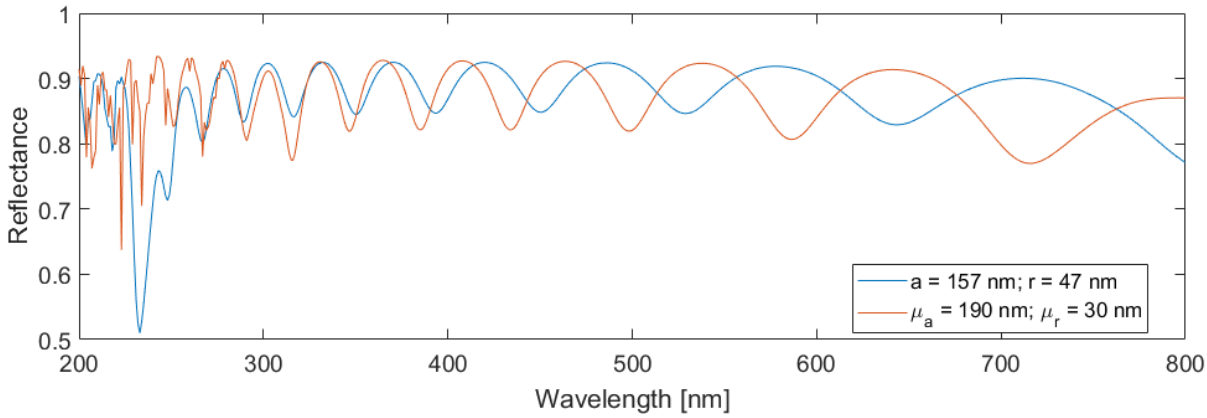

Figure 147: Reflectance spectra of air cylinders in alumina arranged in a triangular lattice on top of an Al substrate with the two different sets of parameters (r, a) and (μ_r, μ_a). The light is incident with an 8° angle on the material surface and not polarized. The incidence plane contains the ΓM direction. The material thickness is $1\ \mu m$.

Two major changes are observed here. First, the band of reflectance holes observed in the [200 nm – 300 nm] wavelength range for the (r, a) set of parameters is enlarged to the [200 nm – 400 nm] wavelength range for the (μ_r, μ_a) set of parameters. This is because this band, related to the photonic band structure, depends on the ratio between the cylinder radius and the cell parameter. Second, the oscillations observed at longer wavelengths, due to thin film interferences, have an increased frequency for the (μ_r, μ_a) set of parameters. This can be explained by *Equation* (5. *10*) . Indeed, a lower cylinder radius and higher cell parameter means that cylinders are smaller and more spaced. In total, this leads to less air and more alumina in the material. The volume ratio of the air cylinders decreases from about 33 vol% to 9 vol%. Since the alumina refractive index is about 1.67, which is higher than

this of air, the material effective index becomes higher with the increased quantity of alumina. This translates into an increase of the term $n_{eff}\cos(\theta_r)$ in *Equation* (5. *9*), which explains that the oscillations due to thin film interferences are influenced as the set of parameters changes from (r, a) to (μ_r, μ_a). Indeed, we can estimate this term considering an effective refractive index n_{eff} derived from a Maxwell-Garnett approximation and the angle of the refracted light inside the material θ_r derived from Snell law's in this effective material. With an 8° incidence angle, this $n_{eff}\cos(\theta_r)$ term increases from about 1.45 to 1.60.

5.4.2. Modelling the optical behavior of the material

In this section, the structural disorder will be introduced in order to better model the optical properties of the experimental material.

5.4.2.1. Introduction of the disorder parameters extracted from SEM micrographs

In this section, the disorder parameters $\sigma_a = 10$ nm and $\sigma_r = 3$ nm extracted from the real material (see **Figure 119**) are introduced into the model. A top view of this material is shown in **Figure 148**. A 3x3 supercell is used as the primitive cell. The mean parameters $\mu_a = 190$ nm and $\mu_r = 30$ nm are kept, as long as the aluminum substrate.

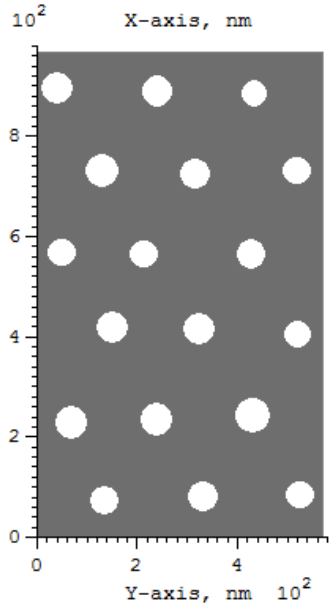

Figure 148: Top view of an alumina 2D photonic crystal modelled by a 3x3 supercell consisting of 18 cylinders of radius $\mu_r = 30\ nm$. The cell parameter is $\mu_a = 190\ nm$. The structure is disordered with parameters $\sigma_a = 10\ nm$ and $\sigma_r = 3\ nm$.

The spectral reflectance of this material is calculated with an unpolarized light incident with an 8° angle on the material surface for different angles ϕ from 0° to 180° with a 10° step. The results are averaged over all these angles and shown in **Figure 149**. The spectral reflectance of the same material in the case where $\sigma_a = \sigma_r = 0$ nm (perfectly ordered) is also displayed.

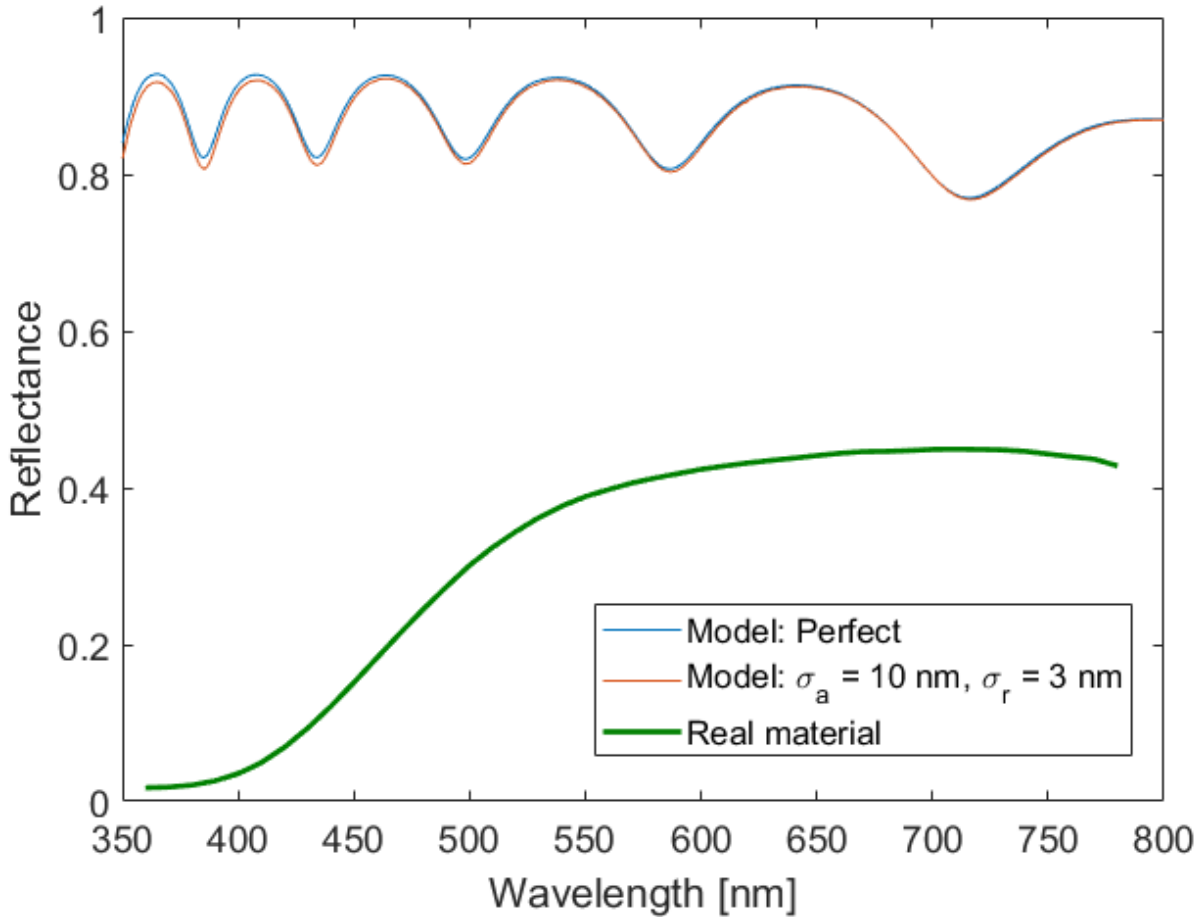

Figure 149: Calculated reflectance spectra of a perfectly ordered (blue) and disordered (orange) alumina 2D photonic crystal modelled by a 3x3 supercell consisting of 18 cylinders, averaged over the ϕ angles, and measured total reflectance spectrum of the real material (green). The mean parameters are $\mu_a = 190\ nm$ and $\mu_r = 30\ nm$. The light is unpolarized and incident with an 8° angle on the material surface. The material thickness is 1 µm. The substrate is pure aluminum.

Comparing both calculated reflectance spectra (blue and orange lines), it appears that introducing this disorder has little impact on the material reflectance properties. A small difference is observed for shorter wavelengths as structural disorder seems to reduce the spectral reflectance at shorter wavelengths. Yet here, this variation does not seem significant.

It is also possible that the oscillations slightly vary due to the variations of the cylinders size. Indeed, these variations in cylinders size lead to variations of the air-alumina volume ratio in the material, and thus the material effective refractive index slightly changes. According to *Equation* (5. *9*), this lead to small changes of the positions of the oscillations local minima.

Both curves are still very far from the experimentally measured reflectance (green line). Indeed, the measured reflectance is much lower than the calculated one. Also, while the calculated reflectance globally slightly decreases with longer wavelengths, the measured reflectance highly decreases around wavelengths from 400 nm to 550 nm. It is possible that this different curve shape between the calculated and measured reflectance spectra is due to an underestimated disorder in our model. A higher disorder would probably further decrease the spectral reflectance at shorter wavelengths and may thus lead to a more similar shape. Looking back at the SEM micrographs (**Figure 117a** and **Figure 118a**), the pores shape varies quite a lot: some are indeed circular while other are more elliptic. We have approximated them all as perfect cylinders, but this approximation may have led to an underestimated disorder in the model.

In addition, only one single SEM micrograph showing a small region (2.6 µm x 1.9 µm) of the sample was used to extract the parameters related to the structural disorder, while the spectrophotometer analyses a larger area (17 mm diameter). In such a large area, the material may have higher variations than the one observed on the micrograph and the extracted disorder parameters may have been underestimated.

For these reasons, we decide to increase the parameter σ_r related to the pores size. Doing so allows the program to generate a wider range of cylinders sizes, in order to mimic the large variation of the pores shape.

5.4.2.2. Larger variations in the cylinders size

A new structure is generated with a larger σ_r parameter. In this section, we decide to set it to $\sigma_r = 20\ \text{nm}$. The other parameters are kept the same ($\mu_a = 190\ \text{nm}, \sigma_a = 10\ \text{nm}, \mu_r = 30\ \text{nm}; e = 1\ \mu\text{m}$). A top view of the 3x3 supercell primitive cell of such material is given in **Figure 150**.

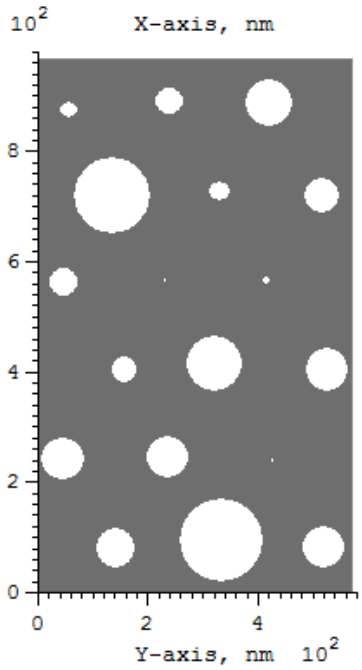

Figure 150: Top view of an alumina 2D photonic crystal modelled by a 3x3 supercell consisting of 18 cylinders of average radius $\mu_r = 30\ nm$. The cell parameter is $\mu_a = 190\ nm$. The structure is disordered with parameters $\sigma_a = 10\ nm$ and $\sigma_r = 20\ nm$.

The spectral reflectance of such material with an 8° unpolarized incident light is calculated for different ϕ angles from 0° to 180° with a 10° step. Results are averaged over these angles and presented in **Figure 151** as a yellow line. The curves from **Figure 149** are also represented. Comparing the perfect and both disordered cases, it appears that an increase of the disorder parameters reduces the spectral reflectance, especially at shorter wavelengths, as it was guessed from the previous case.

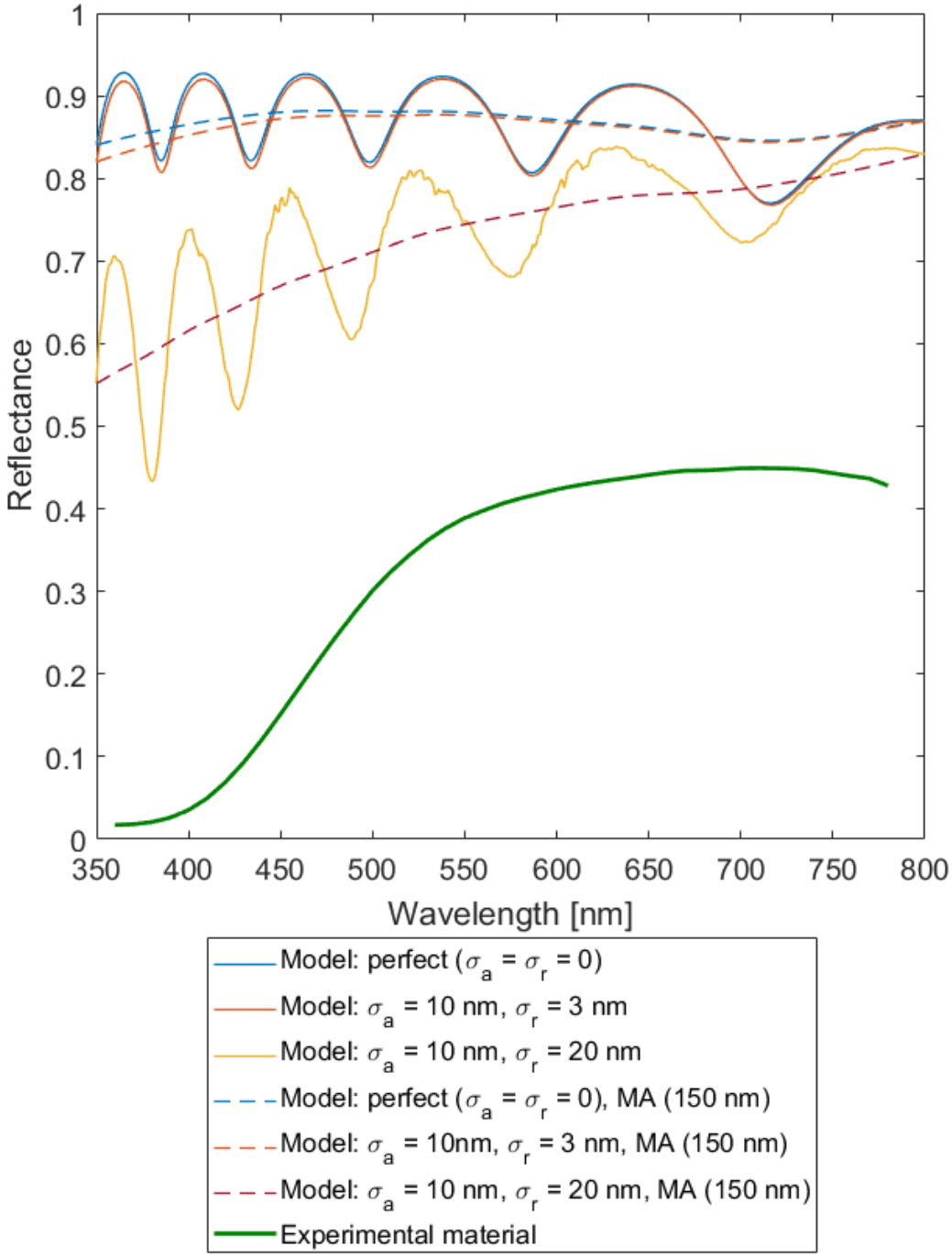

Figure 151: Reflectance spectra of the perfectly ordered (blue) and deformed (orange, yellow) alumina 2D photonic crystal modelled by a 3x3 supercell primitive cell, their averaged spectra (moving average filter with a 150 nm window) (dashed lines) and the measured total reflectance of the real material (green). The incident light is unpolarized and incident with an 8° angle on the material surface. The model material thickness is 1 µm. All calculated spectra are averaged over the ϕ angles.

In order to simulate the spectral resolution of the spectrophotometer, this last calculated reflectance spectrum (yellow line) is averaged with a moving average filter having a 150 nm window (dark red dashed line). This window size corresponds to the largest oscillation (observed at the longest wavelength considered, 800 nm) for a 1 µm thick material. This averaged reflectance spectrum correctly follows the variations of the spectrum before being filtered, except at longer wavelengths

where the averaged reflectance increases due to the edges effect at 800 nm. This effect does not appear at 350 nm as the reflectance is there equal to the average value. The two other displayed reflectance are also averaged with the same window size. When excluding the edges effect, their average spectra both slightly decrease with increasing wavelengths. Their reflectance is about 0.88 at a 450 nm wavelength, and reaches 0.84 at 720 nm.

Comparing these two averaged calculated reflectance spectra to the measured one, it appears that introducing disorder, and then increasing it, leads to a reflectance spectrum shape getting closer to the experimental spectrum, in terms of both values and curve shape. However, they both remain significantly different from the experimental reflectance.

The shape difference between experimental and calculated spectra may be explained by a modelled material still too ordered compared to the experimental material. Another reason for underestimated disorder lies in the fact that our model considers perfect cylinders extending in a straight line from the top surface to the substrate. This may not be the case in the real material, the pores may not be perfectly straight from the top surface to the surface. Also, the substrate surface may not be perfectly planar. In order to investigate these possibilities, an analysis inside the material depth is required.

Also, the higher reflectance value for the calculated spectrum compared to the experimental measurement can be explained by the same reasons: an underestimated disorder. Another possible explanation could be some absorption in the material, possibly by the oxide layer which may not be pure alumina. Indeed, impurities may be present in the material. A chemical analysis would be necessary in order to investigate this possibility.

5.5. Conclusion of this chapter

In this chapter, structural disorder was introduced into the model in the case of 2D and 3D photonic crystals in order to better model real materials for which undesired structural disorder is often introduced during the manufacturing process. However, we focused on an alumina 2D photonic crystal as such material was available in our laboratory, allowing for comparisons between the measured and calculated spectral reflectances. After a verification of the simulation results on a perfectly ordered porous alumina photonic crystal with a comparison to literature results, disorder is introduced into the material. Two kinds of disorder were described and implemented: one related to the cylinders (or pores) position and the other to their size (cylinder radius). The effect of this disorder is first studied on a nanoporous alumina layer surrounded by air. Then, the model is used to simulate the reflectance of a nanoporous anodized aluminum sample. In order to model this experimental material, structural parameters are extracted from SEM micrographs of the material. Very little variations of the spectral reflectance relatively to the perfectly ordered case are observed due to a too little amount of disorder in the structure. The experimental material may have a higher amount of disorder due to the wide variety of the pores shape, how they extend in the material depth and the small SEM micrograph area compared to the size of the spectrophotometer beam used to measure the material reflectance. Because of these reasons, the disorder parameter linked to the cylinders size is increased. The resulting reflectance spectrum becomes much closer to the measured one but remains significantly different, in particular the calculated reflectance remains higher than the measured one, possibly due to the presence of impurities inside the material resulting in an increased light absorption. A chemical analysis would be required to further investigate this possibility.

Conclusion

The optical behavior of a polymer opal photonic crystal containing VO_2 spherical nanoparticles in the opal interstices has been studied from the visible to the mid infrared spectral range, through a numerical optical model based on the Fourier modal method combined with a staircase approximation and an S-matrix formalism. Each material is modelled by its respective refractive index, and the opal interstices are modelled by an effective refractive index derived from a Maxwell-Garnett approximation. The model was first validated on both material and structure aspects, separately, by comparing our simulations results to results obtained by other methods. With no real polymer opal photonic crystal containing VO_2 nanoparticles available, we could only prove that the model is able to model the behavior of individual materials on one hand, and of a polymer opal photonic crystal on the other hand, through comparisons with literature data. Then the spectral reflectance and transmittance of the system were calculated in the visible and near infrared spectral ranges in order to calculate the material luminous and solar transmittances in order to optimize its performances as an energy efficient coating for windows. In order to keep a sufficient level of transparency ($T_{lum,warm} \approx 30\%$), only 1 vol% VO_2 was introduced inside the material. A 13 µm-thick compact opal photonic crystal consisting of polymer spheres of low refractive index ($n = 1.3$) surrounded by a mixture of VO_2 nanoparticles and that same polymer performs promising results in regard to this specific application ($\Delta T_{sol} = 28\%$). However, due to the limited VO_2 concentration and thus the relatively low refractive index contrast in the photonic crystal, the impact of the structure remains limited. Interested in other applications which do not require a transparent material, like energy efficient coating for buildings and satellites or camouflage applications, the spectral reflectance of the material was calculated in the mid infrared region where the reflectance highly impacts the material emissivity, the main performance parameter used for these applications. Adjusting the structural parameters (such as the cell parameter) in order to adjust the position of the photonic bandgap to the position of the blackbody emittance peak at the temperature of interest leads to a maximum impact of this bandgap on the material emissivity. The simulations show that stronger PBG peaks were obtained at lower VO_2 concentrations, but too low concentrations lead to a reduced effect on the emissivity as the transmittance increases. An optimized case for buildings and satellites applications is found for a 26 vol% VO_2 concentration, when all interstices of the compact opal photonic crystal are filled with pure VO_2 and still with a polymer spheres refractive index of 1.3, for a total thickness of 117 µm. In this case, the emissivity modulation at the VO_2 phase transition is reduced from $\Delta\epsilon = 0.42$ to $\Delta\epsilon = 0.33$ due to the material structure, leading to a surface temperature modulation increase from $\Delta T_{surf} = -11.8°C$ to $\Delta T_{surf} = -9.1°C$. This is an improvement in regard to the building and satellite applications which require high values of ΔT_{surf}. However, these values are still negative, so further improvement would be required. For the camouflage application which requires high values of $\Delta\epsilon$, high VO_2 concentrations seem to be interesting, but in these cases, the impact of the structure is very limited as the material becomes absorbent. We should keep in mind that these calculations are performed on a modelled material whose structure may be very different from real materials. Indeed, as the self-assembly techniques typically used to manufacture opal photonic crystals generally introduces undesired structural disorder in the material, two kinds of structural disorder (variation of the particles size and position) are introduced in the model in order to better model the optical behavior of real materials. The spectral reflectance of a disordered porous alumina 2D photonic crystal is calculated and compared with the measured reflectance of a real material. This test is performed on a 2D photonic crystal instead of an opal photonic crystal as manufacturing an opal photonic crystal containing VO_2 nanoparticles is significantly more challenging, but the numerical program works in a similar way in the case of a 3D photonic crystal. Due to the relative complexity of the real material, our simplified model is still unable to perfectly model this real material as a lot of simplifications have been introduced in the model. For

example, the amount of disorder was significantly underestimated due to a wide variation of the pores shape, possible bending of the pores inside the material depth and possible impurities in the material. However, structural disorder was successfully introduced in the model and the results showed that the optical behavior of this modelled disordered material is much closer to the one of the real material, even though further improvement is still possible. Taking into account the variations of the pores diameter in the material depth, or refractive index values extracted from measurements on the real material instead of literature ones, would be the next possible steps for this study. In order to really validate this model, a real polymer opal photonic crystal containing VO_2 nanoparticles would be required. However, manufacturing such complex material remains a challenge.

References

[1] F.J. Morin, Oxides Which Show a Metal-to-Insulator Transition at the Neel Temperature, Phys. Rev. Lett. 3 (1959) 34–36. https://doi.org/10.1103/PhysRevLett.3.34.

[2] C. Granqvist, G. Niklasson, Thermochromic Oxide-Based Thin Films and Nanoparticle Composites for Energy-Efficient Glazings, Buildings. 7 (2016) 3. https://doi.org/10.3390/buildings7010003.

[3] L. Kang, Y. Gao, H. Luo, Z. Chen, J. Du, Z. Zhang, Nanoporous thermochromic VO2 films with low optical constants, ACS Appl. Mater. Interfaces. 3 (2011) 135–138. https://doi.org/https://doi.org/10.1021/am1011172.

[4] R.O. Dillon, K. Le, N. Ianno, Thermochromic VO2 sputtered by control of a vanadium-oxygen emission ratio, Thin Solid Films. 398–399 (2001) 10–16. https://doi.org/10.1016/S0040-6090(01)01296-2.

[5] H. Ji, D. Liu, H. Cheng, C. Zhang, L. Yang, Vanadium dioxide nanopowders with tunable emissivity for adaptive infrared camouflage in both thermal atmospheric windows, Sol. Energy Mater. Sol. Cells. 175 (2018) 96–101. https://doi.org/10.1016/j.solmat.2017.10.013.

[6] M. Benkahoul, M. Chaker, J. Margot, E. Haddad, R. Kruzelecky, B. Wong, W. Jamroz, P. Poinas, Thermochromic VO2 film deposited on Al with tunable thermal emissivity for space applications, Sol. Energy Mater. Sol. Cells. 95 (2011) 3504–3508. https://doi.org/10.1016/j.solmat.2011.08.014.

[7] N.R. Mlyuka, G.A. Niklasson, C.G. Granqvist, Thermochromic VO 2-based multilayer films with enhanced luminous transmittance and solar modulation, Phys. Status Solidi Appl. Mater. Sci. 206 (2009) 2155–2160. https://doi.org/10.1002/pssa.200881798.

[8] Z. Chen, Y. Gao, L. Kang, C. Cao, S. Chen, H. Luo, Fine crystalline VO2 nanoparticles: Synthesis, abnormal phase transition temperatures and excellent optical properties of a derived VO 2 nanocomposite foil, J. Mater. Chem. A. 2 (2014) 2718–2727. https://doi.org/10.1039/c3ta14612j.

[9] V.N. Astratov, A.M. Adawi, S. Fricker, M.S. Skolnick, D.M. Whittaker, P.N. Pusey, Interplay of order and disorder in the optical properties of opal photonic crystals, Phys. Rev. B - Condens. Matter Mater. Phys. 66 (2002) 1–13. https://doi.org/10.1103/PhysRevB.66.165215.

[10] J.J. Baumberg, O.L. Pursiainen, P. Spahn, Resonant optical scattering in nanoparticle-doped polymer photonic crystals, Phys. Rev. B - Condens. Matter Mater. Phys. 80 (2009) 1–4. https://doi.org/10.1103/PhysRevB.80.201103.

[11] W. Jacob, A. Von Keudell, T. Schwarz-Selinger, Infrared analysis of thin films: Amorphous, hydrogenated carbon on silicon, Brazilian J. Phys. 30 (2000) 508–516. https://doi.org/10.1590/S0103-97332000000300006.

[12] M.G. Villalva, J.R. Gazoli, E.R. Filho, Comprehensive approach to modeling and simulation of photovoltaic arrays, IEEE Trans. Power Electron. 24 (2009) 1198–1208. https://doi.org/10.1109/TPEL.2009.2013862.

[13] ASTM G173-03, Standard Tables for Reference Solar Spectral Irradiances: Direct Normal and Hemispherical on 37° Tilted Surface, 2ASTM. G173-03E1 (2003) DOI: 10.1520/G0173-03R08 www.astm.org. https://doi.org/10.1520/G0173-03R08.

[14] G. Wyszecki, W.S. (Walter S. Stiles, Color science : concepts and methods, quantitative data, and formulae, John Wiley & Sons, 2000.

[15] G.B. Rybicki, A.P. Lightman, Radiative processes in astrophysics, John Wiley & Sons, 1979.

[16] P. Robitaille, Kirchhoff ' s Law of Thermal Emission : 150 Years, Prog. Phys. 4 (2009) 3.

[17] F.P. Incropera, D.P. DeWitt, Fundamentals of Heat and Mass Transfer, 1996. https://doi.org/10.1016/j.applthermaleng.2011.03.022.

[18] M. Santamouris, A. Synnefa, T. Karlessi, Using advanced cool materials in the urban built environment to mitigate heat islands and improve thermal comfort conditions, Sol. Energy. 85 (2011) 3085–3102. https://doi.org/10.1016/j.solener.2010.12.023.

[19] L. Adelard, F. Pignolet-Tardan, T. Mara, P. Lauret, F. Garde, H. Boyer, Sky temperature modelisation and applications in building simulation, Renew. Energy. 15 (1998) 418–430. https://doi.org/10.1016/s0960-1481(98)00198-0.

[20] W.C. Swinbank, Long-wave radiation from clear skies, Q. J. R. Meteorol. Soc. 89 (1963) 339–348. https://doi.org/10.1002/qj.49708938105.

[21] A.M. Makarevich, I.I. Sadykov, D.I. Sharovarov, V.A. Amelichev, A.A. Adamenkov, D.M. Tsymbarenko, A. V. Plokhih, M.N. Esaulkov, P.M. Solyankin, A.R. Kaul, Chemical synthesis of high quality epitaxial vanadium dioxide films with sharp electrical and optical switch properties, J. Mater. Chem. C. 3 (2015) 9197–9205. https://doi.org/10.1039/c5tc01811k.

[22] Y. Chen, S. Zhang, F. Ke, C. Ko, S. Lee, K. Liu, B. Chen, J.W. Ager, R. Jeanloz, V. Eyert, J. Wu, Pressure-Temperature Phase Diagram of Vanadium Dioxide, Nano Lett. 17 (2017) 2512–2516. https://doi.org/10.1021/acs.nanolett.7b00233.

[23] W.W. Li, J.J. Zhu, X.F. Xu, K. Jiang, Z.G. Hu, M. Zhu, J.H. Chu, Ultraviolet-infrared dielectric functions and electronic band structures of monoclinic VO2 nanocrystalline film: Temperature-dependent spectral transmittance, J. Appl. Phys. 110 (2011) 1–5. https://doi.org/10.1063/1.3601357.

[24] H. Kakiuchida, P. Jin, M. Tazawa, Control of thermochromic spectrum in vanadium dioxide by amorphous silicon suboxide layer, Sol. Energy Mater. Sol. Cells. 92 (2008) 1279–1284. https://doi.org/10.1016/j.solmat.2008.04.025.

[25] N.R. Mlyuka, G.A. Niklasson, C.G. Granqvist, Mg doping of thermochromic VO2films enhances the optical transmittance and decreases the metal-insulator transition temperature, Appl. Phys. Lett. 95 (2009) 2–4. https://doi.org/10.1063/1.3229949.

[26] M. Tazawa, P. Jin, S. Tanemura, Optical constants of V_1-xW_xO_2 films, Appl. Opt. 37 (1998) 1858. https://doi.org/10.1364/ao.37.001858.

[27] J.B. Kana Kana, J.M. Ndjaka, G. Vignaud, A. Gibaud, M. Maaza, Thermally tunable optical constants of vanadium dioxide thin films measured by spectroscopic ellipsometry, Opt. Commun. 284 (2011) 807–812. https://doi.org/10.1016/j.optcom.2010.10.009.

[28] S. Li, VO2-based Thermochromic and Nanothermochromic Materials for Energy-Efficient Windows, 2013.

[29] Y. Muraoka, Z. Hiroi, Metal-insulator transition of VO2 thin films grown on TiO 2 (001) and (110) substrates, Appl. Phys. Lett. 80 (2002) 583–585. https://doi.org/10.1063/1.1446215.

[30] D. Li, M. Li, J. Pan, Y. Luo, H. Wu, Y. Zhang, G. Li, Hydrothermal synthesis of Mo-doped VO2/TiO2 composite nanocrystals with enhanced thermochromic performance, ACS Appl. Mater. Interfaces. 6 (2014) 6555–6561. https://doi.org/10.1021/am500135d.

[31] S. Loquai, B. Baloukas, O. Zabeida, J.E. Klemberg-Sapieha, L. Martinu, HiPIMS-deposited

thermochromic VO2 films on polymeric substrates, Sol. Energy Mater. Sol. Cells. 155 (2016) 60–69. https://doi.org/10.1016/j.solmat.2016.04.048.

[32] L. Yang, P. Zhou, T. Huang, G. Zhen, L. Zhang, L. Bi, X. Weng, J. Xie, L. Deng, Broadband thermal tunable infrared absorber based on the coupling between standing wave and magnetic resonance, Opt. Mater. Express. 7 (2017) 2767. https://doi.org/10.1364/ome.7.002767.

[33] J.A. Ramirez-Rincon, C.L. Gomez-Heredia, A. Corvisier, J. Ordonez-Miranda, T. Girardeau, F. Paumier, C. Champeaux, F. Dumas-Bouchiat, Y. Ezzahri, K. Joulain, O. Ares, J.J. Alvarado-Gil, Thermal hysteresis measurement of the VO2 dielectric function for its metal-insulator transition by visible-IR ellipsometry, J. Appl. Phys. 124 (2018). https://doi.org/10.1063/1.5049747.

[34] J.P. Fortier, B. Baloukas, O. Zabeida, J.E. Klemberg-Sapieha, L. Martinu, Thermochromic VO2 thin films deposited by HiPIMS, Sol. Energy Mater. Sol. Cells. 125 (2014) 291–296. https://doi.org/10.1016/j.solmat.2014.03.007.

[35] Max Born, Emil Wolf, Principles of optics, 7th ed., Cambridge, 1999.

[36] S.Y. Li, G.A. Niklasson, C.G. Granqvist, Nanothermochromics: Calculations for VO2 nanoparticles in dielectric hosts show much improved luminous transmittance and solar energy transmittance modulation, J. Appl. Phys. 108 (2010) 1–8. https://doi.org/10.1063/1.3487980.

[37] A. Gonçalves, J. Resende, A.C. Marques, J. V. Pinto, D. Nunes, A. Marie, R. Goncalves, L. Pereira, R. Martins, E. Fortunato, Smart optically active VO2 nanostructured layers applied in roof-type ceramic tiles for energy efficiency, Sol. Energy Mater. Sol. Cells. 150 (2016) 1–9. https://doi.org/10.1016/j.solmat.2016.02.001.

[38] M. Panagopoulou, E. Gagaoudakis, N. Boukos, E. Aperathitis, G. Kiriakidis, D. Tsoukalas, Y.S. Raptis, Thermochromic performance of Mg-doped VO2 thin films on functional substrates for glazing applications, Sol. Energy Mater. Sol. Cells. 157 (2016) 1004–1010. https://doi.org/10.1016/j.solmat.2016.08.021.

[39] E. Gagaoudakis, E. Aperathitis, G. Michail, M. Panagopoulou, D. Katerinopoulou, V. Binas, Y.S. Raptis, G. Kiriakidis, Low-temperature rf sputtered VO2 thin films as thermochromic coatings for smart glazing systems, Sol. Energy. 165 (2018) 115–121. https://doi.org/10.1016/j.solener.2018.03.010.

[40] S. Long, X. Cao, R. Huang, F. Xu, N. Li, A. Huang, G. Sun, S. Bao, H. Luo, P. Jin, Self-Template Synthesis of Nanoporous VO2-Based Films: Localized Surface Plasmon Resonance and Enhanced Optical Performance for Solar Glazing Application, ACS Appl. Mater. Interfaces. (2019). https://doi.org/10.1021/acsami.9b03586.

[41] S. Long, X. Cao, Y. Wang, T. Chang, N. Li, L. Jin, L. Ma, F. Xu, G. Sun, P. Jin, Karst landform-like VO2 single layer solution: Controllable morphology and excellent optical performance for smart glazing applications, Sol. Energy Mater. Sol. Cells. 209 (2020) 110449. https://doi.org/10.1016/j.solmat.2020.110449.

[42] X. Li, S. Chen, S. Wang, J. Lai, C. Chen, X. Yi, Vanadium dioxide nanomaterial for smart thermochromic glazing of windows, in: A.R. Wilson (Ed.), Smart Mater. III, SPIE, 2004: p. 256. https://doi.org/10.1117/12.581995.

[43] E. Haddad, R. V. Kruzelecky, A. Hendaoui, M. Chaker, W. Jamroz, P. Poinas, Large Tuneability IR Emittance Thermal Control Coating for Space Applications, (2013). https://doi.org/10.2514/6.2013-3436.

[44] B. Baloukas, R. Beaini, S. Loquai, O. Zabeida, J.E. Klemberg-Sapieha, L. Martinu, Thermochromic VO2 coatings for energy control, in: Opt. InfoBase Conf. Pap., OSA - The Optical Society, 2019: p. MC.5. https://doi.org/10.1364/OIC.2019.MC.5.

[45] K. Sun, C.A. Riedel, A. Urbani, M. Simeoni, S. Mengali, M. Zalkovskij, B. Bilenberg, C.H. De Groot, O.L. Muskens, VO2 Thermochromic Metamaterial-Based Smart Optical Solar Reflector, ACS Photonics. 5 (2018) 2280–2286. https://doi.org/10.1021/acsphotonics.8b00119.

[46] A. Hendaoui, N. Émond, S. Dorval, M. Chaker, E. Haddad, VO2-based smart coatings with improved emittance-switching properties for an energy-efficient near room-temperature thermal control of spacecrafts, Sol. Energy Mater. Sol. Cells. 117 (2013) 494–498. https://doi.org/10.1016/j.solmat.2013.07.023.

[47] R.L. Voti, M.C. Larciprete, G. Leahu, C. Sibilia, M. Bertolotti, Optimization of thermochromic VO 2 based structures with tunable thermal emissivity, J. Appl. Phys. 112 (2012). https://doi.org/10.1063/1.4739489.

[48] D. Liu, H. Ji, R. Peng, H. Cheng, C. Zhang, Infrared chameleon-like behavior from VO2(M) thin films prepared by transformation of metastable VO2(B) for adaptive camouflage in both thermal atmospheric windows, Sol. Energy Mater. Sol. Cells. 185 (2018) 210–217. https://doi.org/10.1016/j.solmat.2018.05.042.

[49] L. Xiao, H. Ma, J. Liu, W. Zhao, Y. Jia, Q. Zhao, K. Liu, Y. Wu, Y. Wei, S. Fan, K. Jiang, Fast Adaptive Thermal Camouflage Based on Flexible VO 2 /Graphene/CNT Thin Films, Nano Lett. 15 (2015) 8365–8370. https://doi.org/10.1021/acs.nanolett.5b04090.

[50] H. Ji, D. Liu, H. Cheng, C. Zhang, L. Yang, D. Ren, Infrared thermochromic properties of monoclinic VO2 nanopowders using a malic acid-assisted hydrothermal method for adaptive camouflage, RSC Adv. 7 (2017) 5189–5194. https://doi.org/10.1039/c6ra26731a.

[51] Z. Mao, W. Wang, Y. Liu, L. Zhang, H. Xu, Y. Zhong, Infrared stealth property based on semiconductor (M)-to-metallic (R) phase transition characteristics of W-doped VO2 thin films coated on cotton fabrics, Thin Solid Films. 558 (2014) 208–214. https://doi.org/10.1016/j.tsf.2014.02.055.

[52] S. Wang, G. Liu, P. Hu, Y. Zhou, Y. Ke, C. Li, J. Chen, T. Cao, Y. Long, Largely Lowered Transition Temperature of a VO $_2$ /Carbon Hybrid Phase Change Material with High Thermal Emissivity Switching Ability and Near Infrared Regulations, Adv. Mater. Interfaces. 5 (2018) 1801063. https://doi.org/10.1002/admi.201801063.

[53] S.M. Babulanam, T.S. Eriksson, G.A. Niklasson, C.G. Granqvist, Thermochromic VO2 films for energy-efficient windows, Sol. Energy Mater. 16 (1987) 347–363. https://doi.org/10.1016/0165-1633(87)90029-3.

[54] J. Zheng, S. Bao, P. Jin, TiO2(R)/VO2(M)/TiO2(A) multilayer film as smart window: Combination of energy-saving, antifogging and self-cleaning functions, Nano Energy. 11 (2015) 136–145. https://doi.org/10.1016/j.nanoen.2014.09.023.

[55] M.J. Powell, R. Quesada-Cabrera, A. Taylor, D. Teixeira, I. Papakonstantinou, R.G. Palgrave, G. Sankar, I.P. Parkin, Intelligent Multifunctional VO2/SiO2/TiO2 Coatings for Self-Cleaning, Energy-Saving Window Panels, Chem. Mater. 28 (2016) 1369–1376. https://doi.org/10.1021/acs.chemmater.5b04419.

[56] X. Cao, N. Wang, J.Y. Law, S.C.J. Loo, S. Magdassi, Y. Long, Nanoporous thermochromic VO2 (M) thin films: Controlled porosity, largely enhanced luminous transmittance and solar modulating ability, Langmuir. 30 (2014) 1710–1715. https://doi.org/10.1021/la404666n.

[57] J.D. Jackson, Classical Electrodynamics, 3rd ed, John Wiley & Sons, New York, 1999.

[58] L. Kang, Y. Gao, Z. Chen, J. Du, Z. Zhang, H. Luo, Pt/VO2 double-layered films combining thermochromic properties with low emissivity, Sol. Energy Mater. Sol. Cells. 94 (2010) 2078–2084. https://doi.org/10.1016/j.solmat.2010.06.023.

[59] J. Faucheu, E. Bourgeat-Lami, V. Prevot, A Review of Vanadium Dioxide as an Actor of Nanothermochromism: Challenges and Perspectives for Polymer Nanocomposites, Adv. Eng. Mater. 21 (2019) 1–26. https://doi.org/10.1002/adem.201800438.

[60] O.M. Osmolovskaya, I. V. Murin, V.M. Smirnov, M.G. Osmolovsky, Synthesis of vanadium dioxide thin films and nanopowders: A brief review, Rev. Adv. Mater. Sci. 36 (2014) 70–74.

[61] J. Nag, R.F. Haglund, Synthesis of vanadium dioxide thin films and nanoparticles, J. Phys. Condens. Matter. 20 (2008). https://doi.org/10.1088/0953-8984/20/26/264016.

[62] M.E.A. Warwick, R. Binions, Advances in thermochromic vanadium dioxide films, J. Mater. Chem. A. 2 (2014) 3275–3292. https://doi.org/10.1039/C3TA14124A.

[63] S. Wang, M. Liu, L. Kong, Y. Long, X. Jiang, A. Yu, Recent progress in VO2 smart coatings: Strategies to improve the thermochromic properties, Prog. Mater. Sci. (2016). https://doi.org/10.1016/j.pmatsci.2016.03.001.

[64] M.M. Seyfouri, R. Binions, Sol-gel approaches to thermochromic vanadium dioxide coating for smart glazing application, Sol. Energy Mater. Sol. Cells. (2017). https://doi.org/10.1016/j.solmat.2016.08.035.

[65] M. Kamalisarvestani, R. Saidur, S. Mekhilef, F.S. Javadi, Performance, materials and coating technologies of thermochromic thin films on smart windows, Renew. Sustain. Energy Rev. (2013). https://doi.org/10.1016/j.rser.2013.05.038.

[66] M. Borek, F. Qian, V. Nagabushnam, R.K. Singh, M. Borek, F. Qian, V. Nagabushnam, F.L.K. Singh, Pulsed laser deposition of oriented VO2 thin films on Rcut sapphire substrates Pulsed laser deposition substrates of oriented V02 thin films on R-cut sapphire, 3288 (2014) 2012–2015. https://doi.org/10.1063/1.110177.

[67] M.J. Powell, P. Marchand, C.J. Denis, J.C. Bear, J.A. Darr, I.P. Parkin, Direct and continuous synthesis of VO 2 nanoparticles, Nanoscale. 7 (2015) 18686–18693. https://doi.org/10.1039/C5NR04444H.

[68] J.H. Son, J. Wei, D. Cobden, G. Cao, Y. Xia, Hydrothermal synthesis of monoclinic VO2 micro- and nanocrystals in one step and their use in fabricating inverse opals, Chem. Mater. 22 (2010) 3043–3050. https://doi.org/10.1021/cm903727u.

[69] L. Dai, C. Cao, Y. Gao, H. Luo, Synthesis and phase transition behavior of undoped VO2 with a strong nano-size effect, Sol. Energy Mater. Sol. Cells. 95 (2011) 712–715. https://doi.org/10.1016/j.solmat.2010.10.008.

[70] S. Ji, F. Zhang, P. Jin, Preparation of high performance pure single phase VO2 nanopowder by hydrothermally reducing the V2O5 gel, Sol. Energy Mater. Sol. Cells. 95 (2011) 3520–3526. https://doi.org/10.1016/j.solmat.2011.08.015.

[71] R. Lopez, T.E. Haynes, L.A. Boatner, L.C. Feldman, R.F. Haglund, Size effects in the structural phase transition of VO2 nanoparticles, Phys. Rev. B - Condens. Matter Mater. Phys. 65 (2002) 2241131–2241135. https://doi.org/10.1103/PhysRevB.65.224113.

[72] R. Lopez, L.C. Feldman, R.F. Haglund, Size-dependent optical properties of VO2 nanoparticle arrays, Phys. Rev. Lett. 93 (2004) 20–23. https://doi.org/10.1103/PhysRevLett.93.177403.

[73] J.B.K. Kana, J.M. Ndjaka, P.O. Ateba, B.D. Ngom, Thermochromic VO 2 thin films synthesized by rf-inverted cylindrical magnetron sputtering, 254 (2008) 3959–3963. https://doi.org/10.1016/j.apsusc.2007.12.021.

[74] G. Fu, A. Polity, N. Volbers, B.K. Meyer, Annealing effects on VO 2 thin films deposited by reactive sputtering, 515 (2006) 2519–2522. https://doi.org/10.1016/j.tsf.2006.04.025.

[75] P. Jin, S. Tanemura, Formation and thermochromism of Vo 2 films deposited by rf magnetron sputtering at low substrate temperature, Jpn. J. Appl. Phys. 33 (1994) 1478–1483. https://doi.org/10.1143/JJAP.33.1478.

[76] T.D. Manning, I.P. Parkin, R.J.H. Clark, D. Sheel, M.E. Pemble, D. Vernadou, Intelligent window coatings: Atmospheric pressure chemical vapour deposition of vanadium oxides, J. Mater. Chem. 12 (2002) 2936–2939. https://doi.org/10.1039/b205427m.

[77] T. Maruyama, T. Tago, Nickel thin films prepared by chemical vapour deposition from nickel acetylacetonate, J. Mater. Sci. 28 (1993) 5345–5348. https://doi.org/10.1007/BF00570088.

[78] D. Vernardou, M.E. Pemble, D.W. Sheel, The growth of thermochromic VO2 films on glass by atmospheric-pressure CVD: A comparative study of precursors, CVD methodology, and substrates, Chem. Vap. Depos. 12 (2006) 263–274. https://doi.org/10.1002/cvde.200506419.

[79] D.H. Kim, H.S. Kwok, Pulsed laser deposition of VO 2 thin films, 65 (1994) 3188–3190.

[80] B. Chae, H. Kim, S. Yun, B. Kim, Y. Lee, D. Youn, K. Kang, Highly oriented VO 2 thin films prepared by sol-gel deposition method, (n.d.) 1–12.

[81] Q. Shi, W. Huang, Y. Zhang, J. Yan, Y. Zhang, M. Mao, Y. Zhang, Giant Phase Transition Properties at Terahertz Range in VO 2 films Deposited by Sol À Gel Method, (2011) 3523–3527.

[82] M. Li, S. Magdassi, Y. Gao, Y. Long, Hydrothermal Synthesis of VO2 Polymorphs: Advantages, Challenges and Prospects for the Application of Energy Efficient Smart Windows, Small. 13 (2017) 1–25. https://doi.org/10.1002/smll.201701147.

[83] Y. Zhang, J. Zhang, X. Zhang, Y. Deng, Y. Zhong, C. Huang, X. Liu, X. Liu, S. Mo, Influence of different additives on the synthesis of VO2 polymorphs, Ceram. Int. 39 (2013) 8363–8376. https://doi.org/10.1016/j.ceramint.2013.04.016.

[84] J. Zhu, Y. Zhou, B. Wang, J. Zheng, S. Ji, H. Yao, H. Luo, P. Jin, Vanadium Dioxide Nanoparticle-based Thermochromic Smart Coating: High Luminous Transmittance, Excellent Solar Regulation Efficiency, and Near Room Temperature Phase Transition, ACS Appl. Mater. Interfaces. 7 (2015) 27796–27803. https://doi.org/10.1021/acsami.5b09011.

[85] Y. Gao, S. Wang, H. Luo, L. Dai, C. Cao, Y. Liu, Z. Chen, M. Kanehira, Enhanced chemical stability of VO 2 nanoparticles by the formation of SiO 2/VO 2 core/shell structures and the application to transparent and flexible VO 2-based composite foils with excellent thermochromic properties for solar heat control, Energy Environ. Sci. 5 (2012) 6104–6110. https://doi.org/10.1039/c2ee02803d.

[86] J.D. Joannopoulous, S.G. Johnson, J.N. Winn, R.D. Meade, Photonic Crystals, Molding the Flow of Light, 2nd ed., Princeton University Press, 2008.

[87] V.A. Tolmachev, T.S. Perova, J.A. Pilyugina, R.A. Moore, Experimental evidence of photonic band gap extension for disordered 1D photonic crystals based on Si, Opt. Commun. 259 (2006) 104–106. https://doi.org/10.1016/j.optcom.2005.08.025.

[88] J.B. Wright, S. Liu, G.T. Wang, Q. Li, D.D. Koleske, P. Lu, H. Xu, L.F. Lester, T.S. Luk, I. Brener,

G.S. Subramania, Multi-color arrays of III-nitride photonic crystal nanowire lasers on a single chip, 2013 Conf. Lasers Electro-Optics, CLEO 2013. (2013) 4–5. https://doi.org/10.1364/cleo_si.2013.cth3g.4.

[89] Eli Yablonovitch, Inhibited Spontaneous Emission in Solid-State Physics and Electronics, Phys. Rev. Lett. 58 (1987) 13–20. https://doi.org/10.1103/PhysRevLett.58.2059.

[90] T. Starkey, P. Vukusic, Light manipulation principles in biological photonic systems, Nanophotonics. 2 (2013) 289–307. https://doi.org/10.1515/nanoph-2013-0015.

[91] J. V. Sanders, IUCr, Diffraction of light by opals, Acta Crystallogr. Sect. A. 24 (1968) 427–434. https://doi.org/10.1107/S0567739468000860.

[92] Y. Nishijima, K. Ueno, S. Juodkazis, V. Mizeikis, H. Misawa, T. Tanimura, K. Maeda, Inverse silica opal photonic crystals for optical sensing applications, Opt. Express. 15 (2007) 12979. https://doi.org/10.1364/oe.15.012979.

[93] V. Berger, From photonic band gaps to refractive index engineering, Opt. Mater. (Amst). 11 (1999) 131–142. https://doi.org/10.1016/S0925-3467(98)00039-1.

[94] H.E. Ruda, N. Matsuura, Nano-Engineered Tunable Photonic Crystals, 2017. https://doi.org/10.1007/978-3-319-48933-9.

[95] I. Piirma, Emulsion polymerization, Academic Press, New York, 1982. https://www.worldcat.org/title/emulsion-polymerization/oclc/7925190 (accessed October 24, 2019).

[96] B. Cheng, P. Ni, C. Jin, Z. Li, D. Zhang, P. Dong, X. Guo, More direct evidence of the fcc arrangement for artificial opal, Opt. Commun. 170 (1999) 41–46. https://doi.org/10.1016/S0030-4018(99)00434-4.

[97] A. Stein, Sphere templating methods for periodic porous solids, 45 (2001) 227–239.

[98] A. Balestreri, L.C. Andreani, M. Agio, Optical properties and diffraction effects in opal photonic crystals, Phys. Rev. E - Stat. Nonlinear, Soft Matter Phys. 74 (2006) 1–8. https://doi.org/10.1103/PhysRevE.74.036603.

[99] J. V. SANDERS, Colour of Precious Opal, Nature. 204 (1964) 1151–1153. https://doi.org/10.1038/2041151a0.

[100] T. Ruhl, P. Spahn, G.P. Hellmann, Artificial opals prepared by melt compression, Polymer (Guildf). 44 (2003) 7625–7634. https://doi.org/10.1016/j.polymer.2003.09.047.

[101] T. Ruhl, P. Spahn, H. Winkler, G.P. Hellmann, Large area monodomain order in colloidal crystals, Macromol. Chem. Phys. 205 (2004) 1385–1393. https://doi.org/10.1002/macp.200400009.

[102] O.L. Pursiainen, J.J. Baumberg, H. Winkler, B. Viel, P. Spahn, T. Ruhl, Nanoparticle-tuned structural color from polymer opals, Opt. Express. 15 (2007) 9553. https://doi.org/10.1364/OE.15.009553.

[103] J.C.M. Garnett, Colours in Metal Glasses and in Metallic Films, Philos. Trans. R. Soc. A Math. Phys. Eng. Sci. 203 (1904) 385–420. https://doi.org/10.1098/rsta.1904.0024.

[104] D.A.G. Bruggeman, Berechnung verschiedener physikalischer Konstanten von heterogenen Substanzen. I. Dielektrizitätskonstanten und Leitfähigkeiten der Mischkörper aus isotropen Substanzen, Ann. Phys. 416 (1935) 636–664. https://doi.org/10.1002/andp.19354160705.

[105] F. Abelès, La théorie générale des couches minces, J. Phys. Radium. 11 (1950) 307–309.

[106] J.R. de Lasson, L.H. Frandsen, P. Gutsche, S. Burger, O.S. Kim, O. Breinbjerg, A. Ivinskaya, F. Wang, O. Sigmund, T. Häyrynen, A. V. Lavrinenko, J. Mørk, N. Gregersen, Benchmarking five numerical simulation techniques for computing resonance wavelengths and quality factors in photonic crystal membrane line defect cavities, Opt. Express. 26 (2018) 11366. https://doi.org/10.1364/oe.26.011366.

[107] D.M. Sullivan, Electromagnetic simulation using the FDTD method, Wiley, 2013.

[108] B. Cowan, FDTD modeling of photonic crystal fibers, EE256 Final Proj. (n.d.) 1–7. http://scholar.google.com/scholar?hl=en&btnG=Search&q=intitle:FDTD+modeling+of+photonic+crystal+fibers#0.

[109] A. Lavrinenko, P.I. Borel, L.H. Frandsen, M. Thorhauge, A. Harpøth, M. Kristensen, T. Niemi, H.M.H. Chong, Comprehensive FDTD modelling of photonic crystal waveguide components, Opt. Express. 12 (2004) 234. https://doi.org/10.1364/opex.12.000234.

[110] M.J. Cryan, D.C.L. Wong, I.J. Craddock, S. Yu, J. Rorison, C.J. Railton, Calculation of losses in 2-D photonic Crystal membrane waveguides using the 3-D FDTD method, IEEE Photonics Technol. Lett. 17 (2005) 58–60. https://doi.org/10.1109/LPT.2004.837914.

[111] A. Taflove, K. Umashankar, Radar Cross Section of General Three-Dimensional Scatterers, IEEE Trans. Electromagn. Compat. EMC-25 (1983) 433–440. https://doi.org/10.1109/TEMC.1983.304133.

[112] C.M. Furse, S.P. Mathur, O.P. Gandhi, Improvements to the finite-difference time-domain method for calculating the radar cross section of a perfectly conducting target, IEEE Trans. Microw. Theory Tech. 38 (1990) 919–927. https://doi.org/10.1109/22.55785.

[113] D.M. Sullivan, A frequency-dependent FDTD method for biological applications, IEEE Trans. Microw. Theory Tech. 40 (1992) 532–539. https://doi.org/10.1109/22.121729.

[114] D. Sullivan, Three-dimensional computer simulation in deep regional hyperthermia using the finite-difference time-domain method, IEEE Trans. Microw. Theory Tech. 38 (1990) 204–211. https://doi.org/10.1109/22.46431.

[115] D.M. Sullivan, D.T. Borup, O.P. Gandhi, Use of the Finite-Difference Time-Domain Method in Calculating EM Absorption in Human Tissues, IEEE Trans. Biomed. Eng. BME-34 (1987) 148–157. https://doi.org/10.1109/TBME.1987.326039.

[116] M.G. Moharam, T.K. Gaylord, Rigorous coupled-wave analysis of planar-grating diffraction, J. Opt. Soc. Am. 71 (1981) 811–818. https://doi.org/10.1364/JOSA.71.000811.

[117] L. Li, C.W. Haggans, Convergence of the coupled-wave method for metallic lamellar diffraction gratings, J. Opt. Soc. Am. A. 10 (1993) 1184. https://doi.org/10.1364/josaa.10.001184.

[118] P. Lalanne, G.M. Morris, Highly improved convergence of the coupled-wave method for TM polarization, J. Opt. Soc. Am. A. 13 (1996) 779–784. https://doi.org/10.1364/josaa.13.000779.

[119] G. Granet, B. Guizal, Efficient implementation of the coupled-wave method for metallic lamellar gratings in TM polarization, J. Opt. Soc. Am. A. 13 (1996) 1019–1023.

[120] L. Li, Use of Fourier series in the analysis of discontinuous periodic structures, J. Opt. Soc. Am. A. 13 (1996) 1870–1876.

[121] E. Silberstein, Généralisation de la méthode modale de Fourier aux problèmes de diffraction en optique intégrée . Application aux convertisseurs modaux par ingénierie des modes de Bloch . To cite this version : HAL Id : tel-00003101 THÈSE DE DOCTORAT DE L ' UNIVERSITÉ PA, Université Pierre et Marie Curie - Paris VI, 2003.

[122] L. Li, 4. Mathematical Reflections on the Fourier Modal Method in Grating Theory, in: Math. Model. Opt. Sci., Society for Industrial and Applied Mathematics, 2001: pp. 111–139. https://doi.org/10.1137/1.9780898717594.ch4.

[123] D.Y.K. Ko, J.R. Sambles, Scattering matrix method for propagation of radiation in stratified media: attenuated total reflection studies of liquid crystals, J. Opt. Soc. Am. A. 5 (1988) 1863. https://doi.org/10.1364/josaa.5.001863.

[124] N.P.K. Cotter, T.W. Preist, J.R. Sambles, Scattering-matrix approach to multilayer diffraction, J. Opt. Soc. Am. A. 12 (1995) 1097. https://doi.org/10.1364/josaa.12.001097.

[125] D.Y.K. Ko, J.C. Inkson, Matrix method for tunneling in heterostructures: Resonant tunneling in multilayer systems, Phys. Rev. B. 38 (1988) 9945–9951. https://doi.org/10.1103/PhysRevB.38.9945.

[126] M. Auslender, S. Hava, Scattering-matrix propagation algorithm in full-vectorial optics of multilayer grating structures, Opt. Lett. 21 (1996) 1765. https://doi.org/10.1364/ol.21.001765.

[127] E.L. Tan, A concise and efficient scattering matrix formalism for stable analysis of elastic wave propagation in multilayered anisotropic solids, Ultrasonics. 41 (2003) 229–236. https://doi.org/10.1016/S0041-624X(02)00447-X.

[128] N. Lyndin, MC Grating design and analysis by Modal and Chandezon methods, (2018).

[129] I.C. Botten, M.S. Craig, R.C. McPhedran, J.L. Adams, J.R. Andrewartha, The dielectric lamellar diffraction grating, Opt. Acta (Lond). 28 (1981) 413–428. https://doi.org/10.1080/713820571.

[130] M. Foresti, L. Menez, A. V. Tishchenko, Modal method in deep metal-dielectric gratings: the decisive role of hidden modes, J. Opt. Soc. Am. A. 23 (2006) 2501. https://doi.org/10.1364/josaa.23.002501.

[131] D.D. Johnson, Introduction to Engineering Materials, (2004). https://nanohub.org/resources/5488/download/ch3_p3.pdf.

[132] C. Kittel, Physique de l'état solide - Cours et problèmes - Livre Physique et sciences de l'univers de Charles Kittel - Dunod, 8th ed., 2019. https://www.dunod.com/sciences-techniques/physique-etat-solide-cours-et-problemes-0.

[133] C. Kittel, Physique de l'état solide - Cours et problèmes - Livre Physique et sciences de l'univers de Charles Kittel - Dunod, 8th ed., 2019.

[134] Q. Cridling, Influence of the substrate surface on optical properties and color of anodized titanium, École nationale supérieure des mines (Saint-Etienne), 2018.

[135] A. Avoine, P.N. Hong, H. Frederich, J.M. Frigerio, L. Coolen, C. Schwob, P.T. Nga, B. Gallas, A. Maître, Measurement and modelization of silica opal reflection properties: Optical determination of the silica index, Phys. Rev. B - Condens. Matter Mater. Phys. 86 (2012) 1–7. https://doi.org/10.1103/PhysRevB.86.165432.

[136] B.J. C Maxwell Garnett, VII. Colours in metal glasses, in metallic films, and in metallic solutions.—II, Philos. Trans. R. Soc. London. Ser. A, Contain. Pap. a Math. or Phys. Character. 205 (1906) 237–288. https://doi.org/10.1098/rsta.1906.0007.

[137] G.A. Niklasson, C.G. Granqvist, O. Hunderi, Effective medium models for the optical properties of inhomogeneous materials, Appl. Opt. 20 (1981) 26. https://doi.org/10.1364/ao.20.000026.

[138] G.A. Niklasson, C.G. Granqvist, O. Hunderi, Effective medium models for the optical properties

of inhomogeneous materials, Appl. Opt. 20 (1981) 26. https://doi.org/10.1364/ao.20.000026.

[139] R. Ruppin, Validity Range of the Maxwell-Garnett Theory, Phys. Status Solidi. 87 (1978) 619–624. https://doi.org/10.1002/pssb.2220870227.

[140] E. Hutter, J.H. Fendler, Exploitation of localized surface plasmon resonance, Adv. Mater. 16 (2004) 1685–1706. https://doi.org/10.1002/adma.200400271.

[141] K. Busch, S. John, Photonic band gap formation in certain self-organizing systems, Phys. Rev. E - Stat. Physics, Plasmas, Fluids, Relat. Interdiscip. Top. 58 (1998) 3896–3908. https://doi.org/10.1103/PhysRevE.58.3896.

[142] L.D. Tuyen, C.Y. Wu, T.K. Anh, L.Q. Minh, H.-C. Kan, C.C. Hsu, Fabrication and optical characterisation of SiO_2 opal and SU-8 inverse opal photonic crystals, J. Exp. Nanosci. 7 (2012) 198–204. https://doi.org/10.1080/17458080.2010.515249.

[143] E. Palacios-Lidón, B.H. Juárez, E. Castillo-Martínez, C. López, Optical and morphological study of disorder in opals, J. Appl. Phys. 97 (2005) 1–7. https://doi.org/10.1063/1.1851014.

[144] Z.Y. Li, Z.Q. Zhang, Photonic bandgaps in disordered inverse-opal photonic crystals, Adv. Mater. 13 (2001) 433–436. https://doi.org/10.1002/1521-4095(200103)13:6<433::AID-ADMA433>3.0.CO;2-O.

[145] Z. Král, L. Vojkůvka, E. Garcia-Caurel, J. Ferré-Borrull, L.F. Marsal, J. Pallarès, Calculation of Angular-Dependent Reflectance and Polarimetry Spectra of Nanoporous Anodic Alumina-Based Photonic Crystal Slabs, Photonics Nanostructures - Fundam. Appl. 7 (2009) 12–18. https://doi.org/10.1016/j.photonics.2008.11.005.

[146] R. Charrière, Q. Cridling, M. Maillet, M. Pedeferri, D. Delafosse, Determination of oxidized metals' oxide layer thickness from local extrema of reflectance spectra: theoretical basis and application to anodized titanium, Meas. Sci. Technol. 31 (2020) 125601. https://doi.org/10.1088/1361-6501/ab9cde.

[147] A.D. Rakić, Algorithm for the determination of intrinsic optical constants of metal films: application to aluminum, Appl. Opt. 34 (2009) 4755. https://doi.org/10.1364/ao.34.004755.

École Nationale Supérieure des Mines
de Saint-Étienne

NNT : 2020LYSEM025

Cindy PERALLE

ETUDE DES PROPRIETES OPTIQUES DE REVETEMENTS THERMOCHROMES NANOSTRUCTURES A BASE DE VO2

Spécialité : Sciences et Génie des Matériaux

Mots clefs : dioxyde de vanadium, opale, cristal photonique, bande interdite photonique, modèle optique, méthode modale de Fourier

Résumé :

Le dioxyde de vanadium (VO_2) subit une transition de phase de semi-conducteur vers métallique à une certaine température de transition. Ceci se traduit par des changements de ses propriétés physiques, en particulier optiques, faisant de lui un matériau prometteur pour des applications comme revêtement pour les vitres, bâtiments et satellites, à fort rendement énergétique, ainsi que pour du camouflage. Le comportement optique d'une opale contenant des nanoparticules de VO_2 est étudié à travers un modèle optique basé sur la méthode modale de Fourier (FMM) adaptée aux cristaux photoniques 3D. La périodicité introduite génère un pic de réflectance lié à une bande interdite photonique (PBG) qui dépend de différents paramètres tels que l'indice de réfraction des matériaux, la taille des sphères de l'opale et la concentration de VO_2. Pour répondre aux différentes applications ciblées, les propriétés optiques du matériau sont étudiées du visible au mid-infrarouge, afin de calculer les transmittances lumineuse et solaire d'une part, et l'émissivité d'autre part. L'impact de la structure est limité par la condition de transparence liée à l'application vitres. Un plus fort effet de PBG est observé dans le cas de matériaux opaques, principalement à faibles températures. Il permet une diminution de 27% de la différence d'émissivité entre les cas chaud et froid, ce qui se traduit par une hausse de 3°C de la température de surface du matériau dans le cas froid, résultat intéressant pour les applications bâtiments et satellites. Enfin, afin de mieux modéliser le comportement de matériaux réels, du désordre dans la structure est apportée au modèle.

École Nationale Supérieure des Mines
de Saint-Étienne

NNT : 2020LYSEM025

Cindy PERALLE

STUDY OF THE OPTICAL PROPERTIES OF NANOSTRUCTURED THERMOCHROMIC COATINGS CONTAINING VO2 NANOPARTICLES

Specialty: Sciences et Génie des Matériaux

Keywords: vanadium dioxide, opal photonic crystal, photonic crystal, photonic bandgap, optical model, Fourier modal method

Abstract:

Vanadium dioxide (VO_2) encounters a phase transition from semiconducting to metallic at a certain transition temperature, which results in a change of its physical properties, in particular its optical properties, making it a promising material for applications like energy efficient coating for windows, buildings, satellites and camouflage. The optical behavior of a polymer opal photonic crystal containing VO_2 nanoparticles is studied through an optical model based on the Fourier modal method adapted to 3D photonic crystals. The introduced periodicity generates a reflectance peak related to a photonic bandgap (PBG) which depends on various parameters like the materials refractive indexes, the opal spheres size and the VO_2 concentration. In response to the target applications, the material optical properties are studied from the visible to the mid-infrared spectral range, in order to calculate the luminous and solar transmittance on one hand, and the emissivity on the other hand. The structure impact is limited due to the transparency condition linked to the glazing application. However, a stronger PBG effect is observed in the case of opaque materials, especially at low temperatures. This PBG causes a 27% decrease of the emissivity modulation at the VO_2 phase transition which translates into a 3 °C rise of the material surface temperature in cold conditions. This property is interesting for applications as energy efficient coating for buildings and satellites. Finally, in order to mimic the behavior of real materials, structural disorder is introduced in the model.